High-gradient and high-efficiency linear accelerators for hadron therapy

THÈSE N^{O} 8246 (2018)

PRÉSENTÉE LE 16 FÉVRIER 2018

À LA FACULTÉ DES SCIENCES DE BASE
LABORATOIRE DE PHYSIQUE DES ACCÉLÉRATEURS DE PARTICULES
PROGRAMME DOCTORAL EN PHYSIQUE

ÉCOLE POLYTECHNIQUE FÉDÉRALE DE LAUSANNE

POUR L'OBTENTION DU GRADE DE DOCTEUR ÈS SCIENCES

PAR

Stefano BENEDETTI

acceptée sur proposition du jury:

Prof. R. Houdré, président du jury
Prof. L. Rivkin, Dr A. Grudiev, directeurs de thèse
Prof. A. Faus-Golfe, rapporteuse
Dr M. Dehler, rapporteur
Prof. G. Burt, rapporteur

ÉCOLE POLYTECHNIQUE
FÉDÉRALE DE LAUSANNE

Suisse
2018

Ai miei genitori

Acknowledgements

I would like to first thank my thesis supervisor Dr. Alexej Grudiev for his consistent support during these years. His most precious advice that I will take with me is to start a simulation only when the result is already known, or at least guessed. If I will reach only one half of his analytical skills I will be satisfied by my professional career.

I am grateful to Prof. Leonid Rivkin for having me accepted as PhD student and for the support in participating to the CERN accelerator schools in Prague and Wien, and to the JUAS school in Archamps.

I am deeply indebted to Prof. Ugo Amaldi. He first motivated and allowed me to work in the field of medical particle accelerators. I did not plan to start a PhD thesis in this field, but his enthusiasm pushed me in this direction. If someone can be called "guilty" for this thesis, that is him.

Thanks to Dr. Andrea Latina, who has been half a supervisor and half a colleague and a friend. I will always remember his patience in driving me through the secrets of beam dynamics.

Thanks to all my TERA colleagues of the first generation: Valeria, Alessandra, Daniele, Caterina, Fabrizio, Carlo, Mattia, Mohammad. And in particular thanks to Alberto, my first supervisor, and to Martina and Giovanni, for their precious advices and help in reviewing documents. From a professional point of view, those first years spent with you was the happiest period of my thesis.

I am grateful to my CERN colleagues Daniel, Anastasiya, Theo, Ben and Benjamin for their help in setting up and running the cavity experiment. Thanks to my office-mate Sam who, besides all the work she put in the experiment, bore me during some very stressful last months of writing. And I would like to thank Dr. Igor. Syratchev and Dr. Walter Wuensch, whose passion towards physics animated in a pleasant way multiple CLIC RF meetings and inspired me.

Thanks to the TERA colleagues of the second generation, Mohammad, Pedro and in particular to Vittorio and Enrico, who took the not easy task to carry the torch of hadron therapy research. May it always shine!

Acknowledgements

Last but not least, I wish to express my gratitude to my family, who probably absorbed mostly the low moments, and helped me through them, without getting the nice periods. For this I am foremost thankful.

Plateau des Glières, 19 Août 2017

S. B.

Abstract

Hadron beams – approximately 200 MeV protons a nd 400 MeV/u fully stripped carbon ions – are better suited to treat deep-seated tumours than X ray beams – produced by electrons accelerated by linear accelerators (linacs) to 5-25 MeV – because they leave the maximum energy density at the end of their range in matter, in the so-called Bragg peak. This physical property allows dose depositions that are more conformal to the tumour target and spare much better the surrounding healthy tissues, so that hadron therapy treatment rooms could substitute X ray therapy rooms (about 20 000 worldwide) if the needed accelerators could be made of similar dimensions and costs.

Cyclotrons and synchrotrons are at the heart of today proton and carbon ion therapy centres, respectively. At the end of 2015, more than 130 000 patients have been treated with proton beams and almost 20 000 with carbon ions [Particle Therapy Co-Operative Group data, https://www.ptcog.ch/index.php/patient-statistics]. High frequency hadron therapy linacs have been studied in the last 30 years. Their main advantage is represented by their active beam energy modulation, which permits quick treatments with superior beam quality and novel dose delivery techniques.

This thesis is the last of many research works on the development of linear accelerators for hadron therapy. The preliminary design of two linear accelerator facilities, for proton therapy (TULIP) and carbon ion therapy (CABOTO), was completed. This closed an activity that started well before the begin of this PhD.

The introductory Chapter will quickly review the rationale of hadron therapy as a treatment methodology, which has been nicely covered in a number of articles and thesis before. More space will be dedicated to discuss the advantages of linacs in hadron therapy compared to state-of-art technologies, and to discuss the differences between *cyclinac* and *all-linac* solutions. Finally, the most important past research activities based on which this thesis started will be presented. The theory of linear accelerators is not presented, since many books cover it in detail. Instead, along the different Chapters, short theoretical discussions will be given when judged necessary to fully explain the choices made.

The second Chapter is the largest of this thesis. It describes the RF design of accelerating structures performed for the proton and carbon ion therapy facilities later on presented. The

first cavity presented is a 750 MHz IH structure, which represents an ideal continuation of the recently built 750 MHz CERN RFQ. Both RF efficiency and beam dynamics considerations will be presented to prove this statement. For beam energies higher than 10 MeV/u, a side coupled DTL cavity was considered. Both these two accelerating structures require a fairly low accelerating gradient, and their design is in common between the two projects studied in this thesis. Finally, for the proton therapy linac, two high-gradient optimized cavities were considered for beam energies above 70 MeV. A backward travelling wave cavity, magnetically coupled, which has been built and tested. And a side coupled cavity, which has been 3D RF designed but not built. For the carbon ion therapy linac, the RF efficiency is the most important parameter, and the accelerating structure could not be optimized in terms of high gradient. Thus, for this project, for energies higher than 100 MeV/u a high efficiency side coupled cavity was considered. As discussed in detail, this is a fundamentally different RF design from the high gradient one.

A not negligible time of the present thesis was devoted to the development of beam dynamics codes. Partially, this was motivated by the will to better learn beam dynamics. However, the linear accelerators studied have substantial differences between each other, and non black-box tools permit to add features as necessary, adapting to the design needs. To ease the reading, the discussion of these tools has been put in the Appendix.

After the second Chapter, and ideally the Appendix on beam dynamics, the reader has all the means to fully comprehend the following Chapters, where the proton and carbon ion linac designs are eventually presented.

The third Chapter is dedicated to the proton linac design, called TULIP: TUrning LInac for Protontherapy. TULIP main characteristic is its compactness, which required the study of the high gradient accelerating structures previously discussed. The Chapter starts with a general overview of the linac layout, followed by the detailed description of the beam dynamics studies performed. An error study of quadrupoles misalignment completes the Chapter.

The forth Chapter describes the carbon ion linac design, called CABOTO: CArbon BOoster for Therapy in Oncology. This Chapter follows the same scheme of the TULIP one. In addition, given some recent interest towards this technology, and given the similarities with carbon ions from a linac point of view, a preliminary design of an He therapy facility is discussed. The Chapter is concluded by a preliminary characterization of hadron therapy linacs costs.

The fifth Chapter presents the experimental activity performed on the backward travelling wave prototype built. Goal of the test is to study the high-gradient break-down limitation of S-Band cavities. Such studies were conducted extensively by CLIC (Compact Linear Collider) on 12 and 30 GHz accelerating structures. TERA Foundation, in collaboration with CLIC, started a high gradient test on S-Band and C-Band standing wave single RF cells. The present test profited of the results of these experiments, and it represents the first attempt to study the high gradient limits of a full accelerating structure operating at 3 GHz. After the description of the cavity RF tuning, the status of the test is presented, highlighting some interesting

peculiarities of the design. The Chapter is concluded by the study of dark current capture in non ultra-relativistic cavities.

Keywords: hadron therapy, linac, RF cavity, high gradient test, beam dynamics, breakdown rate

Sintesi

I fasci di adroni - protoni di circa 200 MeV e ioni carbonio completamente strippati di circa 400 MeV/u - sono più indicati nel trattamento di tumori profondi rispetto ai raggi X - prodotti da elettroni accelerati da acceleratori lineari (linacs) fino a 5-25 MeV - in quanto i primi rilasciano il massimo della densità di energia alla fine del proprio percorso attraverso la materia, nel cosiddetto picco di Bragg. Questa proprietà fisica permette deposizioni di dose più conformi al volume del tumore che si vuole colpire, e permette di diminuire la deposizione di dose nei tessuti sani circostanti. Per queste ragioni, le sale di trattamento con adroni potrebbero sostituire le sale di radio terapia, all'incirca 20 000 nel mondo, se gli acceleratori di adroni potessero essere costruiti in dimensioni e costi simili rispetto agli acceleratori di elettroni.

Ciclotroni e sincrotroni sono gli acceleratori di particelle usati attualmente nei centri di terapia con, rispettivamente, protoni e ioni carbonio. Alla fine del 2015, piu' di 150 000 pazienti sono stati trattati con fasci di protoni e quasi 20 000 con fasci di ioni carbonio [dati da Particle Therapy Co-Operative Group, https://www.ptcog.ch/index.php/patient-statistics]. I linacs ad alta frequenza per adronterapia sono stati studiati negli ultimi 30 anni. Il loro principale vantaggio è rappresentato dalla possibilita' di variare l'energia del fascio in modo attivo, permettendo trattamenti veloci con una superiore qualità del fascio e attraverso l'utilizzo di metodi di trattamento innovativi.

Questa tesi è l'ultima di una serie di lavori di ricerca sullo sviluppo di acceleratori lineari per adronterapia. È stato completato il disegno preliminare di due centri di terapia, con protoni (TULIP) e ioni carbonio (CABOTO), basati su acceleratori lineari, concludendo un'attività che è cominciata ben prima dell'inizio di questa tesi di dottorato.

Il Capitolo introduttivo argomenterà sinteticamente i benefici dell'utilizzo dell'adronterapia come metodo di trattamento, tema già trattato in dettaglio in molteplici articoli e tesi precendentemente. Maggiore spazio verrà dedicato alla discussione dei vantaggi dei linac per adronterapia rispetto alle tecnologie attuali, e al confronto tra i concetti di *cyclinac* e *all-linac* Infine, verranno elencate le più importanti ricerche passate sulla base delle quali questa tesi è cominciata. La teoria degli acceleratori lineari non sarà affrontata, in quanto molti libri la affrontano già in dettaglio. Invece, nei capitoli successivi, brevi discussioni teoriche verranno proposte, qualore ritenuto necessario, per motivare appieno le scelte progettuali proposte.

Il secondo Capitolo è il più corposo della presente tesi. Descrive il disegno RF delle strutture acceleranti condotto nel contesto della progettazione dei centri di terapia per protoni e ioni carbonio discussi in seguito. La prima cavità accelerante presentata è una struttura IH a 750 MHz, che rappresenta una continuazione ideale del RFQ a 750 MHz recentemente construito al CERN. Verranno presentate motivazioni, sia dal punto di vista RF che di dinamica delle particelle, per motivare tale asserzione. Per energie maggiori di 10 MeV/u, una cavità DTL è stata considerata. Sia l'IH che il DTL richiedono, per i progetti in esame, gradienti acceleranti modesti, e il loro disegno è in comune per i progetti con protoni e ioni carbonio. Infine, per il linac per protoni, due cavità ottimizzate per alti gradienti sono state considerate per energie superiori a 70 MeV. Una cavità con propagazione inversa dell'onda elettromagnetica, che è stata costruita e testata. E una cavità con celle accoppianti, che è stata progetta con disegno RF 3D, ma non costruita. Per il progetto con ioni carbonio, l'efficienza RF è il parametro più importante, e dunque le cavità non sono state ottimizzate in termini di alti gradienti acceleranti. Di conseguenza, per quest'ultimo progetto, per energie maggiori di 100 MeV/u è stato considerata una cavità con celle accoppianti ad alta efficienza RF. Come verrà discusso, si tratta di una differenza fondamentale, a livello di disegno RF, rispetto a una cavità ad alto gradiente.

Un tempo non trascurabile della presente tesi di dottorato è stato dedicato allo sviluppo di codici usati per il disegno dei linac e per il tracciamento dei fasci di particelle. L'utilizzo di codici sviluppati ad-hoc è parzialmente motivata dalla volontà di apprendimento. Ciononostante, gli acceleratori lineari studiati presentano differenze sostanziali gli uni dagli altri, e codici sviluppati in proprio permettono di essere modificati e/o di aggiungere funzionalità a secaonda delle necessità del progetto. Per rendere più snella la lettura della tesi, la discussione di questi codici è riportata in Appendice.

Alla fine del secondo Capitolo, e idealmente dell'Appendice dedicata ai codici di dinamica del fascio, il lettore possiede tutti gli strumenti necessari a comprendere i Capitoli tre e quattro, dove il progetto degli acceleratori lineari per terapia con protoni e ioni carbonio è infine discusso.

Il terzo Capitolo è dedicato al linac per protoni, chiamato TULIP: TUrnin LInac for Protontherapy. La principale caratteristica di TULIP è la sua dimensione compatta, che ha richiesto lo studio delle cavità ad alto gradiente precedentemente discusse. Il Capitolo inizia con una panoramica sulla struttura del progetto, seguita da una discussione approfondita degli studi di dinamica delle particelle effettuati. Uno studio di disallineamento dei quadrupoli completa il Capitolo.

Il quarto Capitolo descrive il linac per ioni carbonio, chiamato CABOTO: CArbon BOoster for Therapy in Oncology. Questo Capitolo segue lo stesso schema del precedente dedicato a TULIP. In aggiunta, visto il recente interesse verso questa tecnologia, e considerate le simulitudini con un progetto ad ioni carbonio da un punto di vista tecnico, verrà presentato un disegno preliminare di linac per terapia con ioni elio. Il Capitolo si conclude con una discussione

preliminare sul costo di linac per adronterapia.

Il quinto Capitolo presenta le attività sperimentali sulla prototipo di cavità con propagazione inversa dell'onda elettromagnetica. L'obiettivo dell'esperimento è stato lo studio dei limiti in termini di scariche di elettroni in funzione del gradiente accelerante, per cavità in banda S. Questi studi sono stati condotti in modo estensivo da CLIC (Compact Linear Collider study) su strutture acceleranti a 12 e 30 GHz. La Fondazione TERA, in collaborazione con CLIC, ha iniziato un serie di esperimenti di alto gradiente su celle RF con onda stazionaria in banda S e C. L'esperimento attuale parte da questi risultati, e rappresenta il primo tentativo di studio di una struttura accelerante completa operante a 3 GHz in termini di massimo gradiente accelerante raggiungibile. Dopo la descrizione dell'aggiustamento in frequenza della cavità prodotta, lo stato dell'esperimento verrà presentato, sottolineando alcuni aspetti interessanti del disegno proposto. Il Capitolo si conclude con lo studio della cattura di correnti parassite di elettroni in strutture acceleranti per particelle non ultra-relativistiche.

Keywords: Adroterapia, linac, cavità RF, test ad alto gradientie, dinamica dei fasci di particelle, breakdown rate

Contents

Acknowledgements **v**

Abstract (English/Italiano) **vii**

List of figures **xix**

List of tables **xxv**

Acronyms **xxvii**

1 Introduction **1**
1.1 Physics of hadron therapy . . . 3
1.1.1 Longitudinal dose profile . . . 3
1.1.2 Lateral dose profile . . . 8
1.1.3 Radiobiology . . . 9
1.1.4 Summary on hadron therapy physics . . . 13
1.2 Rationale of linear accelerators for hadron therapy . . . 13
1.2.1 Dose delivery systems for hadron therapy . . . 15
1.2.2 Advantages of linacs for hadron therapy other than dose delivery system 16
1.3 The starting point . . . 17
1.3.1 Comparison between *cyclinac* and *all-linac* concepts . . . 18

2 RF design of accelerating structures for TULIP and CABOTO **23**
2.1 Main codes and assumptions used . . . 24
2.2 The high-efficiency 750 MHz IH accelerating structure . . . 28
2.2.1 The choice of low beta section accelerators . . . 28
2.2.2 RF optimization of TM and TE mode DTL cavities . . . 32
2.2.3 Regular cell design . . . 34
2.2.4 Thermal analysis . . . 36
2.2.5 End-cells design . . . 37
2.2.6 Dipole kicks and transversally focusing IH cavities . . . 39
2.3 The high-efficiency 3 GHz DTL . . . 44
2.3.1 Regular cell design . . . 45
2.3.2 Criticality and points of strength . . . 48
2.4 The high-gradient 3 GHz BTW accelerating structure . . . 50

2.4.1 A backward travelling wave accelerator 52
2.4.2 Regular cell design 53
2.4.3 Single cell mechanical studies 58
2.4.4 End-cells design 63
2.4.5 The final prototype 65
2.4.6 Power recirculation in a TW structure 68
2.5 The high-gradient 3 GHz CCL accelerating structure 71
2.5.1 Regular cell and quintuplet design 71
2.5.2 End-cells design 73
2.5.3 Machinability considerations 76
2.6 RF comparison between CCL and BTW HG solutions 77
2.7 The high-efficiency 3 GHz CCL accelerating structure 82
2.7.1 100 MeV/u cell 82
2.7.2 430 MeV/u cell 86
2.7.3 Summary and some interesting sensitivity considerations 87
2.7.4 Assessment of a different RF coupling 90

3 TULIP: a high-gradient linear accelerator for proton therapy 93
3.1 General layout 93
3.1.1 From 5 to 10 MeV 95
3.1.2 From 10 to 70 MeV 96
3.1.3 From 70 to 230 MeV 99
3.2 Beam dynamics in a *cyclinac* solution 103
3.3 Quadrupole misalignments 105
3.4 Start-to-end simulation: from 5 MeV to 230 MeV 107

4 CABOTO: a high-efficiency linear accelerator for carbon ion therapy 113
4.1 General layout 114
4.1.1 From 2.5 MeV/u to 10 MeV/u 116
4.1.2 From 10 MeV/u to 100 MeV/u 118
4.1.3 From 100 MeV/u to 430 MeV/u 120
4.2 Quadrupole misalignments 121
4.3 Start-to-end simulation: from 2.5 MeV/u to 430 MeV/u 124
4.4 A He therapy facility based on the CABOTO design 127
4.5 Cost estimation of linacs for hadron therapy 127

5 Low and high power measurements of the BTW structure prototype 133
5.1 RF measurements and tuning of the prototype 133
5.1.1 Second tuning test 135
5.2 High power test 138
5.2.1 High power test set-up 138
5.2.2 First check - The pulse shape 142

5.2.3 Conditioning phase 142
5.2.4 BD identification 144
5.3 Dark current analysis 154
5.4 First results of the high gradient test 160
5.4.1 Remarks on frequency dependence and the Kilpatrick criterion 161

6 Conclusions **165**

A Beam dynamics and linac design codes used **169**
A.1 Linac design code 170
A.2 RF-Track: a minimalistic multipurpose tracking code 172
A.2.1 Code description 173
A.2.2 Benchmark of RF-Track with other codes 176
A.2.3 Field map generation and main assumptions 176

B Selected publications **183**

Bibliography **223**

Curriculum Vitae **225**

List of Figures

1.1 Cumulative number of hadron therapy centers as a function of time 2
1.2 Proton therapy centres in Europe and worldwide 2
1.3 Longitudinal dose profile of X-rays, protons and carbon ions 4
1.4 Specific energy loss vs relativistic momentum for different ions 6
1.5 C^{6+} dose deposition and Spread Out Bragg Peak (SOPB) 7
1.6 2D dose profile of proton, helium, and carbon ion beams 10
1.7 DNA damages and cell survival curve 11
1.8 Fractioning principle 12
1.9 RBE vs LET data 13
1.10 Linacs active energy variation timescale 15
1.11 Passive and active dose delivery systems 16
1.12 Sketch of TULIP *all-linac* and *cyclinac* solution 20
1.13 Sketch of CABOTO *all-linac* and *cyclinac* solution 21

2.1 Field analysis of the 10 MeV/u IH RF cell with the metod of Eq. 2.1 25
2.2 Field analysis of the 10 MeV/u IH RF cell with the metod of Eq. 2.2 26
2.3 Field analysis of the 153 MeV/u BTW RF cell with the metod of Eq. 2.2 27
2.4 Mechaical view of selcted 5 MeV/u cells and cutoff frequencies 29
2.5 ZTT as a function of the geometric βs for the optimized low β cavities considered. 30
2.6 Q-factor and R'/Q as a function of the geometric βs for the optimized low β cavities considered 31
2.7 Optimum cell gap and radius as a function of the geometric βs for the low β cavities considered 31
2.8 Mechanical comparison between selected 5 MeV/u cells 33
2.9 3 GHz DTL structure at 70 MeV/u 33
2.10 Transverse section of 5 MeV/u cells: CERN RFQ and IH cavity 34
2.11 Optimization of an IH cavity 35
2.12 Results of the 5 MeV/u IH cavity optimization 36
2.13 Regular cell designs and assembly view of the IH 750 MHz cavity 37
2.14 Thermo-structural analysis of the 5 MeV/u IH cell 37
2.15 E-field distribution in the IH end-cells 38
2.16 End-cells 2D optimization result and E-field distribution along the z axis 38
2.17 End-cells design with the parameters studied in the optimization 39

2.18 Single particle tracking through the IH structure 40
2.19 E-field lines in the 5 MeV/u IH cell and voltages analysis 41
2.20 5 MeV/u cavity with "racetrack" drift shape 42
2.21 Transverse voltage along x axis normalized to the accelerating voltage in the 5 MeV/u IH RF cell with "racetrack" drift shape 43
2.22 Racetrack optimization results for the 5 MeV/u cell 43
2.23 The 5 MeV/u reference 3 GHz DTL cavity 45
2.24 Transverse voltage along x and y axis normalized to the accelerating voltage for the 15 MeV/u DTL RF cell with symmetric stems 46
2.25 ZTT profile in the DTL linac, for a constant and a tapered bore aperture 47
2.26 Thermal analysis of the 10 MeV/u DTL cell, fro different stems geometries. . . . 47
2.27 Filamentation in a DTL solution 49
2.28 Beam dynamics in a DTL structure from 5 to 20 MeV/u 51
2.29 Beam dynamics in an IH+DTL structure from 5 to 20 MeV/u 51
2.30 The 3 GHz BTW prototype 52
2.31 Fields distribution in a BTW RF cell 54
2.32 Results of the optimization of the first BTW cell, with scan of gap and nose cone angle 55
2.33 Geometrical parameters of the optimized HG BTW RF cells for different geometric β 56
2.34 Main accelerating parameters and field distribution along the BTW structure . 57
2.35 RF assembly methodology of the BTW structure 58
2.36 Creep results in the nose region for the different cells tested 59
2.37 Example of a tuning simulation performed with HFSS. 60
2.38 Results of the tuning test performed. 61
2.39 Picture of the tuning test performed for the BTW prototype. 62
2.40 Local Sc enhancement in the end-cell due to the coupling slot 63
2.41 Input coupler design and final Ez field distribution in the BTW structure 64
2.42 Output end-cell matching results 65
2.43 Input end-cell matching results 66
2.44 Comparison between S-parameters from HFSS and CATIA models on the full 3D structure 67
2.45 Cut view of the BTW prototype mechanical design 68
2.46 Thermo-structural analysis of the BTW prototype 69
2.47 Complex Ez field distribution along the BTW structure and in the complex plane 69
2.48 S11 and S22 of the BTW prototype 70
2.49 3dB hybrid 71
2.50 Complex Mag Electric field distribution in BTW structure connected to 3db hybrid 72
2.51 HG CCL full assembly cut view 73
2.52 Mechanical view of the optimized cells: HG BTW, HG CCL and 30 MV/m CCL . 74
2.53 Geometrical parameters of the optimized HG CCL RF cells for different geometric β 75
2.54 HG CCL end-cells design 75

2.55 Field distribution along the HG CCL structure 76
2.56 S11 as a function of frequency in the HG CCL structure 77
2.57 Cut view with Complex Mag Electric field distribution in the high gradient BTW and CCL structures at $\beta = 0.38$ 79
2.58 Thermal analysis comparison between HG BTW and CCL solutions 80
2.59 Uncoupled HG CCL and HG BTW cells at 230 MeV/u 81
2.60 TT factor, Q factor and ZTT comparison between HG CCL and BTW linacs . . . 83
2.61 100 MeV/u HE CCL cell optimization 84
2.62 Sc, E-field and H-field distribution on the nose region 84
2.63 ZTT as a function of the outer corner radius of the cell 85
2.64 Thermo-structural analysis of the 100 MeV/u RF cell for CABOTO 86
2.65 430 MeV/u HE CCL cell optimization 87
2.66 ZTT as a function of the outer corner radius of the cell 88
2.67 430 MeV/u HE CCL cell with 3mm septum thickness optimization 88
2.68 Electric coupling of a on-axis coupled cavity 91
2.69 Magnetic coupling of a on-axis coupled cavity 92
2.70 E field distribution in the 16 coupling holes solution 92

3.1 Sketch of TULIP *all-linac* 94
3.2 Beam dynamics in the TULIP IH linac from 5 to 10 MeV/u 96
3.3 Beam dynamics in the TULIP DTL from 10 to 70 MeV/u 98
3.4 Beam dynamics in the TULIP BTW linac at 70 MeV/u constant energy 102
3.5 Beam dynamics in the TULIP BTW linac from 70 to 230 MeV/u 102
3.6 Beam dynamics in the TULIP with *cyclinac* solution 104
3.7 Beam dynamics in the TULIP with *all-linac* solution 104
3.8 Energy spread comparison between a *cyclinac* and a *all-linac* solution 105
3.9 Methodology adopted in the TULIP quadrupole misalignments study 105
3.10 Misalignment study for the IH section of TULIP 106
3.11 Misalignment study for the DTL section of TULIP 107
3.12 Misalignment study for the BTW section of TULIP 107
3.13 TULIP *all-linac* main accelerating parameters 109
3.14 Summary of the beam dynamics in TULIP 110
3.15 Summary of the beam envelopes in TULIP 111

4.1 Sketch of CABOTO *all-linac* 114
4.2 Beam dynamics in the CABOTO IH linac from 5 to 10 MeV/u 117
4.3 Preliminary beam tracking in the 10-100 MeV/u section of CABOTO 119
4.4 Beam dynamics in the TULIPCABOTO DTL from 10 to 100 MeV/u 119
4.5 Beam dynamics in the CABOTO CCL at 100 MeV/u constant energy 121
4.6 Beam dynamics in the CABOTO CCL from 100 to 430 MeV/u 123
4.7 Misalignment study for the IH section of CABOTO 123
4.8 Misalignment study for the DTL section of CABOTO 124
4.9 Misalignment study for the CCL section of CABOTO 124

4.10 Misalignment sensitivity to a larger bore radius in the CCL section of CABOTO 125
4.11 CABOTO *all-linac* main accelerating parameters 126
4.12 Summary of the beam dynamics in TULIP 128
4.13 Summary of the beam envelopes in CABOTO 129
4.14 Sketch of the He linac longitudinal dimensions 129
4.15 He linac main accelerating parameters 130

5.1 BTW prototype disk alignment procedure 134
5.2 LLRF test and S11 comparison between measured configuration and simulation design results 134
5.3 Scheme of the RF tests performed on the accelerating structure 135
5.4 Electric field pattern along the 1st prototype RF cells, before and after tuning . 136
5.5 Electric field pattern along the 2nd prototype RF cells, before and after tuning . 137
5.6 Input and output S-parameters of the tuned structure 138
5.7 Layout with the main components of the high power test set-up 139
5.8 Layout with the cabling of the Klystron-modulator control system 140
5.9 Calibration curves for incident, reflected and transmitted power 141
5.10 Fourier analysis of the acquired pulse shapes 142
5.11 Incident, reflected and transmitted pulse in the structure during the conditioning phase 143
5.12 Accelerating gradient and cumulative number of BDs in the structure as a function of the number of RF pulses 144
5.13 Summary of CERN TD26CC and KEK TD24R05#4 high gradient tests 145
5.14 Nominal incident (INC) reflected (REF) and transmitted (TRA) RF signals (left) and upstream FC and downstream FC signals (right) 146
5.15 BD incident (INC) reflected (REF) and transmitted (TRA) RF signals (left) and upstream FC and downstream FC signals (right), with comparison with a nominal pulse before the BD event, in case of a strong RF perturbation. 350 ns RF pulse length 146
5.16 BD incident (INC) reflected (REF) and transmitted (TRA) RF signals (left) and upstream FC and downstream FC signals (right), with comparison with a nominal pulse before the BD event, in case of a weak RF perturbation. 350 ns RF pulse length 147
5.17 BD incident (INC) reflected (REF) and transmitted (TRA) RF signals (left) and upstream FC and downstream FC signals (right), with comparison with a nominal pulse before the BD event, in case of a strong RF perturbation. 900 ns RF pulse length. 148
5.18 BD incident (INC) reflected (REF) and transmitted (TRA) RF signals (left) and upstream FC and downstream FC signals (right), with comparison with a nominal pulse before the BD event, in case of a weak RF perturbation. 900 ns RF pulse length. 148
5.19 Comparison between input and output cell dispersion curves 149

5.20 Sketch of the BTW prototype BD simulation with HFSS 149
5.21 Simulated total structure reflection as a function of the BD positioning along the structure 150
5.22 Simulated total structure reflection as a function of the BD positioning along the structure for a lossless cavity 151
5.23 Reflected signal during normal pulses and BD events to the left, and S11 histogram on the right 152
5.24 CLIC TD26CC structure reflected signal during normal pulses and BD events to the left, and ratio REF/INC on the right 152
5.25 Sketch explaining the edge method 154
5.26 Electric field along z in the BTW structure and first harmonic travelling wave . 157
5.27 Proton tracking in a 50 MV/m field 157
5.28 Comparison between a $\beta = 0.38$ electric field for different accelerating gradient 158
5.29 Comparison between a $\beta = 1$ electric field for different accelerating gradient . . 159
5.30 Simulation of dark current at the FCs as a function of the accelerating gradient 159
5.31 RF-Track 3D tracking of electrons in the BTW cavity. Electrons in red, and synchronous proton in green. Blue circles are lost electrons, i.e. electrons that have hit the cavity walls. 159
5.32 Comparison between scaled maximum surface E-field as a function on the number of RF pulses 162
5.33 Comparison between scaled maximum surface E-field as a function on the number of BD 163
5.34 Comparison between scaled maximum modified Poynting vector Sc as a function on the number of RF pulses 163
5.35 BD density function as a function of the cumulative number of RF pulses and of the longitudinal position in the cavity 164

A.1 10 MeV electron linac preliminary study performed with the code described in this Section 170
A.2 Basic block diagram of subroutine A 171
A.3 Simplified scheme of RF-Track software architecture 175
A.4 Blocks view of the approach adopted for benchmarking the codes 177
A.5 Sketch of a cartesian mesh over a cylindrical region. Points with EM field are in blue, NaN in orange. Small green dots are numerical interpolation points, small red dos are interpolation points which are NaN. 179
A.6 Sketch to illustrate the derivation of Eq. A.8 180
A.7 Ratio of area cover by the cartesian mesh over the total circle area 181

List of Tables

1.1 Carbon ion centers in operation across the world 3

2.1 Design progress status of the RF cavities studied 24
2.2 Main characteristic of the RF cavities studied 24
2.3 Accelerating parameters of the optimized DTL RF cells for different geometric β 45
2.4 Beam dynamics comparison between an IH-DTL and a full DTL solution in the 5 to 20 MeV/u range 50
2.5 Tables summarizing the parameters fixed by the optimization and the accelerating figures of merit 54
2.6 Accelerating parameters of the optimized HG BTW RF cells for different geometric β 56
2.7 Main parameters of the BTW prototype 67
2.8 Accelerating parameters of the optimized HG CCL RF cells for different geometric β 74
2.9 Main geometric and accelerating parameters of $\beta = 0.38$ cells 78
2.10 Geometric and accelerating parameters of the optimized HE CCL RF cells for different geometric β 89
2.11 Sensitivity of selected geometric parameters on the ZTT for the 430 MeV/u CABOTO RF cell 89

3.1 Key parameters of the *all-linac* TULIP solution 95
3.2 TULIP DTL main parameters 97
3.3 TULIP BTW linac main parameters 101
3.4 TULIP *all-linac* - A summary 108

4.1 Key parameters of the *all-linac* CABOTO solution 114
4.2 CABOTO IH section main linac parameters 117
4.3 CABOTO DTL main parameters 120
4.4 CABOTO CCL main parameters 122
4.5 CABOTO *all-linac* - A summary 126
4.6 Key parameters of the He linac studied 128
4.7 Cost estimation of the major components of a linac for hadron therapy 130
4.8 Cost estimation of linacs for hadron therapy 131

5.1 Initial conditions of the two structures prior to tuning. 135

5.2 Measured attenuations and maximum power coupled to PXI 141

A.1 Summary of the RF-Track get phase space function options 174
A.2 Summary of the RF-Track get transport table function options 175
A.3 Twiss parameters comparison from the benchmark simulation on a three structures linac 177

Acronyms

BD	BreakDown
BDR	BreakDown Rate
BL	BaseLine
BTW	Backward Travelling Wave
CABOTO	CArbon BOster for Therapy in Oncology
CCL	Cell Coupled Linac
CTF3	CLIC Test Facility 3
CH	Crossbar H-type
DF	Duty Factor
DTL	Drift Tube Linac
EBIS	Electron Beam Ion Source
ECRIS	Electron Cyclotron Resonance Ion Source
EM	ElectroMagnetic
FC	Faraday Cup
FT	Fourier Transform
FWHM	Full Width Half Maximum
HE	High-Efficiency
HFSS	High Frequency Structure Simulator
HG	High-Gradient
IH	Interdigital H-type
IOT	Inductive Output Tube
LET	Linear Energy Transfer
LIBO	LInac BOoster
LLRF	Low Level Radio Frequency
OAR	Organ At Risk
PMQ	Permanent Magnet Quadrupole
PXI	PCI eXtensions for Instrumentation
RBE	Radio Biological Effectiveness
RF	Radio Frequency
RFQ	Radio Frequency Quadrupole
RFT	RF-Track
SCDTL	Side-Coupled Drift Tube Linac

SOBP	Spread-Out Bragg Peak
SW	Standing Wave
TE	Transverse Electric
TEM	Transverse ElectroMagnetic
TERA	TErapia con Radiazioni Adroniche
TM	Transverse Magnetic
TULIP	TUrning LInac for Protontherapy
TW	Travelling Wave

1 Introduction

Hadron [1] therapy refers to the treatment of tumours with hadrons. Though different ions, like He, are under study, the two main ones used in daily treatments are carbon ions and protons, with the latter taking the bigger part. At the time of writing, May 2017, 74 facilities are in operation in the world, 11 of which accelerate carbon ions [1].

The treatment of patients with hadrons, in this case protons, was first proposed by Wilson in 1946 [2], and the first patient was treated in 1954 at the Lawrence Berkeley National Laboratory. Despite these early recognition of the intrinsic physical and radio-biological advantages of hadrons over other forms of radiation, such as X-rays, the diffusion of hadron therapy centres was slow. Nevertheless, the number is rapidly increasing in the recent years. In Fig. 1.1 is reported the cumulative number of proton and carbon ion centres as a function of time. One can observe that proton centres are growing remarkably faster than carbon ion ones. This different trend is explained mainly by the lower dimensions and costs of proton centres compared to carbon ion ones. From a medical point view however, protons and light ions are fundamentally different, as discussed in Section 1.1.3.

The distribution of proton therapy centres across the world sees an almost even split between Europe, North America, and Asia (Fig. 1.2 bottom). In Europe, currently Germany leads the pack. A considerable number of centres is under construction in the UK, and the treatment rooms distribution across Europe at 2020 is shown in Fig. 1.2 top. Concerning carbon ions (Table 1.1), Japan was the country that first believed in this technology, and has now 5 centres. The Italian and Austrian centres are an adaptation of a design study called PIMMS (Proton-Ion Medical Machine Study), hosted at CERN [3].

Though the boom of the last decade, hadron therapy remains a relatively unknown treatment methodology to the general public. The three currently major treatment methodologies for tumour therapy are in fact surgery, chemotherapy and radiotherapy. In the next Section, the physical and radio-biological rationales of hadron therapy are discussed. Particular effort is devoted into highlighting the differences between X-rays, protons, and carbon ions for

[1] non elementary particle made of quarks

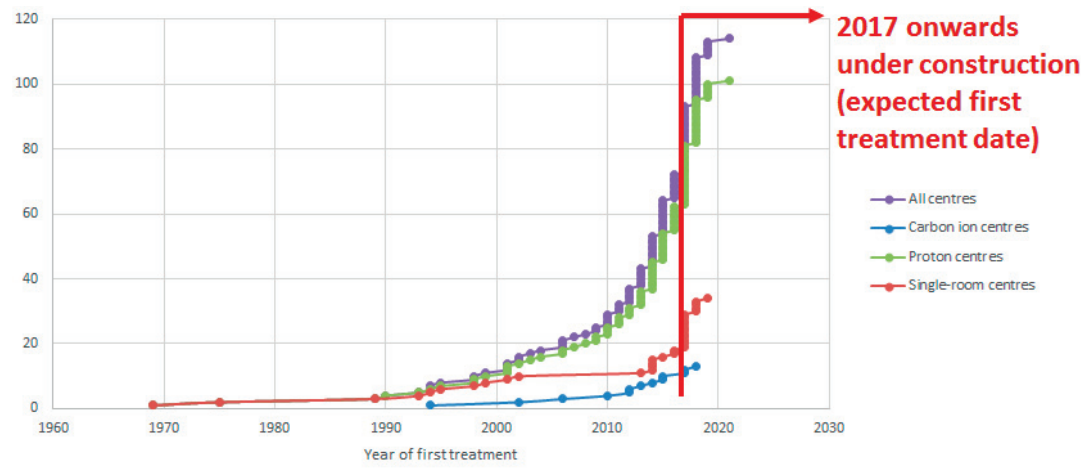

Figure 1.1 – Cumulative number of hadron therapy centers as a function of time. Elaboration from PTCOG (Particle Therapy Co-Operative Group) data, updated to February 2017. Planned facilities are not reported.

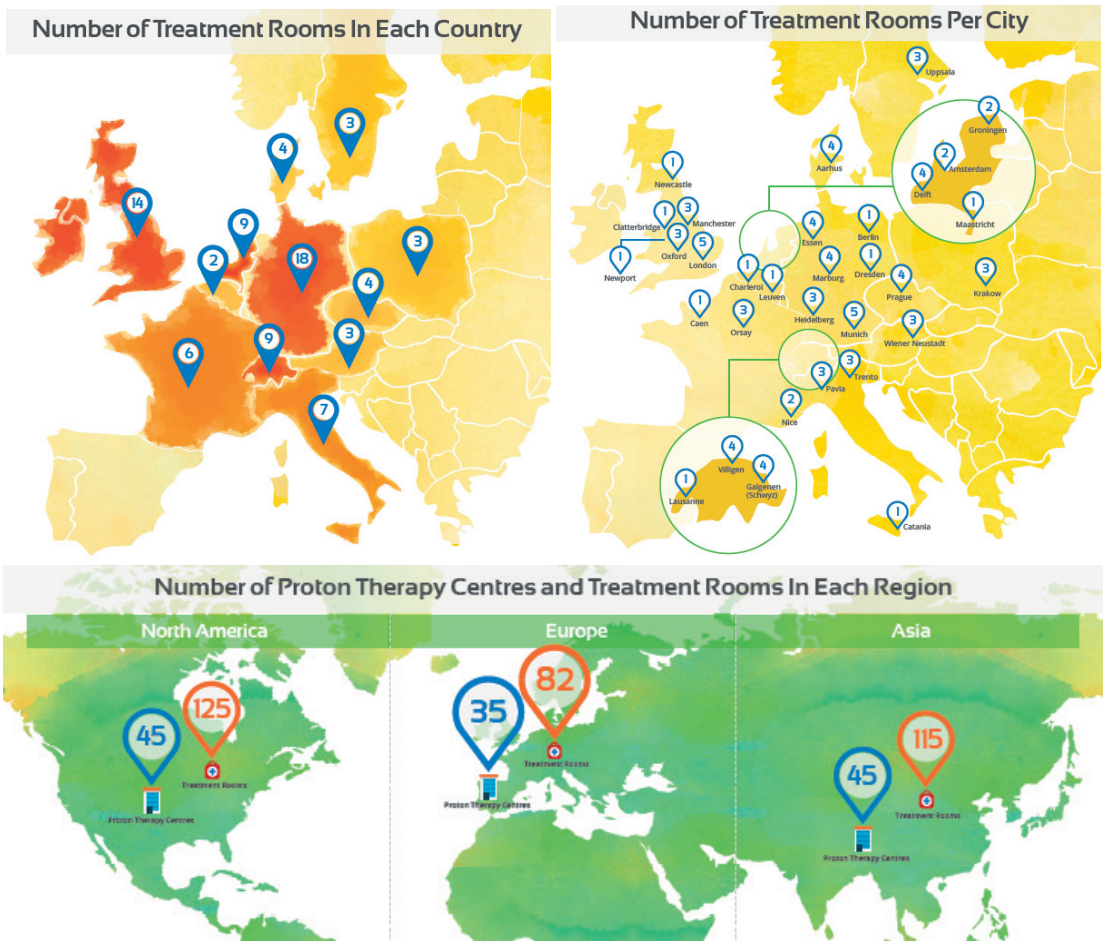

Figure 1.2 – Proton therapy centres in Europe at 2020 (top) and worldwide (bottom). Proton Therapy Congress, London, September 20-21, 2016.

Table 1.1 – Carbon ion centres in operation across the world [from PTCOG data].

1994	HIMAC	Japan
2002	HIBMC	Japan
2006	IMP-CAS	China
2009	HIT	Germany
2010	GHMC	Japan
2011	CNAO	Italy
2013	SAGA-HIMAT	Japan
2014	SPHIC	China
2015	i-Rock Kanagava Cancer Center	Japan
2015	MIT	Germany
2017	MedAustron	Austria

treatment purposes.

1.1 Physics of hadron therapy

Hadron therapy, as radiotherapy, aims at delivering a *dose* to the tumour tissues. The dose D is measured in Gray (Gy, 1Gy=1J/kg), and defined as:

$$D = \frac{E}{m}, \tag{1.1}$$

where E is the energy deposited in a material volume, and m is the mass of that volume.

The dose deposition, or dose profile, along the path of the radiation, differs for every type of radiation. However, there is a fundamental difference between hadrons and X-rays. Hadrons shows a characteristic peak, called Bragg peak, at the end of their path through matter (Fig. 1.3). X-rays instead have an almost decreasing exponential trend. As a result, deep seated tumours can be targeted by hadrons more precisely, sparing dose to the the surrounding healthy tissues. The dose distribution is shown in Fig. 1.3. In the following Section the physics of radiation travelling through matter will be further discussed, in order to highlight the differences between X-rays, protons and carbon ions, and give the reader the instruments to understand some important design assumptions adopted in this thesis.

1.1.1 Longitudinal dose profile

X-rays dose profile is driven by two main mechanism, the photoelectric absorption and the Compton scattering. The photoelectric effect is predominant at low X-rays energies, while Compton scattering is main interaction mechanism involved in the slowing down of X-rays. The dose deposition curve has an exponential behaviour. The peak that characterizes the initial few centimeters of penetration (see Fig. 1.3) is due to the build-up of short range secondary electrons, produced by the primary photons in the superficial layers of the irradiated tissue.

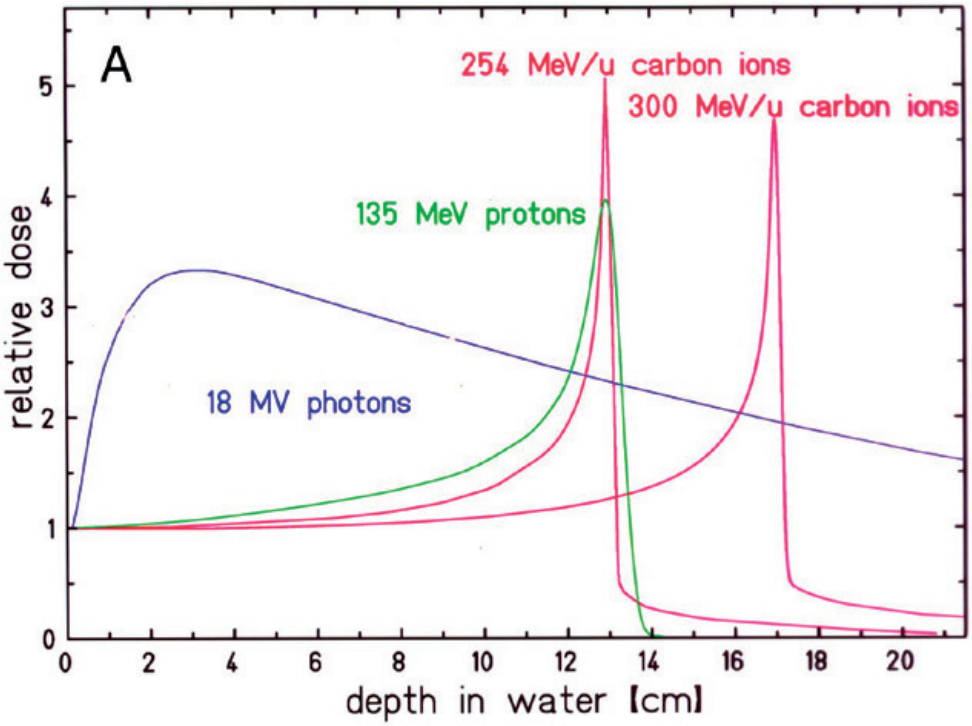

Figure 1.3 – Longitudinal dose profile of X-rays, protons and carbon ions. Image from GSI Helmholtz Centre library, Darmstadt, Germany.

The dose profile of hadrons along their direction of propagation in a medium is defined by many mechanism, the main one being the inelastic electromagnetic interaction of the ions with the atomic electrons of the medium. The Bethe-Block expression [4] defines the linear rate of energy loss for ionization, or stopping power S_p, of a particle travelling through a medium :

$$S_p = -\frac{dE}{dx} = K z_{eff}^2 \frac{Z}{A}\frac{1}{\beta^2}\Big[\frac{1}{2}\cdot log\Big(\frac{2m_e c^2\beta^2\gamma^2 T_{max}}{I^2}\Big) - \beta^2 - \frac{\delta}{2}\Big], \tag{1.2}$$

where:

- K is a constant equal to $4\pi N_A r_e^2 m_e c^2$ ($K = 0.307 MeV g^{-1} cm^2$);
- z_{eff}^2 is the effective charge of the incident particle, i.e. the charge shielded by the attached electrons;
- $\frac{Z}{A}$ is the ratio between the atomic number Z and the atomic mass number A express in $[g mol^-1]$ of the medium;
- β and γ are the relativistic factors of the particle;
- I is the ionization potential of the medium;

- T_{max} is the maximum kinetic energy transferred to the free electron in a single collision;
- δ is the density correction to the ionization energy loss.

Eq. 1.2 is a simplified formula, and more complete models have been studied [5]. Typically, Monte Carlo simulations are used nowadays to simulate the dose deposition curve of a particle beam through matter.

In particle radiobiology, the stopping power is referred as linear energy transfer (LET), and given in units of keV per μm of water. This notation will be used throughout this thesis.

An useful, and simplified, formula relates the range in water of a particle beam with its energy [6]:

$$R = \int_W^0 \left(\frac{dE}{dx}\right)^{-1} dW = R_0 \frac{A}{z^2}\left(\frac{W}{mc^2}\right)^{1.82}, \tag{1.3}$$

where:

- R_0 is a constant equal to 425 cm of water;
- W is the kinetic energy of the particle;
- mc^2 is the rest energy.

The accuracy of Eq. 1.3 is better than 5%. Few important figure of merits can be highlighted from Eq. 1.3 and 1.2. In particular, for non ultra-relativistic hadrons:

- the energy loss is inversely proportional to the particle kinetic energy;
- for a given speed, the energy loss is proportional to the square charge z;
- for a given range, the energy per unit mass W/A is proportional to $z^{1.1}/A^{0.55}$ (from Eq. 1.3).

In Fig. 1.4 , the linear energy loss of different ions is plotted versus their relativistic momentum. The increase at low energies is due to the longer time spent by the particles in the proximity of the atoms of the traversed medium, and so by an enhanced probability to eject electrons per unit path length. If the x-axis of Fig. 1.4 is inverted, and one takes the dose (see Eq. 1.1) instead of the LET, one obtains the Bragg peak previously discussed.

As a second remark, the higher is the mass of the ion, and the lower is its speed, the narrower is the Bragg peak. So for instance, a carbon ion beam has a more localized energy deposition

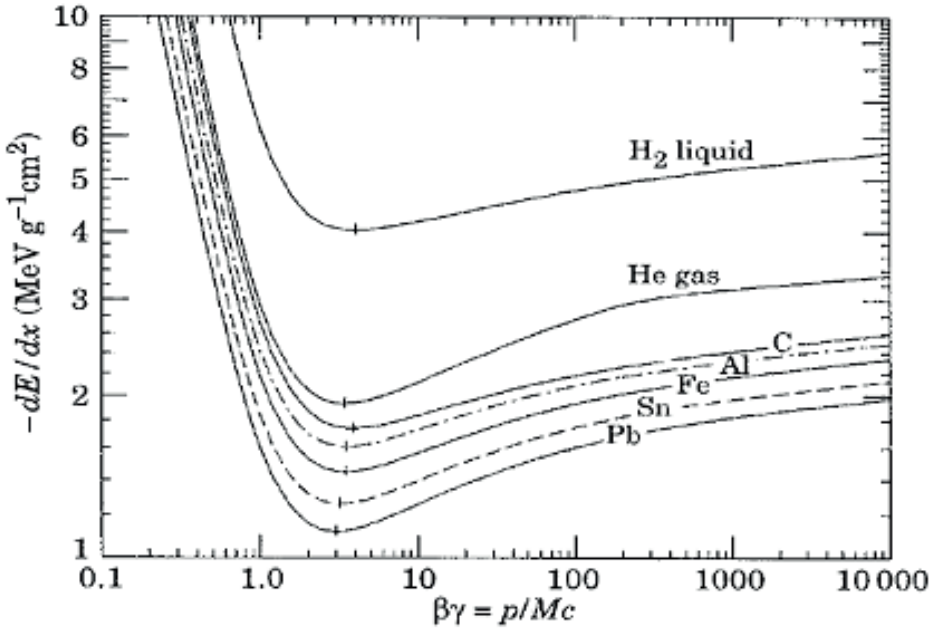

Figure 1.4 – Specific energy loss as a function of the relativistic momentum for different ions [7].

than a proton beam for the same depth of penetration (Fig. 1.3), and a 100 MeV proton beam has a more localized energy deposition than a 200 MeV one (Fig. 1.5 left). The dose associated with heavier ions is characterized by a tail that extends after the Bragg peak, which is caused by the fragmentation of the incoming hadrons. These projectile fragmentation products have approximately the same velocity of the ion [5] and contribute to the deposition curve with an unwanted un-localized dose.

The Bragg peak is typically too narrow to fully irradiate longitudinally an average tumour. In this case, a superposition of many Bragg peak of different energies creates a so-called spread-out Bragg peak (SOPB), whose result is a constant dose on a given range (Fig. 1.5 right). Different techniques are used to deliver the correct longitudinal dose, and these are discussed in Section 1.2. Indeed, one of the advantages of linacs for hadron therapy lies in the dose distribution that they can rapidly produce over other accelerator technologies.

The highly localized dose of hadrons can be sometimes unwanted, since to an error in the dose delivery system may correspond a relatively higher damage to sensitive tissues surrounding the tumour. A recent study [8] suggested that a too precise Bragg peak is too risky, and not beneficial. If the tumour is close to organs at risk (OAR), the range uncertainty, together with a too precise dose localization, could eventually be harmful, though methods for controlling this effect have been developed.

A final remark helps clarifying the difference between light ions. Heavier ions need, in general, a greater energy per unit mass to reach the same range. As noted above, Eq. 1.3 implies that

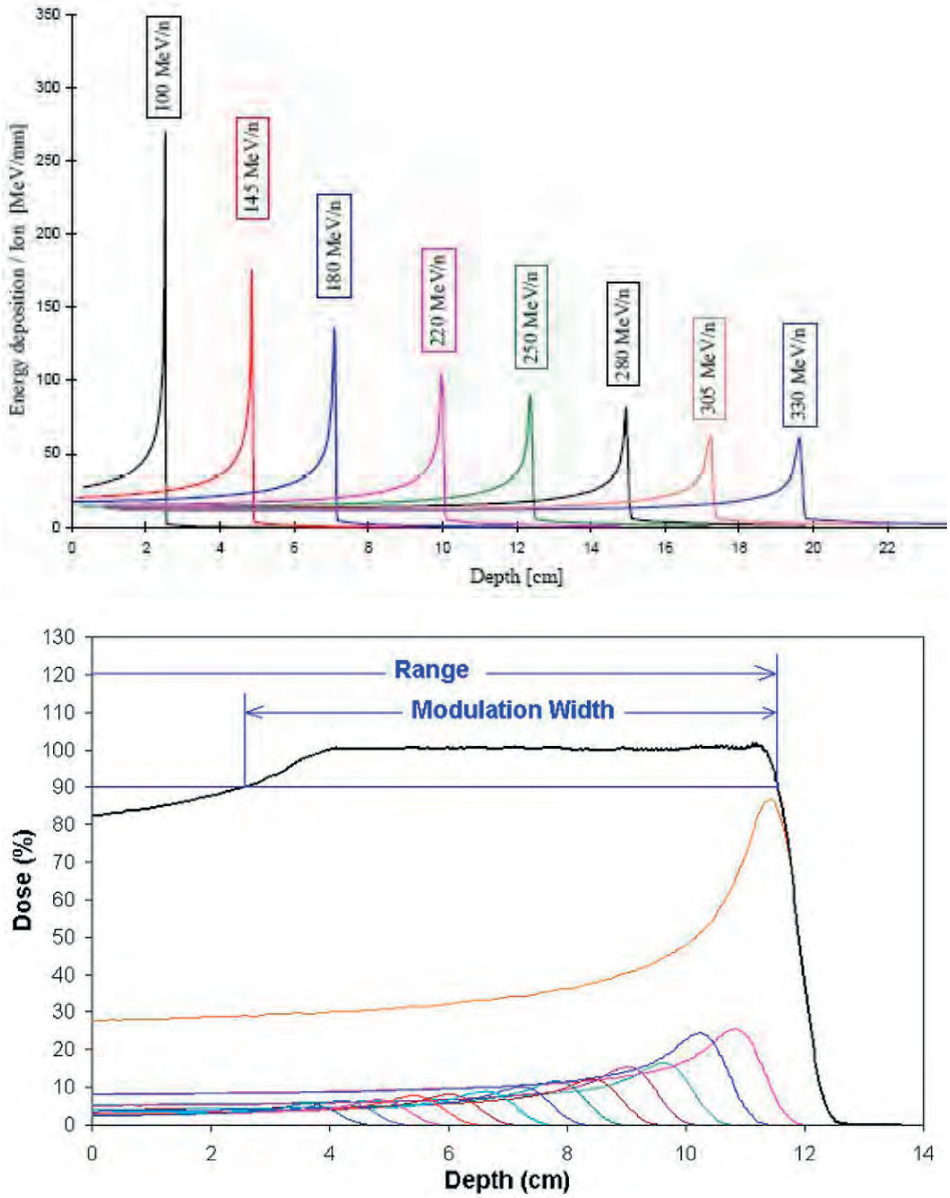

Figure 1.5 – Dose deposition of C^{6+} beam at different initial energies (top, courtesy of GSI) and SOBP example (bottom) [7].

for a given range the energy per unit mass is proportional to $f = z^{1.1}/A^{0.55}$. For protons and helium f is equal to 1.00, for carbon ions to 1.85 and for oxygen ions to 2.15. Since protons and helium ions have a 32 cm water range for W = 230 MeV/u, to reach the same depth with carbon (A=12) and oxygen (A=16) ions one needs about 430 MeV/u and 500 MeV/u respectively. These figures multiplied by A/z give the overall accelerating voltages that the particles have to experience: protons: 230 MV; helium ions: 460 MV; carbon ions: 860 MV; oxygen ions: 1000 MV. In particular, for carbon ions the overall voltage is 3.7 times larger than for protons. Note that, for this range, the ratio of the carbon ion and proton momenta is 2.85, smaller than 3.7.

As a result, carbon ions need to be accelerated to about four times the energy per unit mass of protons to have the same penetration range. From this fundamental physical difference originate the different design choices adopted in Chapter 3 and 4.

Interestingly, and worth commenting, a fully stripped He ion needs the same energy per unit mass of a proton to have the same penetration range. So a He ion facility has a factor two difference with respect to a proton one, and not a factor four, or more exactly 3.7, as in the case of carbon ions. This is one of the reason why He are attracting the research interest of many laboratories. A preliminary design of a therapy He linac, though beyond the goal of this thesis, was studied and is presented in Section 4.4.

1.1.2 Lateral dose profile

While travelling through a medium, both photons and charged particles pencil beams experience an increase in the transverse size, causing what is called lateral penumbra. Both the longitudinal and the lateral beam profile concur in determining the dose distribution in matter, so it is important to highlight the key aspects of this phenomenon.

For photons, which are an indirect ionizing radiation, the beam lateral spreading is due to Compton scattering, and it does not change the energy of the un-scattered photons. For charged particles, which are directly ionizing radiations, the energy decreases continuously due to ionizations and excitations of the encountered atoms and molecules, while the lateral spread of the pencil beam increases due to the Multiple Coulomb Scattering (MCS), which is due to collisions with the atomic nuclei and does not change the particle energy. The physics behind [5] is much more complex and would require a dedicated dissertation.

The penumbra is lower for higher atomic numbers, thus representing an advantage of carbon ions over protons. Also the penumbra of a penetrating pencil beam is lower at higher energies, meaning that in the initial trajectory the beam remains more collimated than in the final part. This is the fundamental of the High Energy Proton Therapy (HEPT) [7], and the rationale of proton imaging [9] [10].

As shown in Fig. 1.6, the Full Width Half Maximum (FWHM) decreases with the mass number. The rule of the thumb is that, for a zero width incoming beam, the FWHM decreases as $1/\sqrt{m}$, where m is the ion mass. The Montecarlo simulation data of Fig. 1.6 are consistent with

this rule: for a 15 cm range FWHM = 10, 5.0, 3.0 mm for protons, helium ions and carbon ions respectively. The longitudinal FWHM of the Bragg peak has a similar behaviour. For a "conformal" dose distribution carbon ions and helium ions are thus to be preferred to protons. Since helium accelerators are less expensive than carbon ion accelerators (see Section 4.5), helium ion beam could become an important type of treatment.

1.1.3 Radiobiology

The previous Chapter discussed briefly the physics of hadron therapy. However, the same dose delivered to a tissue can cause different damages, or in other words, have a different radio-biological effectiveness.

The main biological effect of ionizing radiation in living cells is a damage to the DNA. This is caused either by direct ionization of the DNA molecule, or by indirect effects. As discussed later, these latter are predominant for protons, but not for carbon ions, and consist in the formation of reactive oxygen species (ROS) from the interaction of the ionizing radiation with the water present in the cell.

A variety of damages can occur to the DNA, as summarized in Fig. 1.7 left. After the damage has occurred, the cell can either repair, mis-repair, or die (apoptosis). The mis-repair itself can lead to the cell death (lethal mutation) or to a DNA mutation, that is propagated in the cell daughters.

The direct tumour cell death is the goal of hadron therapy, as well as radiotherapy, and it is accomplished primarily by double-strand breaks (DBSs) of the DNA. Though also in this case cells can repair, this is not as likely as for the single-strand breaks (SSBs). There is evidence [11] that the likelihood of cell death is correlated to the number of incorrectly repaired damages caused by *pairs* of DSBs not well isolated from each other.

The response of cells as a function of the dose is referred as survival curve (Fig. 1.7 right). A simplified, though widely adopted, model for cell survival is the linear-quadratic one:

$$S = e^{-\alpha D - \beta D^2}, \tag{1.4}$$

where S is the surviving fraction, D is the dose, and α and β are the curve parameters that defines the radio-sensitivity of tissues. The logarithm of the survival fraction is thus not linear with the dose.

Most of the tumour cells are more sensitive to ionizing radiation that healthy tissue cells. Though more complex, the reason is mainly reducible to the different speed of division: cancerous cells, proliferating more rapidly that normal ones, are more sensitive to a given dose. Thus a steeper curve in Fig. 1.7 right, i.e. a high $\frac{\alpha}{\beta}$ ratio, characterizes tumour cells.

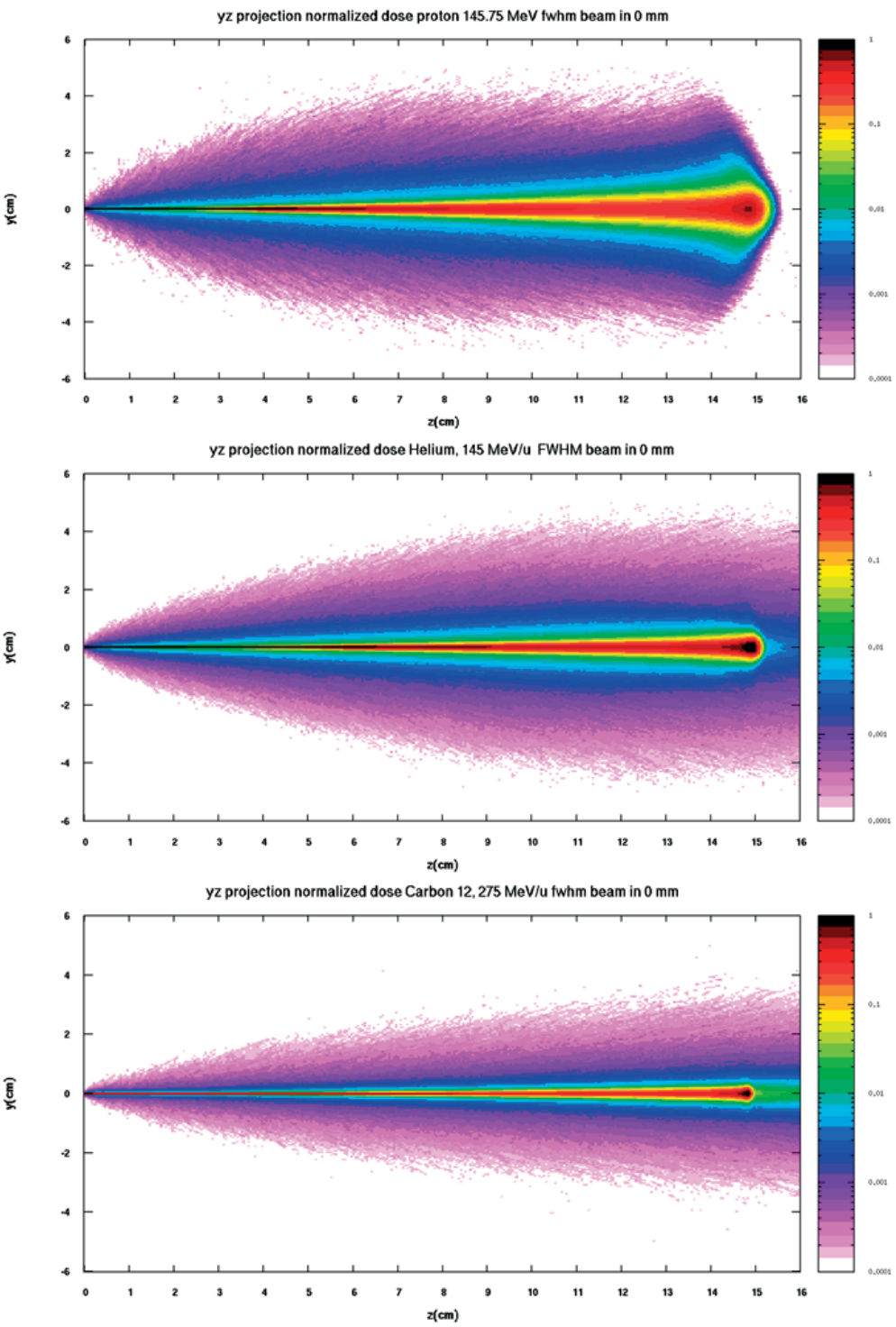

Figure 1.6 – 2D dose profile of proton (top), helium (middle), and carbon ion (bottom) beams, for the same penetration depth in water. One can observe the different kinetic energy needed to reach the same longitudinal position of the Bragg peak, together with the different lateral spreading and the dose deposited by the tails. Images courtesy of Caterina Cuccagna, TERA Foundation.

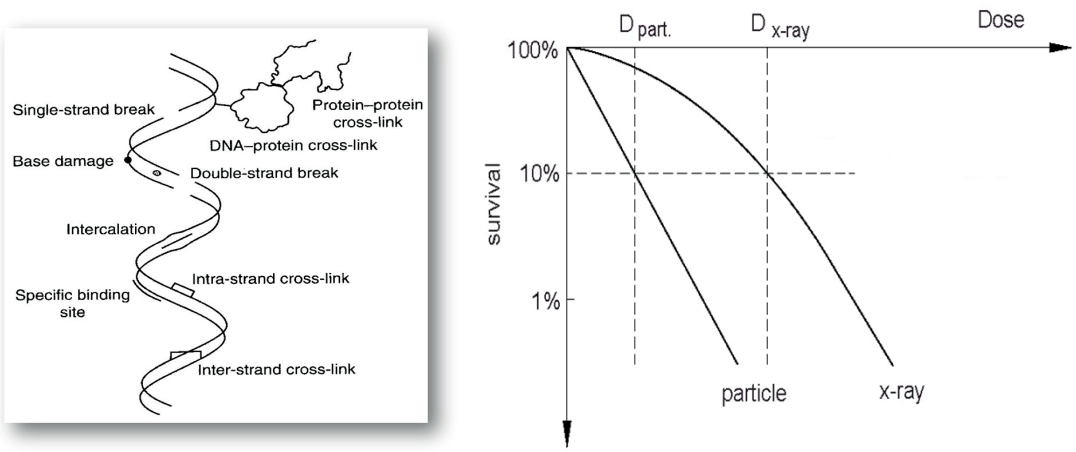

Figure 1.7 – Sketch of DNA damages produced by ionizing radiation (left) [12] and example of cell survival curve (right) [13].

Radiotherapy goal of destroying the tumour cells is inherently associated to side-effects to surrounding tissues. A way to reduce the dose to healthy tissues, thus preserving the same overall effect on the tumour, is fractioning (Fig. 1.8). Taking advantage of the different slope of survival fraction, if the same overall dose is divided in many (usually up to forty) fractions, the same effect on the tumour can be reached with lower side effects on the surrounding tissues.

To quantify the radio-biology effect of radiation, two parameter are useful. The density of energy deposition along the radiation track is expressed by the *Linear Energy Transfer* (LET), and given by the Bethe-Block formula (see Eq. 1.2).

A second parameter, the *Relative Biological Effectiveness* (RBE), measures the effects of the irradiation. It is defined as the ratio between the absorbed dose of a reference radiation, which is usually a Co^{60} 2 MeV gamma photons, and that of the test radiation required to produce the same biological effect:

$$RBE = \frac{D_{photon}}{D}|_{isoeffect}. \tag{1.5}$$

For example, a RBE_{10} indicates the RBE for a 10% survival of the cells. The higher the RBE of a given radiation, the higher its radio-biological effectiveness.

The RBE depends on many parameters, as discussed in [5], and all the data shows a remarkable variance [14]. The most important parameter is the LET. It is useful to discuss the dependencies between these two quantities. RBE is low for low LET (ionization not dense enough, multiple events are needed to kill the cell) and very high LET. This last result, that may appear counter-intuitive, is due to the so-called overkilling effect: the dose delivered in the tissue is too high and does not produce any more harm, so there is a "waste" of dose.

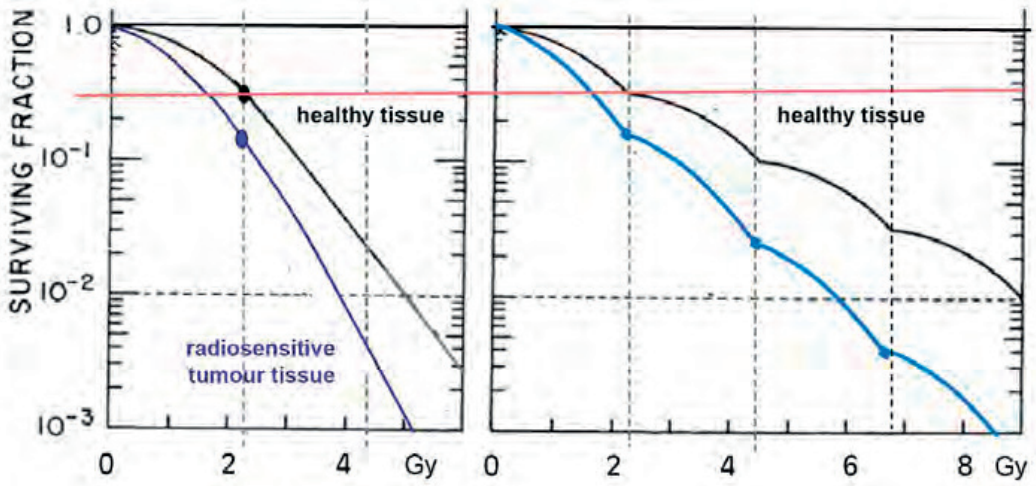

Figure 1.8 – Fractioning principle: comparison between single fraction effect and 4 fractions case. Healthy tissue is black, tumour tissue in blue/purple [7].

Given the relatively lo values of LET in most of the range, a constant RBE value equal to 1.1 for protons is considered by the scientific community [5].

In the last centimetres, high values of RBE are reached with ions heavier than protons, like carbon ions, making them suitable for treatment of radio-resistant tumours. Though, as previously discussed, carbon ions have a more concentrated dose deposition curve than protons, the ultimate rationale of their adoption over protons lies in their greater RBE (Fig. 1.9).

Helium ions are densely ionizing only in the last millimetres of their range and their overall biological and clinical effects are more similar to the ones of protons than of carbon ions. However, as discussed above, the intrinsic diameter of a Bragg spot is twice smaller than the one of protons. For these reasons in the last years many radiation oncologists have been advocating the use of helium ions for radio sensitive tumours located closely to organs at risk, which cannot be irradiated without unwanted negative long term effects on the health of the patient.

It has to be remarked that the use of carbon ions for radio-resistant tumours has been and is criticized by some radiotherapist because, in their opinion, the high values of RBE of charged particles over photons, represents at the present stage a drawback. The uncertainty in RBE can in fact lead to not correct biological dose distributions. Carbon ion therapy has models to account for the variable RBE, and in particular two models have been developed so far, by NIRS in Japan, and GSI in Germany.

For these reasons, any research that better defines the RBE of charged ions represents a major step forward for hadron therapy. In this regard, a recent study proved clinically a variable RBE for protons [16].

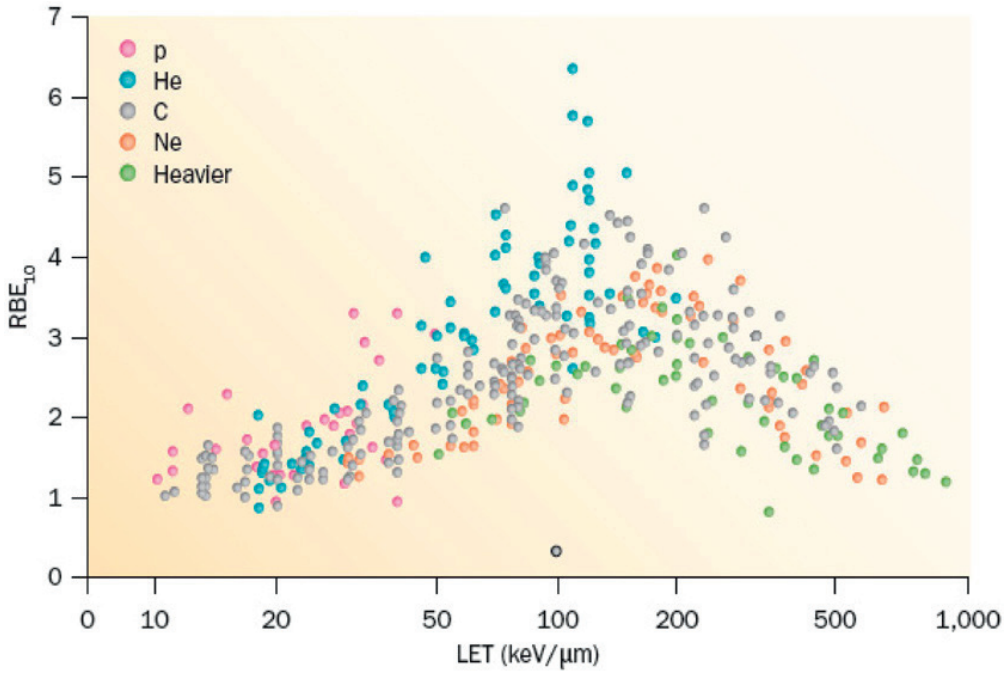

Figure 1.9 – RBE compared with LET from published experiments on *in vitro* cell lines [15].

1.1.4 Summary on hadron therapy physics

The physical advantage in the dose distribution of hadron therapy over radiotherapy makes it a very suitable technology when tumours are closed to OAR, or when treating children and more generally patients more sensible to side-effects of radiation. Nowadays, a number of tumours in adults are recommended to be treated with hadron therapy, together with all the paediatric tumours [5].

As discussed, the biological effect of hadron therapy is similar to conventional X-ray and electron therapy when using proton beams, and in practically all the range, also helium ions. Instead it increases by a factor 3-4 in the last centimeters when using heavier particles like carbon ions. This is the reason why radio-resistant tumours are targeted with these last particles.

In the following Section, the use of linear accelerators for hadrontherapy is discussed.

1.2 Rationale of linear accelerators for hadron therapy

Cyclotrons, for protons, and synchrotrons, for carbon ions and protons, are the two accelerator types used in state of art hadron therapy facilities. Cyclotrons in particular proved to be a very suitable technology for proton therapy facilities, which require beam energies up to 250 MeV, and so do not encounter the ultra relativistic limitations of cyclotron technology. Moreover, the relatively low beam rigidity permits the use of magnets of reasonable size and

power consumption. For the same reasons, carbon ion facilities are all based on synchrotron accelerators.

Present available cyclotrons for proton therapy deliver beams with fixed energy in the range 230-250 MeV. As a consequence, to scan longitudinally the tumour, one needs to reduce the particles energy, by degrading the beam with passive absorbers. This comes at the cost of emittance increase and energy straggling (see Section 3.2 for a detailed discussion), with repercussions on the beam line design and a lower beam quality. In addition, there is a significant activation of the area, since the beam intensity is reduced by up to 3 orders of magnitude [17]. Lastly, if the beam degradation occurs close to the patient, secondary particles may not be fully clean by the beam line, and cause unwanted background dose. Current cyclotrons for proton therapy are either normal conducting and super conducting, and usually isochronous, so with a continuous extracted beam. Few more recent models, as the Mevion S250, are superconducting synchrocyclotrons, with a lower intensity, pulsed beam. These developments have still a fixed extraction energy, but very interesting repetition rate, of 500 Hz or even 1 kHz in the case of IBA S2C2. The advantage of an high repetition rate is discussed in Section 1.2.1. The research towards proton cyclotrons capable of varying the energy in the 70-230 MeV range focuses on synchrocyclotrons [18] and movable stripper foil [17]. A notable research direction is represented by superconducting cyclotrons for carbon ion therapy, as the IBA C400 project [19], which however did not reach the commercialization stage.

Synchrotrons can vary the extraction energy, but their main drawback lies in the extraction time, of the order of few seconds. The beam currents are typically lower than the ones achieved by cyclotrons, particularly isochronous ones, but are still sufficient for hadron therapy purposes. The losses are lower than in a cyclotron with passive degraders, and so is the activation of the area and the shielding required. The research in this field focuses mostly on reducing the footprint and increasing the extraction rate [20].

In this very competitive and fast growing market (see Fig. 1.1), a linac solution could seem unreasonable. Nevertheless, as discussed both cyclotrons and synchrotrons present drawbacks, and these can be overcome by linear accelerators.

The key advantage of linacs lies in the possibility to actively change the output beam energy, as proposed by TERA Foundation and discussed in [21]. This can be accomplished by varying electronically the RF amplitude and phase in the last active accelerating structure at a repetition rate typically of 100 to 200 Hz, though higher values can be considered. At the same time, the source intensity can be varies at the same repetition rate, so to achieve an energy-intensity variation from pulse to pulse (Fig. 1.10). These features translate into a quick treatment, with no activation and no scattering of the beam. In addition, this feature is ideal for treating moving organs with pencil beam scanning and *multi-painting* of the tumour volume. In the following, the different dose delivery systems will be briefly discussed to highlight the advantages of linac solutions.

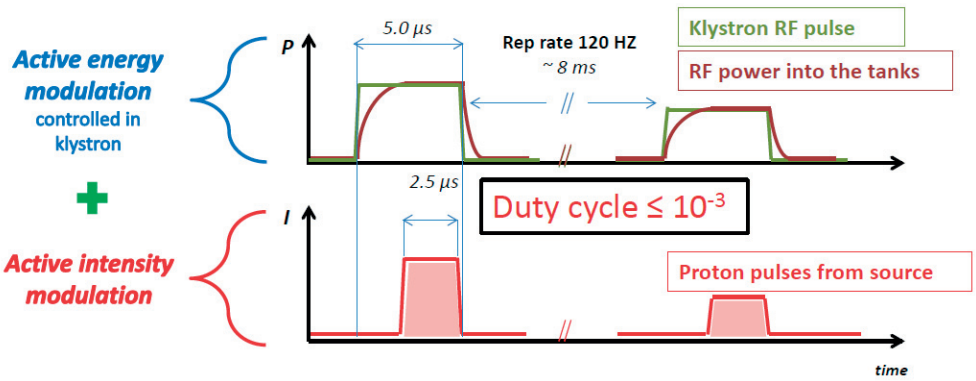

Figure 1.10 – Theoretical time scale with linacs active energy variation [7].

1.2.1 Dose delivery systems for hadron therapy

Currently, more than 90% [5] of the patients have been treated with a passive modulation of the hadron beam, in order to create the SOBP illustrated in Fig. 1.5 right. A passive modulation dose delivery system is required to cover the tumour volume when the beam is continuous. As shown in Fig. 1.11 top, the beam is first scattered to increase its transverse dimension, then collimated and shaped to the shape of the tumour, and finally filtered to create a SOBP. As previously discussed, this methods delivers unwanted dose to the patient. A pulsed, variable energy beam can instead adopt the so-called pencil beam scanning (Fig. 1.11 bottom). In this method, each pulse is deliver to a well defined sub-volume of the tumour, called voxel. The transverse position is adjusted by means of two scanning magnets, while the longitudinal one by varying the beam pulse energy.

Pencil beam scanning is now offered by all state-of-art technologies for both proton and carbon ion therapy, and is emerging as the main dose delivery modality. However, it can become problematic if the beam scanning is too slow:

- tumours close to moving organs, for instance the lungs, can be mis-targeted, and the dose delivered to surrounding tissues;
- the uncertainty in the beam stopping power, previously discussed, can be harmful when the beam is too precisely directed towards a single volume;
- the time needed to treat a patient can remarkably increase, with consequences on the patient comfort and on the economical business plan of the facility.

For these reasons, pencil beam scanning only manifests its full benefits when associated with a high repetition rate, typical of linacs and modern synchrocyclotrons. However, while these latest have a slow variation of the beam energy, since they still rely on a mechanical energy degrading system, linacs have a 3D fast scanning feature.

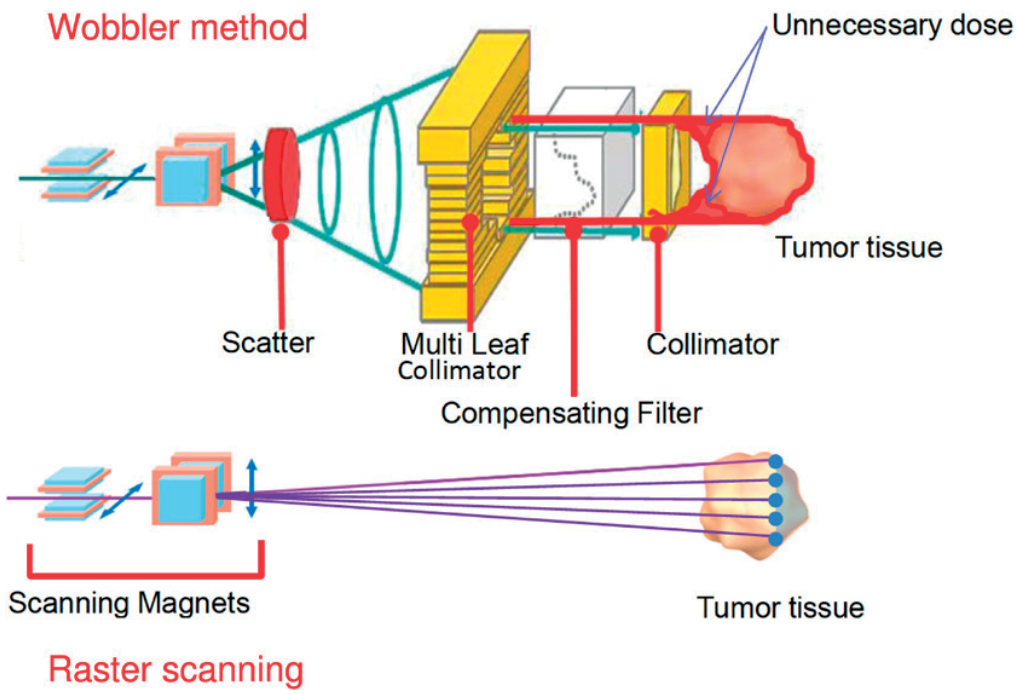

Figure 1.11 – Illustration of passive and active beam delivery systems [Image from Toshiba, Japan].

As a final remark, with pencil beam scanning each tumour voxel can be irradiated once (single-painting), or multiple times (multi-painting). This last technique, as discussed by TERA Foundation , is easily achievable with linacs in a time comparable with current single-painting techniques, and permits to correct possible dose errors during the same treatment, limiting it to less than 3% in case of up to 12 visits per voxels [21].

1.2.2 Advantages of linacs for hadron therapy other than dose delivery system

As discussed, the main rationale of linacs for hadron therapy is their high repetition rate with active energy variation, that allows quick multi-painting pencil beam scanning and treatment of moving tumours close to OAR, with a superior beam quality over cyclotrons.

Other two advantages, specifically over carbon ion synchrotrons, are worth mentioning: the lower power consumption and the higher final beam current.

In a linac the beam is off for the majority of the time. Typically the duty factor (DF), i.e. the product of the repetition rate times the RF pulse width, is around 0.05%. The DF is a major design parameter from a technical point of view, as it affects average power consumption, compactness of a facility, and acceleration efficiency, amongst the others. From the medical point of view, one wants the highest possible repetition rate, together with a pulse width large enough to deliver all the dose required for each pulse.

At the ion source level, one could either choose a continuous source, as an ECRIS (Electron Cyclotron Resonance Ion Source), and chop the beam, or a pulsed source, as an EBIS (Electron Beam Ion Source). A recent CERN project is very promising in this regard, with a design goal of 10^8 fully stripped C^{6+} over a 5 μs long spill and with 180 Hz repetition rate [22]. Associated with an overall transmission of 30% and assuming to double to repetition rate to 360 Hz with two sources (see Chapter 4), this would guarantee a final beam intensity of $6.5 * 10^{11} C^{6+}$ per second, so about two order of magnitude larger than what a synchrotron can deliver [23].

At the same time, the power consumption is estimated in few hundreds of kW, thus remarkably lower than a synchrotron solution (see Section 4.1).

1.3 The starting point

This thesis is the last of many research works on the development of linear accelerators for hadron therapy. Hereafter, a selected list of the most important works relevant to this thesis is presented.

Linacs for proton therapy were first proposed in 1991 [24]. This solution was taken up by TERA Foundation, which in 1994-95 designed in detail a 230 MeV linac for proton therapy [25] and, in collaboration with CERN and INFN, first proved the feasibility of a 3 GHz accelerating structure for protons [26] [27]. Since 2001 the activity of TERA Foundation mostly focused on the so-called *cyclinac* concept. In this solution a commercial cyclotron accelerates particles up to tens of MeV, which are then boosted by a linac up to the energies of medical interest, i.e. 70 to 230 MeV in case of protons.

In particular, TERA proposed a compact "single-room facility" proton linac called TULIP, based on the *cyclinac* concept, in 2013 [28], followed by a more detailed study in [7]. Interestingly, TULIP was first proposed a few months earlier than the first "single-room facility", namely the Mevion S250, treated its first patient, in December 2013. TERA also worked on a carbon ion *cyclinac*, presented in [29] and [30].

Following the design of [25], the ENEA group of Frascati, Italy, worked on a *all-linac* solution, with a Radio Frequency Quadrupole (RFQ) and a Drift Tube Linac (DTL) system covering the particle acceleration up to 40-70 MeV [31], to be followed by the Coupled Cavity Linac (CCL) designed by TERA [26] [27]. All these activities have been described in the review paper of Ref. [21].

Arguably, one of the most recent breakthrough in the field is represented by the design and construction of a 750 MHz RFQ by CERN [32]. This solution was specifically designed to inject particles at 5 MeV into a 3 GHz DTL structure as the one proposed by ENEA. Based on these developments, A.D.A.M [33], a spin-off company of CERN, is building on CERN premises a commercial *all-linac* machine for proton therapy, based on a RFQ-DTL-CCL machine [26] [27].

A parallel research effort was carried out by INFN Naples, called ACLIP [34]. Here a 3 GHz proton accelerating structure similar to the first presented in [26] [27], but at a lower geometric beta, was built and tested. This project later on was taken up by the Italian private company ITEL, which is now developing a *all-linac* solution, called EHRA, in collaboration with INFN [35].

Concerning carbon ions, in recent years a collaboration between Argonne National Laboratory and the private company RadiaBeam is working on a *all-linac* solution [36], adopting the TW structure designed and presented in this thesis (see Section 2.4.1). The RF methodology followed in the design of the same structure raised the interest of FERMI (Trieste, Italy) FEL, for the replacement of the S-band accelerating structure there present [37].

From 2013, TERA launched a high gradient research campaign, in collaboration with the CLIC study at CERN, to investigate the high gradient limit of S-Band accelerating structures [38]. Two high gradient single cell tests were performed, for a C-band cell [30] and for an S-band one [7]. As a follow up results of these tests, the high gradient backward travelling wave accelerating structure for $\beta = 0.38$ presented in Section 2.4.1 was designed built and tested.

This thesis aims at closing the circle by proposing two hadron therapy linac designs. A high gradient proton linac, that ideally concludes the research activity started in [7], and a high-efficiency carbon ion linac, which follows [29] [30]. In both cases, a *all-linac* configuration was studied, instead of the *cyclinac* solutions previously considered. Advantages and disadvantages of an *all-linac* vs *cyclinac* solution are discussed in Section 1.3.1.

Given the number of references that can be consulted, the introductory part on the theory of linear accelerators has been on purpose skipped. Instead, a theoretical discussion will be presented where this is required for the proper understanding of the work accomplished.

1.3.1 Comparison between *cyclinac* and *all-linac* concepts

As discussed, in recent years research works and private companies focused their effort on hadron therapy linac on *all-linac* solutions, but a remarkable research effort exploited the *cyclinac* solution. This thesis studied two *all-linac* solutions, for proton and carbon ion therapy. Hereafter the rationale of the two proposals is discussed, though some more technical arguments are presented in more detail in the following Chapters.

The *cyclinac* solution strength comes from the idea of accelerating up to tens of MeV protons in a commercial cyclotron. This has a number of advantages over linear accelerators, mainly:

- lower complexity, being low beta accelerators often the most critical part of the linac chain;
- smaller footprint.

However, cyclotrons are not technically suited to inject particles in a linac. The transverse emittance of cyclotron beam is too large to fit into the linacs acceptance, at least the one proposed in [28]. Moreover, and most importantly, the time structure of the beam in the two machines is inherently different.

As far as the transverse emittances are concerned, the available external sources are very intense and a 25-30 MeV commercial proton cyclotron accelerates typically 500 μA so that the output beam can be locally collimated to fit the transverse acceptance of the linac.

The linac longitudinal acceptance poses a more serious problem because a 3 GHz linac with a synchronous phase of -20°, a classic value, has a phase acceptance of about 0.06 ns every RF pulse, which has a 0.3 ns period. On this very short time scale, the cyclotron beam is continuous and, as a result, 10% of the beam is accelerated and 90% is outside the longitudinal bucket of the linac.

On a larger time scale, to minimize the losses, the beam injected in the cyclotron is made of 5 μs pulses either by chopping the output of the continuous electron cyclotron resonance (ECR) source or, preferably, by using an intrinsically pulsed Electron Beam Ion Source (EBIS) [39]. The injected proton pulse is about two times longer than 2.5 μs of the accelerated pulse. As a summary, in the longitudinal phase space, only 5% of the beam is accelerated while 95% is lost. The kinetic energy of the lost particles depends on the cyclotron output energy and the specificity of the linac design. For the case study of a 24 MeV output cyclotron beam (see Section 3.2), losses were present up to 70 MeV proton energies.

Another disadvantage of the *cyclinac* solution is that the beam dynamics, being heavily influenced by the longitudinal losses, is unstable and the beam experiences emittance growth. These aspects are discussed in more details in Section 3.2.

A *all-linac* solution instead can reach 100 % transmission with a clean beam dynamics, and thus overcome the above mentioned issues. Linear accelerator chains are used in many laboratories around the world. However, hadron therapy linacs differ from every other application, being characterized by low current and high repetition rate pulsed beam. In addition, the highest possible accelerating gradient is desirable, in order to reduce the overall length of accelerators to be placed in hospital centres. These set of parameters, that can be summarized in small aperture radii and high gradients, are unique amongst linear accelerators, and thus call for specific designs driven to higher RF frequencies.

A sketch of the TULIP *all-linac* solution studied is presented in Fig. 1.12, and compared with the previously considered *cyclinac* design. Similarly, the two CABOTO proposals are illustrated in Fig. 1.13.

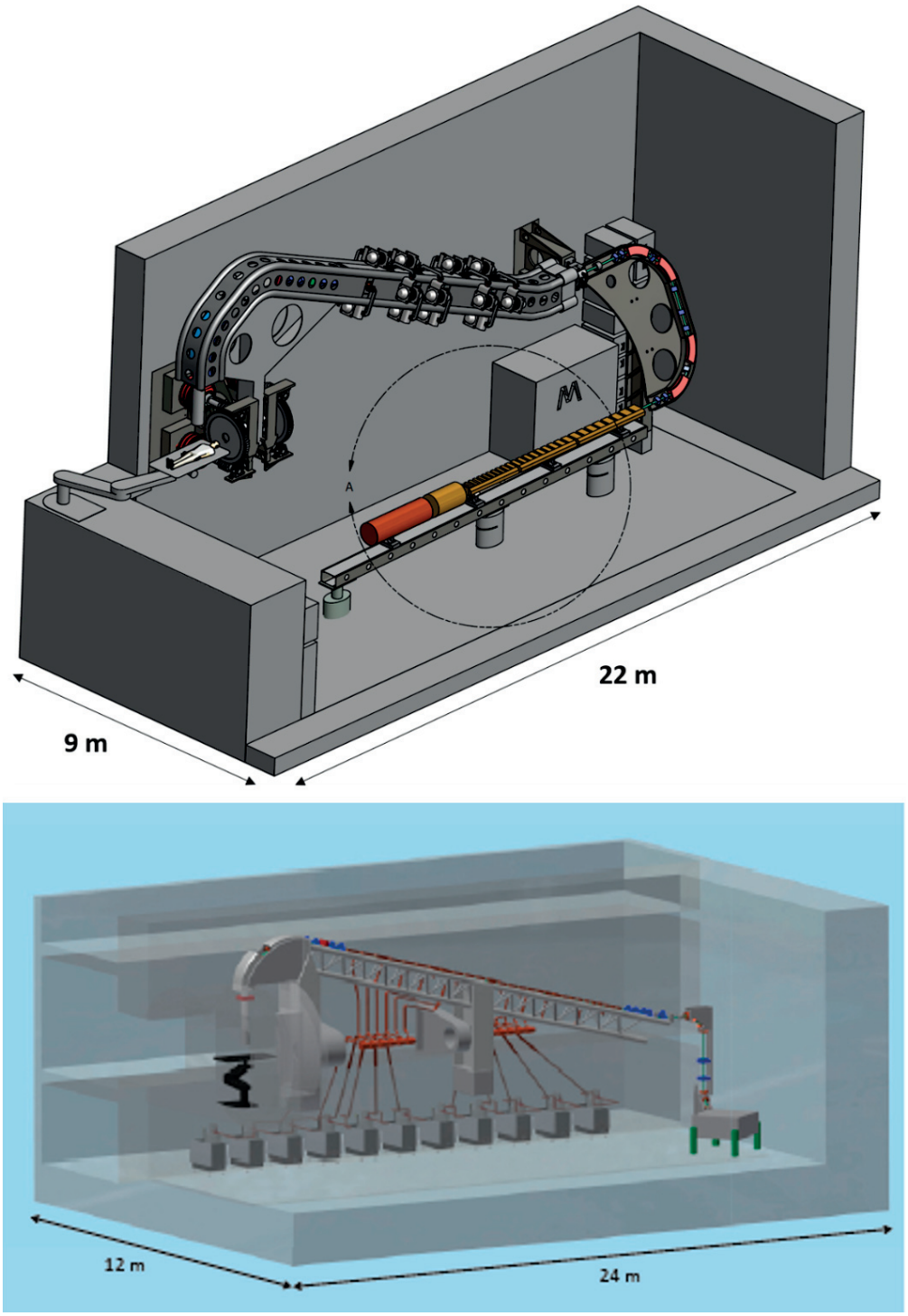

Figure 1.12 – Sketch of TULIP *all-linac* (top) and *cyclinac* solution (bottom). Courtesy of M. Vaziri - TERA Foundation

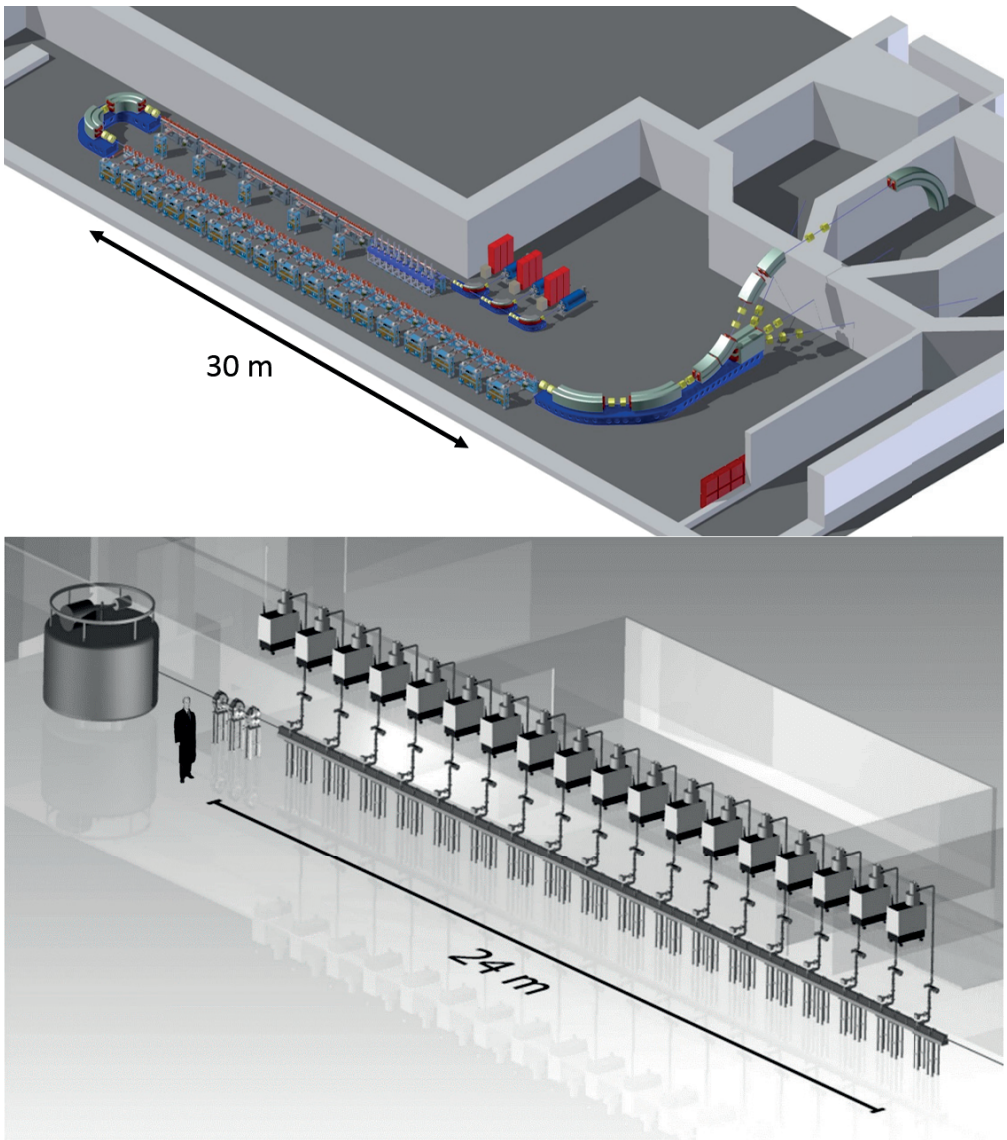

Figure 1.13 – Sketch of CABOTO *all-linac* (top) and *cyclinac* solution (bottom). Courtesy of M. Vaziri and M. Garlasche' - TERA Foundation

2 RF design of accelerating structures for TULIP and CABOTO

This thesis discusses two fairly different designs of linear accelerators for medical applications, a high-gradient proton linac - TULIP, and a high-efficiency carbon ion linac - CABOTO.

Nevertheless, the two designs share many technologies. In particular, the different accelerating cavities that form the linac are similar in the two cases. As a consequence, it has been preferred to discuss the RF design of the accelerating cavities in a this chapter, and to leave the discussion specific to each design to separate ones.

Hereafter, the RF design of four different accelerating cavities will be presented:

- a 750 MHz high-efficiency (HE) IH cavity;
- a 3 GHz HE DTL cavity;
- a 3 GHz high-gradient (HG) BTW cavity;
- a 3 GHz HG CCL cavity
- a 3 GHz HE CCL cavity.

The status of the four cavities is different: while the 3 GHz HG BTW cavity was fully 3D design, built and tested (see Chapter 5), the other structures are at an earlier stage. One could divide the design of a normal conducting accelerating structure in six steps:

- RF design and optimization of regular cells (RC);
- RF power coupling between RC (or field stability);
- end-cells design;
- power couplers and matching with waveguides;
- sensitivity and tuning analysis;

Table 2.1 – Design progress status of the RF cavities studied.

Cavity	Regular cells	Cells coupling	End-cells	Power couplers	Sensitivity and tuning	Mechanical design
750 MHz HE IH	Yes	No	Preliminary	No	No	Preliminary
3 GHz HE DTL	Yes	No	No	No	No	No
3 GHz HG BTW	Yes	Yes	Yes	Yes	Yes	Yes
3 GHz HG CCL	Yes	Yes	Yes	Yes	No	Preliminary
3 GHz HE CCL	Yes	No	No	No	No	No

Table 2.2 – Main characteristic of the RF cavities studied.

Cavity	Studied energy range [MeV/u]	Acc. Gradient [MV/m]	Project	Previously studied[1]
750 MHz HE IH	2.5 to 10	Below 10	TULIP and CABOTO	No
3 GHz HE DTL	5 to 70	Below 20	TULIP and CABOTO	Yes [31]
3 GHz HG BTW	70 to 230	50	TULIP	Started [7]
3 GHz HG CCL	70 to 230	50	TULIP	Similar design [7]
3 GHz HE CCL	100 to 430	30	CABOTO	Multiple designs

- final mechanical design.

Usually thermal analysis start with the first step, and are eventually verified in the final mechanical design on the whole structure. With respect to the steps just listed, the status of the cavities studied in this thesis in summarized in Table 2.1.

Table 2.2 helps the reader in understanding the basic features of the different structures under consideration.

2.1 Main codes and assumptions used

Two ElectroMagnetic (EM) codes have been used in the RF design. For Standing Wave (SW) cavities with cylindrical symmetry, the 2D code Poisson Superfish was used, developed by the Los Alamos Accelerator Code Group [40]. Being a 2D code, Superfish can simulate only cavities with cylindrical symmetry, and provides quick results. In this thesis, this code was used in the preliminary optimization of the accelerating cells of SW cavities.

Since any asymmetries, such as dipole kicks, as well as travelling wave regimes cannot be simulated with SUPERFISH, the main code used in this thesis is ANSYS HFSS [41]. HFSS is a 3D software that solve Maxwell's equations in a geometry based on the finite element method (FEM). The internal mesh is adapted until the simulations converge to the desired accuracy. Two main solvers have been used:

- *eigen mode*, which calculates the eigenmode frequencies (or resonances) of a structure and the fields at those resonant frequencies;
- *driven modal*, which calculates the modal-based S-parameters, expressed in terms of the incident and reflected powers of waveguide modes.

[1] Here the type of design, high-gradient or high-efficiency, and the type of RF cavity, CCL rather than DTL for instance, is considered. Not the exact energy ranges considered in this thesis.

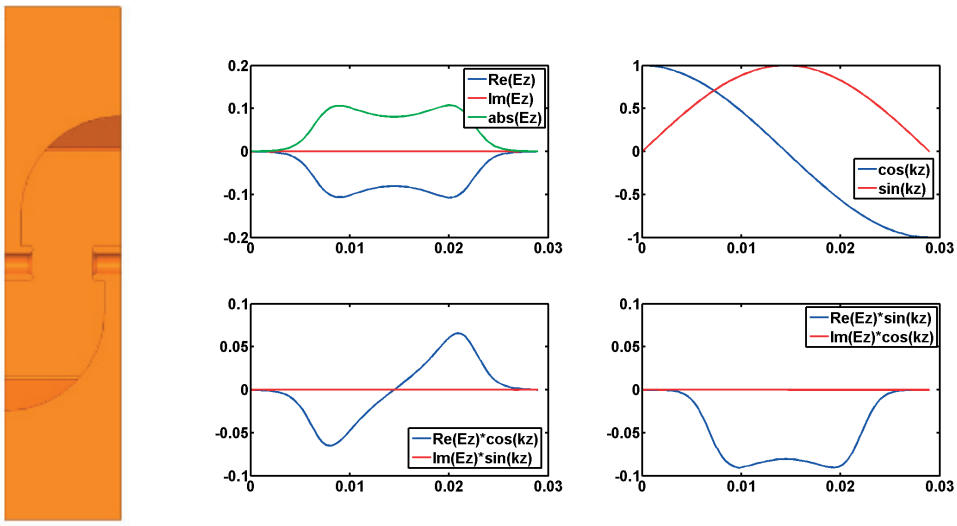

Figure 2.1 – Field analysis of the 10 MeV/u IH RF cell (see Section 2.2) with the method discusses and summarized in Eq. 2.1. E-field along the z axis (top left), integrating functions $cos(kz)$ and $sin(kz)$ (top right), field as seen by the synchronous particle (bottom). Cell length in m on the x axis, arbitrary units on the y axis.

In *eigenmode* the only predefined accelerating parameter set are the frequency and the Quality factor (Q-factor) of the resonant modes. However, a field calculator tool allows to define functions of interest in the design of a cavity, starting from the EM field distribution. Hereafter the most important functions are discussed. able **Transit time factor (TT)**

The classic description of the TT that is found in most literally books [42]:

$$TT = \frac{\int_{-L/2}^{L/2} E(0,z) \cdot cos(\omega t(z) + \phi) dz}{\int_{L/2}^{L/2} E(0,z) dz}, \tag{2.1}$$

is valid for SW cavities, and for TW cavities under very precise conditions. In Eq. 2.1 $E(0,z)$ is the complex magnitude of the electric field along the z-axis, ω is the angular frequency of the cavity of length L, and ϕ is the phase of the field relative to the crest.

It is very common to assume that the particle velocity change in a RF cell is negligible. In this case, one can integrate Eq. 2.1 in space by substituting $\omega t \approx \omega z / v = 2\pi z / \beta c = kz$, where k is the wave number. This assumption has been done in the present thesis.

In SW RF cells, HFSS gives to users the complex number of the EM field distribution with zero imaginary component. In other words, one can straightforwardly apply Eq. 2.1 with $\phi = 0$ [2]. This methodology is presented in Fig. 2.1 for a 10 MeV/u IH RF cell, thus a SW cavity.

[2] In case the electric field is a 90 deg translated symmetric function, one shall not forget to change $cos(\omega t) \rightarrow cos(\omega t + 90) = sin(\omega t)$

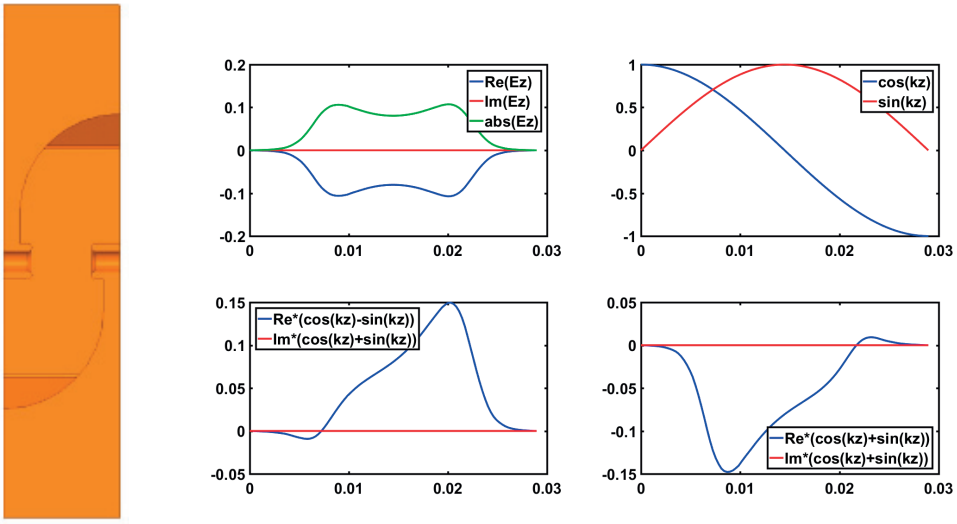

Figure 2.2 – Field analysis of the 10 MeV/u IH RF cell (see Section 2.2) with the method discusses and summarized in Eq. 2.2. Cell length in m on the x axis, arbitrary units on the y axis.

In case of TW RF cells, one could still work with the complex magnitude $E(0,z)$, but it is much more convenient, when one has a code that gives the real and the imaginary component of a field, to work with the complex number $E(z)$. In this case the phase information is hidden in the complex number, so it is possible to simply rotates the fields by $\omega t = kz$, and apply the more general formulation:

$$TT = \frac{\left|\int E(z)e^{\pm jkz}dz\right|}{\left|\int E(z)dz\right|} \tag{2.2}$$

Eq. 2.2 works for both TW (see Fig. 2.3), with a positive exponential in case of backward travelling waves, and SW cavities (see Fig. 2.2), independently on the z axis origin chosen, thus is a much more convenient choice to implement in a field calculator as the HFSS one. In case of SW cavities it does not matter the sign of the exponential. With some arithmetic stretching one can easily find the trigonometric formulation proposed in Fig. 2.2 and 2.3. Note that in Fig. 2.3 only the field decomposition at the bottom left is correct, being the cavity analysed a backward TW one.

Stored energy per unit length W_e

$$W_e = 2\epsilon_0 \int_V E \cdot E^* = W_h = 2\mu_0 \int_V H \cdot H^* \tag{2.3}$$

One can define the stored energy per unit length W_e both from the E-field or the H-field, as the scalar product of complex field by its complex conjugate.

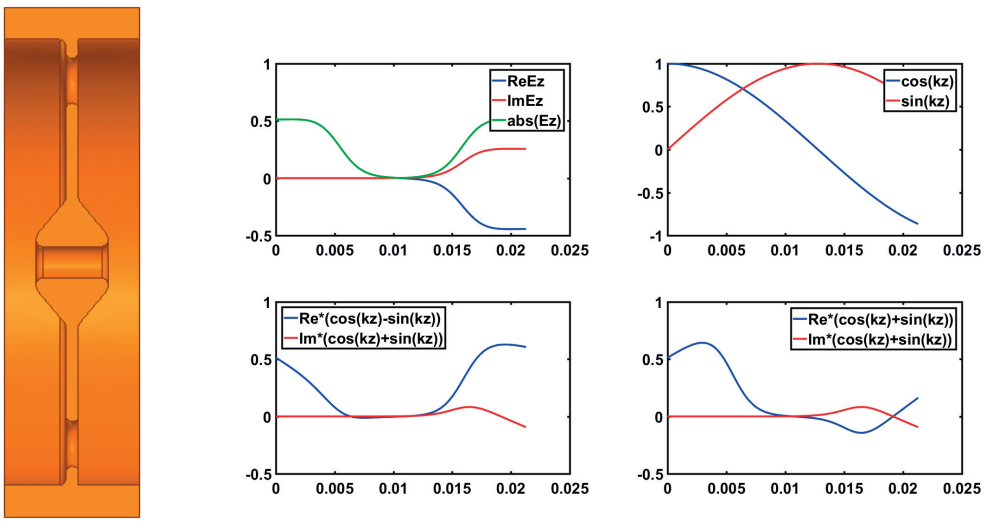

Figure 2.3 – Field analysis of the 153 MeV/u BTW RF cell (see Section 2.4.1) with the method discusses and summarized in Eq. 2.2. Cell length in m on the x axis, arbitrary units on the y axis.

Power flowing through the cavity P_z

$$P_z = \int_S Re(S_z), \tag{2.4}$$

with S is the Poynting vector, and the integral is on the surfaces perpendicular to the z-axis.

Shunt impedance per unit length Z

The shunt impedance is defined as the ratio between the longitudinal voltage in a cavity and the EM power dissipated on the cavity walls [42] [43], and it is usually defined per unit length:

$$Z = \frac{V_0^2}{PL}. \tag{2.5}$$

This the so-called *linac* definition. In some references there is a factor 2 difference, which is the so-called *circuit* definition, but in this thesis Eq. 2.5 will be adopted. One usually works with an effective shunt impedance ZTT, so considering the voltage seen by the synchronous particle $V_0 \cdot TT$. The average power loss P is obtainable from Eq. 2.3 and the Q factor, which is calculated in HFSS from the cavity resonance.

The energy gain ΔW can be then expressed as:

$$\Delta W = \sqrt{ZTT \cdot P \cdot L} \tag{2.6}$$

where ZTT is the effective Shunt impedance of the cavity, P the dissipated peak power and L the active length.

Modified Poynting vector S_c

Though discussed in [44], most of the RF work done in this thesis is based on the modified Poynting vector BD theory. Thus, it is convenient to recall this quantity definition here:

$$S_c = Re\{\bar{S}\} + g_c \cdot Im\{\bar{S}\}, \tag{2.7}$$

where $\bar{S}$ is the complex Poynting vector, $\bar{S} = \bar{E} \times \bar{H}$, and g_c is a weighting factor which is only weakly dependent on the geometrical parameters, and from measurements has been set to 1/6.

All the other accelerating parameters that will be presented in the following are straightforwardly obtainable from the above defined quantities, and are presented in introductory books of accelerator physics. They are thus not discussed here.

The thermo-structural analysis were performed by importing the HFSS™electromagnetic field distribution to the thermal and structural packages of ANSYS™.

2.2 The high-efficiency 750 MHz IH accelerating structure

A 750 MHz IH cavity was chosen as first accelerating structure after the 750 MHz RFQ for both TULIP and CABOTO. This choice was motivated by RF efficiency and beam dynamics considerations. The latest will be discussed in Section 2.3.2, while hereafter the discussion focuses on the RF design. This Section will first discuss a general optimization of low beta cavities, highlighting in particular the difference between TE and TM operating modes. Secondly, the 750 MHz IH cavity studied will be presented in detail.

2.2.1 The choice of low beta section accelerators

The choice of the best accelerating structure for a given application is a cumbersome task. To narrow the possibilities spectrum, it is helpful to fix some constraints. In particular, even though subjective, it is of the author belief that the bore aperture and the operating frequency are two interesting parameters to start with. The bore aperture radius decision comes from beam dynamics considerations, but strongly affects the RF optimization. The scaling [42]:

$$ZTT \propto \sqrt{Freq.} \tag{2.8}$$

is valid only under the assumption that the bore aperture scales, inversely, with the operating

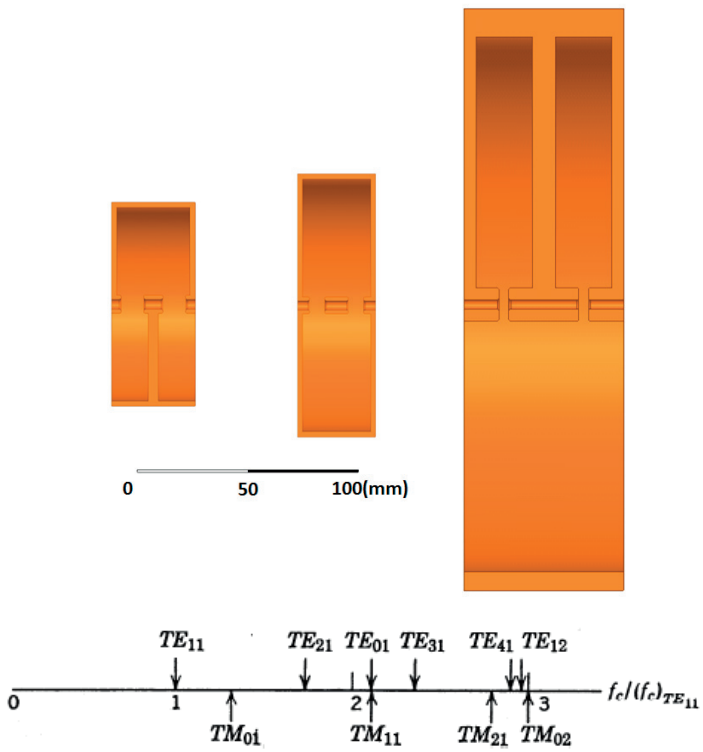

Figure 2.4 – Transverse section comparison between selected 5 MeV/u cells at 750 MHz. IH (left), CH (middle) and DTL (right). Cutoff frequencies relative to the fundamental TE11 (bottom).

frequency.

For the same reasons, the cavity operating frequency is another key parameter to choose. Ideally, one should design a cavity with the operating frequency function of the optimization process. In real world, the RF power sources are limited and with discrete output frequencies, and so it is necessary to choose amongst them.

Even if these two parameters are set, the RF designer is left with a not negligible number of solutions to consider. In particular, one should evaluate the operating mode, TE or TM or even TEM, together with the type of accelerating structures. For instance, let's consider a 5 MeV/u regular RF cell. In Fig. 2.4, the dimension of gap optimized cells working at 750 MHz, but with different operating modes, are reported. The DTL operates in TM010 mode, while IH cavities in TE111 mode, and CH cavities in TE211 mode. The cut-off frequency of the different modes relates to the fundamental TE11 as shown in Fig. 2.4 bottom. However, as discussed in [45], being characterized by a very high capacitive load, the insertion of drift tubes in TE mode cavities reduce the operating frequency with respect to an empty cavity remarkably more than in TM mode ones. This explains the transverse size difference between cells operating at the same frequency and with the same geometric β.

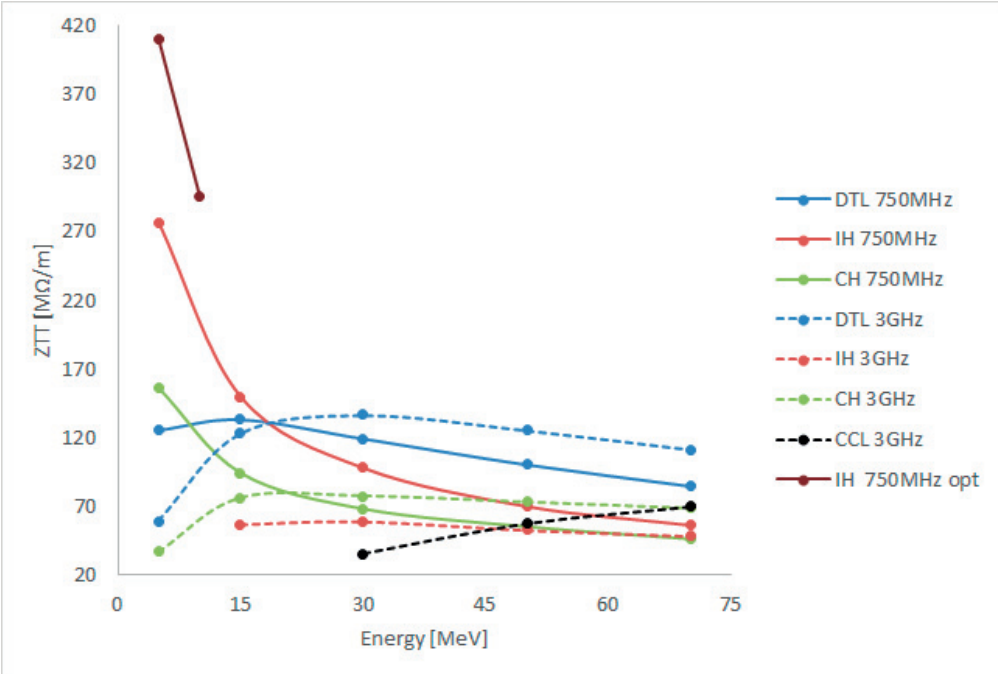

Figure 2.5 – ZTT as a function of the geometric βs for the optimized low β cavities considered.

This short discussion hopefully helped in clarifying some of the challenges of a proper RF cavity design. Hereafter, the results of the optimization performed are discussed.

The 750 MHz CERN RFQ [32] [46] was chosen as the starting point of TULIP. As far as CABOTO is concerned, it is assumed that a 750 MHz 0.5 q/m RFQ accelerating carbon ions up to 2.5 MeV/u can be designed based on the same approach.

It has been thus investigated the best solution to be placed afterwards, in the 5 to 70 MeV/u range. The RF design of this section was mostly driven by the optimization of the ZTT, together with machinability and thermal constraints. Break-Down limitations are not an issue here, since the accelerating gradient is relatively low in this part.

Different type of cavities, both TE and TM modes, were studied, at two operating frequencies, 750 MHz, as the RFQ, and 3 GHz, as the final linac sections of both TULIP and CABOTO. The intermediate frequency of 1.5 GHz was not considered as it has been chosen to have a single frequency jump in the machine. First, a simplified geometry was considered, with constant drift tube thickness and stems radius independently on the geometric β. All the structures were studied by optimizing the cell gap at different geometric βs, from 5 to 70 MeV/u. The bore aperture radius chosen was 2.5 mm, considering the RFQ output emittances and preliminary beam dynamic considerations. The result of this study is shown in Fig. 2.5. The very high values of ZTT found are not common in literature, but should not surprise. Indeed, the very small bore aperture, together with the high operating frequencies, represent an *uniqum* amongst linac designs, and are the reason of these results. The dark red curve in

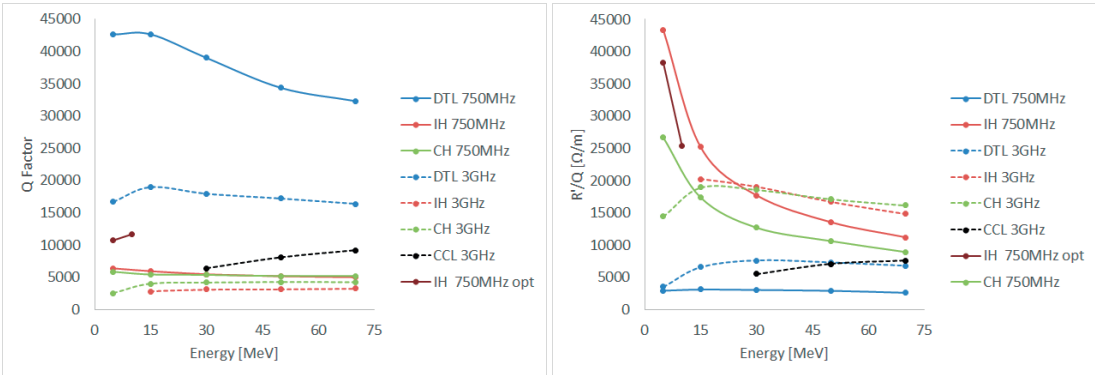

Figure 2.6 – Q-factor (left) and R'/Q (right) as a function of the geometric βs for the low β cavities considered.

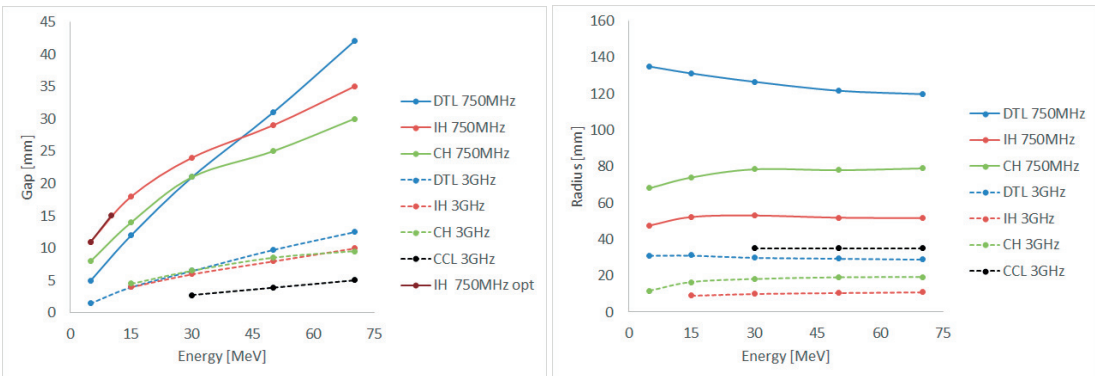

Figure 2.7 – Cell gap (left) and radius (right) as a function of the geometric βs for the low β cavities considered. In the cell radius graph, the 750 MHz IH design is not reported as the cavity does not have anymore a round outer wall (see Section 2.2.3)

Fig. 2.5 refers to the optimize IH cavity studied, presented in detail in section 2.2. Section 2.2.2 discusses why a careful optimization of TE cavities can remarkably increase their efficiency, while instead TM mode cavity have a more straightforward optimization process.

The results of Fig. 2.5 can be further understood by looking at the Quality Factor values, presented in Fig. 2.6 left. One can notice that TM mode cavities have a significantly higher Q value. However, they pay a quite high price in terms of concentration of electric field in the nose region and Transit-Time (TT) factor, being 2π mode cavities. This results in a lower overall efficiency (Fig. 2.6 right). This difference gets narrower for higher geometric βs, where the TE cavities lose their advantage.

The accelerating parameters results discussed can be also understood by observing the cell lengths and radii as a function of the βs for the different cavities (Fig. 2.7).

Promising cavities at 5 MeV/u are the 750 MHz IH and the 750 MHz CH. The 3 GHz DTL cavity, which is the most efficient choice for higher energies, is too small at 5 MeV/u, and ultimately

not as efficient. In Fig. 2.8 one can notice the differences in terms of cell length and diameter of the three solutions.

At 70 MeV/u, the 3 GHz DTL solution reveals to be the better choice. For visual comparison, this cavity dimensions are shown in Fig. 2.9.

The observation of Fig. 2.5 would led towards the conclusion that an IH cavity is favourable up to 15 MeV, and a DTL from 15 MeV onwards, even without considering an optimized IH design. This conclusion is based on a physical argument, and it will always remain unchanged. However, one of the goal of this work is to present a cost estimation of the facilities. Preliminary discussions [47] quantifies in one order of magnitude the cost per peak power of a 750 MHz IOT over a 3 GHz Klystron-modulator.

This difference is largely caused by the high demand of this latter technology working at 3 GHz, caused by the market of X-ray electron linacs. However, even though it is authors belief that this price difference will decrease in the future as a consequence of an higher demand of 750 MHz RF power sources, at the present stage the crossing point between a 750 IH solution and a 3 GHz DTL one has been found at 10 MeV/u. As a consequence, the detailed RF optimization of the 750 MHz IH cavity stops at this energy. Prior to presenting that, it is helpful to further discuss the difference between TE and TM mode cavities.

2.2.2 RF optimization of TM and TE mode DTL cavities

In TM mode DTL cavities no current flows through the stems. These have only a structural and heat dissipation purpose. Concerning ZTT, the thinner the drift tube and the drift stems, the higher is this parameter. Indeed, if it were possible to build a structure with drift tubes suspended in the void, this would be beneficial in terms of ZTT. TM mode cavities are constant gradient structures. In the assumption of constant transit time factor, the voltage gain grows with the geometric β of the structures, given the increased cell length. Low β TM modes cavities usually works in 2 π mode, and this mode was considered in the present study. Some designs considered the use of 4 π mode DTL cavities [48], to further extend their application to low beta regimes.

TE mode DTL cavities have, on the other hand, current flowing through the stems. Here the stems and the drift tubes have again a structural and heat dissipation role, but in addition they have to force the electric field to be parallel to the z axis in the bore aperture region. TE mode cavities usually work in either dipole magnetic mode - TE_{110}, being called inter-digital H (IH) - or as RFQs in quadrupole magnetic mode - TE_{210}, being called cross-bar H (CH) . The current flowing through the stems brings to Ohmic losses that can be minimized increasing the size of drift tubes and stems. However, this reduces the electric field concentration near the z axis. Ultimately, a detailed RF optimization is needed to find the optimum ZTT for a given cell length, taking into consideration machinability and thermal dissipation constraints. TE mode cavities work in π mode, so they are shorter than TM mode cavities for the same

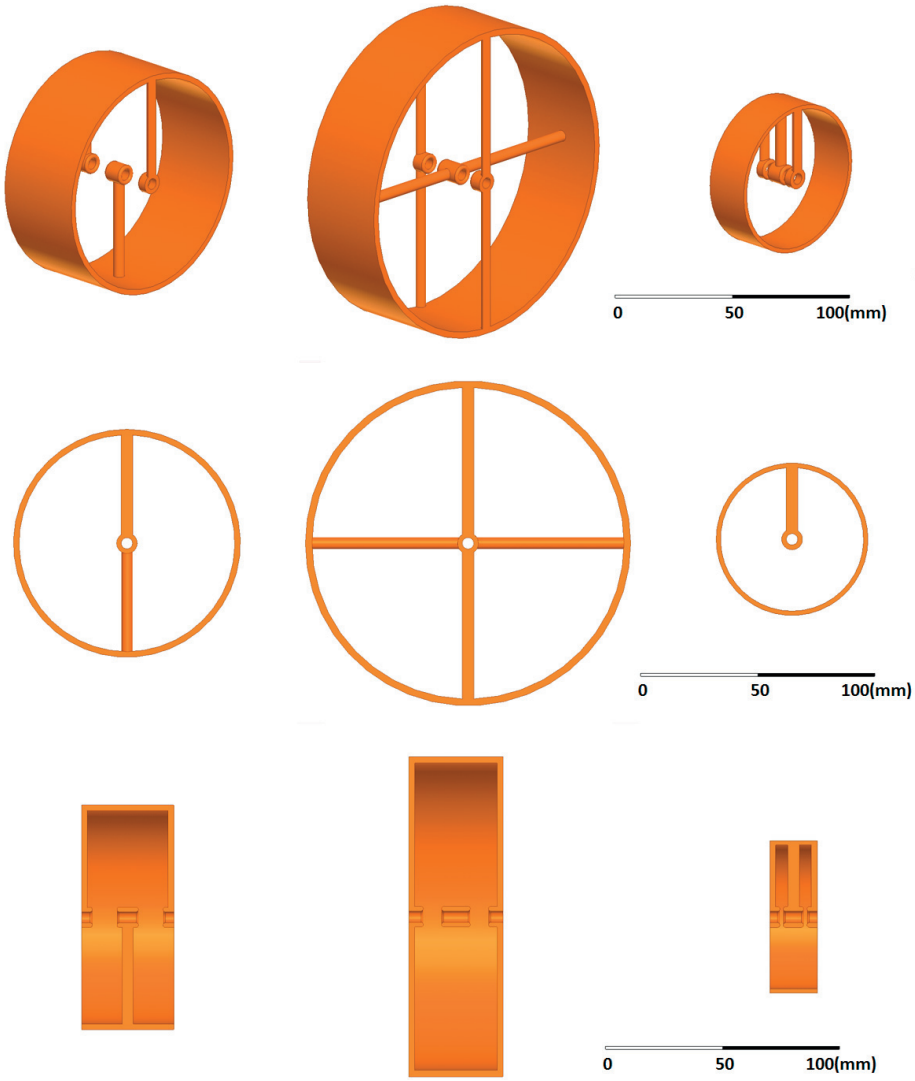

Figure 2.8 – Mechanical comparison between selected 5 MeV/u cells. Asymmetric view (top), transverse (middle) and longitudinal section (bottom). 750 MHz IH (left), 750 MHz CH (middle) and 3 GHz DTL (right)

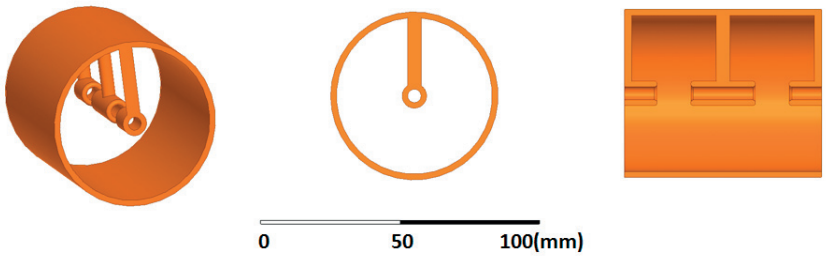

Figure 2.9 – 3 GHz DTL structure at 70 MeV/u. Asymmetric view (left), transverse (middle) and longitudinal section (right)

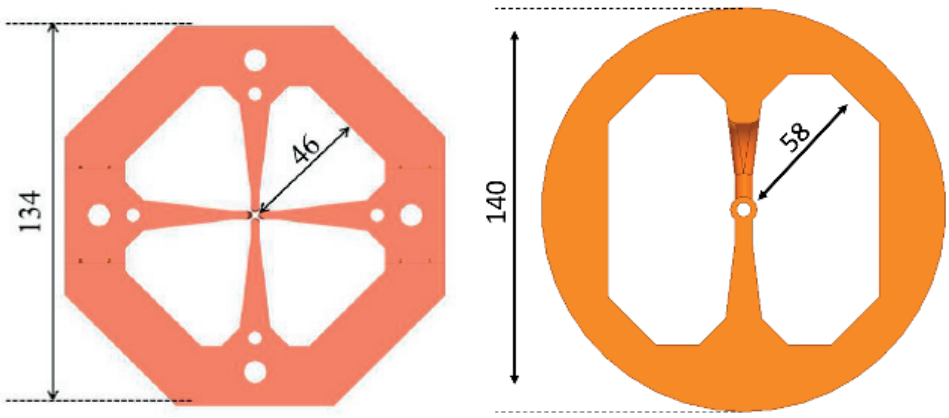

Figure 2.10 – Transverse section of 5 MeV/u cells. CERN RFQ (left) and IH cavity (right). Dimensions are in mm

operating frequency and geometric β. A more detailed discussion on the RF optimization of TE cavities can be found in [45].

2.2.3 Regular cell design

From the preliminary RF optimization summarized in Fig. 2.5, it was already clear that the 750 MHz IH cavity was the best solution in the 5-20 MeV/u regime. The simplified geometry considered in the first comparison was revised [49]. The main goal of the RF design has been to maximize the ZTT, while sticking as much as possible to the cavity geometry considered for the CERN 750 MHz RFQ, to take advantage of the experience gained in the construction of TE cavities at this very high frequency. Indeed both RFQ and H-mode cavities are constant voltage structures, with the only difference that a RFQ is a TE_{210} bunching machine, with vanes, while a H mode cavity is a TE_{110} accelerator, and present drift tubes between cells. This translates in overall comparable dimensions, as shown in Fig. 2.10. In particular the outer cavity walls have a flat section which as large as the RFQ one, to facilitate power coupling and tuning. Worth pointing out, this choice penalizes the Q factor: the ideal RF geometry would be a round one.

Three energies were studied in detail: 2.5, 5 and 10 MeV/u. The 2.5 MeV/u regime was studied, as previously pointed out, for the CABOTO design, since the 750 MHz 0.5 q/m RFQ under consideration will likely deliver up to 2.5 MeV/u particles instead of 5 MeV/u.

A multidimensional optimization was carried out, considering gap, drift tube thickness, stem radius, vane distance from z axis (stem height), as summarized in Fig. 2.11. Stem height refers to the distance between the z-axis and the point where the stem starts to have a conical a divergent angle α, which has been chosen equal to 14 deg, as in the 750 MHz RFQ. Parameters A, B and C were used to reach the desired operating frequency, and they were changed maintaining a flat surface large enough to allocate power couplers and tuning pins as in the RFQ.

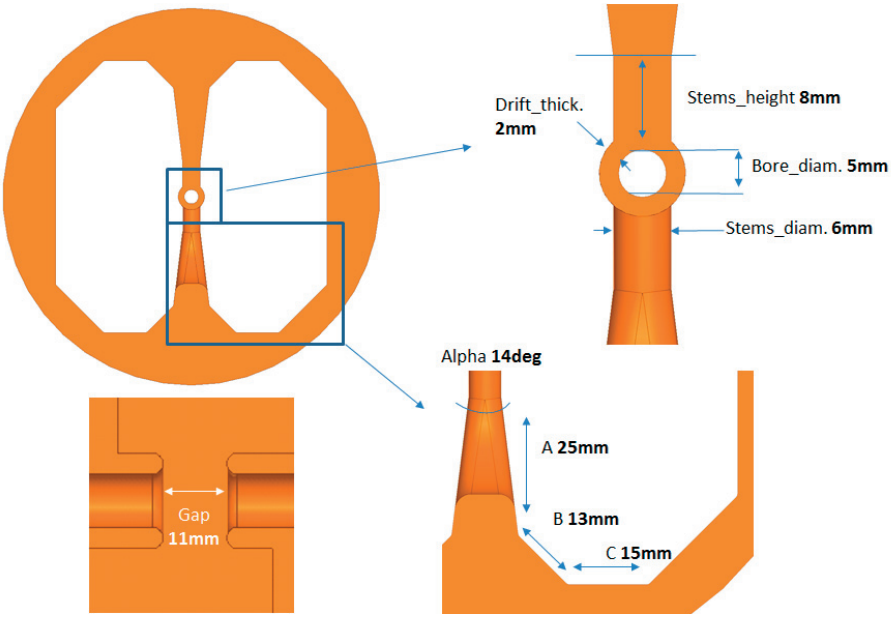

Figure 2.11 – Description of the geometric parameters of the IH cavity studied, and results of the 5 MeV/u cell optimization (in bold).

This constraint met, it was tried to have an outer geometry as round as possible, ideal for Q values maximization.

With respect to the 5 MeV/u RF cell, the optimization results are reported in Fig. 2.12. The optimization was eased by the monotonic behaviour of the ZTT as a function of the drift thickness. This last parameter is by far the most important one for the design considered. It has been chosen to consider a value of 2 mm, though a smaller value would have increase further the ZTT. However, both machining and maximum surface E-field (Fig. 2.12 left) considerations led towards the above decision. A final design could dare considering a smaller one, and maximize even further the ZTT (Fig. 2.12 right). For the other parameters, the ZTT curve shows an optimum (green cells in Fig. 2.12 top table).

The result of this study is a remarkably improved ZTT over previously found values (see dark red curve in Fig. 2.5). In particular, for the 5 MeV/u cell the ZTT goes from 280 $M\Omega/m$ to 410 $M\Omega/m$, with an increase of almost 50%. It is interesting to notice that the improvements does not come from a higher TT factor, since the gap is unchanged (Fig. 2.7), but from a increased Q value (Fig. 2.6).

This is the first time these values have been obtained in literature. As previously pointed out, this is due to the very small bore aperture considered, that allowed for a previously unreached high RF frequency. As discussed in Chapter 2.2.6, such aperture is sufficient to get full transmission of the particles bunched by the RFQ, thanks to the low transverse emittances and low current.

	1	2	3	4
Gap [mm]	10	11	12	13
Drift Thickness [mm]	1.5	2	2.5	3
Stems Radius [mm]	2	2.5	3	3.5
Stems Height [mm]	6	8	10	12

Figure 2.12 – Results of the 5 MeV/u IH cavity optimization. The curve optimum is highlighted in green, if it exists. In the bottom graphs the x-axis values refer to the upper table columns.

The main geometrical and accelerating parameters of the cavities studied are shown in Fig. 2.13, together with a view of two cells joined together.

2.2.4 Thermal analysis

The 5 MeV/u RF cell was studied, considering a 10 MV/m accelerating gradient, and a 1e-3 duty cycle. Both these two numbers represent a conservative assumption, and in particular for both TULIP and CABOTO a lower gradient is proposed (see Chapters 3 and 4).

A constant temperature of 22 °C was considered on the outer wall. This simplifies the thermal study, but it is however a reasonable assumption given that the thermal gradient is driven mainly by the thermal resistance of the stems. The simulated temperature difference is 1.2 °C, which corresponds to a maximum temperature induced deformation of 0.5 μm (Fig. 2.14).

As a preliminary conclusion, the 750 MHz IH cavities do not need cooling channels in the stems and drift tubes at the operating conditions considered for TULIP and CABOTO. It is worth commenting that cooling channels would require, together with an higher machining complexity, larger stems and drift tubes, resulting in a lower ZTT. This would turn out in an higher thermal load per accelerating gradient, that could eventually required an higher cooling flow. This structure is far from this detrimental loop. Instead, the 3 GHz DTL studied and discussed in Section 2.3 is on the edge of it.

The CERN 750 MHz RFQ [32] was designed to reach a 5% duty cycle, in view of potential applications of radioisotopes production. In this regard, a boost up to 10 MeV could be an interesting further development of such application. The IH was then studied considering

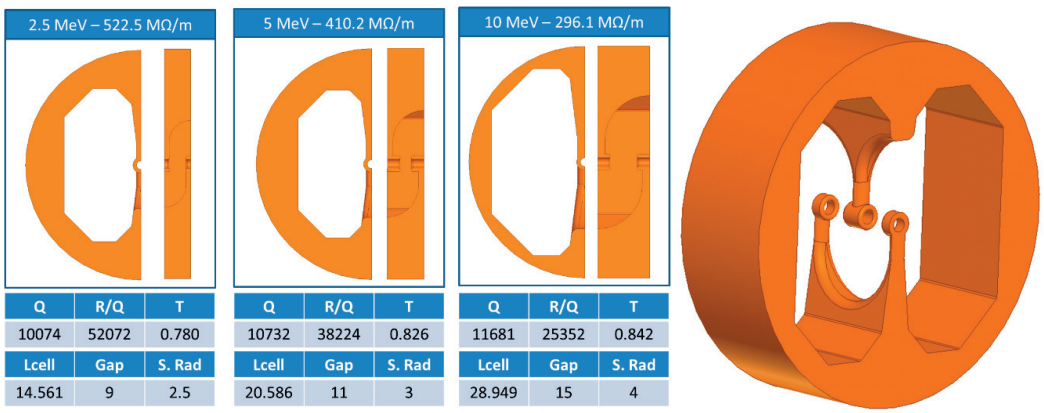

Figure 2.13 – Regular cell designs (left) and assembly view (right) of the IH 750 MHz cavity. Dimensions in mm and R/Q in Ω/m.

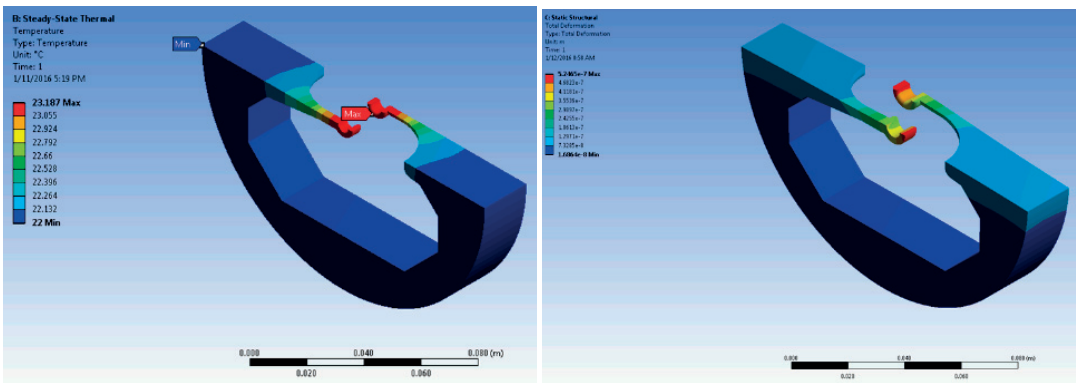

Figure 2.14 – Thermal and structural analysis for the 5 MeV/u IH cell at 10 MV/m accelerating gradient and 10-3 duty cycle.

a 5% duty cycle. In this case, a maximum temperature of 59.1 °C would be reached, with a induced deformation of 16.0 μm. In conclusion, this structure would need modifications in case a 5% duty cycle were needed.

2.2.5 End-cells design

End-cells are probably the most critical part in the design of an H-mode accelerating structure. The transition from a TE mode to a TM one, due to end-cell walls, forces a strong rupture of the symmetric chain, which can propagates along many regular cells and decrease significantly the overall ZTT. Passing from TE to TM translates into the need of increasing the cavity dimension.

Here two different solutions were studied, the first proposed in [50], and the second [51]. For this geometry, the solution of [51] resulted the better choice, as it showed a lower ZTT decrease with respect to regular cell design. As for the thermal study, only the 5 MeV/u cell was considered.

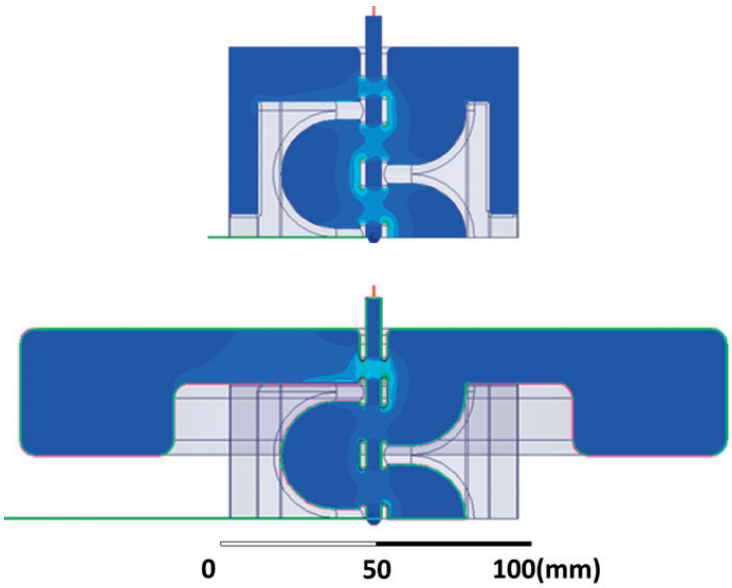

Figure 2.15 – E-field distribution in the IH end-cells with the solution proposed in [50] (bottom) and the one proposed in [51] (top).

As shown in Fig. 2.15, one end cell plus two regular ones were considered. Indeed, it would be more correct to refer to the whole geometry as an end cell, given the perturbation to the symmetric chain that is introduced. As shown in Fig. 2.16 right, the perturbation propagates till the inner RF cell. The matched frequency was adjusted by changing the outer volume of the end cell, while its length and gap were adjusted to maximize the ZTT (Fig. 2.17). A gap equal to approximately one half of the regular one has been found to maximize the ZTT, while the cell length is slightly increased (Fig. 2.16). Interestingly, as discussed in Section 2.2.6, a reduced gap in the end cell is helpful for the beam dynamics of the cavity. A maximum value of 153.7 $M\Omega/m$ was found, that if compared with the ZTT of a regular 5 MeV/u cell of 410.2 $M\Omega/m$ represents a remarkable 63 % reduction.

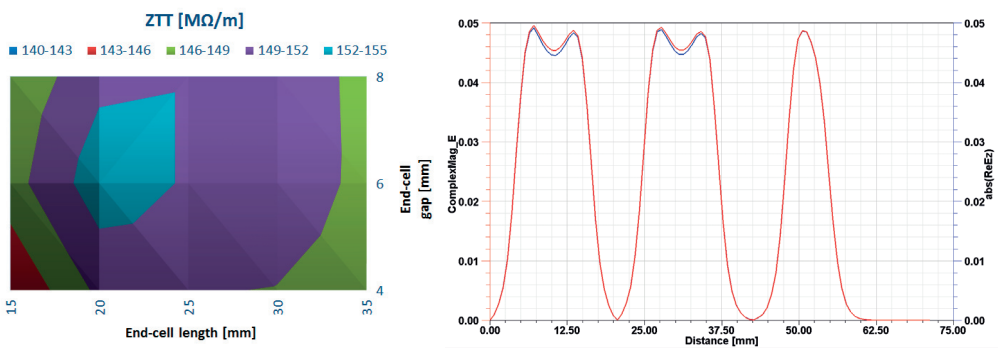

Figure 2.16 – End-cells 2D optimization result (left) and E-field distribution along the z axis (right) in arbitrary units, for the end-cell design of Fig. 2.15 top.

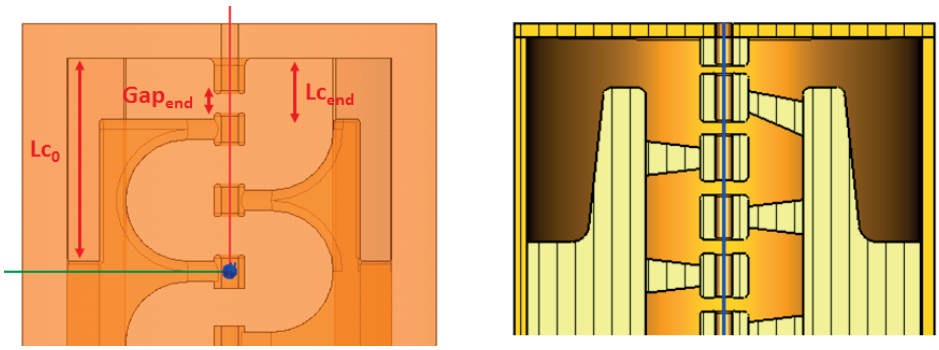

Figure 2.17 – End-cells design with the parameters studied in the optimization (left) and solution presented in [51]. Dimensions are not in scale.

The acceleration efficiency of an IH structure is thus dependent, amongst the other parameters, on the number of RF cells. The higher, the less the end cell ZTT reduction affects the overall efficiency. End cell should be studied also for the 2.5 and the 10 MeV/u RF cells, to obtain a curve that can be interpolated and used depending on the linac design. If, on first order approximation, we assume a constant 63 % reduction due to end cells, an IH structure would have a ZTT reduction, with respect to the single RF cell value, ranging from 63% to zero, in case of end-cells only and infinite long structure, respectively.

The end cells design here proposed is satisfactory from RF point of view, but it still requires a mechanical and machinability study. The design adopted in [51] refers to a 200 MHz (and 5 mm bore aperture radius) design. The present design, being a 750 MHz cavity, is a bit more challenging in that sense and thus require further mechanical studies (Fig. 2.17).

In this regard, a preliminary discussion was held with the responsible of the mechanical design and assembly of the CERN 750 MHz RFQ. The design here proposed was judged feasible at this first stage.

2.2.6 Dipole kicks and transversally focusing IH cavities

The understanding of the particles beam dynamics in the complete accelerating structure influences the RF design of the IH cavity. For this reason, this topic is hereafter discussed.

Given the small bore aperture and thin drift tubes, a not negligible dipole kick component is present in each RF cell, equal to almost 15 % of the longitudinal component. Indeed, when the beam was tracked through the structure field map with the RF-Track code (see Appendix A), it showed a final displacement of about 0.7 mm out of a 2.5 mm bore aperture. This was clearly a not acceptable result, and it has been corrected in the following way.

In Fig. 2.18 top one can notice the x displacement of a single particle that enters the field map with no initial displacement and divergence . The particle gets deflected in the first gap, then drifts away in the drift tubes. In the second gap, the dipole kicks has opposite direction

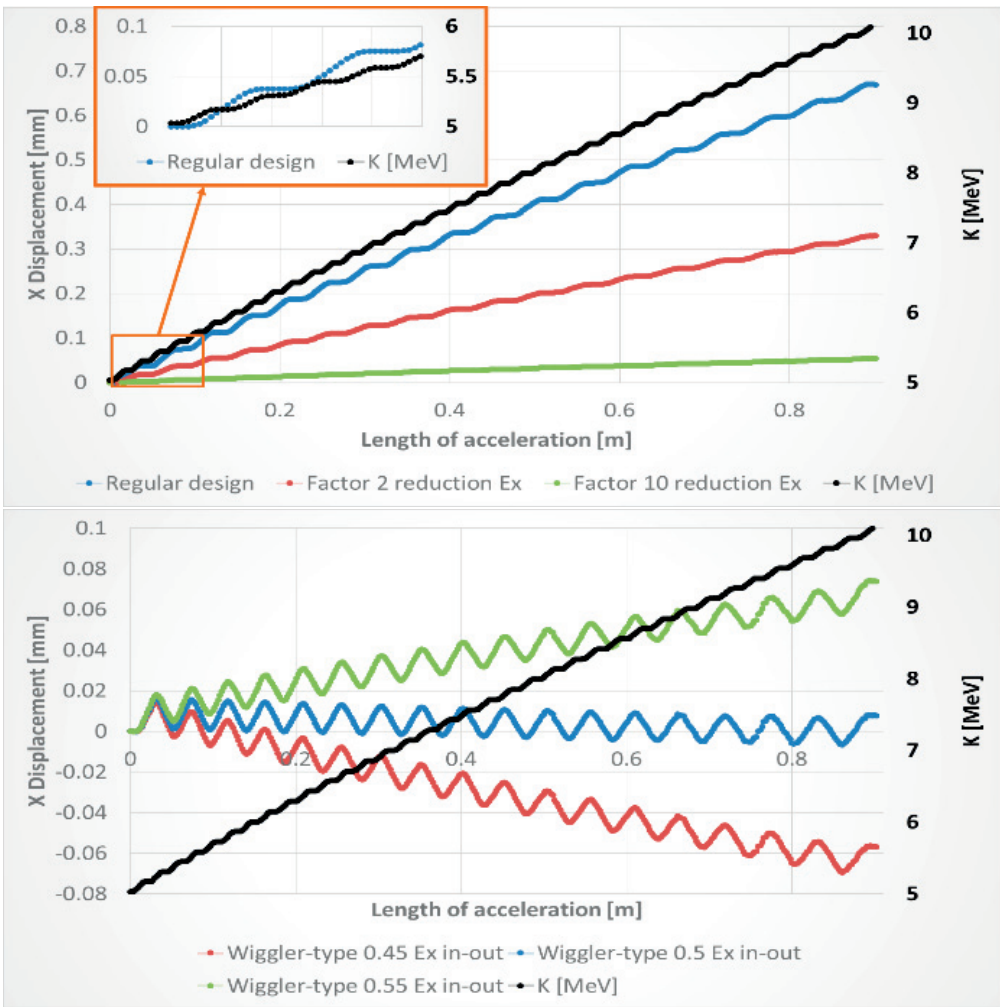

Figure 2.18 – Single particle tracking through the IH structure. Dipole kicks reduction (top) and undulator solution (bottom)

but almost equal magnitude. In fact, a IH cavity is a constant voltage structure, so also the transverse voltage is constant. This is true at first order approximation, given that the dipole kick component increases with longer cell lengths. However, so does the beam rigidity. Overall, the particle divergence gets approximately to zero in the second gap of the structure. Then in the third gap it picks again a x divergence, which gets cancelled again in the forth gap. So, travelling through cells, the particle shows a linear displacement with energy, and zero integrated kick. Solutions proposed in previous works [51] were based on the modification of the drift tube shape and relative position with respect to the x axis, to reduce the dipole component. For the IH cavity under study, this presents the disadvantage of reducing the ZTT with respect to the nominal solution. In addition, particles would still experience a linear displacement, simply a smaller one (Fig. 2.18 top, red and green curve).

In this work a new solution is proposed. By halving the dipole kicks component in the first

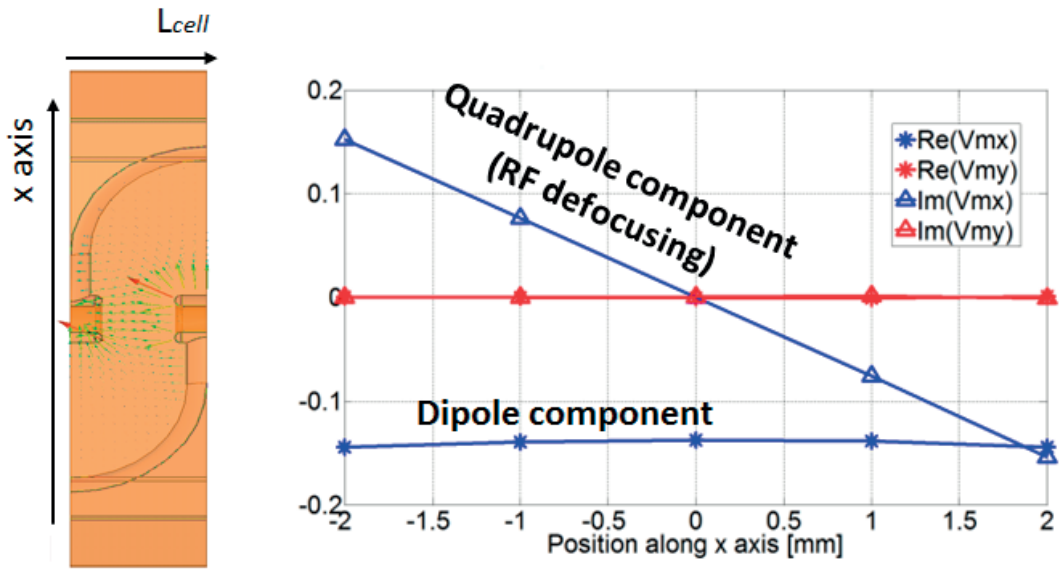

Figure 2.19 – E-field lines in the 5 MeV/u IH cell (left) and transverse voltage along the x axis normalized to the accelerating voltage in the 5 MeV IH cavity (right).

accelerating gap, also the divergence picked up by the particles is halved. As a consequence, the second gap, which has a "nominal" dipole kick, over-steers the beam, that has now a negative divergence. This solution is shown graphically in Fig. 2.18 bottom, which shows the single particle displacement along the IH structure field map with this solution adopted. The trajectory of the particles recalls the one of an undulator. Eventually, the last gap must also have a half dipole kick component, to zero the integrated kick. As pointed out in Section 2.2.5, ZTT optimized end-cells have gap which is about one half a nominal one, thus resulting in an approximately halved transverse voltage as well. This is very convenient, since it permits to efficiently control the beam with minor modifications of the optimum geometry.

The small bore aperture, together with the thin drift tubes and large gaps of the IH cavity, results in a non negligible dipole kick. Analytically, a dipole kick is represented by a real part of transverse voltage:

$$\vec{V}_m = TT \int_0^{L_{cell}} (\vec{E} + \vec{\beta} c \times \vec{B}) dz, \tag{2.9}$$

which is constant across the bore diameter, as shown in Fig. 2.19. In Eq. 2.9 TT is the transit-time factor. A dipole kick is typically negligible in DTL solutions, that have thick drift tubes to allocate the PMQs, and shorter gap to cell length ratios given the 2π mode regime. In contrast, the RF defocusing, which has 90 degree RF phase shift with respect to the dipole kick component, is represented in Fig. 2.19 as an imaginary part of the voltage which is linear along x-axis, the axis on which the stems are placed.

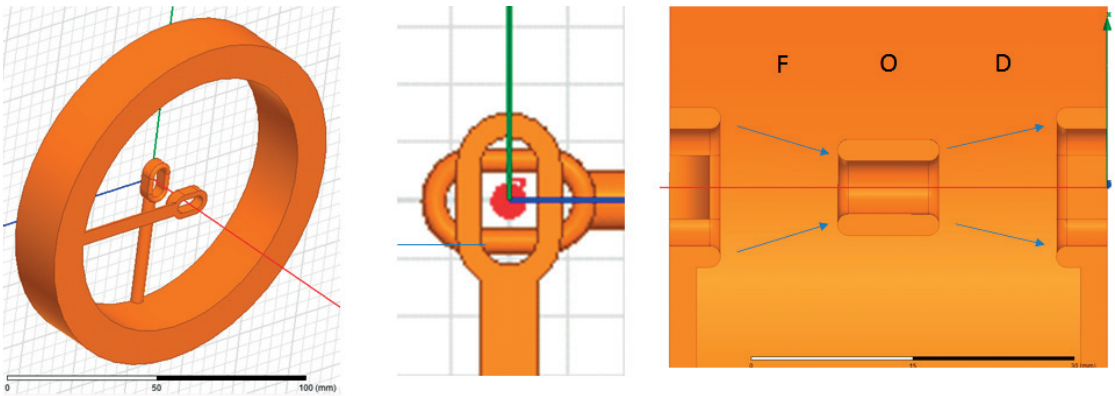

Figure 2.20 – 5 MeV/u cavity with "racetrack" drift shape.

From the results of Fig. 2.19 one can notice that the transverse kick is equal to about 15 % of the longitudinal kick per cell, for the 5 MeV/u cell. This contribution increases with the cell length.

Given this very high value found, a study was carried out to investigate the possibility of designing a transversally focusing IH cavity. Such a solution would allow to control both the longitudinal and the transverse beam dynamics in the structure itself, without loosing accelerating length as with a conventional quadrupole magnets focusing. The strategy adopted was to modify the drift shape, from a cylindrical one to a "racetrack" one, as shown in Fig. 2.20. Indeed the geometry considered is not anymore an IH cavity, since the stems are not 180deg rotated. However, the shape of the drift tubes allows to get a quadrupole focusing in each cell, like in a RFQ, and this is the purpose of the present study.

Analytically, a quadrupole focusing manifests with a linear real part of the voltage, similar to the RF defocusing but out of phase as in an RFQ, as shown in Fig. 2.21. It is possible also to notice a dipolar component along y, together with x, given by the 90deg rotated stems used in this study (Fig. 2.20).

This solution was studied at 2.5, 5 and 10 MeV/u cells, varying the racetrack eccentricity and cell gap. In this case in fact, the shorter the gap, the higher the RF quadrupolar focusing. However, to obtain a strong enough RFQ focusing capable of controlling the particles, the racetrack design has to be such that the ZTT more than halved, as shown in Fig. 2.22. In conclusion, this solution was discarded.

From theoretical point of view, the reason why this solution does not work is hereafter explained.

The EM RF focusing is given, from the Lorentz equation, by:

$$\vec{F} = q(\vec{E} + \vec{\beta} c x \vec{B}), \tag{2.10}$$

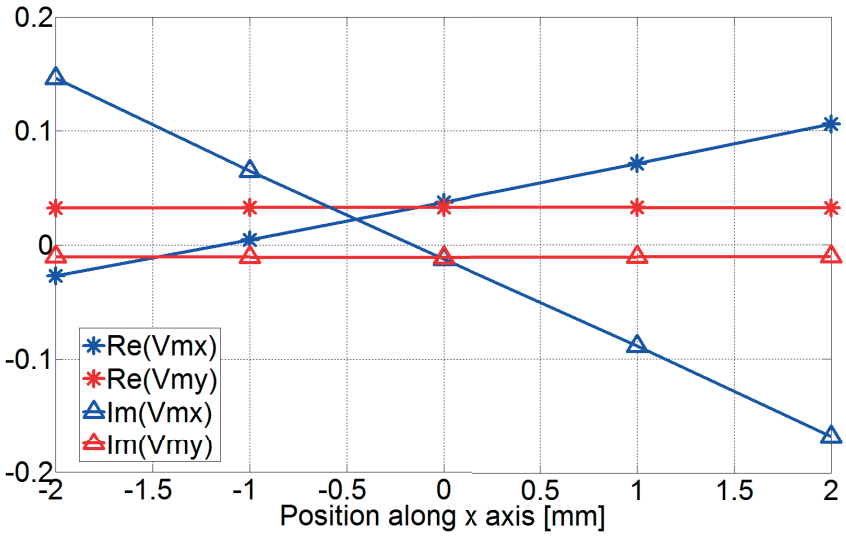

Figure 2.21 – Transverse voltage along x axis normalized to the accelerating voltage in the 5 MeV/u RF cell with "racetrack" drift shape.

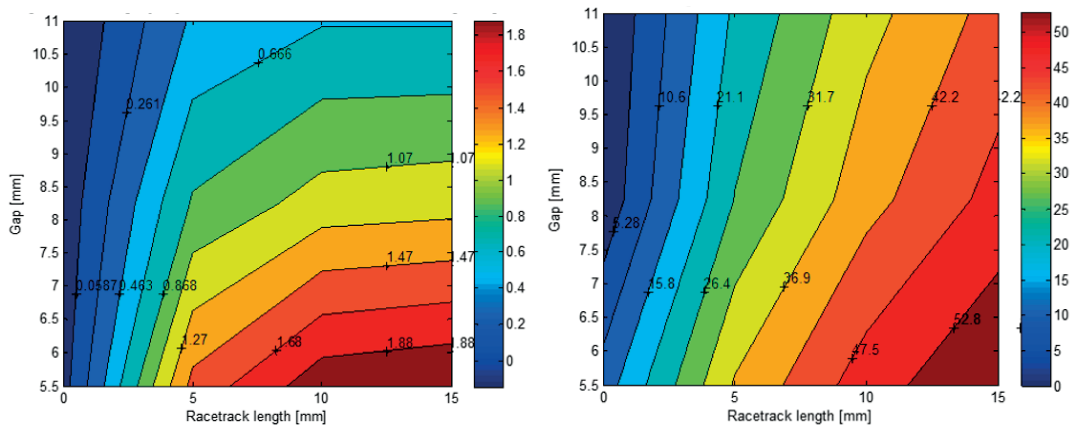

Figure 2.22 – Racetrack optimization results for the 5 MeV/u cell. Integrated focusing strength [1/m], as defined in Eq. 2.16 (left), and correspondent ZTT decrease (right).

so along x we have:

$$F_x = q(E_x + \beta c \cdot B_y + y' \beta c \cdot B_x) \approx q(E_x + \beta c \cdot B_y). \tag{2.11}$$

If we compare this equation with the force impressed on particles by a quadrupole, assuming no fringe fields, we have:

$$F_{xQUAD} = q(\beta c \cdot B_{yQUAD}) = q(\beta c \cdot G \cdot r). \tag{2.12}$$

By integrating over one cell length and equalizing the two expression we finally get :

$$\int F_x = \int F_{xQUAD} \rightarrow \tag{2.13}$$

$$V_{mx} = TT \int (E_x + \beta c \cdot B_y) = (\beta c \cdot G \cdot r) \cdot L_C \tag{2.14}$$

where TT is the transit time factor of the RF cell, so V_{mx} is the average transverse voltage as seen by the particle along the x-axis. Finally, we can relate the force acting on a particle by a quadrupole gradient with the force impressed by a transverse voltage obtaining an *equivalent gradient*:

$$G = \frac{V_{mx}}{\beta c \cdot r \cdot L_C} [\frac{T}{m}]. \tag{2.15}$$

If we integrate Eq. 2.15 over the cell length L_C, and to the particle momentum p, we obtain an *equivalent integrated strength*:

$$k \cdot L_C = \frac{G \cdot L_C}{p} = \frac{V_{mx}}{\beta c \cdot r \cdot p} [\frac{1}{m}]. \tag{2.16}$$

So, as a summary, there is a factor βc between the effect of a magnetic gradient G and a transverse electric voltage V_{mx} on a particle trajectory over one cell length. This is the reason why EM focusing is used only at low energies and in bunching, rather than accelerating, cavities, like RFQs.

2.3 The high-efficiency 3 GHz DTL

The 3 GHz DTL was very shortly studied from RF point of view, mainly due to lack of time. However, a working solution of this technology was built and tested by ENEA in Frascati, Italy [31].

Table 2.3 – Accelerating parameters of the optimized DTL RF cells for different geometric β.

Energy [MeV/u]	Geometric β	Length [mm]	Gap [mm]	Radius [mm]	ZTT [MΩ/m]	Q value	R/Q [Ω/m]	TT factor
5	0.1028	10.281	1.5	31.53	37.3	11422	3266	0.539
10	0.1448	14.482	3.0	32.03	78.2	14913	5247	0.669
15	0.1767	17.667	4.0	31.52	99.2	15713	6316	0.725
30	0.2470	24.695	6.5	30.36	117.0	15812	7400	0.773
50	0.3140	31.399	10.0	30.15	111.0	15892	6986	0.750
70	0.3660	36.603	12.5	29.31	100.5	15046	6681	0.734

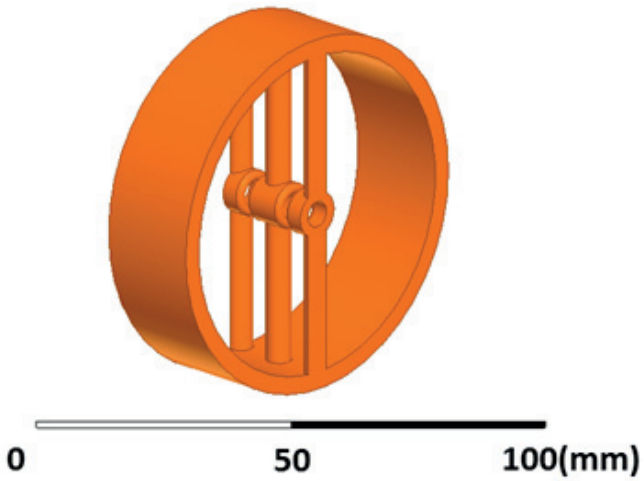

Figure 2.23 – The 5 MeV/u reference 3 GHz DTL cavity.

2.3.1 Regular cell design

The 3 GHz DTL appears to be the most efficient choice amongst the solutions studied in Section 2.2.1 (Fig. 2.5) for energies higher than 15 MeV/u. Nevertheless, the regular cell simplified geometry considered cannot be adopted as the reference one, due to limitations coming from structural and RF heat power dissipation. A two stems geometry has been eventually considered (Fig. 2.23). In [31], a rectangular stem surrounding the drift tube, and with two internal cooling pipes, was considered. Such modification allows for a sufficient heat dissipation and mechanical stability, but impacts on the ZTT profile presented in Fig. 2.5.

The geometry of Fig. 2.23 was optimized in terms of ZTT at different RF cell lengths, from 5 to 70 MeV/u, by varying the cell gap (Table 2.3). A more detail optimization was not performed since, as discussed in Section 2.2.2, DTL cavities have a monotonically increasing ZTT for thin drift tubes and stems. While too thin drift tubes should be avoided to limit the surface electric field concentration, too thin stems limit the heat dissipation, and so the gradient and the duty cycle achievable. In addition, the machining and brazing of thinner pieces is more challenging. The main geometrical and accelerating parameters of the cells optimized are reported in Fig. 2.3. With respect to the preliminary study of Fig. 2.5, the ZTT reduction is around 25 %.

This solution raises a slight quadrupolar asymmetry, i.e. the RF defocusing is stronger in the

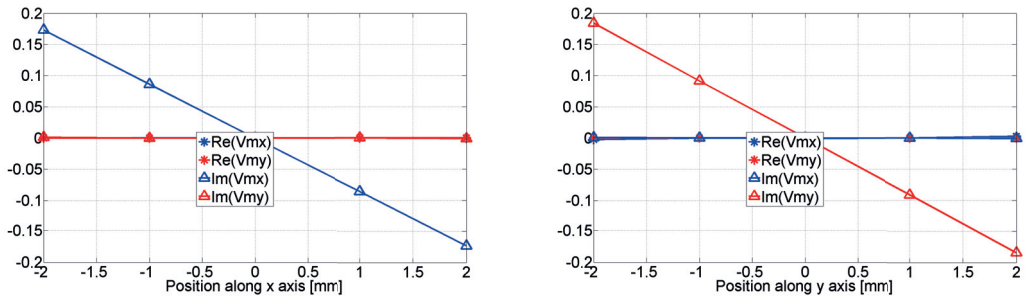

Figure 2.24 – Transverse voltage along x and y axis normalized to the accelerating voltage for the 15 MeV/u DTL RF cell with symmetric stems.

plane of the stems (y-plane in Fig. 2.24). The difference has been taken into account in the beam dynamics design.

For the CABOTO design, following a preliminary particle tracking (see Fig. 4.3), it was decided to taper the DTL bore aperture from 2.5mm radius at 10 MeV/u, to 1.75mm radius at 100 MeV/u. The optimize RF cells (Fig. 2.3) were not re-optimized, but simply recomputed with the new bore aperture. The result of this work is summarized in Fig. 2.25. A gain of approximately 12% in ZTT, with respect to the constant 2.5mm design used in TULIP, has been reached.

The DTL studied has too small drift tubes to allocate focusing elements within them. Thus, a side-coupled DTL (SCDTL) is considered, where the different cavities are magnetically coupled with a side coupling cell in order to allocate quadrupole magnets between the accelerating cavities. This is the solution also proposed in [31]. The author did not study a full 3D RF SCDTL, but only a single RF cell DTL geometry, thus this latter term will be used in the text.

Thermal and structural considerations

From thermal point of view, the 10 MeV/u DTL section is the most critical one. The RF cell has a simulated ZTT of 78.2 $M\Omega/m$. Considering a 10^{-3} DF, and the 12 MV/m accelerating gradient of the TULIP design (see Section 3.1.2), one has a maximum temperature on the noses of 41 °C (Fig. 2.26 left). In the simulation, the outer wall was kept constant at 22 °C. The induced mechanical stress and the RF detuning from the geometry deformation were not studied. However, it is assumed that a 40 °C maximum temperature can be accepted.

If, however, this would not be the case, or if, for brazing easiness, a rectangular stem would be needed, the RF efficiency of the cavity would be further penalized. In particular, in case of a rectangular stem, and maintaining the optimized gap of 2.3, the ZTT would decrease of 33%, to 52 $M\Omega/m$. In this case, the resulting maximum temperature, to achieve the same accelerating gradient, would be 57 °C (Fig. 2.26 middle). So the lower thermal resistance would not be sufficient to counterbalance the higher thermal load. A drift cooling system would then be needed (Fig. 2.26 right).

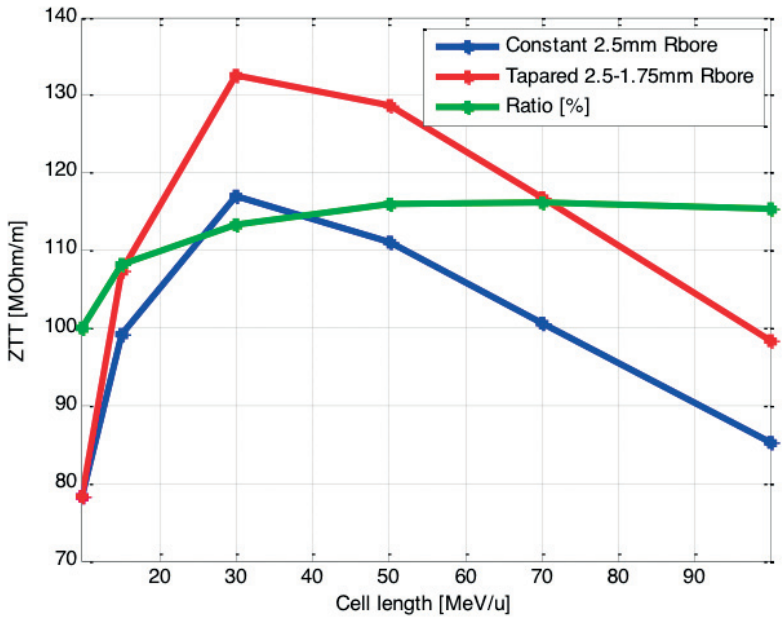

Figure 2.25 – ZTT profile in the DTL linac, for a constant and a tapered bore aperture.

For TULIP, the 12 MV/m - 10^{-3} DF study preliminary simulates the design operating conditions. Thus the design of Fig. 2.26 left is, at this stage, acceptable. For the CABOTO design instead, an higher DF of 360 Hz is under consideration, in addition to a slightly higher accelerating gradient of 15 MV/m (see Section 4.1.2). In this later case, rectangular stems with cooling channels would be required.

This is a good example of how deep the DF and the design voltage of a cavity affect its RF optimization. If one really wants to reach the limits in a RF design, either in terms of maximum gradient or maximum efficiency - it does not really matter, both cases shall be at the limit from thermal point of view - one needs to specify also the DF.

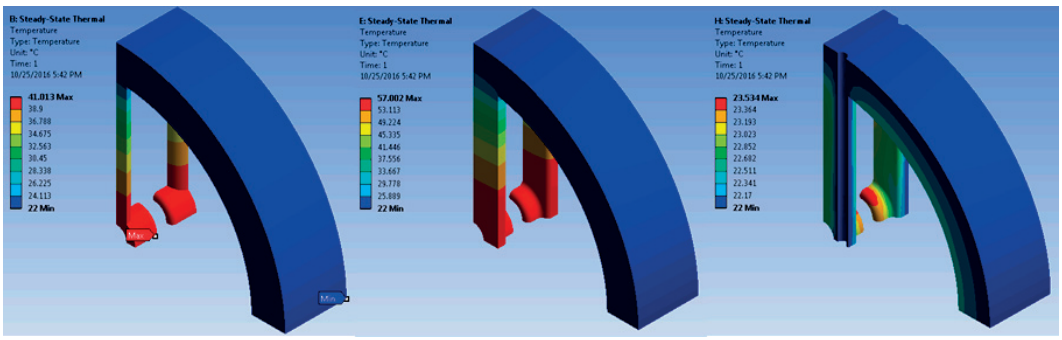

Figure 2.26 – Thermal analysis of the 10 MeV/u DTL cell, fro different stems geometries.

2.3.2 Criticality and points of strength

During this thesis people raised criticisms towards the feasibility of a 3 GHz DTL linac. The main concern were the brazing and alignment tolerances of the drift tubes on one side, and the field stability on another side. None of these arguments was addressed during this thesis. However, a short discussion on the second point, tuning and field stability, is helpful.

Being 0 mode structures, DTLs are very prone to frequency perturbations. For this reason, post couplers are inserted in the geometry, and their resonator band is coupled to the main TM_{01} one [52]. The problem arises when the operating frequency increases: the small dimensions of the tank makes difficult the tuning of the post couplers themselves. In addition, the bandwidth of the cavity gets smaller at higher frequencies, thus making more difficult to reach confluence between the post-couplers and the cavity dispersion curves. As a final note, post couplers affect the Q factor of the cavity due to surface currents, thus the ZTT of the DTL cavity is lower than the RF regular cell one. As an example, in CERN Linac4 DTL - a 352.2 MHz H- machine, working from 3 to 50 MeV - the losses from post couplers lower the ZTT of approximately 2 % [53]. A full 3D RF and mechanical design should thus further address this topic. However, as previously mentioned, a working solution of a 3 GHz DTL was presented in [31].

On the other hand, a 3 GHz structure can be powered by klystron-modulator units at the same frequency. These are worldwide adopted in more than 1000 electron linacs for radiotherapy, and are thus very cheap RF power sources, when compared to 750 MHz IOTs for instance. The cost argument is a key aspect of both TULIP and CABOTO, being medical designs, thus it has been privileged at this stage.

750 MHz IH vs 3 GHz DTL beam dynamics comparison

In Section 2.2.1 it was shown that up to 20 MeV/u, the 750 MHz IH solution is more efficient than a 3 GHz DTL one from a ZTT point of view. In this section, the beam dynamics of the two solutions will be discussed. The reader may wonder why this topic is presented in the RF chapter. The reason is that beam dynamics considerations contributed in defining the transition energy from the 750 MHz IH to the 3 GHz DTL solution. Thus, in defining the energy, or geometric β, of the optimized RF cells for the two cases.

To get a fair comparison, here two solutions will be compared: a IH (5 to 10 MeV/u) plus DTL (10 to 20 MeVu) and a full DTL (5 to 20 MeVu). So it is possible to compare final beam parameters in similar phase space configurations. A beam of proton was considered in the present study.

The main aspects that have been compared are:

- particles transmission;
- emittance growth;

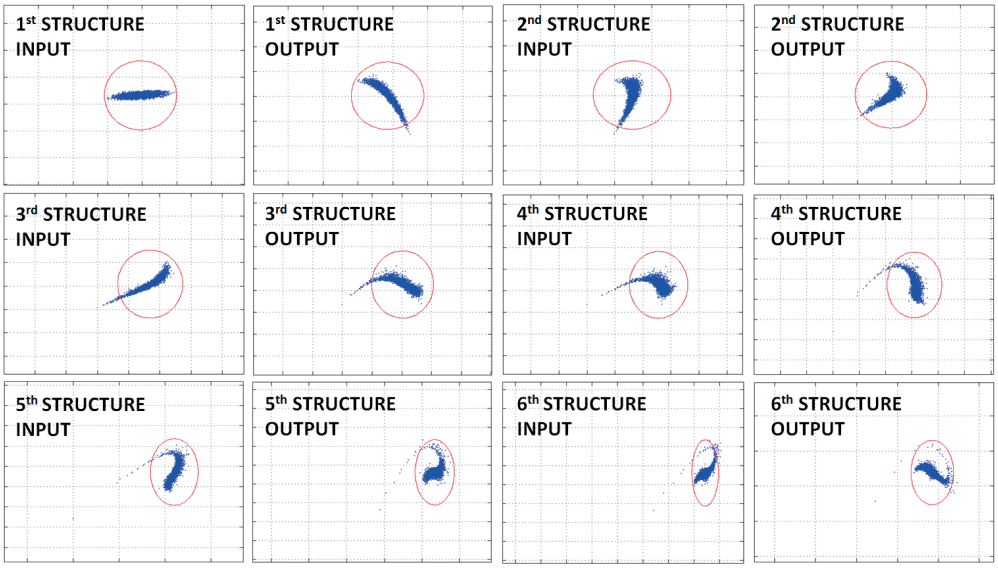

Figure 2.27 – Longitudinal phase space in and out the first 6 accelerating tanks of a DTL solution, from 5 to 7.7 MeV, with simplified buckets contour in red. The different picture are in scale.

- overall length and space for diagnostic;
- number of elements;
- power consumption.

Beam transmission was prioritized amongst all others parameters.

The DTL choice reveals to be particularly challenging in the 5 to 10 MeV/u range. The space between the RFQ and the first DTL module is limited by the longitudinal acceptance of the beam. This limits the transverse matching of the beam, with repercussion on the emittance growth. A solution could be the installation of a buncher cavity, that would allow a longer matching section. A second problem arises from the relatively high accelerating gradient. At 5 MeV, the ratio between active and total length is well below 50 %, since the RF defocusing has a square dependence with particle momentum [54]:

$$\Delta p_r = -\frac{\pi e E_0 T L r \sin\phi}{c\beta^2\gamma^2\lambda}, \tag{2.17}$$

and so it is necessary to have short accelerating tanks with PMQs in between. As a result, to accelerate over the same length, the gradient of the full DTL solution must be higher with respect to the IH-DTL solution. This results in a heavily longitudinally mismatched beam. Fig. 2.27 shows the longitudinal phase space evolution of the beam in the first six DTL accelerating structures.

Table 2.4 – Beam dynamics comparison between an IH-DTL and a full DTL solution in the 5 to 20 MeV/u range.

Parameter	IH+DTL	DTL
Synch. Phase [deg]	-12 (IH) and -20 (DTL)	-30 (5 to 10 MeV) and -25 (10 to 20 MeV)
Transmission	100	99.6
Transverse ϵ growth [%]	7	35
Longitudinal ϵ growth [%]	53	166
Total length [m]	3.01	2.89
Active length [m]	1.68	1.26
Number of accelerating structures	10	19
Number of PMQ	15	20
Peak power consumption [MW]	0.1 (750 MHz) + 2.0 (3 GHz)	3.7

As one can notice, the beam fits well in the first structure longitudinal bucket (red contour). However, the combination of high accelerating gradient and long drift sections between the different DTL tanks led to filamentation, eventually resulting in emittance growth and losses.

An higher synchronous phase would not help, since it will increase the RF defocusing. So shorter structures would be needed to transversally control the beam, and the accelerating gradient should be increased to keep the overall length constant. Two solutions could be followed. One could reduce the accelerating gradient to get a smoother acceleration in the first sections, but resulting in a longer linac. Alternatively, it would be possible to match the beam from tank to tank, by designing the DTL such that the synchronous phase and gradient change adapting to the longitudinal orientation of the beam ellipse. This last proposal would raise significantly the RF design complexity of such linac.

The two designs are summarized in Table 2.4 and displayed graphically in Fig. 2.28 and 2.29. The overall dimensions are comparable in the two designs. However, the full DTL solution shows losses and an higher emittance growth. In addition, there is not space to allocate beam diagnostic. As a final comment, the full DTL solution require more PMQs and accelerating structures, so an higher number of brazing and tuning procedures.

2.4 The high-gradient 3 GHz BTW accelerating structure

A high gradient backward travelling wave (BTW) accelerating structure was designed and built at CERN [55] [56]. The main goal of the study is to define the high gradient limits of S-band cavities in terms of Break-down Rate (BDR). A Modified Poynting Vector (S_c) limit was used in the RF design of the prototype [44]. A picture of the prototype, which is 20 cm long and has a geometric β of 0.38, is shown in Fig. 2.30.

The RF design and optimization of regular cells started before the begin of this thesis, and it is presented in [7]. In this work, the RF cells were optimized considering two intra-cell wall thickness of 1.5mm and 3mm. Following an experimental campaign, the minimum septum thickness that can withstand the creep-induced deformation during the hydrogen bonding

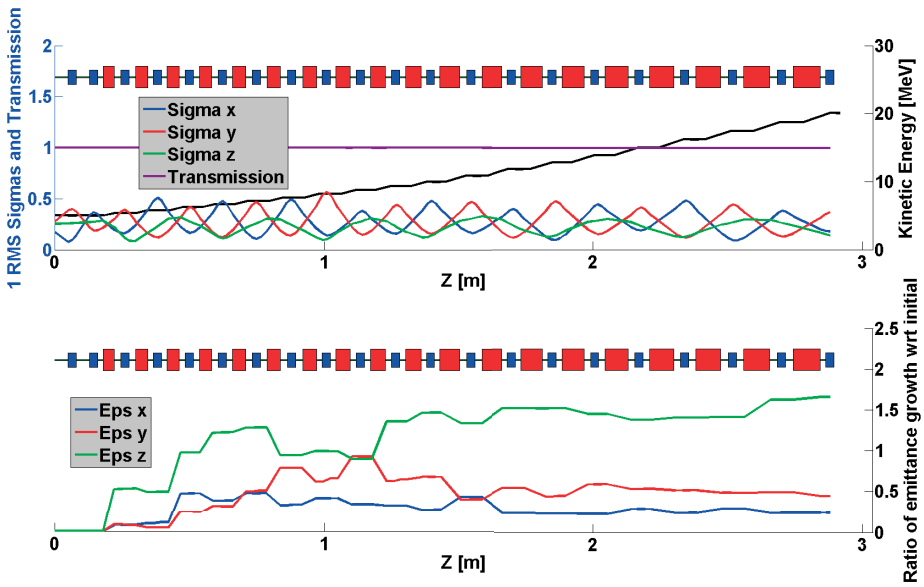

Figure 2.28 – Beam 1 σ RMS envelope through a DTL structure from 5 to 20 MeV/u (top) and ratio of emittance growth with respect to initial (bottom).

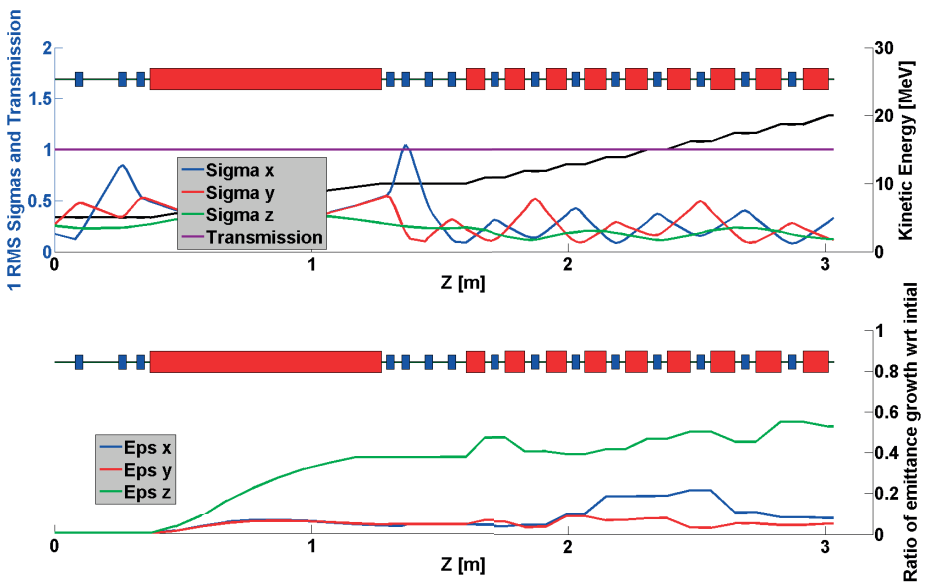

Figure 2.29 – Beam 1 σ RMS envelope through the IH+DTL structure from 5 to 20 MeV (top) and ratio of emittance growth with respect to initial (bottom).

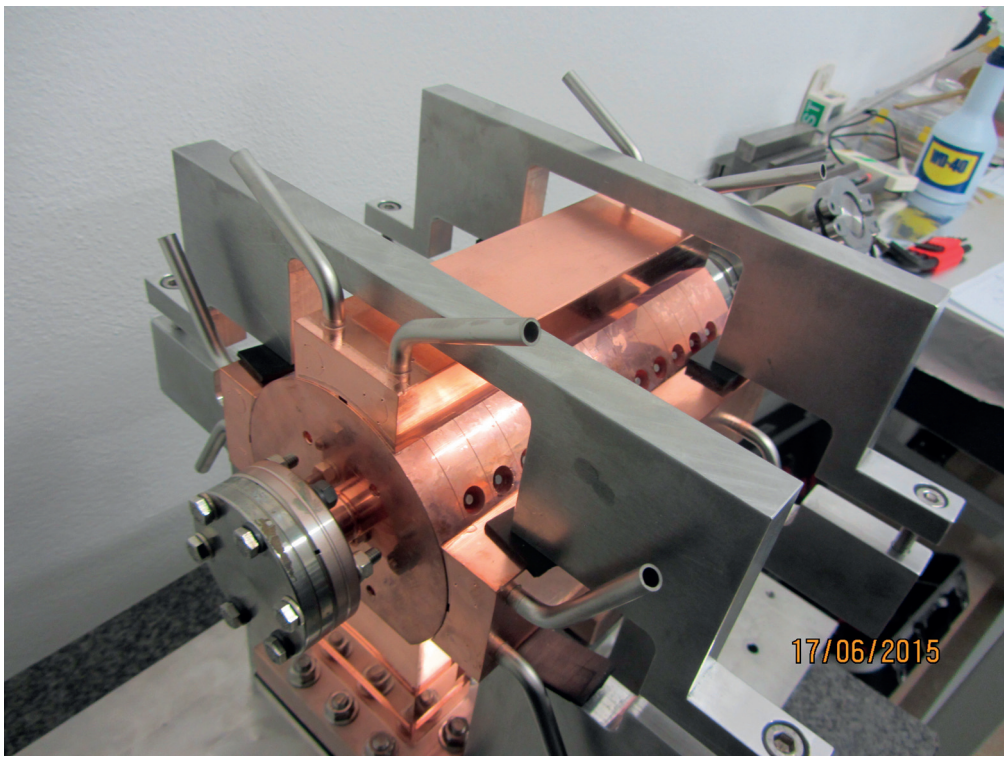

Figure 2.30 – The 3 GHz BTW prototype.

heat cycle (with a maximum temperature of 1050 °C) was found to be 2 mm.

Following this result, the author re-optimized the RF cells, and completed the 3D RF design by designing the end-cells couplers. In the following, the optimization of RF cells is thus presented, being an original work, even though it has been set up in a previous thesis. Instead, the theory of BTW accelerating cavities is just shortly summarized, in order to allow the reader to fully understand the choices made. A more complete introduction on the BTW prototype can be found in [7].

In particular, the choice of the phase advance per RF cell, the choice between a constant-gradient and a constant-impedance structure, and the group velocity profile along the structure were decided and motivated in [7], and are not presented here.

2.4.1 A backward travelling wave accelerator

A travelling wave cavity has a number of advantages over a standing wave one. In particular:

- shorter filling time;
- no resonant modes instabilities;
- in general, easier tuning and machining.

On the other hand, a TW cavity needs two coupling cells, and a part of the RF power is coupled to an external circuit or a load. Unless a power re-circulator is designed, some of the power is lost.

The need to adopt "noses" in the RF cell geometry, to enhance the transit-time factor, led towards the choice of a magnetic coupling between cells, and so of a backward TW rather than forward TW cavity. When a magnetic coupling is implemented, the dispersion curve of a L1 C1 RF cell coupled through an inductance L2 is given by [42] [48]:

$$\omega = \frac{\omega_0}{\sqrt{2(\frac{L_2}{L_1})(1 - cos\phi) + 1}}. \tag{2.18}$$

where ϕ is the phase advance per period, ω_0 is the resonant frequency of the single RF cell, L2 is the coupling inductance, and L1 is the cell inductance. It is easy to verify from Eq. 2.18 that ω_π is lower than ω_0, so the π mode lies lower in frequency than the 0 mode. As a result, group velocity and a phase velocity have opposite sign: this is the so-called *backward-wave mode*.

2.4.2 Regular cell design

The RF cell optimization was driven by the minimization of the quantity:

$$\mu \equiv \frac{P_w}{E_a^2} \cdot \frac{S_c}{E_a^2} = \frac{v_g}{\omega} \cdot \frac{S_c/E_a^2}{R'/Q} \tag{2.19}$$

where P_w is the power dissipated in one cell, E_a is the accelerating gradient, v_g is the group velocity, ω is the angular RF frequency, R' is the effective shunt impedance per unit length and Q is the quality factor per cell. S_c is a Modified Poynting Vector, that has been used as a new local field to predict the breakdown behaviour of the structure.

Eq. 2.19 equally weights the dissipated power and the modified Poynting vector; thus, minimizing it one obtains for a given power the highest accelerating gradient for a given BDR. The $\frac{S_c}{E_a^2}$ threshold was calculated by re-scaling CLIC experimental data to pulse lengths typical of medical linacs, i.e. 2.5 μs flat-top. CLIC data were rescaled according to Eq. 2.20:

$$\frac{S_c^8 \cdot t_{impulse}^3}{BDR} = const \tag{2.20}$$

following a research campaign on S-Band and C-band single cavities carried out by TERA Foundation [38] [30] [7]. From Eq. 2.20 one obtains a limit of 0.7 mA/V for the ratio S_c/E_a^2.

In this particular design, the optimum is found when S_c is minimized simultaneously on the nose, where the electric field is maximum, and on the coupling holes, where the magnetic

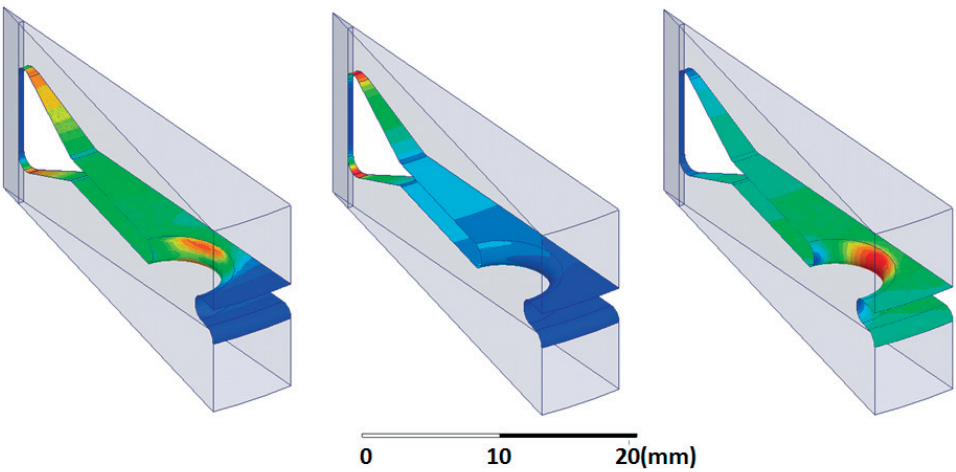

Figure 2.31 – Electric (left), magnetic (centre) and modified Poynting vector (right) field distribution in a regular cell section (1/32 azimuthal symmetry).

Table 2.5 – Tables summarizing the parameters fixed by the optimization (left) and the accelerating figures of merit (right).

Fixed geometric parameters		**Average accelerating parameters**	
Cell length [mm]	15.82	Geometric β	0.38
Iris thickness [mm]	2	Frequency [GHz]	2.9985
Gap [mm]	7	Q value	7194
Nose cone angle [°]	65	R'/Q [Ω/m]	7394
Bore radius [mm]	2.5	ZTT [MΩ/m]	53.2
Nose inner radius [mm]	1	v_g [‰of c]	2.926
Nose outer radius [mm]	2	E_s/E_a	3.86
Corner inner radius [mm]	1	H_s/E_a [1/kΩ]	4.64
Corner outer radius [mm]	1	S_{cnose}/E_a^2 [1/kΩ]	0.26
Number of cells	12	S_{chole}/E_a^2 [1/kΩ]	0.25

field is maximum, as shown in Fig. 2.31. The maximum S_c/E_a^2 ratio on the final design is 0.3 mA/V.

At the same time, the design was limited so to have a maximum surface electric field to accelerating gradient ratio of 4, thus a surface electric field limit of 200 MV/m. The maximum surface magnetic field to accelerating gradient ratio is instead 5 mA/V, thus a surface magnetic field limit of 250 kA/m.

The RF cells were optimized considering the gap and the cone angle. The result of the optimization process is summarized in Fig. 2.32 for the first cell. The final geometrical values chosen, together with the main accelerating figures of merit of the structure, are reported in Table 2.5.

Regular cells were also optimized at 230 MeV/u, corresponding to a geometric β of 0.596, and

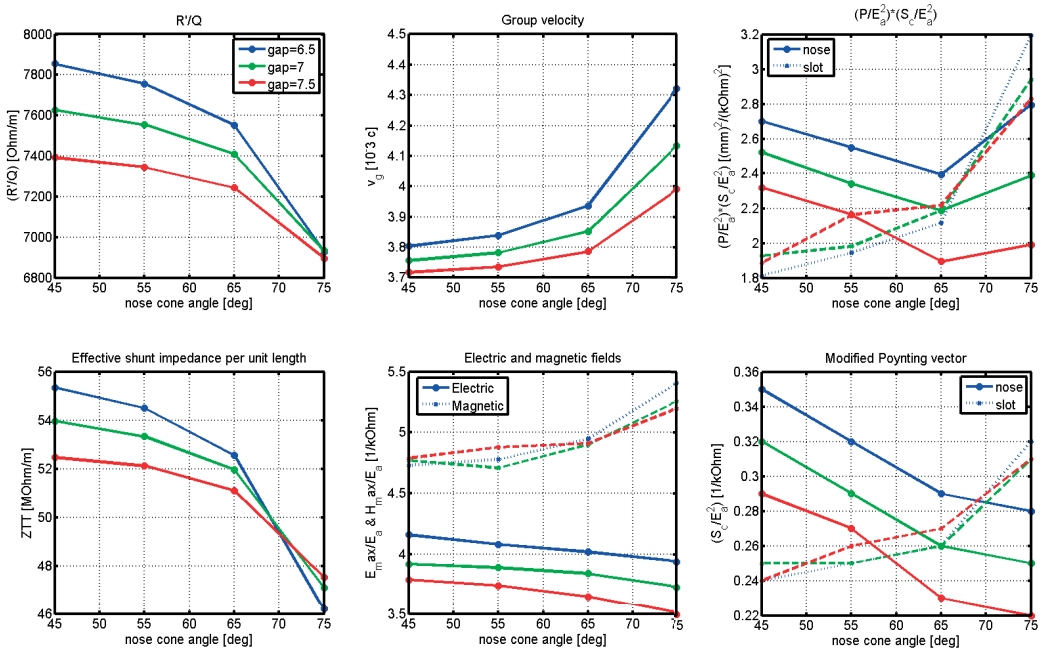

Figure 2.32 – Results of the optimization of the first BTW cell, with scan of gap and nose cone angle.

at the intermediate β of 0.49. Two additional RF cells were designed in order to get a better field map interpolation for the beam dynamics simulations. The main geometrical parameters along the different cells are shown in Fig. 2.33.

The main accelerating parameters are instead reported in Table 2.6, for RF cells with a constant 3.5 mm coupling holes radius. The group velocity slightly changes between the different optimized cells due to their differences in length and diameter. The optimized RF cells were simulated also with a 3.25 mm and a 3 mm coupling holes radius, to obtain a first indication of whole accelerating structures parameters.

Tapering of the structure

The full structure is composed of 10 regular cells, and 2 coupling cells. In a travelling wave linac, the RF power is injected into the structure and propagates along it at the group velocity vg. It is absorbed both by the conductor walls and by the beam, resulting in an attenuation of the field amplitude. At the end of the structure the power is coupled to a load or a re-circulating circuit. A low group velocity leads to a high accelerating gradient but at the same time to a rapid decay of the power. The group velocity can be adjusted by means of cell-to-cell coupling in the disk-loaded accelerating structure. In particular, the larger the coupling, the higher the group velocity is. In the present design, a group velocity ranging between 0.4% and 0.2% of c was chosen as a compromise between acceptable filling time and efficient acceleration of the

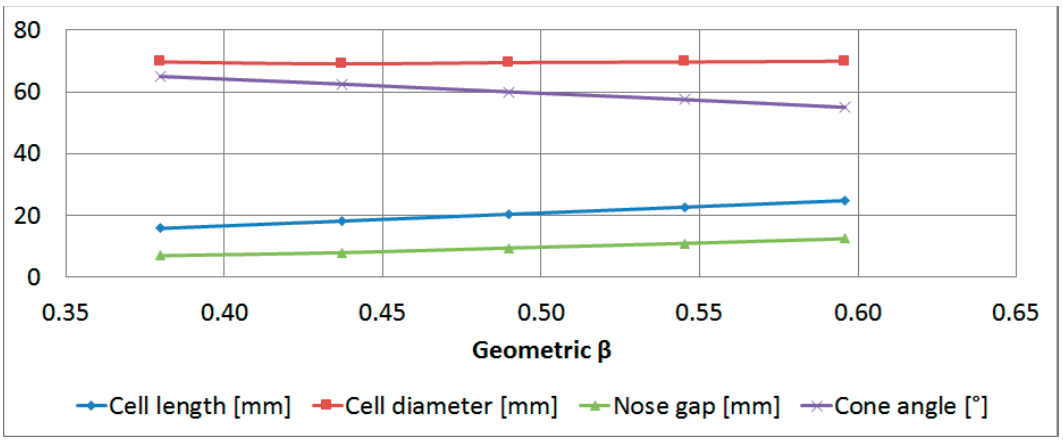

Figure 2.33 – Geometrical parameters of the optimized HG BTW RF cells for different geometric β.

Table 2.6 – Accelerating parameters of the optimized HG BTW RF cells for different geometric β. The values refer to cells with 3.5 mm coupling holes radius. 12 RF cells long structures with the same coupling holes radius tapering have an approximately 4 % increase in ZTT.

Energy [MeV/u]	Geometric β	TT factor	ZTT [MΩ/m]	v_g [‰of c]	Q value	R'/Q [Ω/m]
76	0.380	0.90	51.5	3.878	6954	7412
105	0.437	0.91	59.9	3.883	7737	7746
138	0.490	0.91	66.3	3.812	8466	7831
181	0.545	0.91	72.3	3.768	9148	7900
230	0.596	0.90	77.2	3.726	9745	7923

Energy [MeV/u]	Geometric β	S_{cn}/E_a^2[1/kΩ]	S_{cs}/E_a^2[1/kΩ]	E_{sn}/E_a	H_{sn}/E_a [mA/V]
76	0.380	0.27	0.29	3.85	4.94
105	0.437	0.28	0.28	4.00	4.84
138	0.490	0.29	0.26	3.92	4.77
181	0.545	0.29	0.27	3.86	4.74
230	0.596	0.30	0.25	3.79	4.71

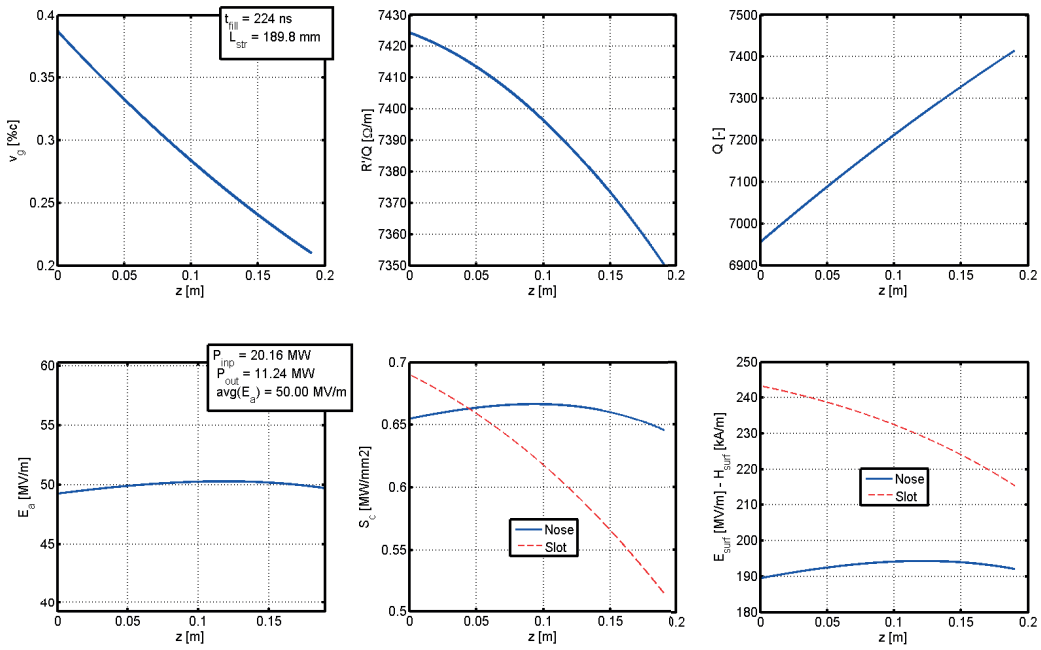

Figure 2.34 – Main accelerating parameters and field distribution along the BTW structure, as a result of the group velocity tapering chosen.

beam [7].

The tapering has been accomplished by varying linearly the coupling holes radii; the cell diameter and the radial distance of the coupling holes have been varied to adjust the resonant frequency. All the other geometrical parameters have been kept constant throughout the structure, i.e. the regular cells are all identical except for the coupling holes region, and overall diameter, that is increasing thorough the structure to compensate for the lower inductance given by the smaller coupling hole radii.

The result of the tapering are summarized in Fig. 2.34, following the analytical formulations presented in [57]. The choice of a constant gradient maintains a constant electric field distribution on the noses, and so a constant Sc distribution in this region along the structure. Instead, the Sc on the coupling holes decreases due to the lower EM density given by the group velocity profile.

Since each regular cell has a different diameter, in the design of the full structure it was decided to take the average of two subsequent cells, as graphically explained in Fig. 2.35. This was done in order to avoid steps in the middle of cells, that would have represented an issue for the cavity tuning and bonding.

Indeed the brazing joint was places in one fo the corner of each cell. This choice required a

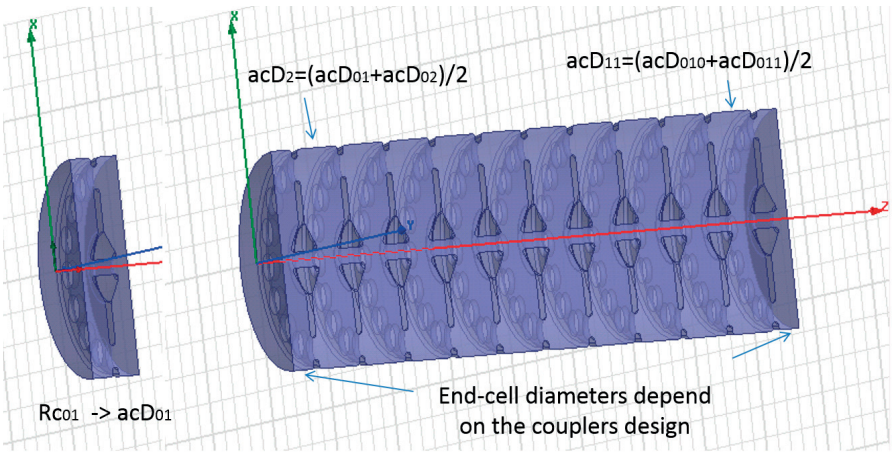

Figure 2.35 – RF assembly methodology of the BTW structure. Each single RF cell designed has a different coupling hole radius Rc_{0x}, and thus a different diameter acD_{0x}, with x number of the cell, from 1 to 11. The final structure has 10 regular cells, with the diameter taken as the average of two subsequent single RF cells diameters.

last iteration in the RF design, since the outer corner radius of 1mm is present only on one side of each cell (opposite to what is shown in Fig. 2.35, where the outer corner radius is visible at both sides of the RF cells).

2.4.3 Single cell mechanical studies

Two mechanical tests were performed on mock-up single cells: a creep test and a tuning one. These are discussed in the following Sections.

Creep tests

Three joining procedures were considered: H2 bonding, gold brazing and silver brazing. H2 bonding, which is used for CLIC accelerating structures, was the preferred choice, being cleaner than brazing. However, its heat cycle reaches also the highest temperature, being thus more critical in terms of creep deformation. In addition, the particular geometry of the RF cells, with 16 holes at the periphery of the septum thickness, is a disadvantage for the mechanical stability.

Following mechanical simulations, an experimental campaign investigated the behaviour of sets of mock-up RF cells with different iris thickness, corresponding to 1.5, 2 and 3 mm. Fig. 2.36 summarizes the results of the creep tests for the 2mm iris thickness, that was eventually chosen. In the case reported, all the the 20 cells tested underwent an H bonding cycle with maximum temperature of 1050 °C.

The results reported refer to the nose region of the cell, the one most subjected to the creep

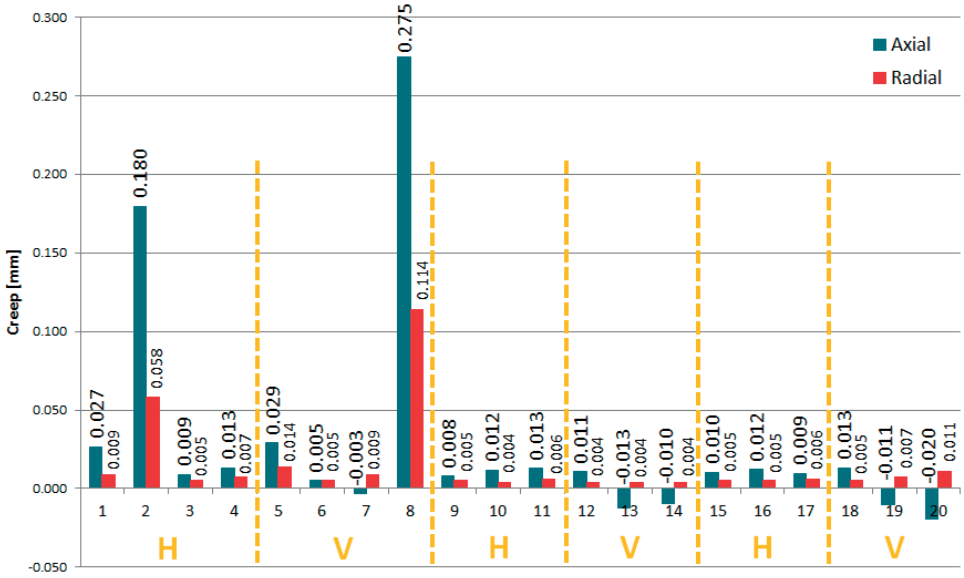

Figure 2.36 – Creep results in the nose region for the different cells tested.

problem. The cells have been positioned both vertically (V mark) and horizontally (H mark) in the oven. Except for cells number two and eight, which show a considerable deformation, the average deformation is quite limited. Excluding these two cases, that likely were not carefully handled, the average axial deformation is 13 μm, while the radial is 6 μm. Both these values were judged acceptable.

Tuning and sensitivity analysis

An RF sensitivity simulation was performed on the final geometry for the first, the middle and the end cell of the structure, following the method explained in [7]. The sum of all the frequency shifts of same sign in case of 10 μm machining error for each geometrical parameter is equal to -3.3 MHz and +3.5 MHz. It is worth commenting that this represents a very conservative assumptions, since it implies that all the machining errors shift the frequency in the same direction. If instead a random generation of the machining errors is considered, a tolerance of $\pm 10 \mu m$ corresponds to a frequency shift of 1.2 MHz with a 90% probability. These are the same results found for the 1.5 mm septum thickness case and presented in [7].

An RF tuning simulation estimated the tuning capability of each cell (Fig. 2.37). Starting with a 10.5 mm diameter, an ellipsoid was simulated in the RF design of the three regular cells as above, both inward (frequency increase) and outwards (frequency decrease). In case of a 1 mm deformation perpendicular from to the cavity wall, the frequency shifts are +4 MHz and -3 MHz in case of four dimple tuners per RF cell.

A final mechanical test was performed to decide the wall thickness for the tuning holes. Two mock-up cells were produced, containing 19 tuning holes each. Except for two cases with 8mm

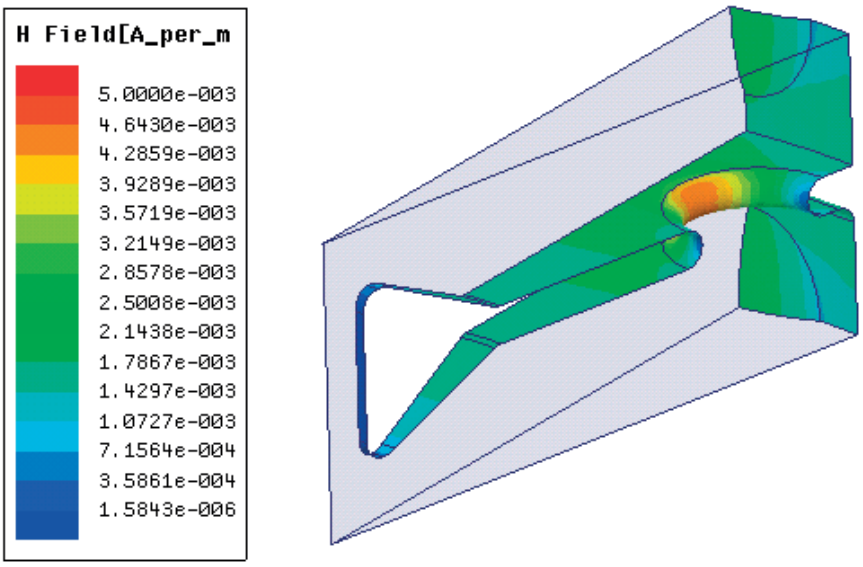

Figure 2.37 – Example of a tuning simulation performed with HFSS, for an inward deformation case. One can notice that the outer wall deformation does not enhance remarkably the H-field distribution, which maintains its maximum on the coupling hole.

diameter, all the holes had a 10.5mm diameter, following the RF simulations, but different final thickness of 1, 1.2 and 1.6mm (Fig. 2.38 top). This last parameter has to allow a sufficient deformability of the outer RF cavity walls, but without rupture. The mock-up cells was connected on the opposite side of the tuning pins to a vacuum pump in the region around the hole under test. This was then hit with an hammer-tool until rupture or leakage, measured with the vacuum pump. Some of holes were tested in pulling and some in pushing mode. Finally, a combination of the two was also tested, in order to simulate an over-tuning to be corrected. The deformation is reported as a function of the number of hits. One shall not drawn ultimate conclusions on the curve trends, since being a manual tool, the force impressed in each hit was subjected to variations. It is worth highlighting that at the end of the test of each holes, the force applied on the hammer had to be increase significantly to continue the deformation, due to the material hardening.

The results of the test are summarized in Fig. 2.39 bottom. Twenty different holes were tested, subdivided into four holes with final wall thickness of 1 mm, four with 1.2 mm, and twelve with 1.6 mm. It was chosen to adopt the most conservative case of 1.6 mm thickness. This latter showed a good sensitivity during tuning, having the highest safety margin with respect to rupture. On average for the 1.6 mm case, the wall broke after 3.5 mm deformation, either pulling or pushing. In the worst case, the wall broke at 2.5 mm. Since the maximum needed tuning capability corresponds to a 1 mm deformation, the test results were considered acceptable. The 1 mm and the 1.2 mm holes tested broke on average at 3 mm and 3.1 mm deformation, respectively.

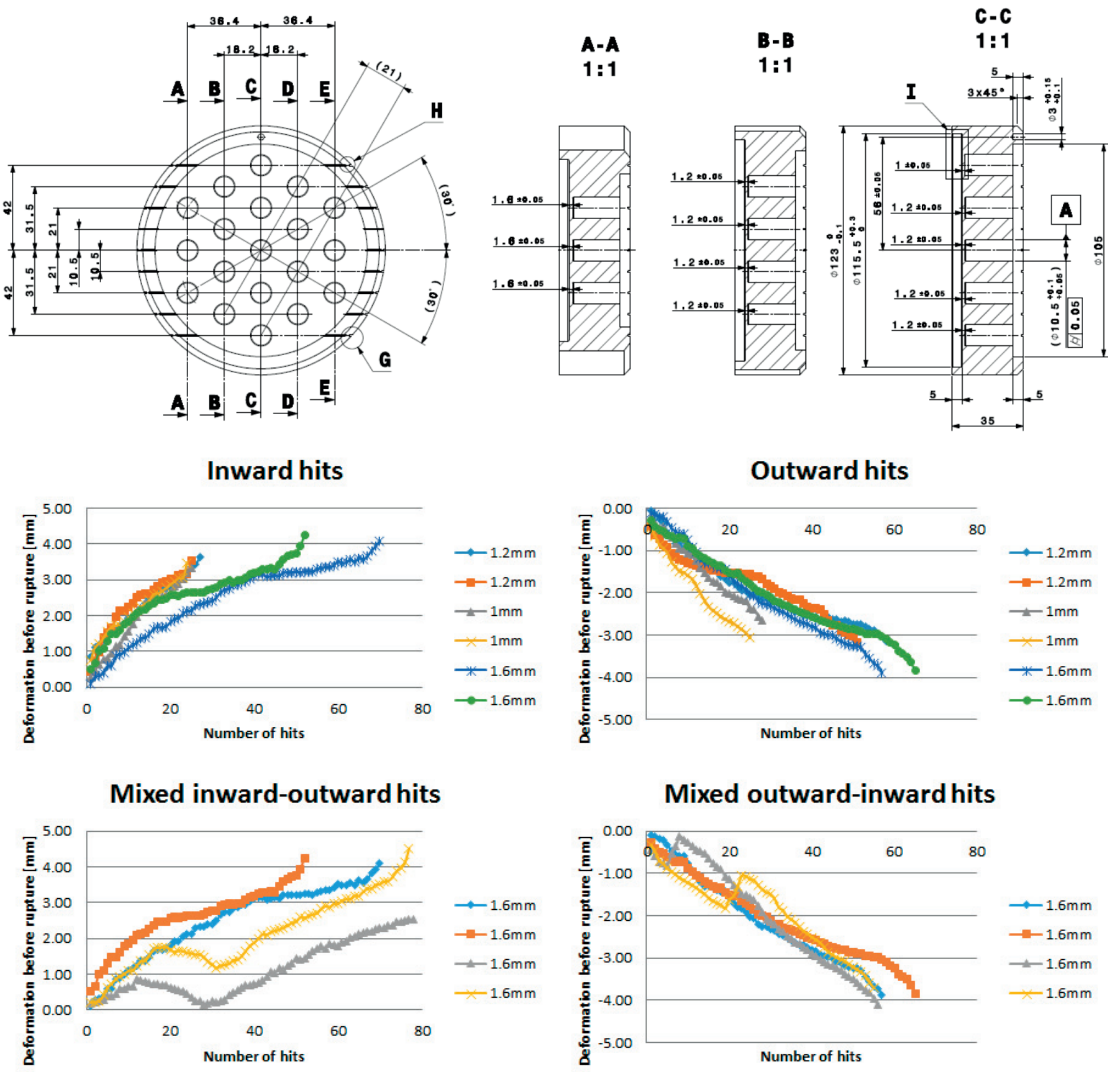

Figure 2.38 – Mock-up cell geometry (top) and results of the tuning test performed (bottom).

Figure 2.39 – Tuning test mock-up cell (top left) and test set-up (top right). Zoom on deformed and broken pins after the experiment (bottom).

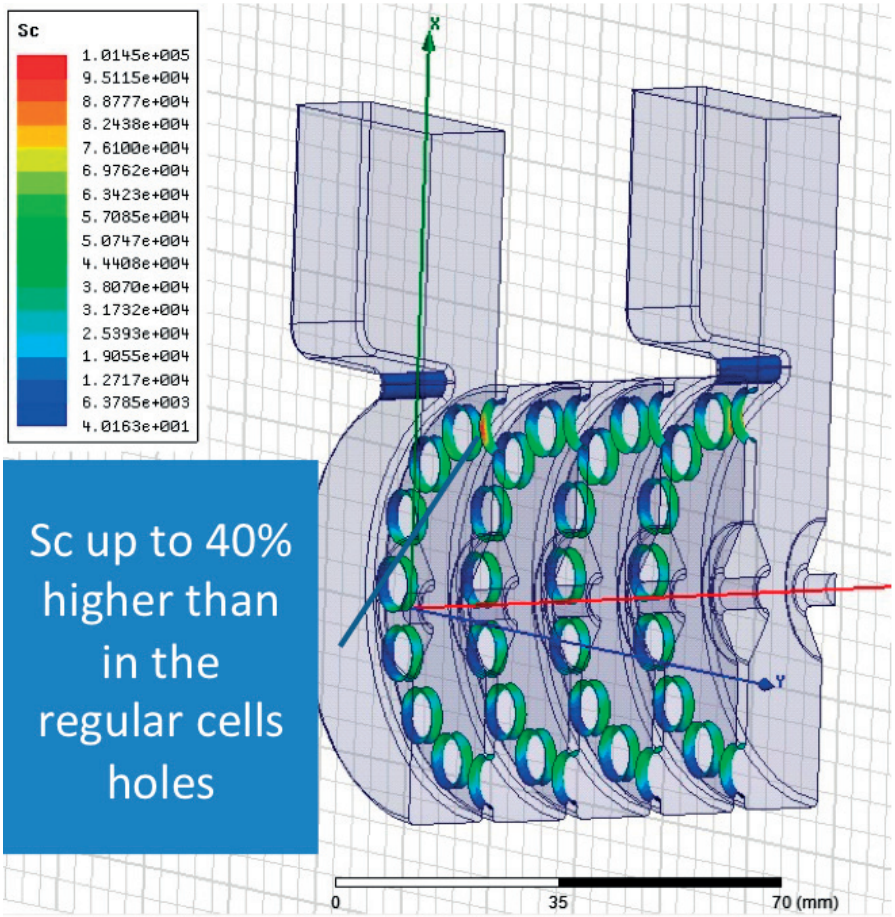

Figure 2.40 – Local Sc enhancement in the end-cell due to the coupling slot.

2.4.4 End-cells design

The input and output power couplers (or end-cells) represent a very delicate part of the design process. The presence of a slot to allow the RF power to penetrate into the structure enhances the electromagnetic field distribution and modifies the accelerating parameters of the coupling cell. Goal of the couplers design is to minimize the power reflections while perturbing as little as possible the field distribution and the accelerating performance of the end-cells.

In the BTW structure, magnetically coupled end-cells were designed. In this configuration, a rectangular waveguide is matched to the end-cell by means of the coupling slot size and of the coupling cell diameter.

A magnetic coupling introduces asymmetries; in particular, in the end-cells the coupling holes close to the coupling slot show an enhanced magnetic flux, and as a result also an enhanced Sc (Fig. 2.40). Interestingly, one could notice in Fig. 2.40 that the Sc does not show a maximum on the coupling slot, which thus are not a critical part of the design in terms of BDs.

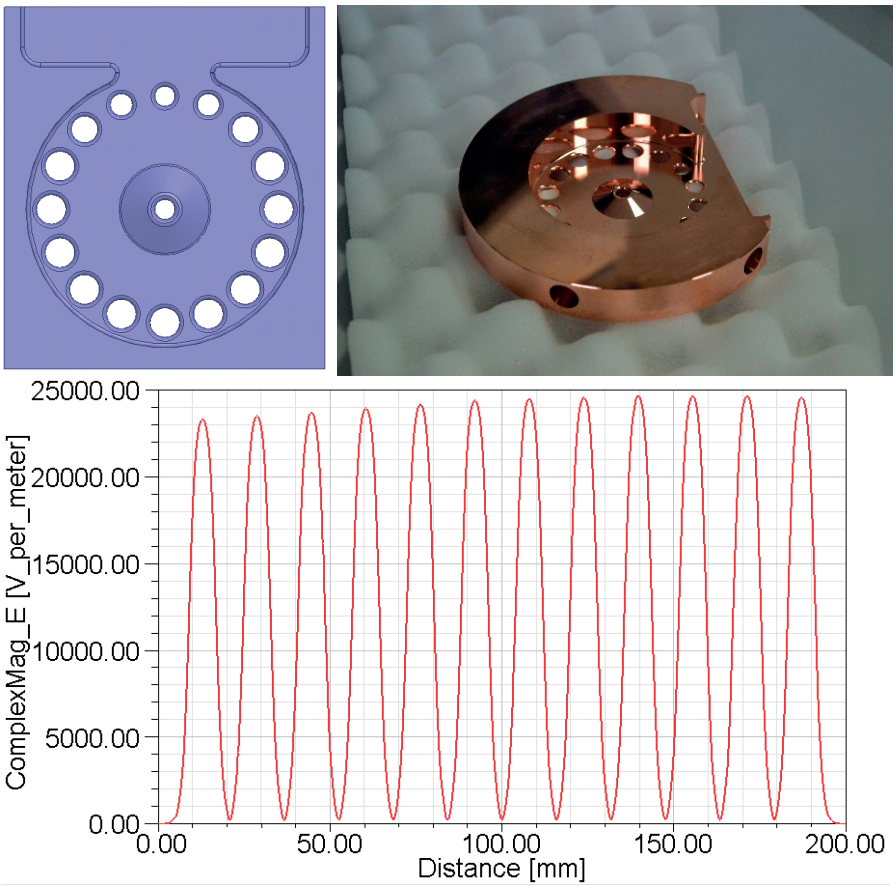

Figure 2.41 – Input coupler design (top left), mechanical cell (top right) and simulated Ez field distribution in the BTW structure (bottom).

Since the whole study goal is to push the high gradient limits of S-Band structures, and since the Sc is the physical quantity chosen to characterize the BDR limit, the results of Fig. 2.40 was judged not acceptable. The magnetic flux enhancement can be straightforwardly reduced by decreasing the coupling holes radii. Though this solved the Sc enhancement problem, it causes also a reduction of the group velocity, eventually resulting in a asymmetry in the Ez field, which increases in case of a lower group velocity.

The solution adopted was to reduce the coupling hole radii closer to the coupling slot, to compensate for the enhancement of the Sc due to the local increase of the power flow. The remaining coupling hole radii have been increased to maintain the design group velocity in the cells (Fig. 2.41 top left). With this solution, the end-cells provide the same acceleration as the regular cells (Fig. 2.41 bottom), while having an even distribution of Sc.

The output end-cell does not present the same criticality. In fact, the constant-gradient structure designed involves a tapering of the coupling holes radii to reduce linearly the group

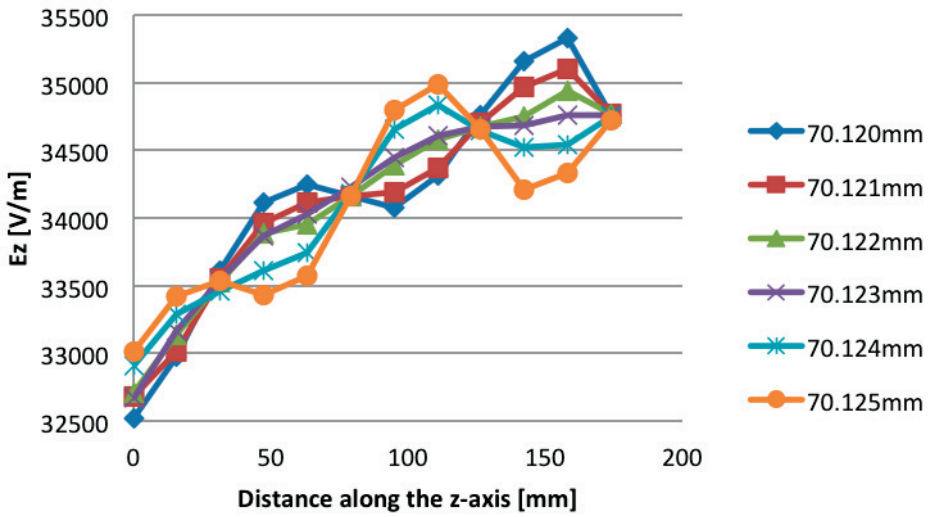

Figure 2.42 – Output end-cell matching results.

velocity [42]:

$$v_g(z) = \frac{\omega L}{Q} \frac{1-(z/L)(1-e^{-2\alpha_0 L})}{(1-e^{-2\alpha_0 L})} \tag{2.21}$$

As a result, the Sc distribution is around 20% lower in the coupling holes of the output cell with respect to the coupling holes of the input cell. Instead, it remains constant on the coupling holes throughout the structure, as shown in Fig. 2.34.

The output end-cell design focuses thus only on the matching with the waveguide, in order to minimize the SW pattern in the structure caused by the reflections from the output cell. The Ez field in the middle of each RF gap is shown in Fig. 2.42 as a function of the output cell diameter.

The final step of the 3D design consisted in minimizing the total reflection considering the whole geometry. This is accomplished, as previously discussed, by varying the coupling slot aperture and cell diameter of the input end-cell. The total reflection of the cavity is reported in Fig. 2.43 as a function of the coupling slot dimension and of the of the input cell diameter.

2.4.5 The final prototype

The final step of the RF design consisted in designing the waveguide transition to standard WR-284, and to check the accuracy of the mechanical drawings. The waveguide transition is a simple stepwise waveguide. The two transitions face each other, to reduce external dimensions. A cu view of the prototype, with RF flanges, vacuum flanges and cooling channels is shown in

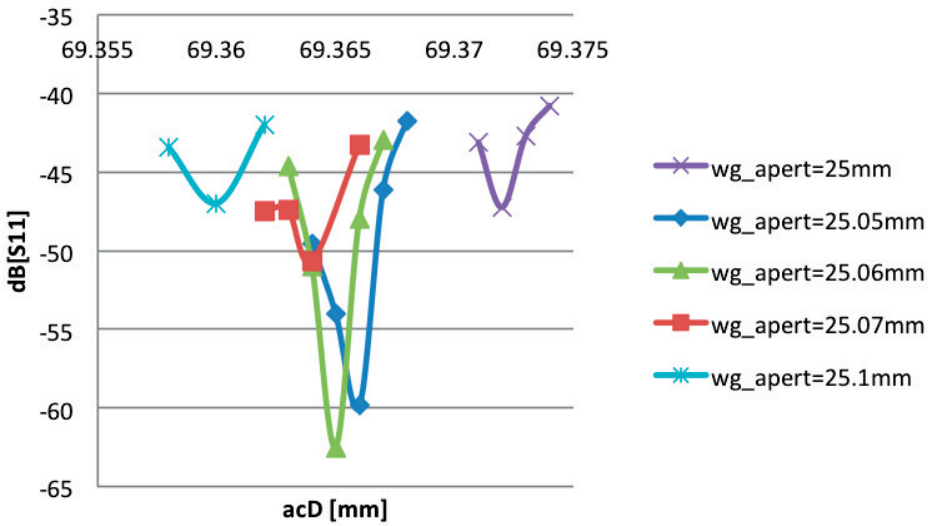

Figure 2.43 – Input end-cell matching results.

Fig. 2.45.

The mechanical design can be checked in a laborious way, by double checking all the dimensions of the final drawings, or in a faster way, by importing the 3D mechanical drawing in HFSS, and verifying that the same result of the HFSS model are obtained. Fig. 2.44 is the result of this latter method, and it shows the total reflection of the cavity as a function of the frequency for the original HFSS model and the correspondent mechanical CATIA model, both with and without waveguide transitions.

Also the numerical convergence of the simulation results with respect to the mesh size was verified. The most important parameters of the structure are reported in Table. 2.7. The power recirculation, mentioned in the table, is discussed in Section 2.4.6.

The mechanical design of the prototype was not followed by the author, but it is hereafter shortly discussed for the sake of completeness.

As discussed, the disks have been bonded in partial hydrogen atmosphere, with a maximum temperature of the heat cycle of 1050 °C, following the CLIC accelerating structures baseline fabrication procedure. Waveguide transitions, cooling plates and vacuum flanges are all brazed to the structure. The coupling slot is part of the end-cells, to avoid brazing in the area critical for the matching. The end-cells wall have been thicken to increase the robustness during handling. A cut view of the final prototype is shown in Fig. 2.45.

The thermal analysis was conducted for the completed accelerating structure, considering the 50 MV/m target accelerating gradient, and different duty factors. The limiting factor is represented by the thermal induced plastification, and the most sensitive region are the

Table 2.7 – Main parameters of the BTW prototype.

Wall thickness [mm]	2	
Gap [mm]	7	
Nose cone angle [deg]	65	
Cell length [mm]	15.82	
Ea avg design [MV/m]	50	
Scnose/Ea2 (first/last) [mA/V]	0.27	0.26
Scholes/Ea2 (first/last) [mA/V]	0.29	0.21
Es/Ea (first/last)	3.85	3.88
Hs/Ea (first/last) [mA/V]	4.94	4.33
Pin (w/o recirculation) [MW]	8.92	20.16
Pout (w/o recirculation) [MW]	-	11.24
Q0 (first/last)	6954	7415
R'/Q (first/last) [Ω/m]	7412	7367
R'/Q (first/last) [MΩ/m]	51.5	54.6
vg (first/last) [‰of c]	3.878	2.098
Filling time (w/o recirculation) [ns]	800 (99%)	224

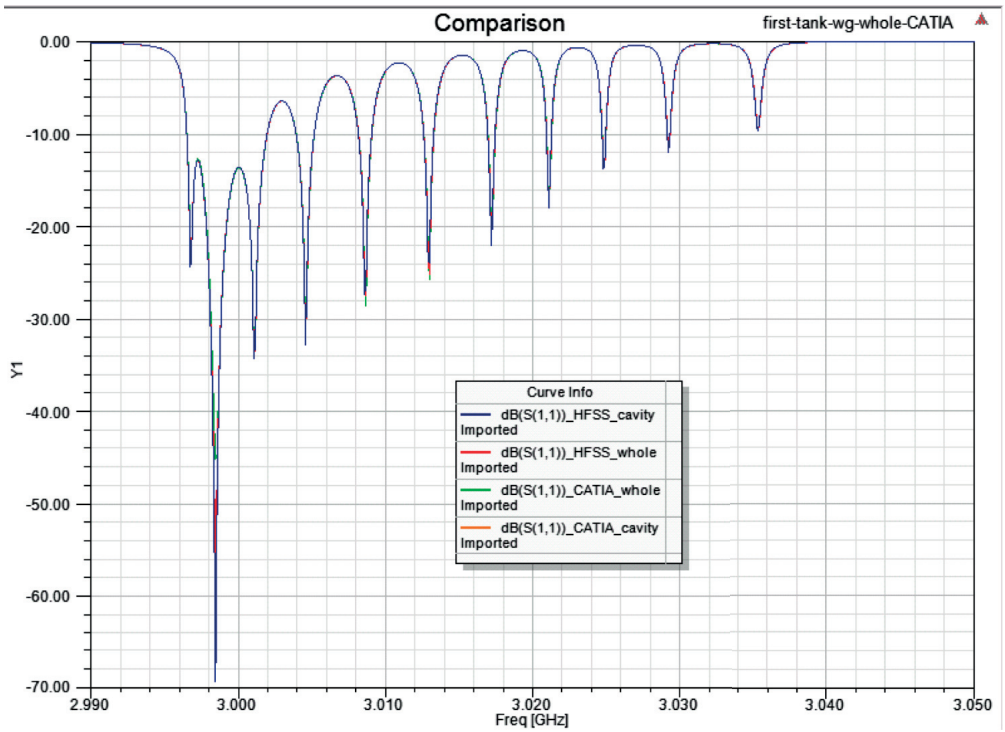

Figure 2.44 – Comparison between S11 from HFSS and CATIA models on the full 3D structure.

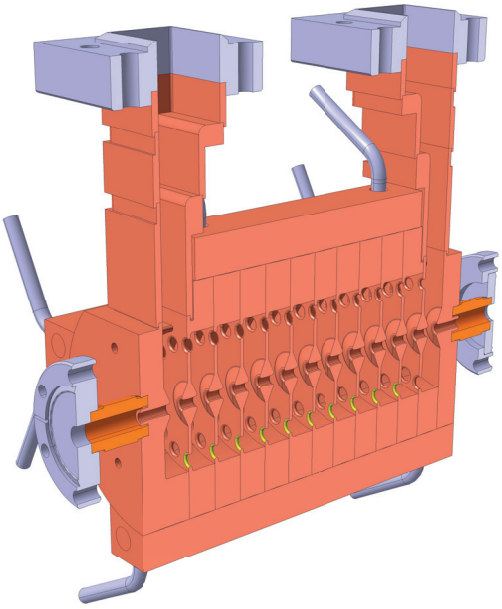

Figure 2.45 – Cut view of the BTW prototype mechanical design. Courtesy of M. Garlasche' and M. Timmins, CERN.

coupling holes (Fig. 2.46 left). An annealing limit of 25 MPa was considered to exclude risks of deformation above the elastic limit. This corresponds to a maximum thermal load of 0.75 kW, that for 50 MV/m (see Table 2.7) translates into a maximum duty cycle of 0.075%. This thermal load corresponds to a limited ΔT of few degree (Fig. 2.46 right), and to an estimated cell diameters increase of tenths of μm. These are not the limiting factors.

Interestingly, the Ez complex distribution in case of a $5\pi/6$ structure shows a 12 arrows distribution in the complex plane (Fig. 2.47 right), since the first common multiple between $5\pi/6$ and 2π is 10π. This is pretty different from the classic 3 arrows representation, characteristic of $2\pi/3$ structure.

As a final plot, the input and output reflections of the simulated full geometry are presented in Fig. 2.48.

2.4.6 Power recirculation in a TW structure

The BTW structure designed has a power transmission ratio of about 3 dB, i.e. half of the input power is transmitted through the structure and is coupled to either a load or a re-circulating circuit. A lower P_{load}/P_{in} ratio could have been obtained, but at the price of a longer filling time. To make an efficient use of TW structures, a passive waveguide component, called 3 dB hybrid splitter, has to be designed.

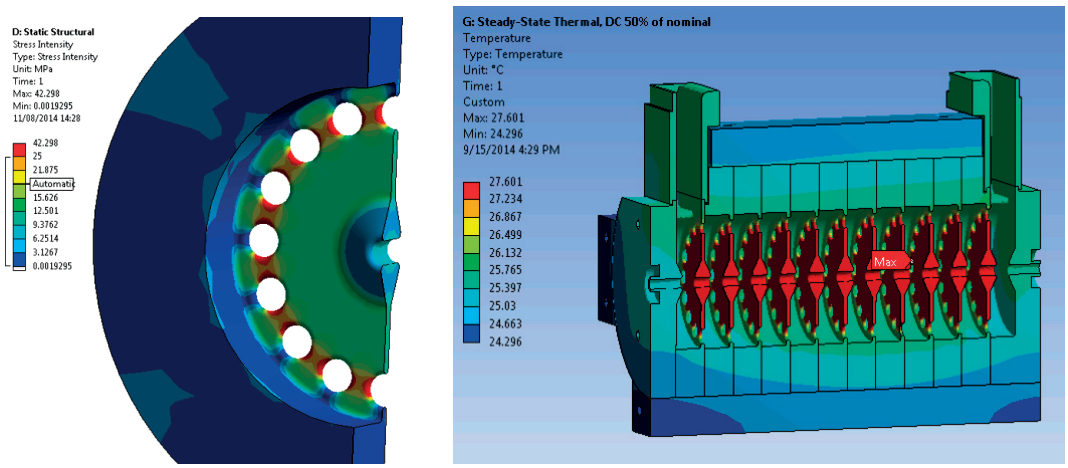

Figure 2.46 – Thermal induced stresses in a regular cells (left) and thermal distribution in the whole geometry (right). Courtesy of M. Garlasche', CERN.

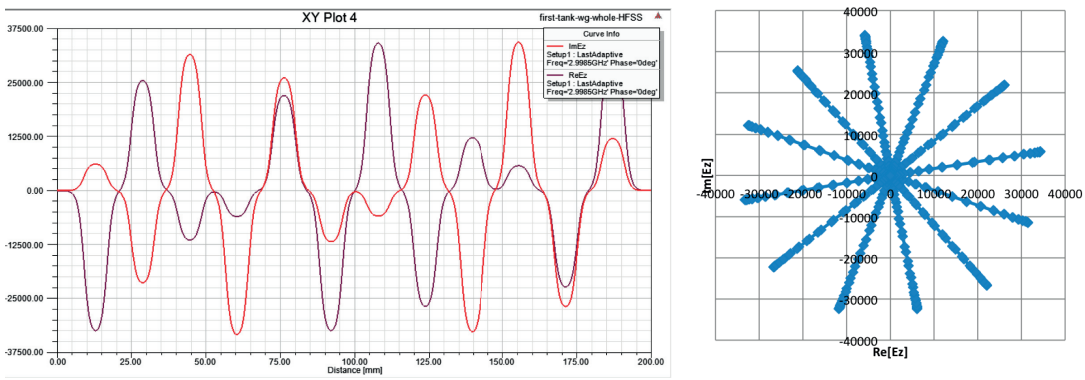

Figure 2.47 – Complex Ez field distribution along the BTW structure (left) and in the complex plane (right).

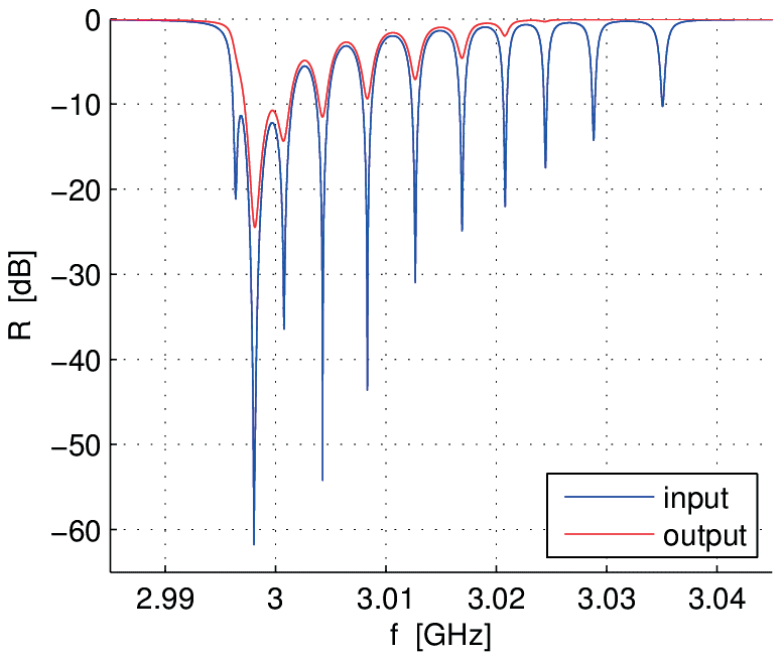

Figure 2.48 – S11 and S22 of the BTW prototype.

A 3dB Hybrid is a 4-port passive device. By proper sizing the geometry between the ports, it is possible to equally split the power entering from port 1 towards port 2 and 3. In this configuration no power goes towards port 4, and there is a 90° phase difference between port 2 and 3 (Fig. 2.49 left).

In the present design, port 1 is connected to the klystron, port 2 to a RF load, port 3 and 4 to the structure input and output cell, respectively. The power which exits from the structure, entering port 4 and being equally split between port 2 and 3, makes interference with the power flowing from port 1. If the phase of the RF power entering ports 1 and 4 is has 90° phase difference, the interference is constructive towards port 3, namely towards the structure, and destructive towards port 2, the load (Fig. 2.49 right).

Taking into consideration the phase difference between the accelerating structure input and output, the length of the transition waveguides which connect the 3dB Hybrid to the accelerating structure can be computed so that there is a 90° phase difference between port 1 and port 4. As a result, this design allows for full power recirculation into a TW accelerating structure.

The power attenuation in S-Band (WR-284) waveguides is around 0.02 dB/m. As a result, the power attenuation in the 3db hybrid is negligible, being lower than 1 %. However the drawback of this solution lies in the transverse size of the assembly and in the longer filling time to reach a flat RF pulse. The field rise time for achieving 99% of the nominal field into the cavity, considering the 3 dB hybrid, is around 800 ns [58]. The 3db attenuation of the structure guarantees that, by adopting a 3dB hybrid, no power goes into the load at steady-state. In fact,

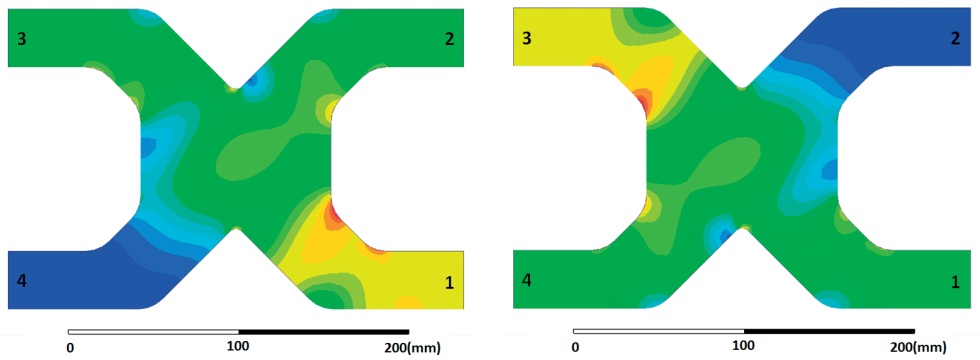

Figure 2.49 – 3dB hybrid with power entering from port 1 (left) and from port 1 and port 4 with 90° phase difference (right)

if the structure output power is not exactly 3dB, the recombined powers do not match.

One could consider designing an asymmetric hybrid and match it with a cavity with different attenuation than 3 dB. In particular, the higher the attenuation of the cavity, and the shorter is the field rise time of an hybrid-cavity system. While the filling time of the structure increases, less iterations are needed to the system to reach steady state, eventually resulting in a shorter transient for the overall system. However, a lower group velocity in a cavity results in a smaller bandwidth.

A cut transverse view of the structure with the BTW design connected to the hybrid, and with RF power coming from port 1, is shown in Fig. 2.50. Being the bandwidth of the hybrid larger than the one of the structure, the first does not affect remarkably the resonance of the cavity.

2.5 The high-gradient 3 GHz CCL accelerating structure

Historically, CCLs have been a preferred solution for proton acceleration above $\beta = 0.3$. However, to the authors knowledge few works addressed the design of 3 GHz high gradient CCL: one for $\beta = 0.38$ [7] and a more recent study for $\beta = 0.6$ [10].

Here the full 3D design of an high gradient CCL for $\beta = 0.38$ is presented. The very same RF methodology used in the RF design of the BTW prototype was adopted, so the two structures are fully comparable in terms of BD limit.

2.5.1 Regular cell and quintuplet design

A CCL regular accelerating cell is not a symmetric part of an infinite chain, like in the TW case, since in the real full 3D design it has to be matched with the coupling cells. As explained in [39], the shortest geometry that replicates an infinite chain is the one of a quintuplet, i.e. 3 coupling cells, two of which halved, and 2 regular accelerating cells. With this geometry setup,

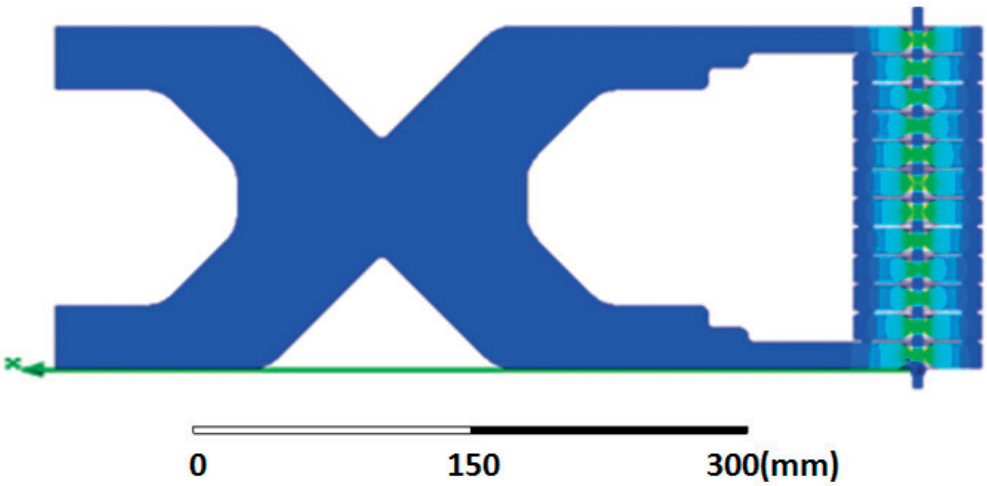

Figure 2.50 – Complex Mag Electric field distribution in BTW structure connected to 3db hybrid.

it is possible to close the passband and have a structure with the desired operating frequency and coupling factor.

This last parameter influences the modes separation, so directly affects the number of cells in the accelerating structure. On the other hand, the higher the coupling factor, the lower the ZTT due to the decrease in Q factor. As a result, the coupling factor should be chosen taking into consideration the linac design. In this work, a quintuplet with coupling factor equal to 5% was designed, in agreement with a previous work of TERA Foundation [39]. A complete work on coupled cavity structures should always report the coupling factor considered.

The regular cell optimization aimed at being as comparable as possible to the BTW design. It has been thus decided to design a CCL with the same bore aperture radius of 2.5mm, and the same septum thickness of 2mm. This last parameter imposed to revisit the mechanical design. CCL cavities presented in [26] are based on the production of two half-cells, that are eventually brazed together. However, a wall thickness of 2mm, like in the BTW solution, poses a serious challenge to the fabrication and brazing with such method, because 1mm walls would be needed. To overcome this issue, a different assembly concept has been proposed (Fig. 2.51), which allows to have the full thickness septum in a single piece. A similar design was proposed in [59].

The design shown in Fig. 2.51 implied a different coupling cell design with respect to more classic geometries (see Fig. 2.52 right). Since now the coupling cells have to be two accelerating cells long, it is possible to have a more compact transverse dimension.

The optimization of the accelerating cells was carried out varying the cone angle and the gap,

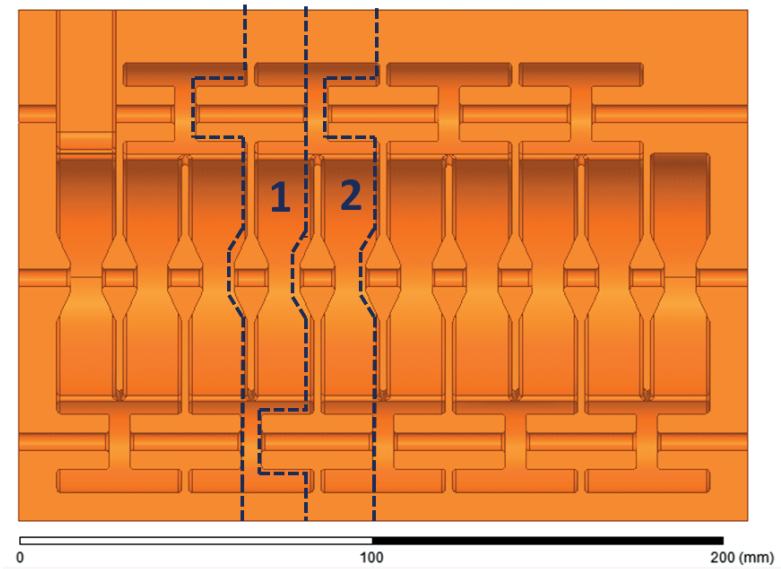

Figure 2.51 – HG CCL full assembly cut view.

and respecting the 2.7e-4 A/V limit in Sc that was reached in the BTW design. The quintuplet was design with a 5% coupling factor, as previously discussed. The Sc distribution reaches a maximum in the nose region. The coupling slot, that is often a critical part in CCL designs in terms of field enhancement, has a lower Sc value.

As for the BTW case, regular cells were also optimized at 0.596 and 0.49 geometric β . Two additional RF cells were designed in order to get a better field map interpolation for the beam dynamics simulations. The main geometrical parameters along the different cells are shown in Fig. 2.53.

The main accelerating parameters are instead reported in Fig. 2.8. The quintuplet solution was studied only for the 0.38 β structure. It has been assumed that to a given coupling factor $k1$ corresponds a ZTT reduction independently on the cell geometry or length. This is an assumption present in Los Alamos Superfish code [40]. For instance, a k_1 of 5 % would decrease the accelerating cell ZTT of 13 % according to Superfish. However, it is worth highlighting that this is a first order approximation, as the Q factor decrease is also function of the geometry of the coupling cell. The solution studied with HFSS, having a quite unusual and optimized coupling cell geometry, has a 7 % reduction of ZTT between the uncoupled and the coupled solution. In this work, it has been assumed that a similar efficient design would be achievable also for geometric β greater than 0.38, thus a 7 % reduction factor is considered in Table 2.8.

2.5.2 End-cells design

The infinite chain symmetry rupture caused by the end-cells has been adjusted by varying the radius of half of the accelerating cell, as shown in Fig. 2.54. In this way, the coupling slot

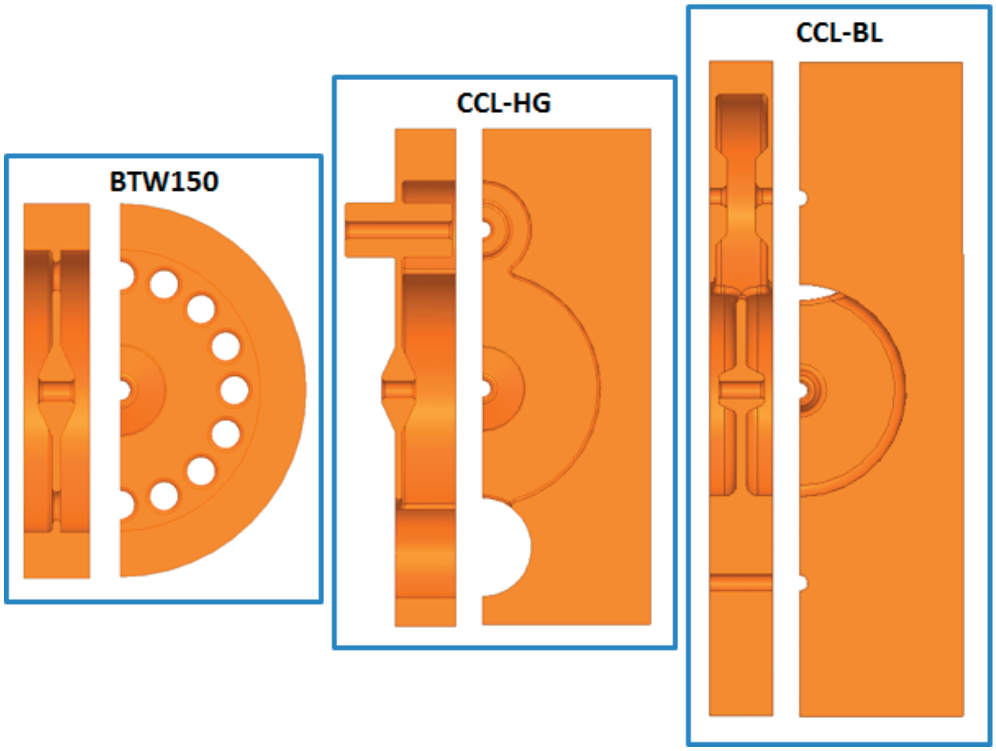

Figure 2.52 – Mechanical view of the optimized cells: HG BTW (left), HG CCL (middle) and 30 MV/m CCL (right).

Table 2.8 – Accelerating parameters of the optimized HG CCL RF cells for different geometric β. The coupling factor Q factor reduction is kept constant and equal to 7%.

Energy [MeV/u]	Geometric β	TT factor	ZTT coupled [MΩ/m]	Q value coupled	S_{cnose}/E_a^2[1/kΩ]	E_{snose}/E_a^2
76	0.380	0.86	60.0	9136	0.27	3.86
105	0.437	0.85	71.5	10037	0.29	3.96
138	0.490	0.85	77.4	10850	0.29	3.87
181	0.545	0.84	81.8	11578	0.30	3.88
230	0.596	0.84	85.5	12045	0.30	3.96

geometry is not changed, and so in first order approximation the coupling factor remains constant. On the other hand, the machining is likely more difficult.

The end cell were first matched considering a "septuplet", as in Fig. 2.54 right, which is the simplest geometry that replicates a symmetric structure with end cells. In this way is possible to speed up the computing time. The results have been then validated on the final structure though, which is composed of 8 regular cells, and 2 end cells. Interestingly, the choice of a 12 cells long structure for the BTW prototype, which has a $5\pi/6$ RF phase advance, permitted to design an equally long CCL structure, composed of 10 cells, given the π phase advance between accelerating cells.

A single magnetic coupler was designed, following beam dynamics considerations that are discussed in Section 3.1.3. The coupling cell can be placed everywhere in the structure. Here,

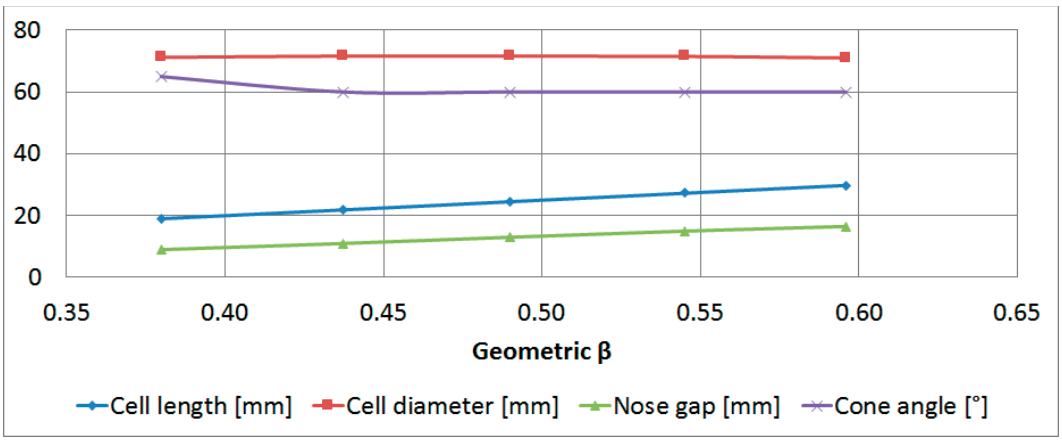

Figure 2.53 – Geometrical parameters of the optimized HG CCL RF cells for different geometric β.

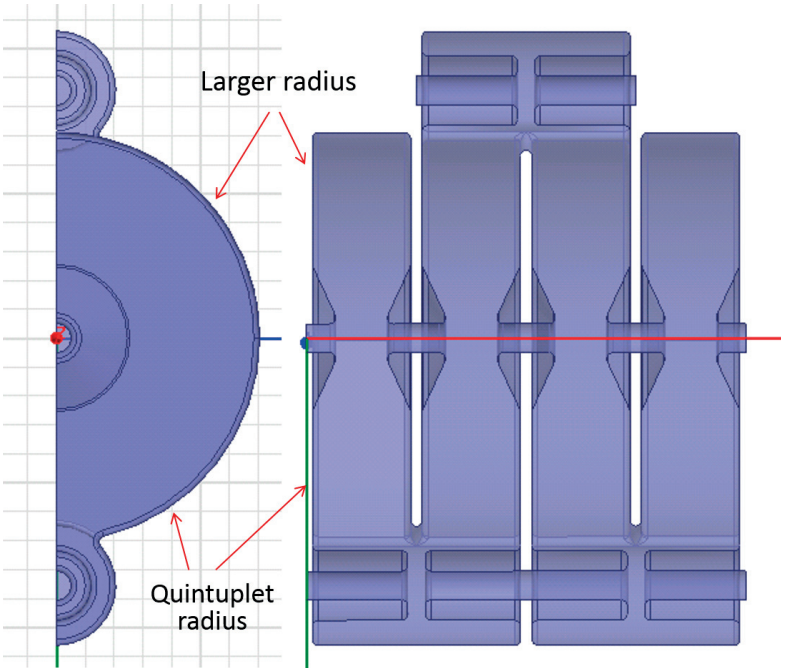

Figure 2.54 – HG CCL end-cells design (left) and "septuplet" view (right).

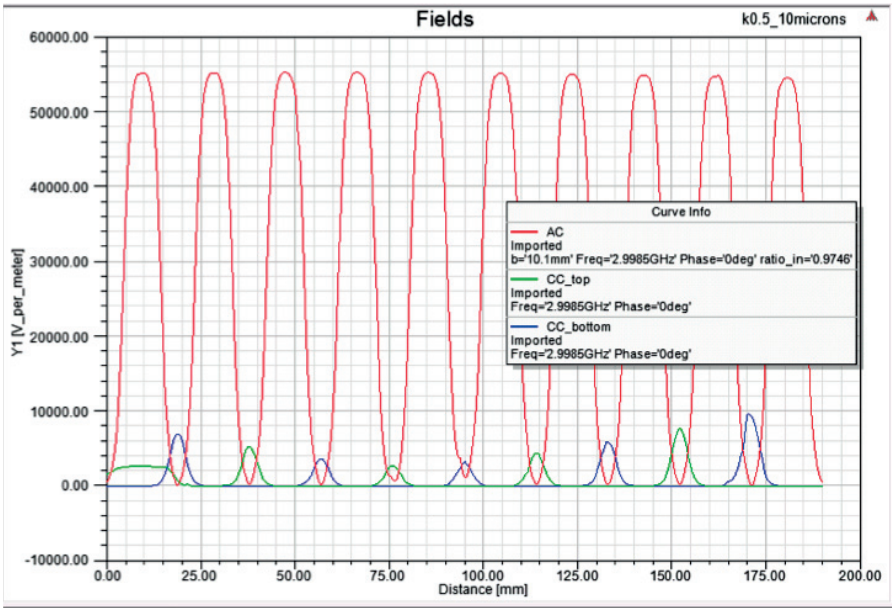

Figure 2.55 – Electric field distribution along the HG CCL structure. Ez on axis (red), in the top coupling cells axis (green) and bottom (blue).

it has been chosen to place it on one of the end-cells. This solution results in a compact design, having the input waveguide on the same axis of the coupling cells, and it represents an advantage for the tuning pins and the cooling plates positioning. One can notice, from Fig. 2.51, that the bore aperture in the top coupling cells passes through the coupled waveguide. From RF point of view, this does not represent an issue, since the bore aperture is too small to propagate the EM power. A more elegant solution would be to avoid the bore aperture in the coupling cells, but then it would not be possible to measure with bead-pull methods the field distribution in the coupling cells. A further study could evaluate the tuning feasibility of bi-periodic structures without coupling cell bead-pull measurements.

The coupler was optimized, as in the BTW, by adjusting the coupling slot aperture and the coupling cell diameter to minimize the total reflection, and a value of -40 dB was reached. For the purposes of the present study, this result was considered acceptable, though a final design ready for production should aim at -60 dB in the design stage.

The Ez field distribution on the full 3D design is presented in Fig. 2.55

2.5.3 Machinability considerations

The main remarks raised on the proposed mechanical solution concerns the feasibility of drilling a 2.5mm radius bore aperture through the coupling cell stems. If it was not possible, the RF design could be quite easily changed by, for instance, reducing the length of the stems, or in other words by increasing the coupling cells gap. This would result in larger coupling cell

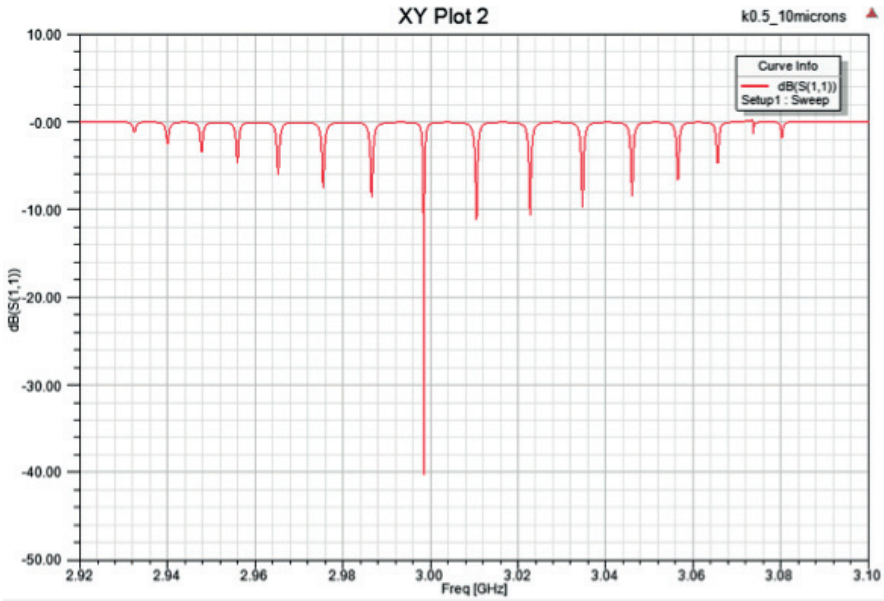

Figure 2.56 – S11 as a function of frequency in the HG CCL structure.

diameter, so a less compact overall dimension.

2.6 RF comparison between CCL and BTW HG solutions

The comparison between the HG BTW and CCL structures is here discussed. The two designs share the same maximum S_c/E_a^2 ratio, and key geometrical parameters, like bore aperture and septum thickness. In the CCL case, the limit of S_c/E_a^2 is reached on the nose of the CCL, not on the coupling slot, which is not the most critical part of the design. In the BTW cavity, as discussed, the maximum of S_c/E_a^2 is reached both in the noses and in the coupling holes. However, the ratio decreases on the coupling holes across the cavity, due to the decrease of the stored energy per unit length.

The main geometrical and accelerating parameters of the two structures are reported in Table 2.9. Here, a third column contains the data of a CCL cavity studied in [7] and optimized for a lower gradient of 30 MV/m, according to the same S_c model. It is possible to notice, graphically, the difference between the three cases in Fig. 2.52. The low gradient case, called BL (Base Line), has a shorter gap, to maximize the TT factor, and a sharper nose, to concentrate as much as possible the E field near the z axis. All the cavities have the same bore aperture radius of 2.5mm.

The result of the comparison study is that the ZTT of the HG CCL solution, even when optimized for high gradients, i.e. 50 MV/m, is higher of about 12 % with respect to the BTW solution with full re-circulation of the power. The BL CCL design, even though was designed with a larger iris thickness, have much better performances, being 30 % more efficient than

Table 2.9 – Main geometric and accelerating parameters of $\beta = 0.38$ cells. HG BTW (left), HG CCL (centre), low gradient CCL (right)

Type of structure	**BTW150**	**CCL-HG**	**CCL-BL**
Phase advance per acc. cell [deg]	150	180	180
Wall thickness septum [mm]	2	2	3
Gap [mm]	7.0	9.0	5.1
Nose con angle [deg]	65	65	25
Number of accelerating cells	12	10	10
Structure active length [mm]	189.9	189.9	189.9
Design acc. gradient Ea=E0*TT factor [MV/m]	50	50	26.3
Max ratio surface E-field to acc. gradient Es/Ea	4	4	6
Max ratio Sc to acc. gradient square Sc/Ea^2 [A/V]	2.710^{-4}	2.710^{-4}	7.810^{-4}
Quality factor Q (first/last)	6997/7463	9136	8290
R'/Q [ω/m] (first/last)	7425/7369	6568	8410
ZTT [Mω/m] (first/last)	52.0/55.0	60.0	69.7

the HG BTW, and 16 % more efficient than the HG CCL. Section 2.7.3 discusses the influence of the different parameters on the overall RF efficiency of a cavity.

Considering the filling time, the CCL structure reaches the nominal accelerating gradient in around 800 ns, as the BTW structure with a circulator.

A visual comparison of the two full length HG structures is shown in Fig. 2.57. In the Figure, the BTW is directly matched to waveguides, and not to the 3dB hybrid, which as shown in Fig. 2.50 remarkably improves the transverse dimensions of the cavity. However, such device can be directly plug into a Klystron and into a load, since the 3dB hybrid protects the klystron from the cavity reflected power. Instead, SW cavities require the installation of circulators on the lines to absorb the reflected power. These devices, being ferrite materials, have an attenuation on the forward power, i.e. the power that goes from the klystron to the cavity, of the order of -0.3dB, so around 7%, or more. If the main driver of the comparison between HG CCL and BTW solutions is the power efficiency, this factor has thus to be taken into account. As a final remark on this topic, circulators needs SF6 atmosphere to prevent sparkling, which instead is not needed in a 3dB hybrid. One could then consider to avoid the installation of SF6 windows, being expensive, and simply have vacuum in the BTW solution. This instead would not be possible in the CCL case.

From a cost point of view, it has to be mentioned that the BTW cavity is much simpler and needs less components than the CCL one. The machining of RF cells is easier, since the nose of the coupling cells in the HG CCL design is likely to pose some serious challenges in the production (see Fig. 2.52, middle). As for vacuum flanges are concerned, a CCL cavity needs 4 times more than a BTW one, to terminate the coupling cells bore aperture. Similarly, a CCL cavity needs to tune the coupling cells together with the accelerating ones, thus the mechanical design has to envisaged more tuning pins, that in turns complicate the design

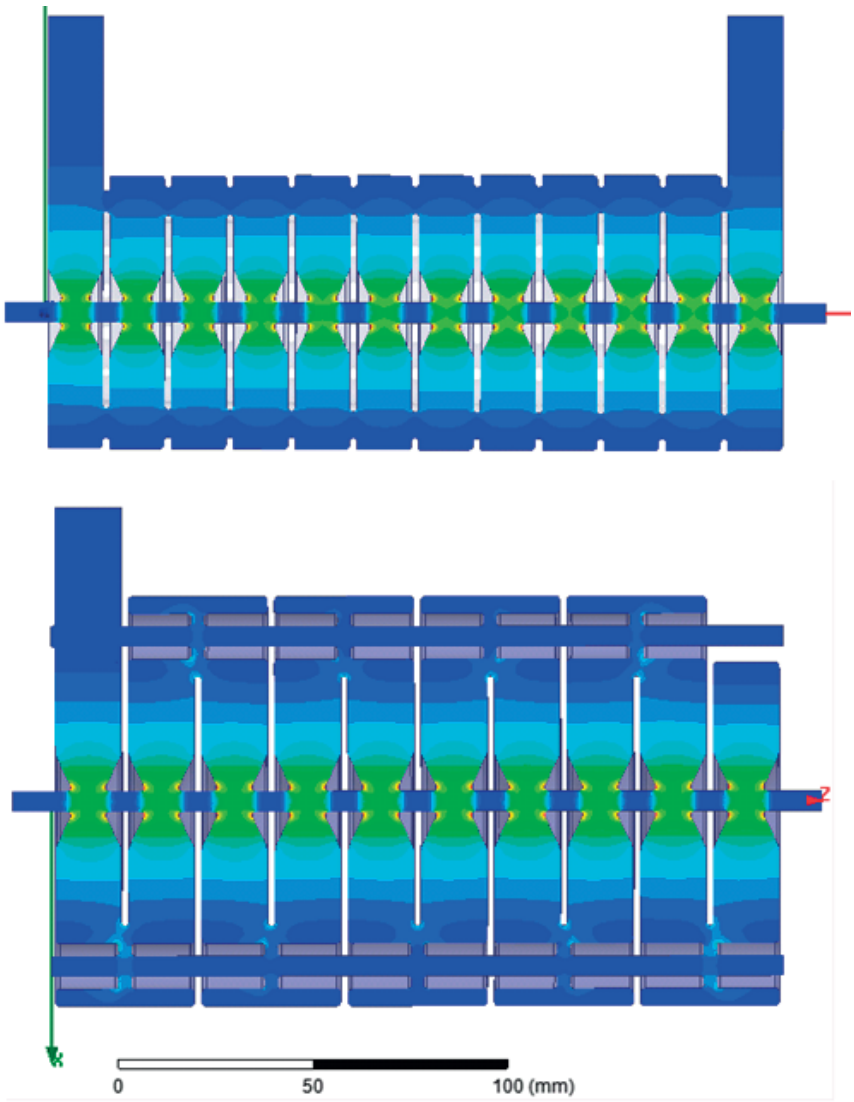

Figure 2.57 – Cut view with Complex Mag Electric field distribution in the high gradient BTW (top) and CCL (bottom) structures at $\beta = 0.38$.

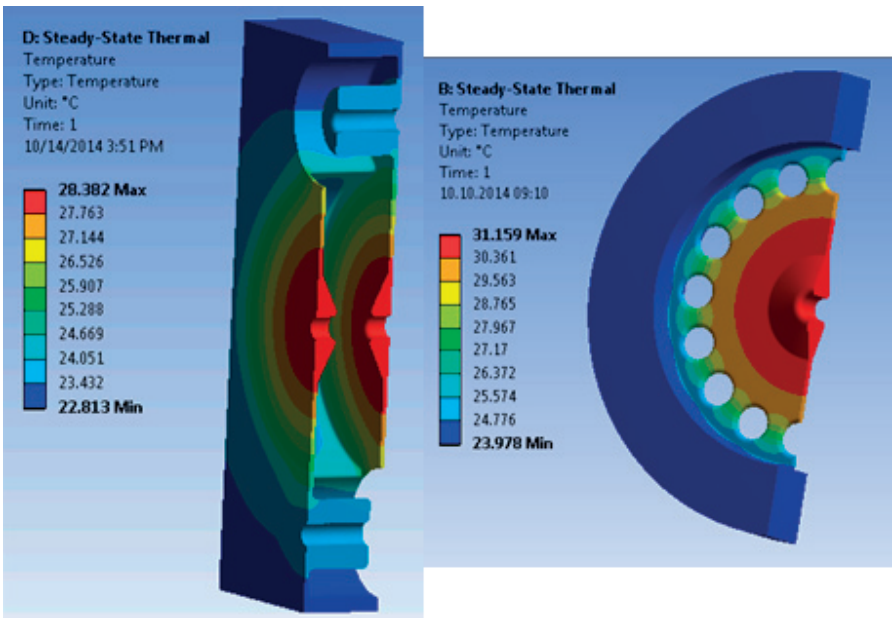

Figure 2.58 – Temperature distribution in the high gradient BTW (right) and CCL (left) structures for a 50 MV/m gradient and 0.0075 % duty cycle

of the cooling channels. At the same time, the tuning of the cavity is more complex, and theoretically more prone to errors. No direct experience on CCL cavities tuning was acquired during this thesis. If one compares the 3 GHz CCL tuning methodology discussed in [39], to the BTW prototype tuning, this latest is remarkably simpler, and required less than a couple of hours of work (see Section 5.1). In conclusion, simplicity is a key aspect that should not be neglected, especially on a commercial design, and the BTW solution has a clear advantage over the CCL one in this regard. If however one could design a 3 GHz CCL with coupling cells that do not need to be tuned, the above considerations would not hold anymore.

The two structures were also compared in terms of RF thermal power dissipation. Here the CCL has two advantages:

- a slightly higher ZTT, which translated into a lower RF power dissipated in the copper walls for the same accelerating gradient;
- a higher thermal conductivity with respect to the BTW solutions, where the coupling holes are an obstacle to the power dissipation.

The temperature distribution in the two cases is shown in Fig. 2.58.

Heat transfer in a metal follows Fourier's law of heat conduction:

$$\vec{q} = -k\Delta T, \tag{2.22}$$

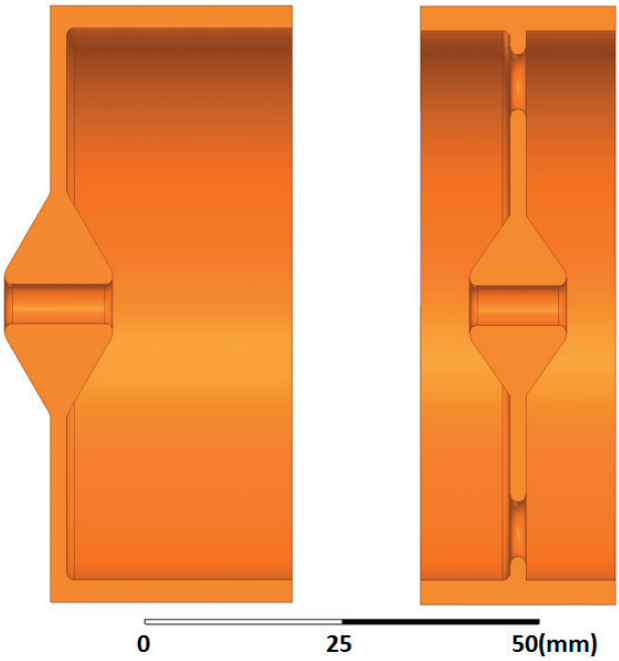

Figure 2.59 – Uncoupled CCL (left) and BTW (right) cells at 230 MeV/u.

with $\vec{q}$ heat flux density, k material thermal conductivity, and ΔT temperature gradient. In the case of a simplified 1D geometry, as a bar, one has a linear dependence with the cross section, and a inverse dependence with the length between the two extremes. This simple law allows to discuss more in detail the difference between the BTW and the CCL structure.

The thermal load in the two structure for an equivalent accelerating gradient scales as the ratio of the shunt impedances, since the length is equal. The CCL cavity design would have then 12% less thermal load to dissipate (Table 2.9). However, the simulated temperature gradient is lower in the CCL than in the BTW. Since the cell diameters are similar, this is caused by the reduced cross section given by the coupling holes in the BTW geometry.

If one extends the ZTT comparison up to 230 MeV/u, the results change, as already discussed with Table 2.8. In particular, a 50 MV/m BTW optimized structure for a 230 MeV/u beam shows about a ZTT 7 % lower than the CCL solution. The ZTT ratio between the two designs is not constant due to the difference cell length between the two solutions: the BTW, being shorter, allows for a higher optimization of TT factor (shorter gap) and nose region (sharper nose cone angle) at higher energies. The difference can be observed graphically in Fig. 2.59.

Three intermediate energies were studied, corresponding to 105, 138 and 181 MeV/u. The TT factor, Q factor and the ZTT along the linac for the two high gradient solutions is showed in Fig. 2.60. The BTW solution has a lower Q factor with respect to the CCL one, but this difference however gets narrower with the increase of the cell lengths, and so does the ZTT. As previously motivated at the end of Section 2.5.1, in this comparison a constant 7 % reduction

of the Q factor was considered for the CCL case from the uncoupled solution studied and the coupled results presented. If instead one considers a 13 % reduction between the simulated uncoupled Q factor and the coupled one, as in Superfish and as presented in [7] and [30], the ZTT difference between the two solution is lower, and it is almost zero at 230 MeV/u.

2.7 The high-efficiency 3 GHz CCL accelerating structure

The choice of a lower accelerating gradient in CABOTO with respect to TULIP opened the possibility to work on a more aggressive RF design. The absolute limiting quantities, Sc and maximum Es, adopted for TULIP have been kept constant, and equal to 0.75 MW/mm^2 and 200 MV/m. These limits have been fully exploited consistently thorough the linac. In addition to the smaller bore aperture of 2 mm, this translated into a remarkable increase of the ZTT. In the following, the RF optimization is discussed, pointing out the most important parameters, and presenting some scaling laws.

The approach adopted was to optimize the cell gap and cone angle. On the optimized solution found, a sensitivity analysis on inner and outer nose radius, and inner corner radius was performed. Three RF cells were optimized, corresponding to 100 MeV/u, 430 MeV/u, and the intermediate 211 MeV/u, with respect to the relativistic β. Hereafter only the 100 and the 430 MeV/u cases are presented.

In this work, machining limitations of the RF disks were not considered. For instance, fillet radius smaller than 1mm were studied, and are presented. As for previously discussed structures, this is an aspect that needs further studies.

2.7.1 100 MeV/u cell

The 100 MeV/u cell optimization is summarized in Fig. 2.61, where a cut view of the geometry is also reported.

The optimum that respects the field limits is obtained for a 6mm gap, 10deg cone angle, and corresponds to 96 MΩ/m.

The sensitivity analysis on inner/outer nose/cone radii showed that a reduction of the inner nose radius is beneficial both in terms of ZTT, as expected, but also it translates into a lower S_c/E_a^2 peak. The reason of this behaviour can be explained by observing (Fig. 2.62). A smaller inner nose radius increase the surface E-field peak, but it also distances it from the maximum of the H-field. Overall, the Sc is actually reduced. This trend is monotonic for Sc, but at the same time a smaller nose radius increase the maximum surface E-field, which then becomes the limiting quantity. For the 100 MeV/u cell, the optimum was found for 0.8 mm inner nose radius, with a 2% increase in ZTT, a 6% decrease in Sc/Ea^2, and a 7% increase in Es/Ea over the initially considered solution with 1 mm inner nose radius.

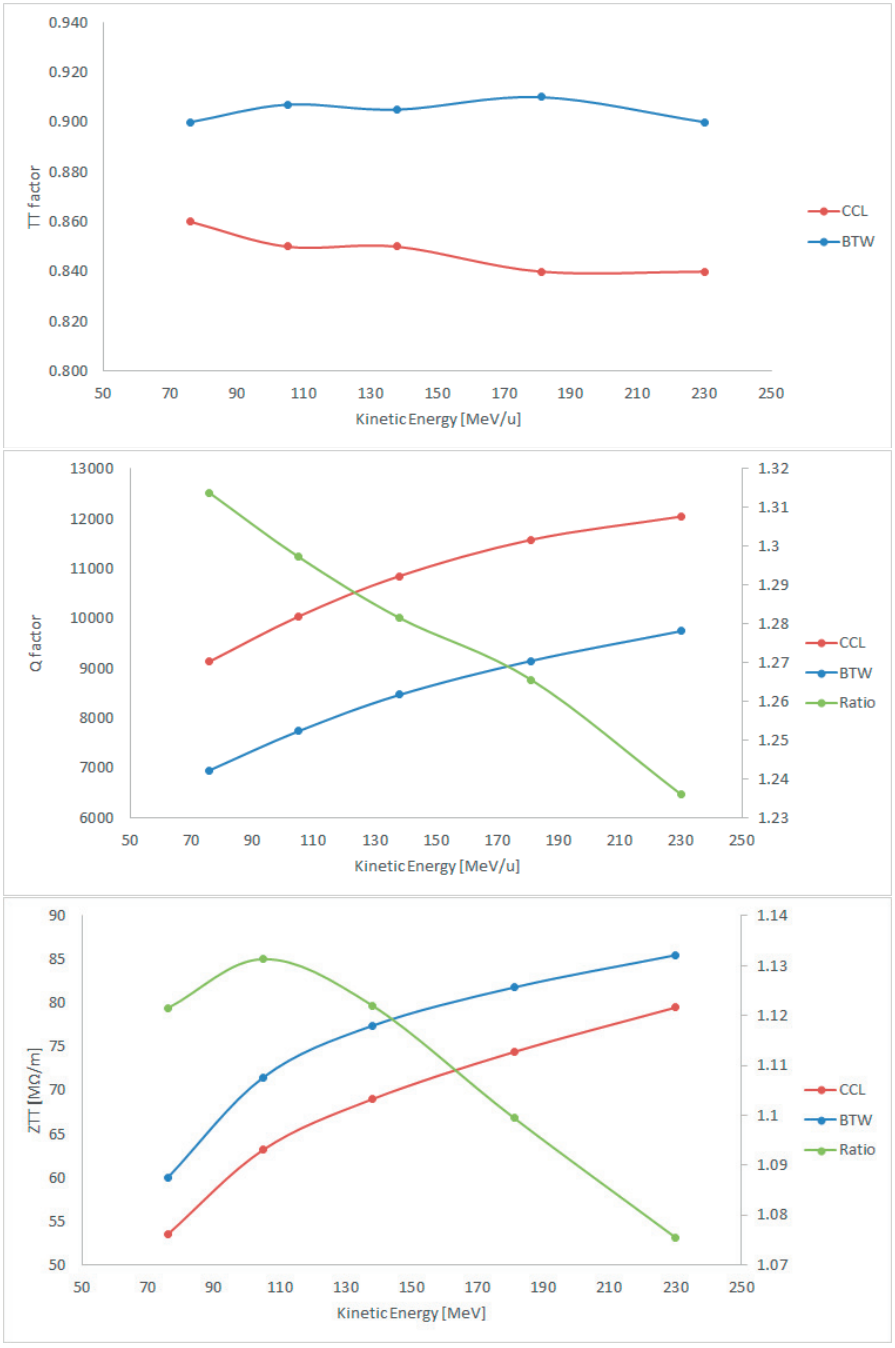

Figure 2.60 – TT factor (top), Q factor (middle) and ZTT (bottom) comparison between a CCL and a BTW high gradient linacs, with CCL values as in Table 2.8 and BTW values as in Table 2.6, considering 12 RF cells per structure.

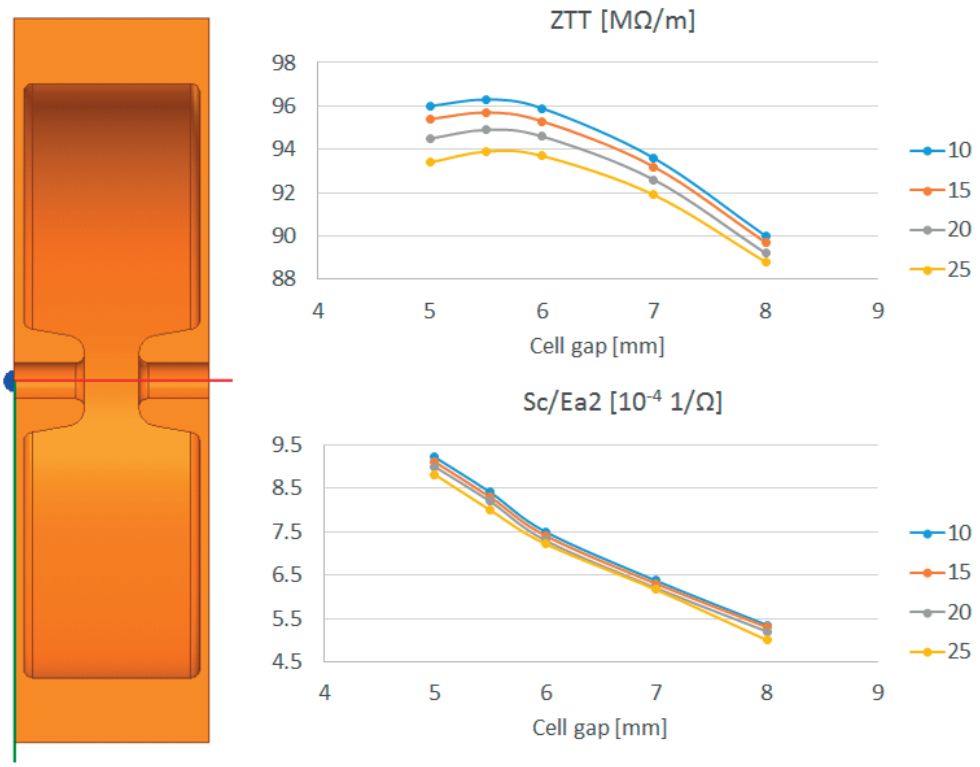

Figure 2.61 – 100 MeV/u HE CCL cell optimization, for different cone angle. The optimum ZTT respecting the Sc/Ea2 constraint correspond to 6mm gap, 10deg cone angle.

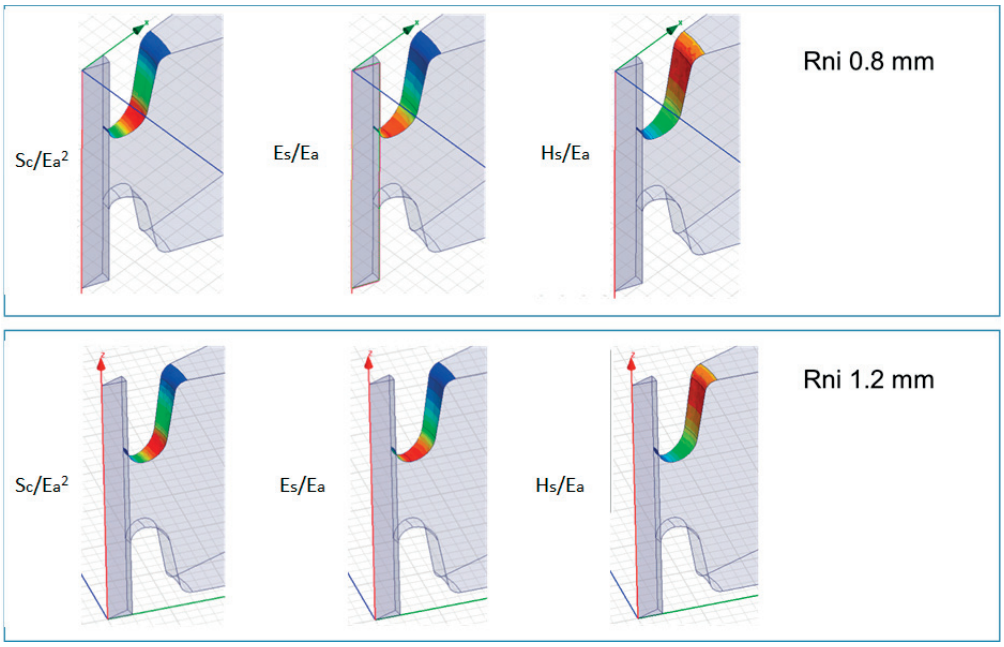

Figure 2.62 – Sc, E-field and H-field distribution on the nose region, normalized to the accelerating gradient, in case of a 0.8mm inner nose radius (top) and 1.2mm (bottom).

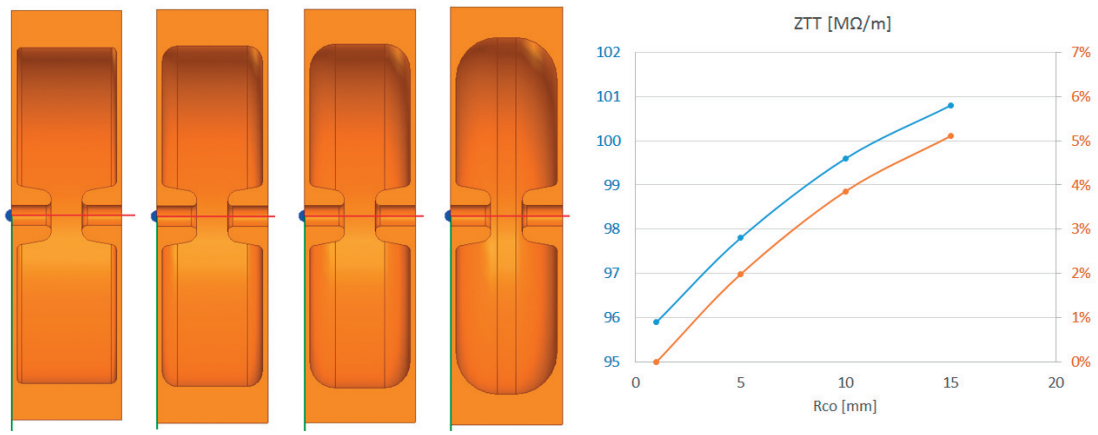

Figure 2.63 – ZTT as a function of the outer corner radius of the cell, in absolute values and percentage difference on the right y-axis. Cut view of the different studied geometries on the left.

The outer region of an RF cavity, independently on the type, should be rounded. This condition in fact ensure the maximum of the Q factor for a given cell, and so of the ZTT. However, other considerations play a role, like tuning capability, machining complexity, and RF coupling feasibility. The ZTT behaviour as a function of the outer corner radius was studied, and it is presented in Fig. 2.63. An almost full rounded solution would increase the ZTT of about 5% with respect to the flat (1mm fillet) geometry. However, the thin septum thickness of 2mm chosen required the use of the mechanic design explained in Section 2.5.1, which needs an almost flat outer cavity wall.

On the other hand, one could consider to adopt a thicker septum, and a more classic brazing procedure as the one proposed in [26]. As presented in Section 2.7.2, for the 430 MeV/u cell there is a 3 % reduction on ZTT going from 2mm to 3 mm septum, but a gain of 9 % going from a flat to a round outer cavity wall. In conclusion, two coupled cavities should be studied, considering the two solutions. The final design should be chosen taking into account the different machining complexity of the two geometries, as well as the tuning higher complexity of a round solution.

From a thermo-structural point of view, the 100 MeV/u cell is the most delicate part of the linac, given the lower ZTT. The RF cell was studied considering an accelerating gradient of 30 MV/m, and a DF of $1 * 10^{-3}$. These are limit conditions for the RF cell, since the thermal gradient reaches 20 °C and the thermal-induced deformation a maximum value of 8 μm on the noses, as shown in Fig. 2.64. On a final design, one shall address whether these values are acceptable, and if not whether to privilege a lower gradient - lower DF solution, or a larger septum thickness with then higher power consumptions.

The linearity of heat conduction in metals (see Section 2.6 for discussion) allows to draw some quick considerations. The ZTT reduction in the 430 MeV/u cell from a 2 mm to a 3 mm septum

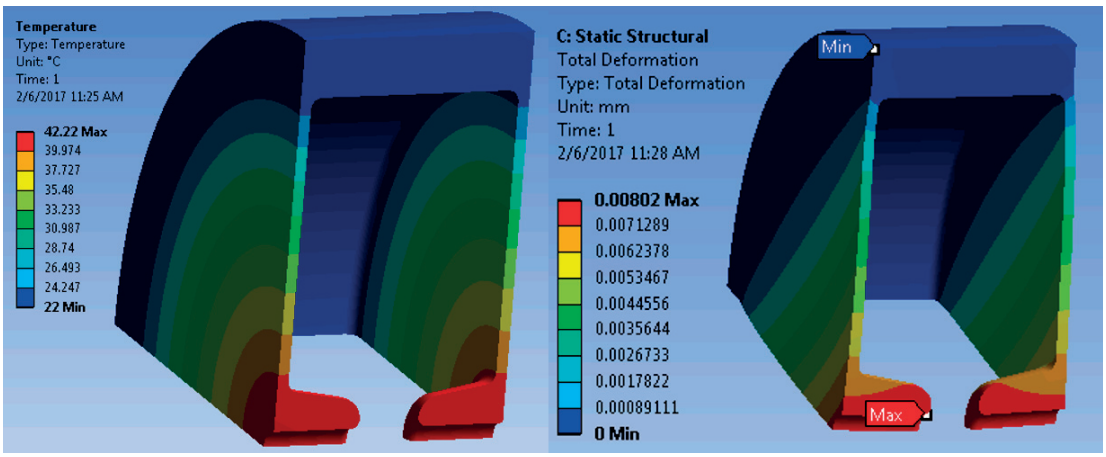

Figure 2.64 – Thermo-structural analysis of the 100 MeV/u RF cell for CABOTO, for a 30 MV/m accelerating gradient and $1 * 10^{-3}$ DC. Temperature distribution (left) and thermal-induced deformation (right).

is almost 3 %. In the 100 MeV/u cell, being shorter, the percent reduction is higher, and it could be estimated in 5 %, or being conservative in 10 %. The section increase on the other hand is 50 %. Thus the thermal gradient reduction can be safely estimated in 40 %, with a maximum temperature for the identical operating conditions of 36 °C instead of 42 °C.

For comparison, the BTW prototype is limited to a thermal gradient of 5 °C, due to the plasticization limit in the coupling holes. A CCL design does not present such a critical feature, and it is likely to withstand safely higher gradients. A detail mechanical study is however needed to address the matter.

2.7.2 430 MeV/u cell

The 430 MeV/u cell optimization is summarized in Fig. 2.65, where a cut view of the geometry is also reported.

The optimum that respects the field limits is obtained for a 15mm gap, 15deg cone angle, and corresponds to 117 MΩ/m.

As for the 100 MeV/u case, a reduction in the inner cone radius increases the ZTT and decreases the Sc/Ea^2 ratio. In this case, the optimum was found for a 0.4 mm inner nose radius, with a 4% increase in ZTT, a 7% decrease in Sc/Ea^2, and a 16% increase in Es/Ea over the initially considered solution with 1 mm inner nose radius. With respect to the 100 MeV/u case, it was possible to push a bit further the optimization since the longer cell length decreases the Es/Ea ratio, so there is more margin in this regard.

The outer corner radius optimization (Fig. 2.66) showed an higher increase of ZTT for larger radii with respect to the 100 MeV/u case. This was expected, since longer cells have a larger Q

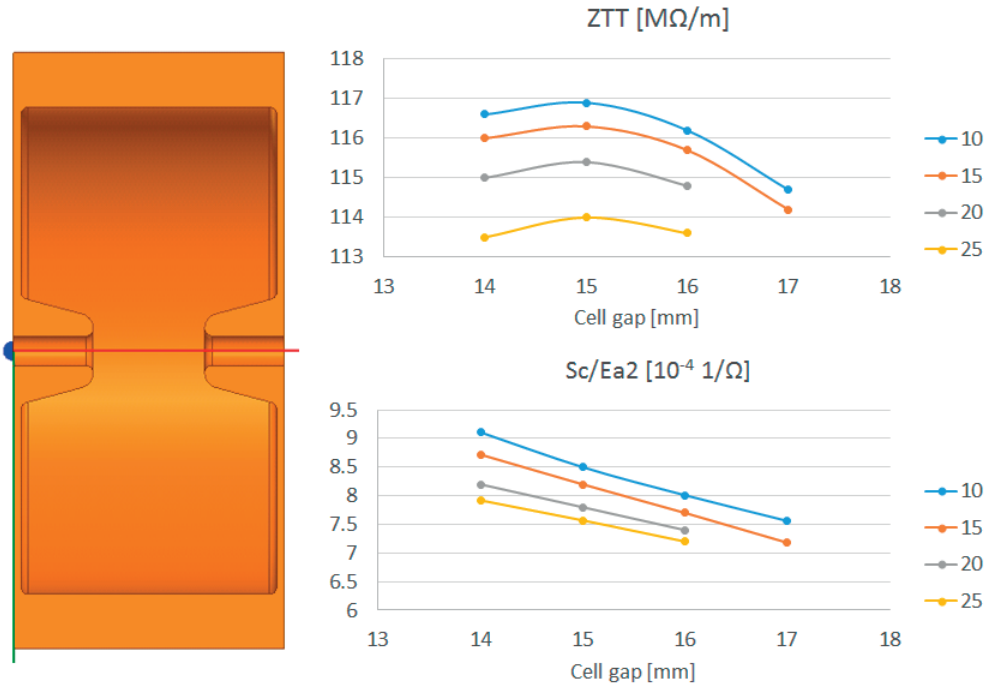

Figure 2.65 – 430 MeV/u HE CCL cell optimization, for different cone angle. The optimum ZTT respecting the Sc/Ea2 constraint correspond to 15mm gap, 15deg cone angle.

factor, and so also the relative gain is larger.

For the 430 MeV/u cell, the behaviour of ZTT as a function of the cell septum was studied. In fact, to longer cells correspond bigger and so heavier nose regions, while the cavity radius is usually almost unchanged. So it could happen that the same septum thickness is achievable at a low energy cell, but not anymore at an higher one. The optimized cell corresponding to a 3mm septum is reported in Fig. 2.67, together with the ZTT trend as a function of the wall thickness (left).

2.7.3 Summary and some interesting sensitivity considerations

It is worth here to draw a line and recap the sensitivity of the different solutions studied. The main geometric and accelerating data of the three optimized RF cells, plus two more simply interpolated, are reported in Table 2.10. Fixed notable geometrical parameters are the bore radius (2 mm), the iris thickness (2 mm) and the outer corner radius (1 mm). For the coupled values of Q factor and ZTT, a 7 % reduction with respect to the uncoupled values was considered, as discussed in Section 2.5.1.

The results summarize in Table 2.10 represents a 16% increase in average ZTT over a similar design studied in [7], that considered S-band CCL optimized for 30 MV/m, with a 2 mm iris thickness, but a 2.5 mm bore aperture radius.

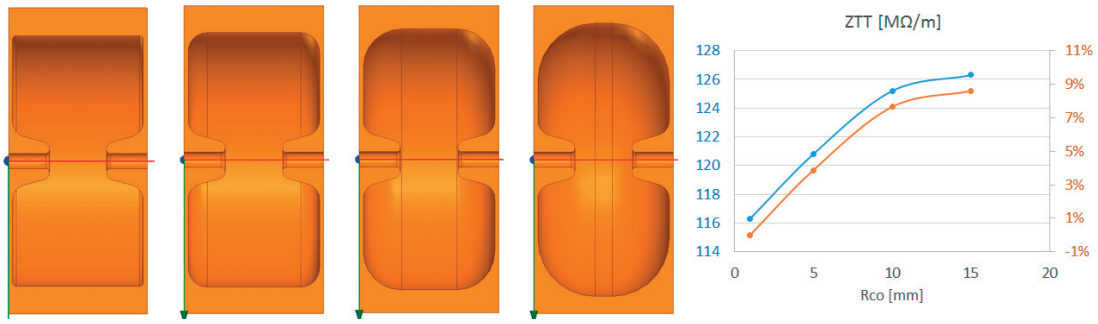

Figure 2.66 – ZTT as a function of the outer corner radius of the cell. Cut view of the different studied geometry on the left.

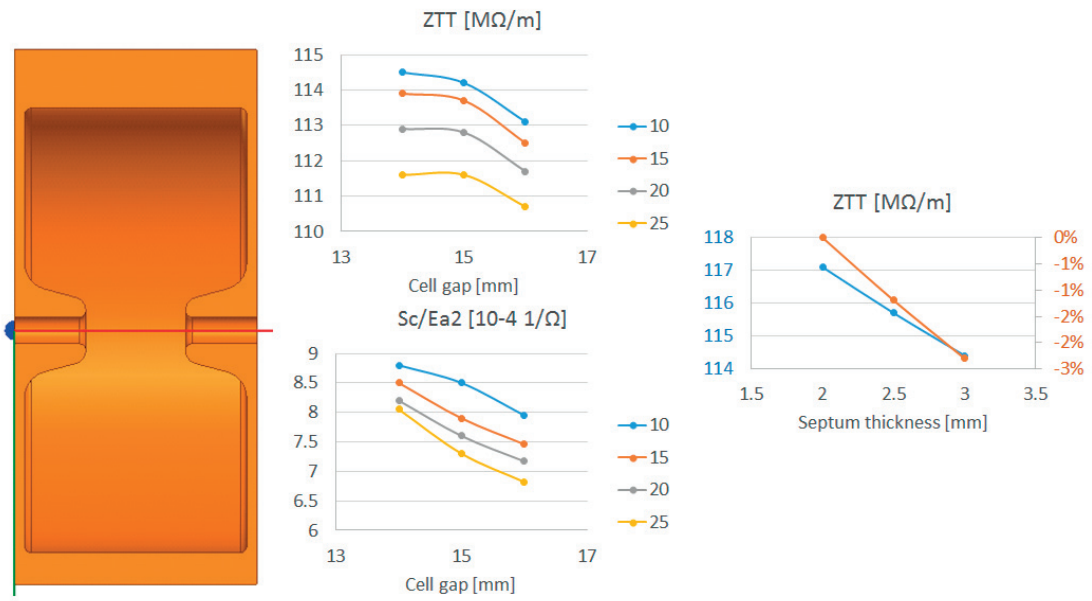

Figure 2.67 – 430 MeV/u HE CCL cell with 3mm septum thickness optimization, for different cone angle. The optimum ZTT respecting the Sc/Ea2 constraint correspond to 15mm gap, 15deg cone angle. ZTT as a function of the septum thickness of the cell on the right.

Table 2.10 – Geometric and accelerating parameters of the optimized HE CCL RF cells for different geometric β.

Energy [MeV/u]	Geometric β	Length [mm]	Gap [mm]	ConeA [deg]	Rni [mm]
100	0.430	21.47	5.5	5.0	0.8
147	0.504	25.21	7.7	7.5	0.7
211	0.579	28.95	10.0	10.0	0.6
300	0.654	32.70	12.4	12.5	0.5
430	0.729	36.46	15.0	15.0	0.4

Energy [MeV/u]	Geometric β	TT factor	Q value coupled	ZTT coupled [MΩ/m]	S_{cn}/E_a^2[1/kΩ]	E_{sn}/E_a^2
100	0.430	0.945	9242	91.5	0.78	6.56
147	0.504	0.939	10188	101.1	0.72	6.34
211	0.579	0.930	11007	106.9	0.75	6.30
300	0.654	0.920	11712	111.1	0.72	6.38
430	0.729	0.908	12323	113.2	0.76	6.39

Table 2.11 – Sensitivity of selected geometric parameters on the ZTT for the 430 MeV/u CABOTO RF cell.

Geometric parameter	ZTT variation [%]	Geometric variation	Normalized variation (ZTT % / Variation %)
Intra-wall thickness	3%	3mm to 2mm (-33%)	0.09
Outer corner radius	9%	1mm to 15mm (+1500%)	0.01
Inner nose radius	4%	1mm to 0.4mm (-60%)	0.07
Bore aperture	14%	2.5mm to 2mm (-20%)	0.7

The previous discussion highlighted that, in a cavity with an optimized nose region, i.e. where cell gap and cone angle are optimized, four parameters have a major impact on the ZTT. These are the septum thickness, the outer corner radius, the inner nose radius, and the bore aperture. In Table 2.11 this sensitivity study is summarized for the 430 MeV/u cell. The ZTT value of an optimized 430 MeV/u CCL cell with 2.5 mm bore radius is taken from [7].

The most important result of Table 2.11 is that, as pointed out at the beginning of this Chapter, the bore aperture is the most important parameter that defines the shunt impedance of a cavity, in the assumption that the nose region has been optimized. After that, the second most important contribution is the septum thickness. The septum thickness is the most important geometrical parameter that defines the thermal gradient in a cavity, thus it defines the maximum DF and thermal gradient achievable. The inner nose radius is another quite important parameter, and in these simulations relates to the maximum surface fields in the cavity (see discussion in Section 2.7.2). The outer corner radius, often regarded as an important parameter in the optimization, is indeed not so important for CCL cavities. First, because is sensitivity to ZTT is the smallest amongst the parameters considered, but secondly, and most importantly, because it cannot being solely studied on a uncoupled solution, since it affects the type of quintuplet that is possible to design.

If one cares for an efficient and quick optimization of a linac, one shall consider just beam dynamics studies and nose region optimization of the cavities. Thus define a bore radius, that could also be variable across the linac, and then optimize gap and cone angle of the cavities

according to the BD field limiting quantities. All the other cell parameters have a good order of magnitude lower impact on ZTT than what one can obtain working as above. This is the reason why so much effort has been put into the linac and beam dynamics design of CABOTO.

As a final remark, let's consider the difference between the TULIP and the CABOTO CCL optimization. If for instance one compares the 100 MeV/u cell, the HE CCL cell has a coupled ZTT of 101.1 $M\Omega/m$, while the HG CCL 63.6 $M\Omega/m$. Thus a 37% reduction. However, the HG CCL has a 2.5 mm bore radius. To compare a equal 2.5 mm bore radius, one could consider the HE CCL design presented in [7], with an uncoupled ZTT of 77.0 $M\Omega/m$, thus a 17% reduction. If we normalize this reduction to the maximum gradient achievable, 50 MV/m versus 30 MV/m, one has a normalized variation ZTT [%] over Gradient [%] of 0.25. This number should be consider as a first order indication, since is based on the results obtained by two different works, that cannot be fully compared. However, it represents an useful indication of what occurs when changing the design gradient in a design. This consideration permits to comment also on the understanding of BD phenomenon in normal conducting cavities. This research activity is important not only to design compact linacs with previously un-reached accelerating gradients, but also to optimize the RF cells, so to maximize the ZTT for a given BD limits.

This Section tried to highlight the number of connexions that lie behind a linac design. As a final summary, in order of priority one shall:

- define the input beam characteristics to the linac, and the beam dynamics requirement at the end of it; beam dynamics and RF design are strongly interconnected; one should look after what a minimum reasonable bore aperture could be, having in mind that one could consider different active to total linac length, so beam envelopes;
- define the target gradient and BD limits of the linac; this has the second to biggest impact on the RF design, quite closely to the bore aperture decision;
- with these informations, one shall optimize the cell nose region to maximize the TT factor;
- eventually, one shall optimize the outer region of the cell, though privileging at this point other constraints of the design, such as easiness of machining and tuning.

2.7.4 Assessment of a different RF coupling

The 430 MeV/u cell was the perfect candidate to investigate the feasibility of a different RF coupling between accelerating cells. In fact, being the longest of the linac, a novel solution is either advantageous here, or it does not work at all for the entire linac.

A on-axis coupling was attempted, both electrically (Fig 2.68), through the bore aperture, and magnetically (Fig 2.69), through coupling holes like in the BTW structure.

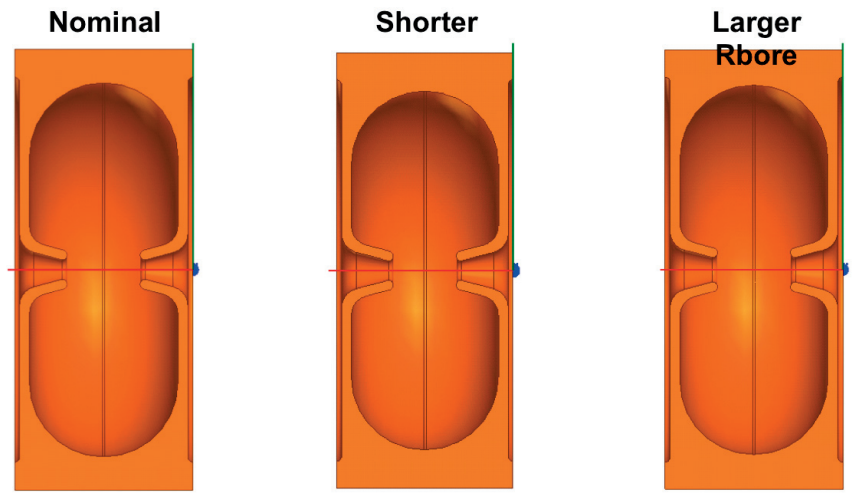

Gap 15mm, Rb 2mm	
K1 [%]	0.04
Q factor	14569
ZTT	111.9

Gap 13mm, Rb 2mm	
K1 [%]	0.05
Q factor	14063
ZTT	117.2

Gap 15mm, Rb 2.5mm	
K1 [%]	0.03
Q factor	14427
ZTT	109.5

Figure 2.68 – Electric coupling of a on-axis coupled cavity, for different gap geometries.

The advantage of this solution consists in an higher Q factor of the accelerating cell. However, this comes at the cost of an equivalent larger RF cell septum thickness (septum). In this study, maintained fixed to 2 mm the wall septum, 2 mm were considered for the coupling cell, bringing the total equivalent septum thickness to 6 mm, instead of the 2 mm of the classic solution.

The electrically coupled solution, as expected, does not have enough coupling. Two other solutions have been studied, considering a shorter gap with respect to nominal, and larger bore radius. In addition, the nose region was modified to increase the coupling. Nonetheless, the coupling factor is approximately 0.05 %, thus not sufficient.

The magnetically coupled solution works a bit better, but it is not comparable with the reference CCL cell. Two solutions were studied, considering 8 and 16 coupling holes. In both cases, the coupling factor is almost 0.5 %. This represents a working solution, as shown in Fig. 2.70, and also an interesting one, having a coupled solution ZTT of 109.8 MΩ/m, in contrast to 116.3 MΩ/m of a uncoupled accelerating cell with 1 mm outer corner radius. Nevertheless, the 0.5 % k1 is one of order of magnitude lower than the reference of 5 %, and too low for a full structure with stable operating condition. Also, it is not clear how to increase this number, without having a longer coupling cell, but then also a significant decrease in the coupled ZTT.

As a final remark, though the magnetic coupled solution represents a simplification in the cell machining, it is disadvantageous from a thermal point of view with respect to the side CCL, having the same problem in that sense of the BTW solution.

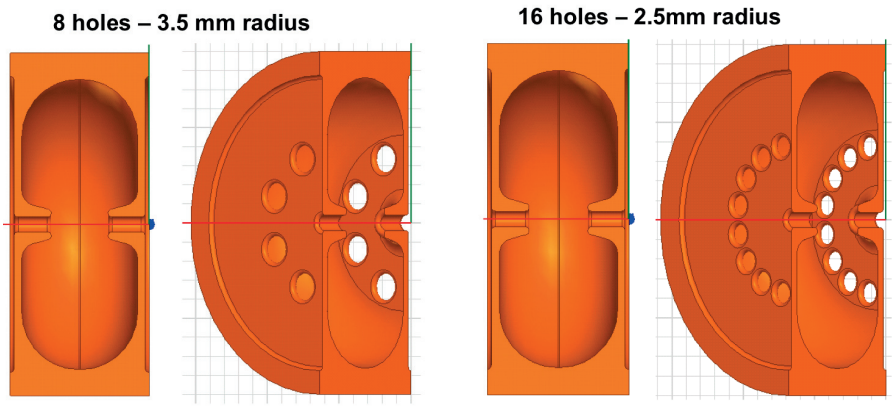

Gap 15mm, Rholes 3.5mm	
K1 [%]	0.49
Q factor	14002
ZTT [MO/m]	109.4

Gap 15mm, Rholes 2.5mm	
K1 [%]	0.43
Q factor	14041
ZTT [MO/m]	109.8

Figure 2.69 – Magnetic coupling of a on-axis coupled cavity, with 8 holes (left) and 16 holes (right).

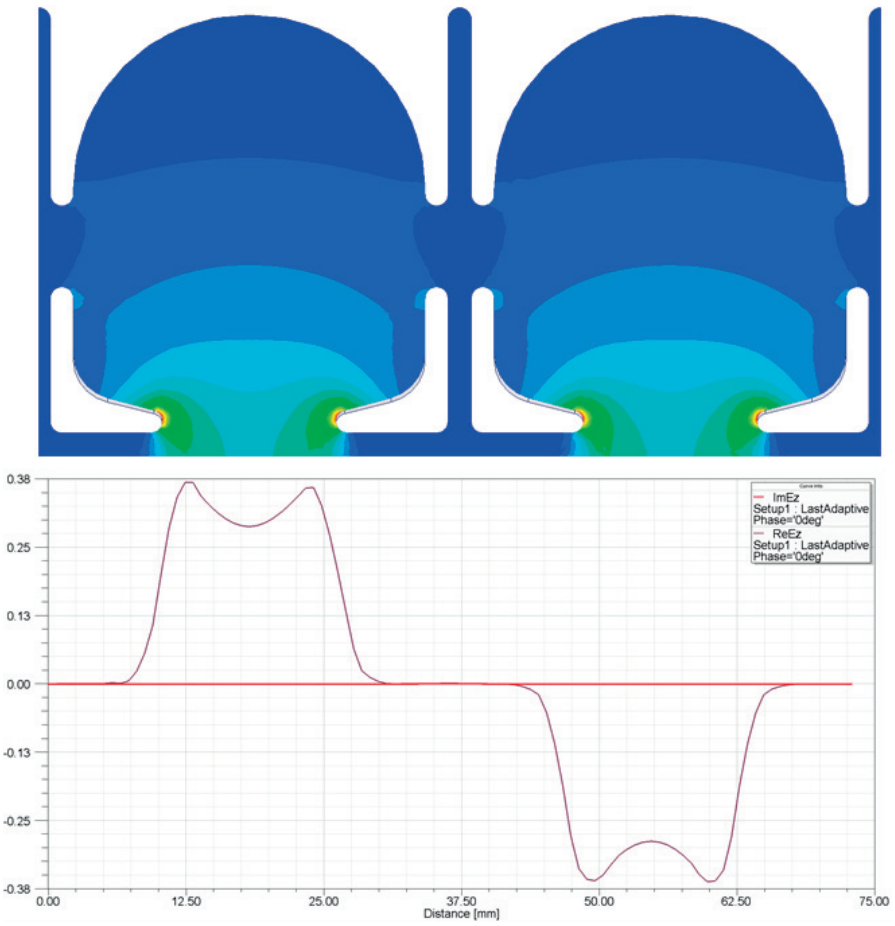

Figure 2.70 – E field distribution in the 16 coupling holes solution.

3 TULIP: a high-gradient linear accelerator for proton therapy

This Chapter discusses in detail the design of a proton linac accelerator, named TULIP. As discussed in Section 1.3, this project was started by TERA Foundation, and proposed in a *cyclinac* solution in [7] and [28]. Here the project was studied in a *all-linac* configuration. The main goal of the project is to design the most compact possible proton linac for conventional proton therapy. For this reason, high gradient structures were studied. Mechanically-wise, one of the linac is supposed to be mounted on a gantry rotating around the patient, to reduce the space. The focus of this thesis is on the linac design, and this topic was not studied by the author. The codes used to design the linacs and to perform the beam dynamics simulations are discussed in Appendix A.

In the present Chapter, as well as in Chapter 4, few linear accelerators technical terms will be frequently used, hereafter explained. The author refers to tanks for accelerating cavities composed of more than one RF cell, and to modules for series of cavities connected to the same RF power source.

3.1 General layout

Conceptually, TULIP (Fig. 3.1) can be split into a low gradient section, that will be placed on the ground, and a high gradient section that will be mounted on a rotating structure, called gantry. The footprint of the facility is driven by the rotating structure, that has to allocate, together with the high gradient linac, also the high energy beam transfer line (HEBT) and the beam diagnostic. As a result, about 10 meters are available on the ground to install the linacs that have to boost the particles up to 70 MeV. This length has been fully exploited, in order to minimize the power consumption for a given energy gain according to Eq. 2.6.

The design is based on a first acceleration up to 10 MeV in 750 MHz structures: the CERN RFQ [32] [46] and the newly designed Inter digital H mode [IH] cavity (Section 2.2). Particles are then injected into a 3 GHz linac chain composed of an DTL (Section 2.3) up to 70 MeV, and a HG BTW (Section 2.4.1) or CCL (Section 2.5) up to 230 MeV. Table 3.1 summarizes the main

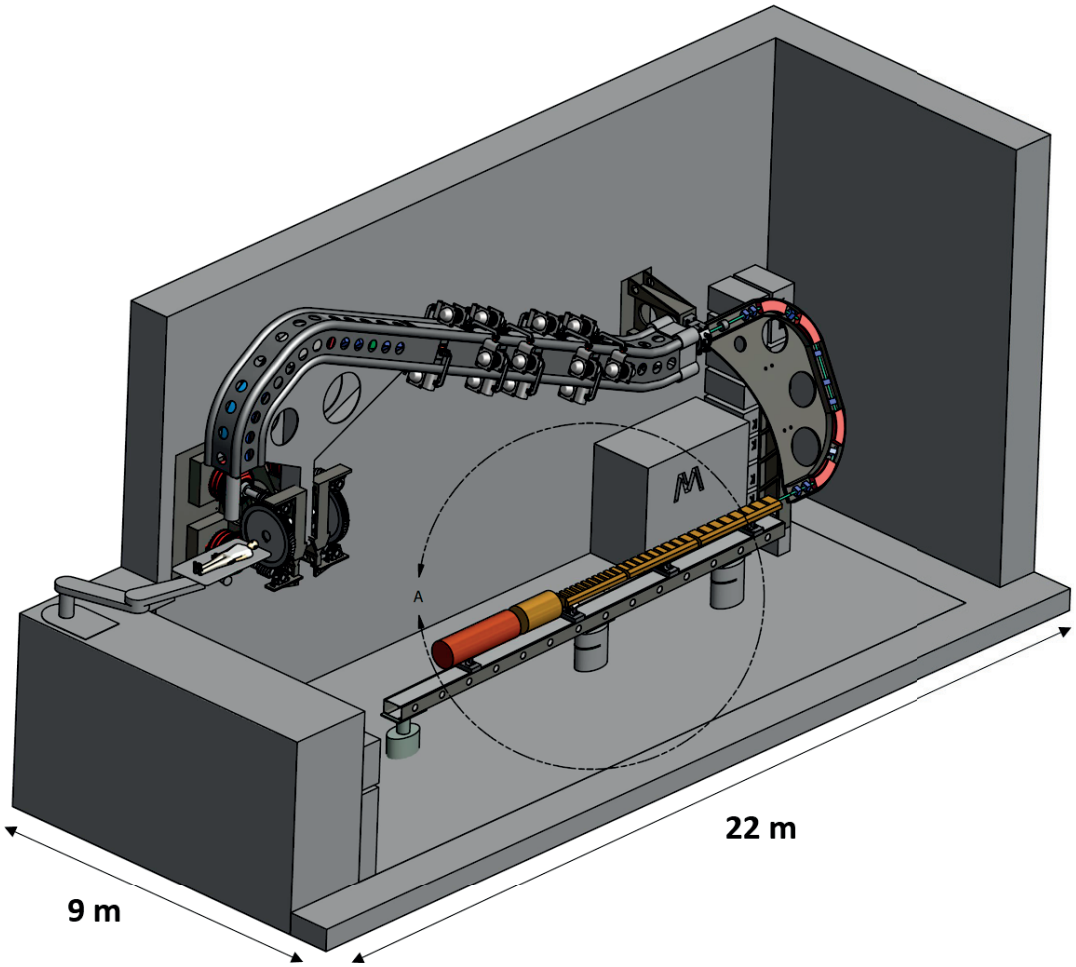

Figure 3.1 – Sketch of TULIP *all-linac*. In the sketch, one can observe on the ground a representation of the RFQ (in dark orange) followed by the IH cavity and by the DTL cavities. The HG BTW linac is hidden by the mechanical frames. The longitudinal dimensions in this artistic illustration are the ones proposed in the present Chapter.

Table 3.1 – Key parameters of the *all-linac* TULIP solution.

Type of structure	Output energy [MeV]	Active Length [m]	Peak power [MW]
750 MHz RFQ	5	2	0.4[1]
750 MHz IH	10	0.9	0.084
3 GHz DTL	70	4.1	11.3
3 GHz HG BTW	70-230	4.4	91.7

parameters of the linac design.

The duty factor of the linac is currently limited by the high gradient section. A typical DF value of 0.1% would be reachable in both the RFQ, the IH and the DTL, but not in the CCL, due to the thin septum wall thickness chosen to maximize the ZTT. As a result, a final design should decide whether to privilege the acceleration efficiency and the linac compactness, but with a lower DF, or a higher DF but with a lower accelerating gradient or an higher peak power. The design presented hereafter will be limited by the high gradient section to a 0.01% DF, as discussed in Section 2.4.5.

The 750 MHz RFQ was not studied by the authors, and it represents the starting point of the present work. The following three accelerating structures forming TULIP has been studied in detailed from both RF and beam dynamics point of view. The high gradient BTW structure was also built and tested.

In the next Sections, the different linacs will be discussed separately. At the end of the Chapter, the start-to-end simulation will be presented.

3.1.1 From 5 to 10 MeV

Protons are accelerated by the IH structure described in Section 2.2 from 5 to 10 MeV. The attentive reader may remember from Section 2.2.1 that the ZTT advantage of IH cavities over the other solutions considered extended well beyond 10 MeV/u. However, at the present stage the cost per unit power of 750 MHz RF sources, currently only IOTs, is about one order of magnitude higher than the corresponding cost in case of 3 GHz Klystron-Modulator based solutions [47]. This difference is largely caused by the high demand of this latter technology working at 3 GHz, caused by the market of X-ray electron linacs. However, even though is the authors belief that this price difference will decrease in the future as a consequence of an higher demand of 750 MHz RF power sources, at the present stage the crossing point between a 750 IH solution and a 3 GHz DTL one has been found at 10 MeV/u, considering the cost issue just explained.

To boost protons from 5 MeV to 10 MeV it has been chosen to use just one 100 kW IOT, resulting in a fairly low gradient of about 5.7 MV/m, and into a 0.9 m long structure. The structure is

[1] total with losses

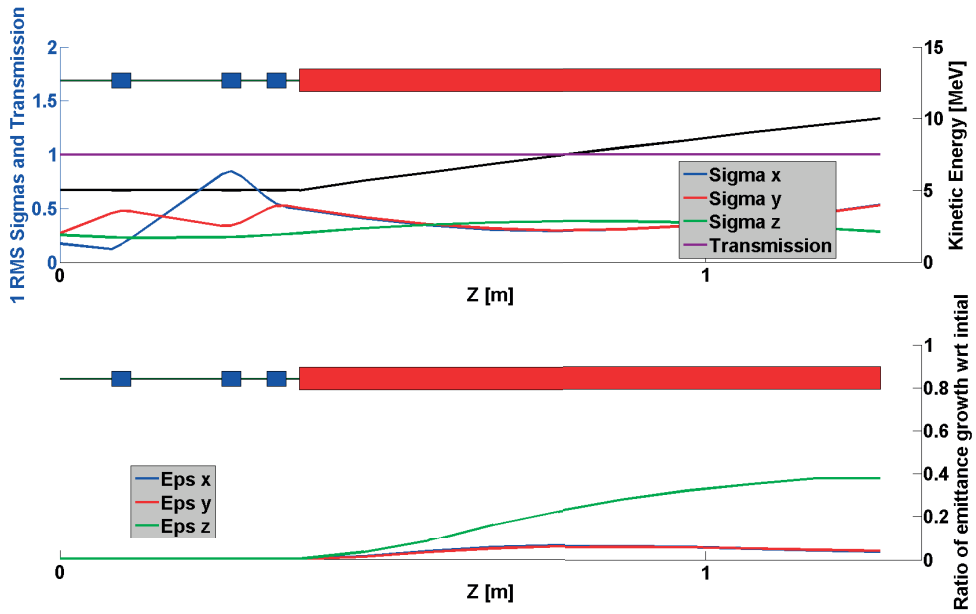

Figure 3.2 – Beam 1 σ RMS envelope through the TULIP IH linac from 5 to 10 MeV (top) and ratio of emittance growth with respect to initial (bottom).

tapered in length, and composed of 36 drift tubes. The first cell is 20.8 mm long, the last one 28.9 mm long. The average ZTT, taking into consideration the end-cells, is around 350 $M\Omega/m$. The beam from the RFQ was transversally matched with a triplet quadrupole focusing, and then accelerated in the IH structure with a constant synchronous phase of -12 deg. A 16 % margin in the IOT nominal power was kept, to take into account waveguides losses, so 84 kW are actually dissipated in the cavity walls.

The beam was transversally matched using a triplet focusing (Fig. 3.2 bottom). A relatively high synchronous phase of -12 deg was chosen only to facilitate the particles injection into the 3 GHz DTL at 10 MeV. Indeed, a much lower synchronous phase (5 to 10 deg) would have been needed to accept and control the particle from the RFQ. Due to its higher simplicity and robustness, a constant synchronous phase solution was adopted rather than the well known KONUS [60].

Concerning the longitudinal phase space, the Twiss α_z parameter of the RFQ beam was modified from 0 to 0.6 to improve the longitudinal matching. At the present stage, it has been assumed that this will be achievable with a different RFQ design [61]. Alternatively, one should consider to install a buncher cavity between the RFQ and the IH structure.

3.1.2 From 10 to 70 MeV

As it was demonstrated in Section 2.2 and 2.3.2, a IH-DTL solution is superior over a DTL from both an RF and a beam dynamics point of view. However, costs considerations led towards the

decision of accelerating particles from 10 MeV onwards with a 3 GHz DTL linac.

Three modules tapered in length have been designed, each composed of 9 accelerating tanks. The number of RF cells per tank goes from 5 in the first module, to 6 and 7 in the second and last modules respectively. This is done in order to increase the ratio of active acceleration length over the total length, taking advantage of the lower RF defocusing at higher particle momentum. The synchronous phase is constant and equal to -20 deg in all the three modules. A solution with an higher number of RF cells in the first module was studied, but it was not feasible due to the too strong RF defocusing.

In the first part of this linac section the ratio between active and total length is relatively low. The space for the PMQs, which are 30 mm long, has to be increased taking into account the space for the flanges. A minimum space of 70 mm was considered following discussions with colleagues. The PMQs considered for both TULIP and CABOTO were not designed by the author, and commercial ones were considered. The maximum gradient and internal diameter needed are 240 T/m and 8 mm. The proposed designs for TULIP and CABOTO could be modified if those values were not achievable by standard PMQs.

The main parameters of this linac section are summarized in Table 3.2.

Table 3.2 – TULIP DTL main parameters.

Module	Output energy [MeV]	Number of cells	Act. length [m]	Act./Tot. length	Avg. act. gradient [MeV]	Peak power [MW]	Avg. ZTT [MΩ/m]
1	20	5	0.78	0.53	13.6	1.9	75
2	40	6	1.31	0.64	16.2	3.7	94
3	70	7	2.05	0.74	15.6	5.7	88

The beam envelopes and emittance growth in this linac section are shown in Fig. 3.3.

Matching from a 750 MHz IH to a 3 GHz DTL

The beam matching between the 750 MHz IH and the 3 GHz DTL is one of the most critical parts of the project. In the longitudinal phase space there is a reduction of factor 4 in the phase acceptance, given by frequency increase. Concerning the energy acceptance, there is a factor 2 reduction, given by the square root dependence of λ, as shown in Eq. 3.1:

$$\omega_{max} = \sqrt{\frac{2qE_0T\beta^3\gamma^3\lambda}{\pi mc^2}(\phi_s\cos\phi_s - \sin\phi_s)} \tag{3.1}$$

However a factor $\sqrt{\beta^3\gamma^3}$ helps in increasing the energy acceptance, which was one of the motivation in delaying the jump at 3 GHz from 5 to 10 MeV/u. In particular, going from 5 to 10 MeV, the acceptance for protons increases of a factor 0.22. As a final remark on the longitudinal acceptance, an higher accelerating gradient E_0T would only slightly increase the

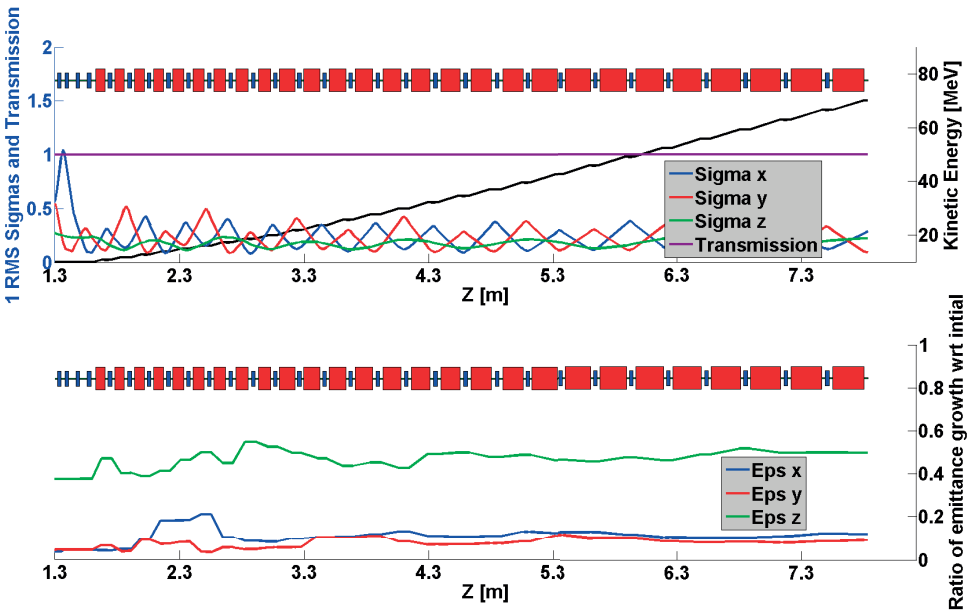

Figure 3.3 – Beam 1 σ RMS envelope through the TULIP DTL from 10 to 70 MeV (top) and ratio of emittance growth with respect to initial (bottom).

energy acceptance, given the square root dependence.

In the transverse phase space, the geometric emittance decreases of a factor $\beta\gamma$, so of about 50 % between 5 and 10 MeV. Nevertheless, while the RFQ is a bunching device, and it was specifically developed to inject particles into a 3 GHz structure, the IH is an accelerating structure, so it was not obvious at the beginning to be capable of reaching a good transition and matching at 10 MeV.

A 33 cm long transverse matching section with 4 PMQs was designed to make the transition from a triplet focusing system, used for the IH structure, to a FODO lattice. The Twiss parameters were matched so to have a phase advance of almost 90 deg in the DTL structures. A full transmission of the beam is reached, and the transverse emittance growth is well below 5 % at the end of the linac (Fig. 3.3). In the first linac sections there is a local transverse emittance growth up to 20 %, due to a residual initial mismatch. This effect cancels out later on.

In this section the PMQs reach the highest design gradients, with a maximum of 240 T/m, though also in the HG section values are above 230 T/m. However, in this matching section the beam envelopes are larger due to the triplet - FODO focusing transition. Having a 1 mm RMS sigma envelope, the quadrupole aperture radius has to be at least 4mm to transmit all particles. Thus, the PMQs in this section would have a maximum pole tip field of $240 * 0.004 = 0.96T$.

3.1.3 From 70 to 230 MeV

The protons are eventually accelerated up to 230 MeV in the high gradient linac.

For this section, two accelerating structures were considered, and they were both optimized in terms of high gradient. These are the BTW structure (Section 2.4.1) and the CCL structure (section 2.5).

The differences between a BTW and a CCL accelerating structure optimized for high gradient operations for a geometric β of 0.38 was discussed in Section 2.6. The conclusion of this comparison is an advantage of the CCL solution in terms of ZTT, and thermal power dissipation, thus maximum DF achievable. Considering the filling time, the CCL solution is comparable to the BTW solution when a RF circulator is installed.

Following the considerations of Section 2.6, the authors consider the BTW and the CCL solutions are ultimately even. However, we will review two designs, based on the two technologies, but comparable in length and number of elements. Before presenting the high gradient linac beam dynamics design, in the following Section we will review the theory of an energy varying beam line.

Maximizing the energy acceptance of a beam line

TULIP is based on the idea of varying the output beam energy in the range of what is needed for patient treatment. In case of protons, to reach the conventional range of penetration in water equivalent tissues, one needs proton ranging from 70 to 230 MeV. For cost and simplicity considerations, it has been decided to design a line with permanent magnets (PMQ), still reaching full transmission at all energies.

In the following, we derive the condition to maximize the energy acceptance of a beam line composed of permanent quadrupole, for a given lattice geometry. One can start from the basic beam dynamics equations that can be found in general particle accelerators book [43] [42].

The normalize transverse acceptance of a linac is given by:

$$A_n = \frac{\beta\gamma}{\beta^+} \cdot {R_{bore}}^2, \tag{3.2}$$

with β^+ maximum of the Twiss beta parameter, and R_{bore} bore aperture radius. For a given bore aperture R_{bore}, the linac transmission can be maximized by minimizing the Twiss betas. Also one can notice that the acceptance increases with the beam energy $\beta\gamma$, because the geometric emittance shrinks. This is valid under the assumption that the normalized emittance remains constant.

It is convenient to express the Twiss betas $\beta^{\pm}$ in terms of phase advance. The FODO theory,

even though not entirely correct when describing a linac, works well enough. The maximum and minimum Twiss beta over a FODO cell are then given by:

$$\beta^{\pm} = 2L\frac{(1 \pm \sin(\mu/2)}{\sin(\mu)} \tag{3.3}$$

Where L is the FODO length and μ is the transverse phase advance per cell.

In case of a magnetic line with PMQs, the transverse phase advance and the Twiss β_s seen by the beam vary with the output energy.

In a round beam, as the RFQ output, we have $\epsilon_x \approx \epsilon_y$, so the geometric dimension of the beam is given by $A = \pi \cdot R^2 = \pi \cdot (\epsilon_x \beta_x + \epsilon_y \beta_y)$. The beam size is minimized in case of phase advance of 90 deg, as one can verify by plugging Eq. 3.3 in the above expression. Having however a varying phase advance as a function of the energy, one needs to find the best compromise that maximize the acceptance in the range of energy of interest.

The optimum is found when the phase advance is 90 deg at the minimum beam line energy, and then decreases as the beam energy increases. The decrease has to be such that:

$$\frac{\beta^{+}_{E_{min}}}{\beta^{+}_{E_{max}}} = \frac{(\beta\gamma)_{E_{min}}}{(\beta\gamma)E_{max}} \tag{3.4}$$

which simply means that the beam envelope must have the same dimension in the two extreme cases at the end of the line. Since the β^{+} and the $\beta\gamma$ curves as a function of the final beam energy have a positive second order derivative, the worst conditions are found at the two extremes.

From Eq. 3.4, it is clear that the larger the momentum difference between the two energies that have to be transmitted through the beam line, the larger has to be its transverse acceptance. So CABOTO (Section 4), where the beam has to be varied between 100 and 430 MeV/u, needs an higher transverse acceptance than TULIP, for a given beam emittance.

In conclusion, one shall follow these steps in the lattice design:

- match transversally the beam for a 90 deg phase advance at the linac minimum energy section, in order to minimize the emittance growth;
- maximize the cumulative transmission at the minimum and maximum linac energy; the transmission in all other cases lies in between these two results;
- if there are losses, reduce the FODO length, or increase the beam aperture.

The high gradient BTW linac

A 18 accelerating structures linac was designed. The target gradient is 40 MV/m. The linac is approximately 6.2 m long, and accelerates the particles up to 230 MeV. The gradient chosen does not fully exploit the limit at which the structure has been designed (50 MV/m) to maintain a safety margin in terms of BDR. In addition, the compactness goal of the structure was already reached with a 40 MV/m gradient. Finally, this 20 % reduction in gradient translates into a 36 % reduction in RF thermal load into the structure, allowing a higher duty cycle of 0.01 %. The synchronous phase is -15 deg in all the accelerating structures, that are all composed of 12 RF cells. The ZTT increases for the higher energies cavities, and so does their length. Interestingly, it has been possible to have an almost constant accelerating gradient throughout the different cavities with an approximately constant peak power consumption per cavity of 5 MW.

The main parameters of this linac section are summarized in Table 3.3.

Table 3.3 – TULIP BTW linac main parameters.

Cavity	Output energy [MeV]	Act. length [m]	Avg. act. gradient [MeV]	Peak power [MW]	Avg. ZTT [MΩ/m]
1	76.9	0.187	37.5	5.06	52
2	84.2	0.195	38.0	5.12	55
3	91.7	0.203	37.7	5.07	57
4	99.4	0.210	37.7	5.08	59
5	107.4	0.218	37.7	5.08	61
6	115.7	0.225	37.7	5.05	63
7	124.3	0.231	37.7	5.05	65
8	133.1	0.239	37.7	5.11	67
9	142.1	0.246	37.6	5.08	68
10	151.3	0.258	37.6	5.12	70
11	160.8	0.258	37.6	5.10	71
12	170.5	0.265	37.5	5.10	73
13	180.4	0.270	37.4	5.12	74
14	190.5	0.276	37.4	5.13	75
15	200.8	0.282	37.2	5.13	76
16	211.2	0.287	37.1	5.15	77
17	221.8	0.293	36.9	5.12	78
18	232.5	0.298	36.8	5.10	79

Varying the phase and amplitude of the RF power in each accelerating structure allows for a smooth variation of the final energy. For this reason, a single coupler solution has been studied (see Section 2.6).

The emittances and beam envelopes are shown in Fig. 3.4 and 3.5 for the two extreme cases of no acceleration and full acceleration, respectively.

The matching section between the DTL and the BTW linac was considerably easier than the 10 MeV transition. The solution proposed here comprises 4 PMQs and a buncher cavity to improve the longitudinal matching. This is just a temporary solution, given that the MEBT, as shown in Fig. 1.12, is much longer and involves also dipoles. This part has not been studied

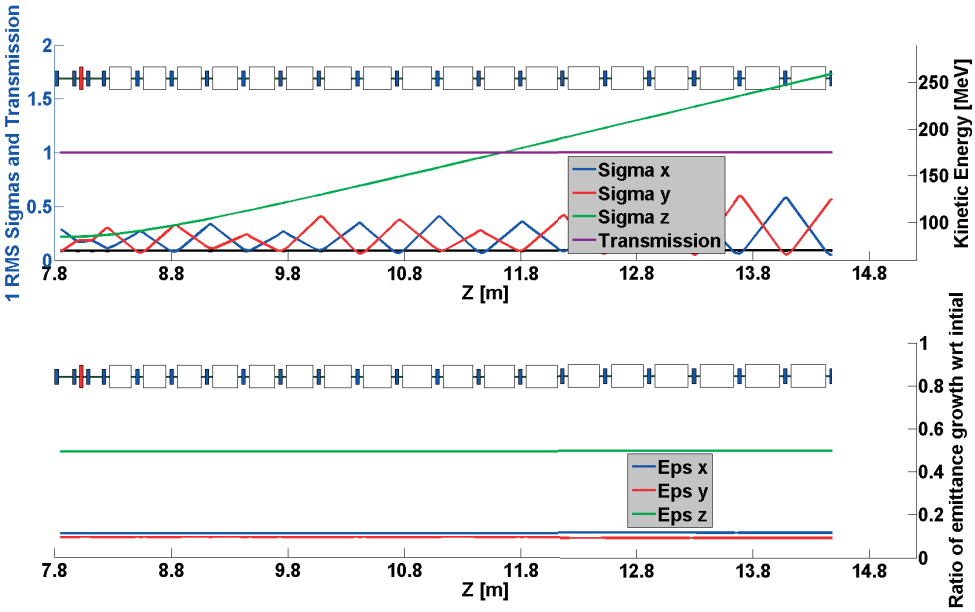

Figure 3.4 – Beam 1 σ RMS envelope through the TULIP BTW linac with no acceleration after 70 MeV (top) and ratio of emittance growth with respect to initial (bottom).

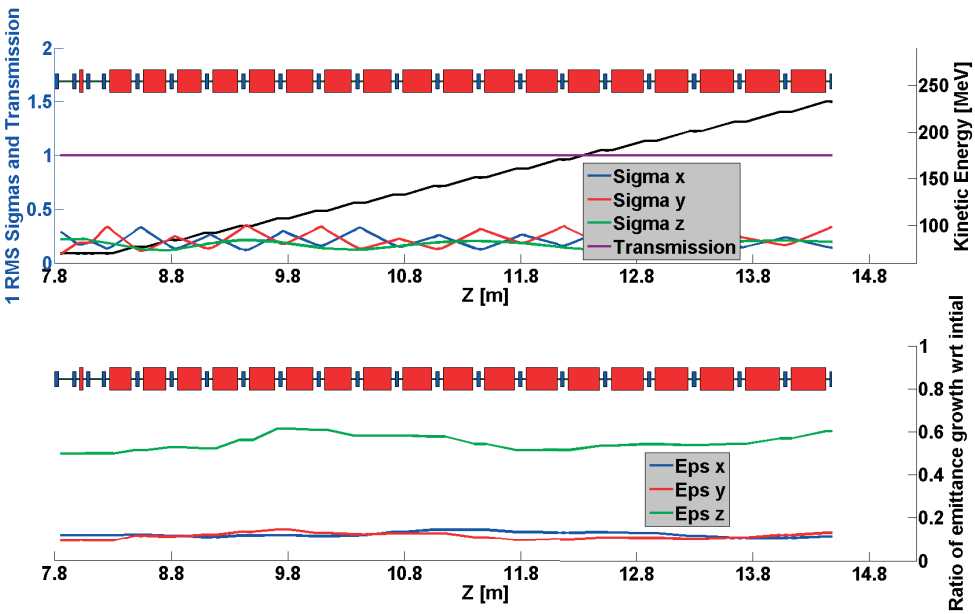

Figure 3.5 – Beam 1 σ RMS envelope through the TULIP BTW linac with full acceleration up to 230 MeV (top) and ratio of emittance growth with respect to initial (bottom).

yet since the mechanical design has yet to be finalized.

The high gradient CCL linac and comparison with the BTW one

The design above presented reaches full transmission of the particles between 70 and 230 MeV, but is however quite at the limit in terms of maximum Twiss beta. All the BTW accelerating structures are 12 cells long. This means that it is possible to obtain an exactly equivalent CCL design, composed of 18 accelerating structures, 10 cells long.

As a result, the difference between the two solutions translates in a different peak power consumption, accordingly to ZTT difference reported in Fig. 2.60. This difference is about 7 % at 70 MeV and gets null at 230 MeV.

3.2 Beam dynamics in a *cyclinac* solution

This section discusses the first design of a *all-linac* solution for the TULIP project. As mentioned, the majority of the studies carried out in the past focused instead on a *cyclinac* solution. Here a detailed beam dynamics study of this concept is presented, in order to point out the major differences.

The 11th accelerating structure of the DTL linac accepts as input particles at 24 MeV. It has been supposed to replace the previous linac section with a commercial 24 MeV cyclotron. This would result in a bigger transverse emittance, and a continuous beam for the 3 GHz RF frequency, as discussed in Section 2.3.2. The transverse emittance can be collimated, however the beam cannot be chopped at 3 GHz. As a result, the beam will be lost in the linac section, with losses that are proportional to the ratio synchronous phase - 360 deg . This situation has been simulated, and the results are presented in Fig. 3.6 and 3.7

The losses are concentrated in the first 3 m of this design, causing strong material activations in all the area. However, here we would like to draw the reader attention on the emittance growth. While the transverse one is "controlled" by the linac acceptance, so it does not grow uncontrolled, the longitudinal phase space is heavily influenced.

These two aspects reflect into an higher complexity and costs of the beam transport line from the linac output to the patient. The increase in normalized transverse emittance requires bigger magnets aperture, therefore eventually costs. On the other hand, the increased longitudinal emittance results in a strongly variable energy spread as a function of the beam output energy. This impacts on the design of the magnetic channel, which needs a high momentum acceptance to control the dispersion.

In Fig. 3.8 one can notice the difference just explained. The transverse Twiss parameters are instead comparable in magnitude for the two solutions.

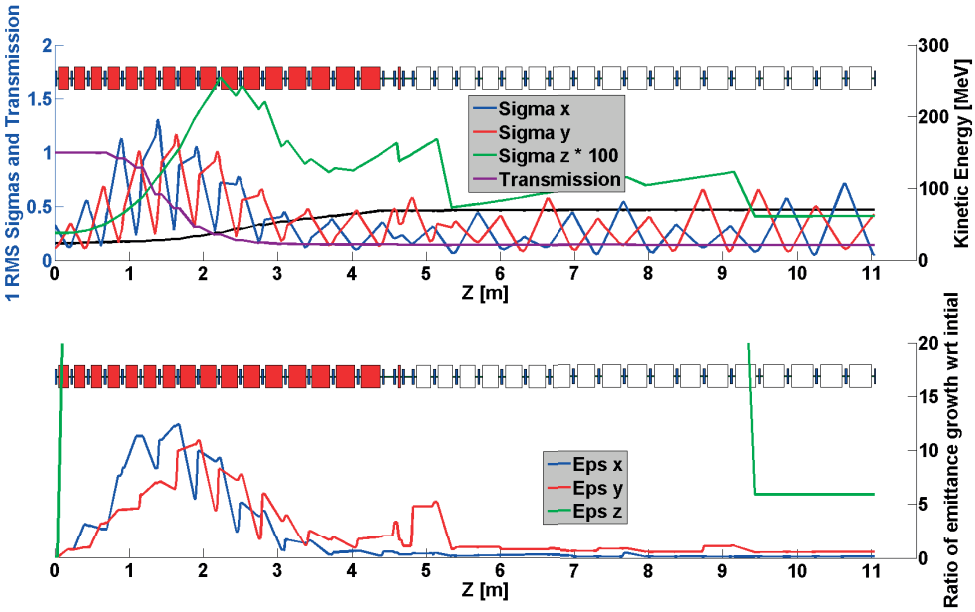

Figure 3.6 – Beam 1 σ RMS envelope through a *cyclinac* TULIP solution with no acceleration after 70 MeV (top) and ratio of emittance growth with respect to initial (bottom)

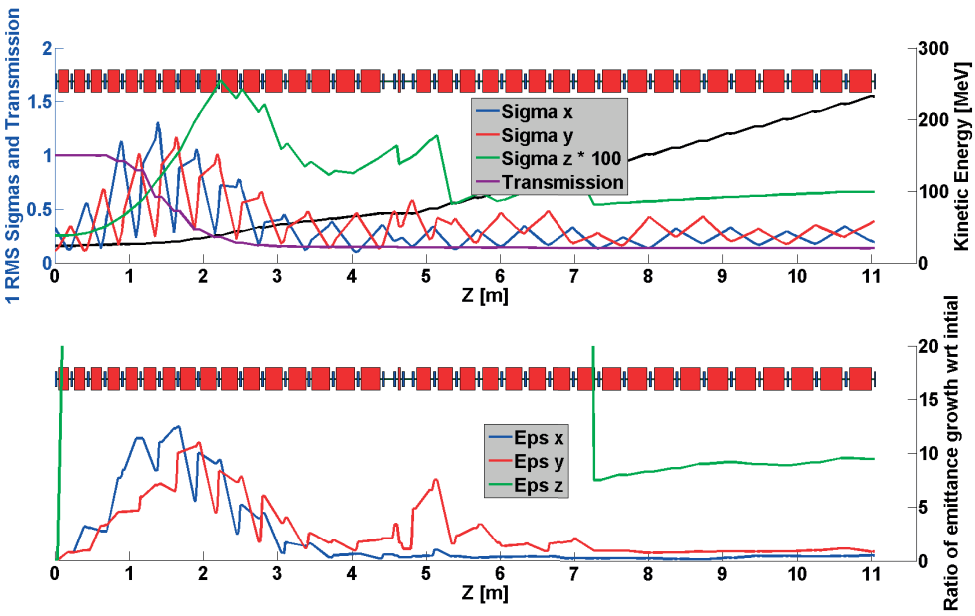

Figure 3.7 – Beam 1 σ RMS envelope through a *cyclinac* TULIP solution with full acceleration up to 230 MeV (top) and ratio of emittance growth with respect to initial (bottom)

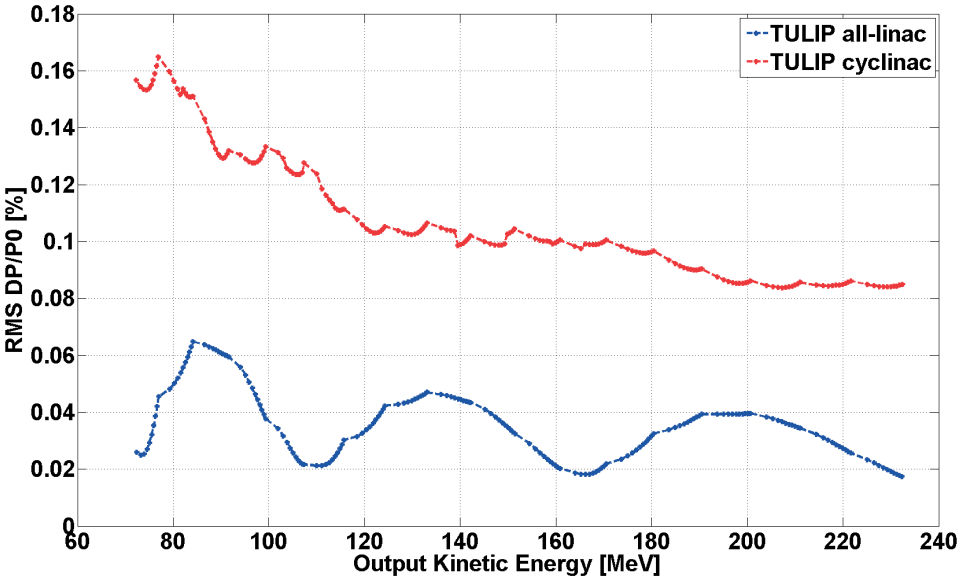

Figure 3.8 – Beam output energy spread in TULIP *all-linac* and *cyclinac* as a function of the final kinetic energy

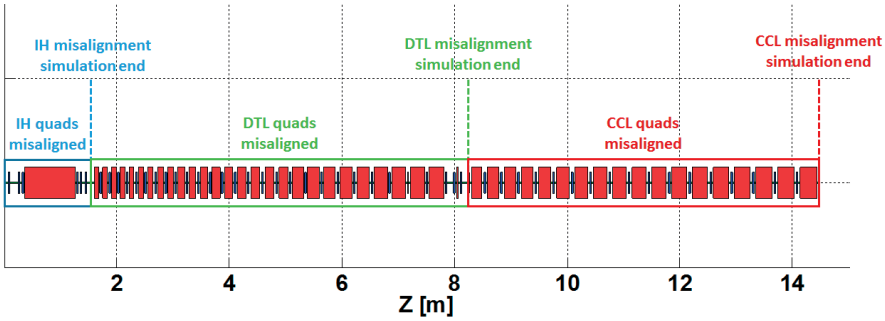

Figure 3.9 – Methodology adopted in the TULIP quadrupole misalignments study.

3.3 Quadrupole misalignments

The tolerance to quadrupole misalignments has been studied considering the three linac sections separately, in order to untangle possible criticality and to highlight the more sensitive areas. So, for example, the CCL results referred to the misalignment of the CCL quadrupoles only, assuming the previous quadrupoles correctly aligned. On the other hand, the IH results refer to the analysis up to the beginning of the DTL linac. In total, the misaligned quadrupoles are 7 for the IH section, 31 for the DTL section, and 19 for the CCL section. The methodology adopted is summarized in Fig. 3.9.

The quadrupoles were misaligned with an x/y translation first, and then with an x/y rotation. Following the CLIC methodology, the quadrupoles are rotated around the longitudinal mid point. Lastly, the tolerances in terms of quadrupole gradients were also studied. The misalign-

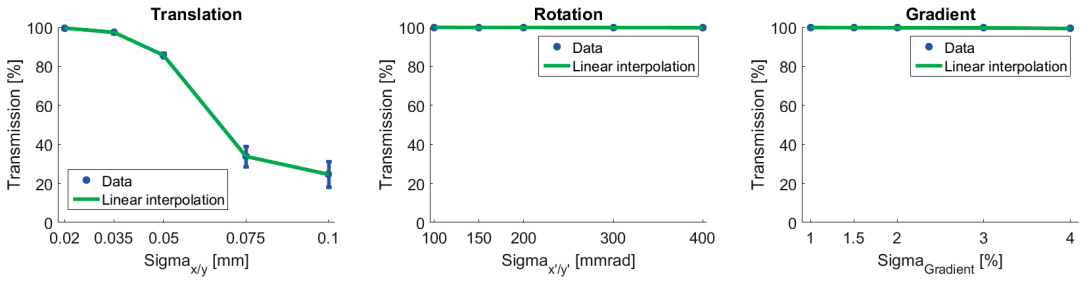

Figure 3.10 – Transverse and rotational quadrupole misalignment study for the IH section of TULIP. Gradient tolerances to the right.

ment follows a Gaussian distribution, and the results are presented as a function of the $\sigma_{x/y}$ and $\sigma_{x'/y'}$ considered. For simplicity, the σ along x and y were considered equal. Lastly, the quadrupoles gradient was also studied.

The analysis followed a Monte-Carlo approach, with 100 simulations (N) for each experiment. For each σ, the correspondence final mean expected value $E[x]$ and percent relative standard deviation $PRSD$ as error bar are presented:

$$E[x] = \frac{\sum_{i=1}^{N} x_i}{N}, \tag{3.5}$$

$$\sigma^2 = \frac{\sum_{i=1}^{N} (x_i)^2 - (E[x])^2}{N}, \tag{3.6}$$

$$PRSD = 100 \cdot \frac{\sqrt{\sigma^2}}{\sqrt{N} \cdot E[x]}^{2}, \tag{3.7}$$

The studied variable is the final beam transmission, in percent. The final emittance is not presented since it is biased by the losses. The results are presented in Fig. 3.10 3.11 3.12 for the three linac sections.

The most sensitive section is the DTL one (Fig. 3.11). This was somehow expected, given the efforts put in the matching section between the 750 MHz IH and the 3 GHz DTL part, discussed in Section 3.1.2. If one considers a 95% total transmission as a threshold, and under the assumption of a Gaussian distribution of the quadrupole misalignments, one would need a transverse misalignment smaller than 0.035 mm for the IH quadrupoles, of 0.02 mm for the DTL one, and of 0.035 mm for the CCL one. These are very strict requirements, and are a consequence of the design proposed, that intentionally explored the limits in terms of maximum gradient and compactness.

[2] In Monte Carlo analysis, the error goes with the square root inverse of the number of experiments.

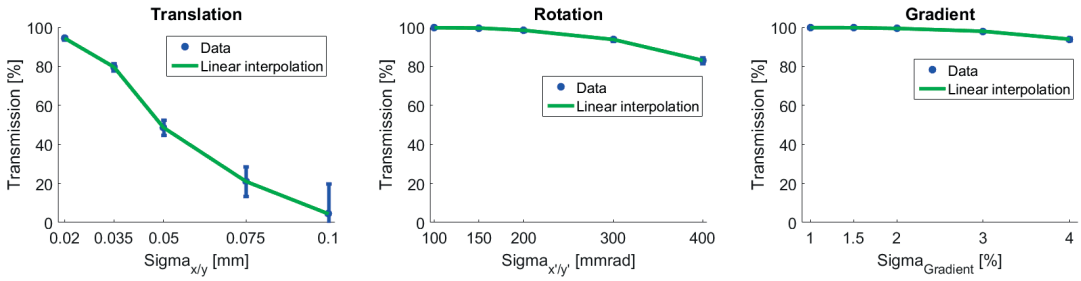

Figure 3.11 – Transverse and rotational quadrupole misalignment study for the DTL section of TULIP. Gradient tolerances to the right.

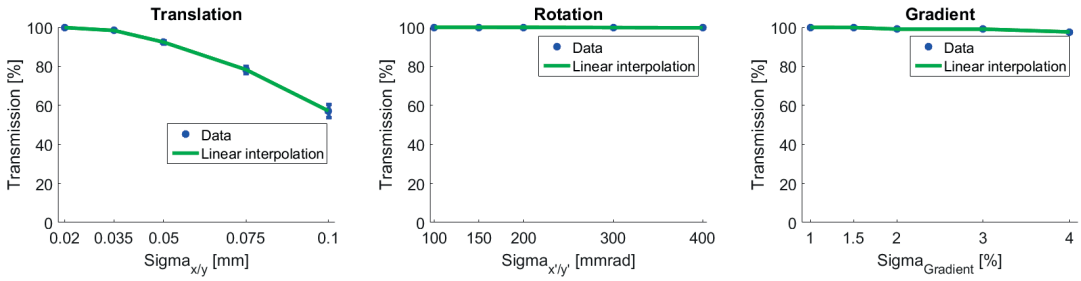

Figure 3.12 – Transverse and rotational quadrupole misalignment study for the CCL section of TULIP, when all the accelerating cavities are at the nominal voltage. Gradient tolerances to the right.

A way to ease these requirements would be to increase the matching section between IH and DTL, adopting one or more buncher cavities. Or one would need to increase the linac bore apertures.

Alternatively, one should consider the installation of beam positioning monitors (BPM) and steering magnets (SM) along the linac. The number and location of these should be decided following, for example, the procedure discussed in [62] for CERN Linac4.

3.4 Start-to-end simulation: from 5 MeV to 230 MeV

The first *all-linac* solution of the TULIP project has been presented.

The beam dynamics linac design features full transmission and minimized emittance growth, and it has been accomplished with full tracking of the particles from the RFQ output till 230 MeV, using RF EM field maps for the accelerating structures computed with HFSS. This is unique for such a long linac. The effort is justified by the peculiar cavities considered, that as we discussed, show di-polar components, asymmetries and travelling wave regimes that cannot be simulated with standard tracking codes. This is the reason why the novel tracking code RF-Track has been developed explicitly for this project (see Appendix A).

Fig. 3.13 shows the main linac design parameters. A graphical way of reporting this data was

used, with the aim of having a fast-to-read and complete source of information. It is worth commenting again a few characteristic of the design. The linac is composed by a IH 0.9 m long cavity, followed by a DTL, a buncher cavity, and the high gradient CCL/BTW. The accelerating gradient step is clearly observable in Fig. 3.13 top left. A similar way to discuss this difference is by considering Fig. 3.13 bottom left. Here a key characteristic of this design is reported, i.e. the peak power consumption distribution along the linac. The combination of high gradient and lower ZTT, given by the high gradient RF optimization, leads to a major concentration of the peak power installed, approximately 90% of the total, in the high gradient section. The first part of the linac, up to the buncher cavity, was optimized in terms of ZTT. In Fig. 3.13 top right, one can notice the ZTT trend along the structures. In particular, the DTL ZTT optimum saturates well before 70 MeV, due to the RF cells getting too long. As a last piece of information, the RF cell length and diameter is reported in Fig. 3.13 bottom right. This is another way to present the ZTT behaviour of the linac. The DTL section, being 2π mode, gets too long towards the end of the linac, and so it looses in ZTT. Interestingly, the resonant mode for the optimum ZTT is obtained mostly by varying the gap, while the overall cell diameter is approximately constant throughout the linac.

Table 3.4 summarizes similar information in a more common numeric form.

The linac dissipated power, rather than the total RF power to be installed. This choice is motivated by the uncertainty on the exact power losses occurring across the RF network between klystron and accelerating structures. For instance, as discussed in Section 2.4.6, there could be a significant decrease in the waveguide losses whether a BTW solution were chosen upon a CCL one. If, however, one is interested in an estimation of the total installed RF peak power, one could increase the values of Table 3.4 of a factor 10%, being optimistic, or 20%, being more conservative. In this latter case, one should account for approximately 125 MW RF peak power for the TULIP project. The only exception is the RFQ, where the total installed power is reported, being a design already finalized and not studied by the author.

Table 3.4 – TULIP *all-linac* - A summary.

Linac Section	Operating Freq. [MHz]	Output En. [MeV]	Avg. Grad. [MV/m]	Synch. Phase [deg]	Act. Length [m]	Tot. Cum. Length [m]	Avg.ZTT [MΩ/m]	Peak Power [MW]
RFQ	750	5	2.6	15 (final)	2	2	38	0.4[3]
IH	750	10	5.7	12	0.9	3.3	350	0.084
DTL	2998.5	70	15.5	20	4.1	9.8	86	11.3
BTW-CCL	2998.5	70-230	37.7	15	4.4	17.5	68	91.7

The beam dynamic design is summarized in Fig. 3.14 for the two extreme cases of no acceleration and full acceleration. One can notice the beating in the beam envelopes, especially after the IH-DTL transition. This part was explained in detail in the previous Sections, but as a reminder, the two critical aspects were introduced by the abrupt change in accelerating gradient, observable by the longitudinal phase advance increase (green curve), and by the change in operating frequency, from 750 MHz to 3 GHz.

[3] total with losses

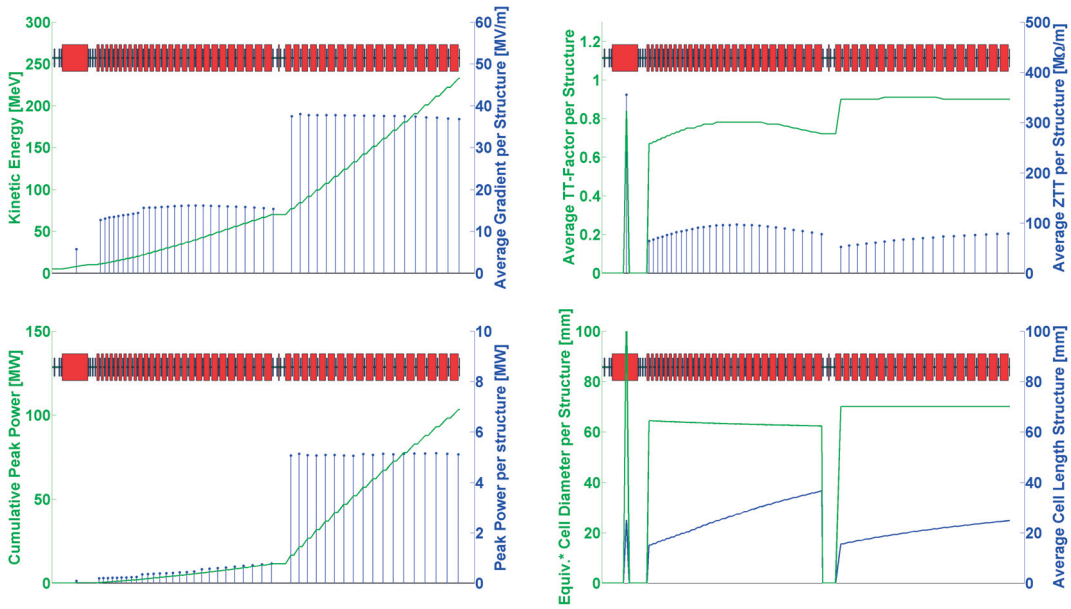

Figure 3.13 – TULIP *all-linac* main accelerating parameters.

Continuing on along the linac, one can observe the difference final beam envelopes, in the two cases of no acceleration and full acceleration. As discussed in Section 3.1.3, an optimized line should have the same beam envelopes in this two extreme cases. However, some residual mismatch a the beginning of the line, together with a transverse phase advance too high, thus penalizing for the no acceleration case, are the reasons of this difference. Nonetheless, the main goals of the project, i.e. full transmission and emittance growth control in a compact proton linac, have been achieved.

Finally, Fig. 3.15 shows the classic representation of the transverse and longitudinal envelopes mirrored around the centre. The case of no acceleration after 70 MeV is easily recognizable by the growth of σ_z - in green colour in the plot - as soon as the particles are not accelerated anymore.

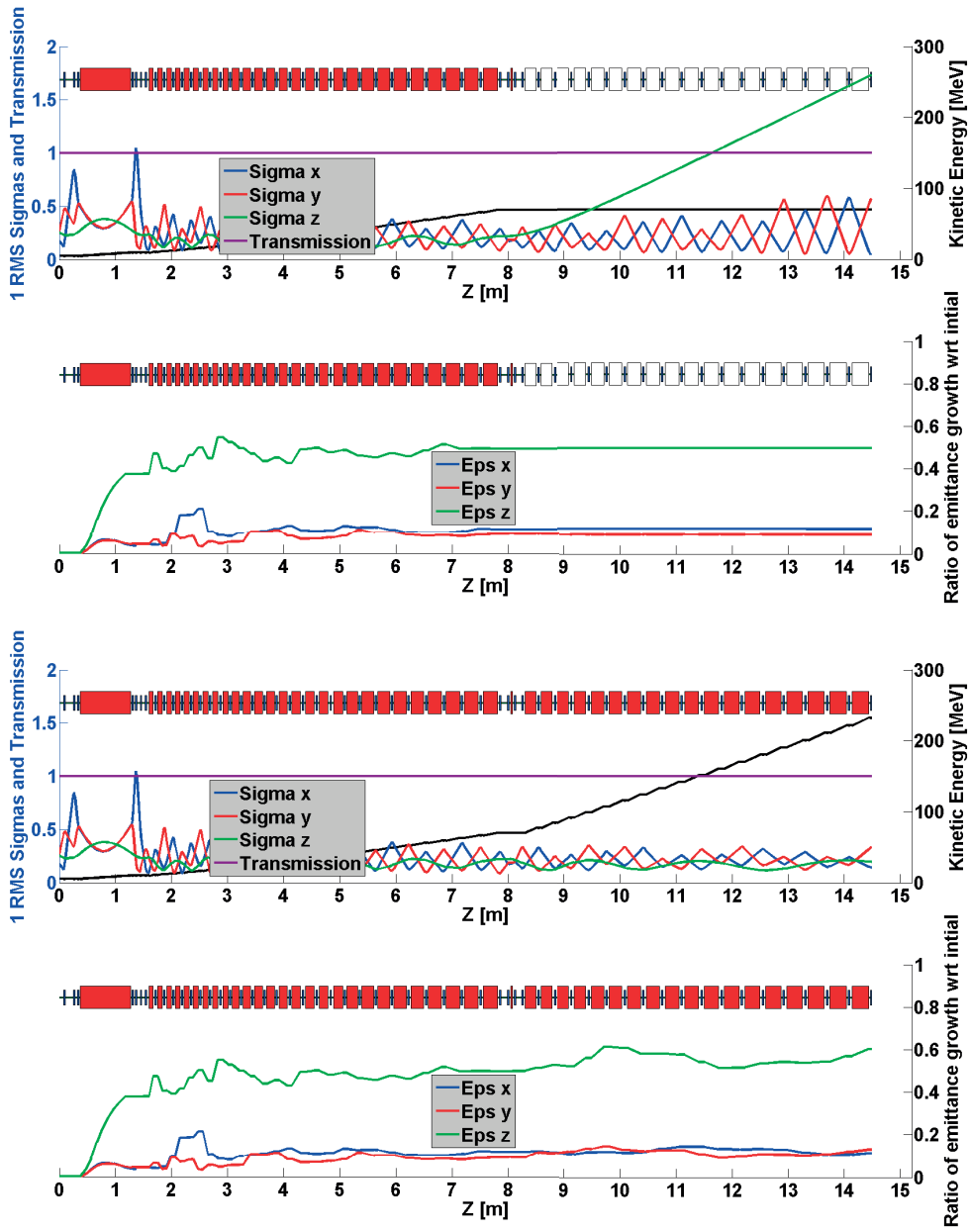

Figure 3.14 – Beam 1 σ RMS envelope through the TULIP *all-linac* solution and ratio of emittance growth with respect to initial. No acceleration after 70 MeV (top) and full acceleration up to 230 MeV (bottom).

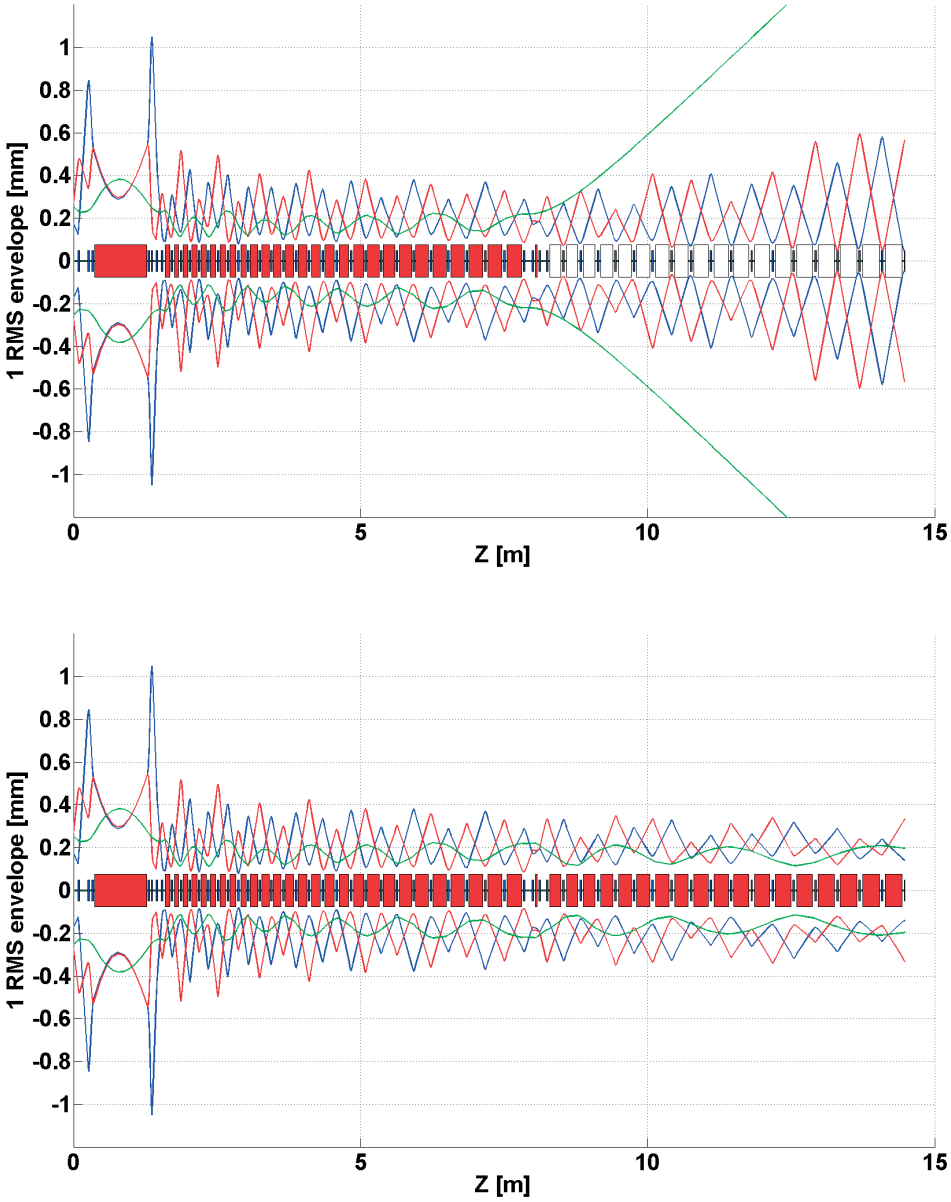

Figure 3.15 – The 70 MeV (top) and 230 MeV (bottom) beam envelopes along TULIP *all-linac*. 1 RMS σ_x (red), σ_y (blue) and σ_z (green).

4 CABOTO: a high-efficiency linear accelerator for carbon ion therapy

CABOTO differs substantially from TULIP. Not just because of type of particles accelerated, carbon ions instead of protons, but mostly because of what this choice implies in terms of design.

To obtain the same equivalent penetration in water-equivalent tissue of a 230 MeV proton beam, one needs a 430 MeV/u carbon ion beam, according to Eq. 1.3.

To this difference, one shall add the difference in q/m. In the best case scenario, a ion source is capable of delivering fully stripped carbon ions, thus having a 0.5 q/m. In other words, it is four time more challenging, in terms of either accelerating gradient, linac length or a combination of the two, to accelerate carbon ions with respect to protons for the same tissue penetration.

If one would simply take the TULIP design, and maintain the same overall dimensions, one would need a 4 times higher accelerating gradient. Neglecting for the moment BD and thermal limitations, such design would result in a total peak power 16 times higher than the TULIP one, due to the square dependence between gradient and power. This is clearly not feasible: in case of carbon ion linac for hadron therapy, one cannot design a realistic facility with compact footprint. For this reason, CABOTO is a combination of longer linacs and lower accelerating gradients with respect to TULIP.

The lower accelerating gradients permitted to increase the linac efficiency. To achieve this goal, two main directions were followed. First of all, a more aggressive optimization of the nose cell region, with benefits for TT and ZTT. Second of all, the linac design aimed at a reduced bore aperture, though always maintaining a 100% transmission as first goal. As discussed in Section 2.7.3, the bore aperture reduction is the most effective way to increase the ZTT.

A new idea from TERA Foundation and Prof. Amaldi proposes the use of He. In this case, there would be only a factor 0.5 q/m of difference between He and proton beams. In fact, from Eq. 1.3, one can notice that the stopping power is the same between He and protons. An adaptation of the CABOTO design in view of an He facility is discussed in Section 4.4.

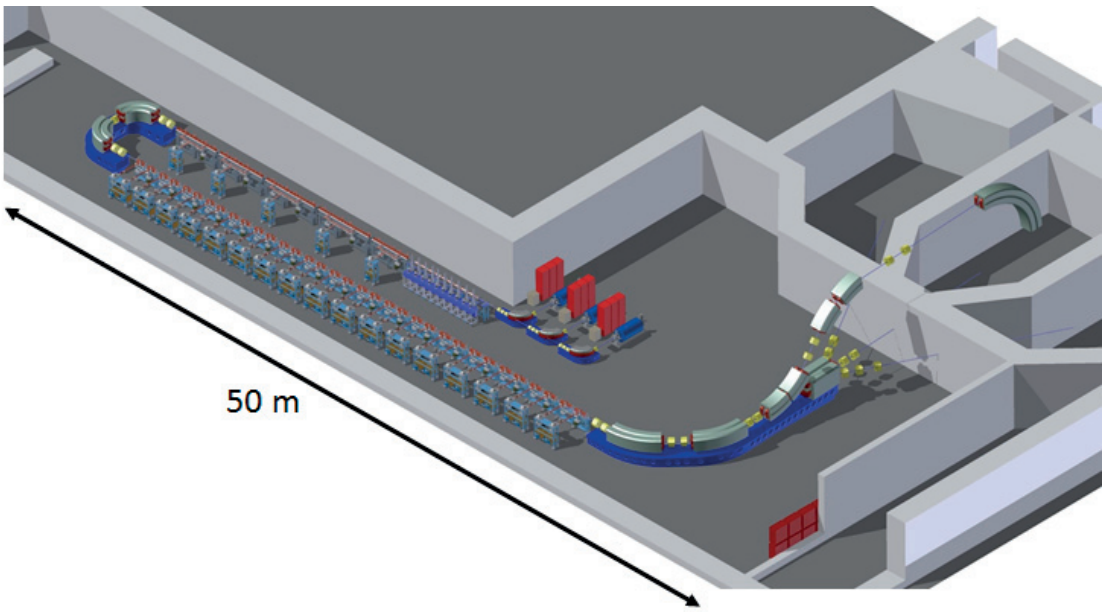

Figure 4.1 – Sketch of CABOTO *all-linac*. In the sketch, one can observe the separation in two branches of the proposed design. The CCL linac section is updated with the number of cavities and with the longitudinal dimensions proposed in the present Chapter. Instead the section from the RFQ to the DTL at 100 MeV/u is not up to date.

Table 4.1 – Key parameters of the *all-linac* CABOTO solution.

Type of structure	Output energy [MeV/u]	Active Length [m]	Peak power [MW]
750 MHz RFQ	2.5	ND	ND
750 MHz IH	10	2.5	0.257
3 GHz DTL	100	11.7	26.3
3 GHz CCL	100-430	23.1	189.1

The C-11 acceleration, of interest in different projects arising worldwide [63], has not been studied, but it would be possible. In fact, to maintain the synchronous acceleration of the beam, one could reduce the accelerating gradient of around 8%, according to the ratio of q/m $\frac{6/12}{6/11} = 11/12$.

4.1 General layout

The general layout of CABOTO is shown in Fig. 4.1. Not all the dimensions are up to date with the design proposed in this thesis, but Fig. 4.1 helps in discussing the general layout.

To reduce the footprint, the linac is split into two branches of equal length. The ion sources, RFQ, IH (Section 2.2) and DTL (Section 2.3) shall form one branch, and the CCL (Section 2.7) the other one. Table 4.1 summarizes the main parameters of the linac design.

The bottleneck is represented by the CCL section, that has to boost C6+ from 100 MeV/u to 430 MeV/u, thus an energy gain of 660 MeV. For this Section, an average accelerating gradient of 30 MV/m was chosen, following power consumption considerations that will be discussed further on.

This choice results in an approximately 30 m long CCL section, which then represents the target for the other branch. Given that ion sources, RFQ and IH cavities are more driven by beam dynamics and power consumption optimization, the length constraint reflects mostly in the accelerating gradient of the DTL linac, resulting in an average value of 15 MV/m. As discussed in Section 2.3.1, this higher gradient with respect to TULIP, together with a possible higher DF, likely will call for a drift cooling system design.

As a final comment, the 100 MeV/u bend was chosen on purpose. In fact, modulation of the beam energy should start at this level, which is equivalent to the 70 MeV of protons, as one can verify from Eq. 1.3. This is convenient, since the beam momentum will change just after the 180 deg bend, thus there dipoles and quadrupoles can have a static field.

In conclusion, the CABOTO design is composed of three sections, that have been studied by the author:

- four 750 MHz IH cavities, from 2.5 MeV/u to 10 Mev/u;
- a 3 GHz DTL, from 10 MeV/u to 100 MeV/u;
- a 3 GHz HE CCL, from 100 MeV/u to 430 MeV/u.

Prior to the IH cavities, it has been assumed that a 750 MHz RFQ will deliver 2.5 MeV/u C6+ beam with similar emittance with respect to the proton RFQ [32], after a discussion with one of the designer of the proton RFQ [61]. The project of a 750 MHz 1/2 q/m RFQ is currently under study by the same group at CERN.

Each of these sections is discussed separately in the following.

Main advantages of CABOTO over synchrotron based C ions solutions

Current carbon ion therapy facilities worldwide are only based on synchrotrons. The absolute winning technology for proton therapy, cyclotrons, so far failed in dealing with the higher momentum needed by carbon ions for medical purposes. Probably the best known effort in this regard, IBA C400 [19], is under study since many years, but prototypes have not been delivered yet.

Together with the fast energy modulation advantage discussed in Section 1.2, a carbon ion linac would have two other main advantages over a synchrotron.

The first one is the final beam current. Final of $6 * 10^{10} C^{6+}$ per second, which is around two order of magnitude higher that what you get in a synchrotron. This advantage could be exploited in two ways: one could simply propose a machine with an higher current, thus capable of delivering an higher dose and so likely advantageous from a medical point of view. Alternatively, one could collimate the beam output even further, so to reach a current equivalent to state-of-art synchrotron solutions. In return, this would allow to decrease even further the bore aperture, so ultimately the RF power consumption of the facility.

The second advantage is the average power. Here a comparison between the particle accelerator power is proposed. CABOTO has total peak power of approximately 240 MW. Assuming a $1 * 10^3$ DF, one would have an average power of 240 kW. For comparison, the MedAustron synchrotron has an average power during an high energy extraction of approximately of 700 kW for quadrupoles, sextupoles and correctors, and of 1000 kW for the dipoles [64]. In addition, the power required by the injection linac is not counted here. As a final remark, since linacs have a faster treatment time over synchrotrons, also their average energy consumption per treatment is lower.

4.1.1 From 2.5 MeV/u to 10 MeV/u

For the linac design described this section, the experience gained in the corresponding TULIP part was very valuable.

Here, a total of 15 MeV energy gain is needed, while in TULIP just 5 MeV were required. To fill this gap, it has been decided to consider three 100 kW IOTs, and to increase the active length by a factor 3. In fact, from Eq. 2.6, to a factor three increase in the energy gain, it corresponds, for the same shunt impedance, a factor 3^2 increase in the product of the dissipated power times the cavity length.

Another possible solution is to increase the shunt impedance, but this would have been only possible by reducing the bore aperture, since the IH cavity has been already optimized in terms of ZTT.

The initial, straightforward, choice of considering three IH cavities, with the same gradient and length as the TULIP IH cavity, did not guarantee the full transmission of the beam, due to the RF defocusing inverse dependence on the particle momentum. So the first IH cavity was actually split into two cavities, both considered to be powered by the same IOT.

In summary, the design proposed comprise four IH cavities, as reported in Table 4.2.

There is a little lower margin, in terms of peak power, with respect to the TULIP design. This because the total active length of the 4 cavities is not exactly three time the TULIP IH cavity length, so this was compensated with a slightly higher accelerating gradient and power consumption. Also, higher synchronous phases were chosen here with respect to TULIP (12 deg). Rationales of this choice is discussed afterwards.

Table 4.2 – CABOTO IH section main linac parameters.

Cavity	Output energy [MeV]	Number of cells	Act. length [m]	Avg. act. gradient [MeV]	Synch. phase [deg]	Peak power [MW]	Avg. ZTT [MΩ/m]
1	3.75	20	0.33	7.6	8	39	487
2	5	20	0.38	6.7	18	40	432
3	7.5	36	0.82	6.4	18	90	372
4	10	36	0.98	5.3	16	88	316

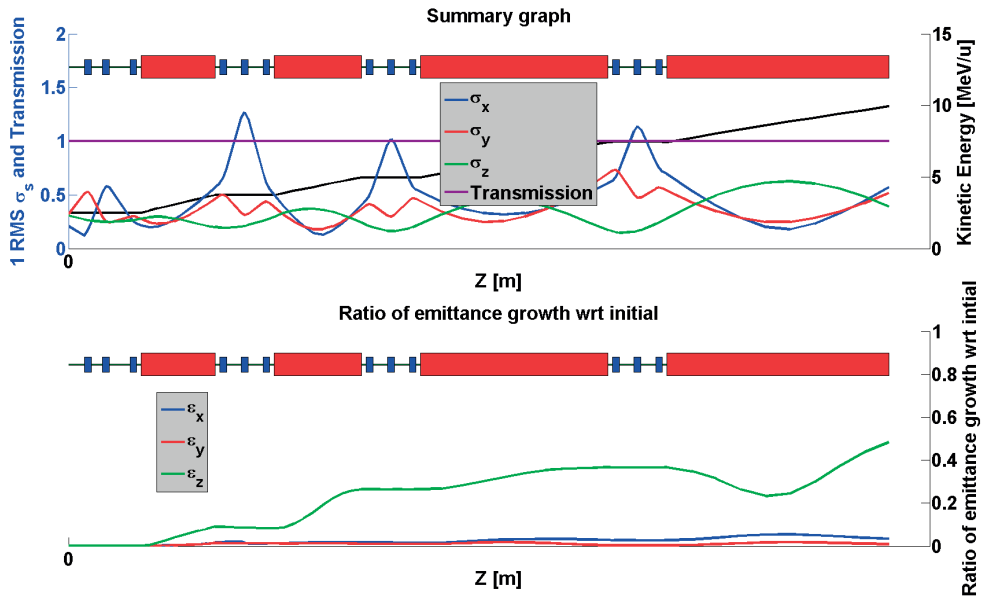

Figure 4.2 – Beam 1 σ RMS envelope through the CABOTO IH linac from 2.5 to 10 MeV/u (top) and ratio of emittance growth with respect to initial (bottom).

As discussed in Section 2.2.5, the overall efficiency of an IH cavity is a function, amongst the other parameters, of the number of RF cells. In particular, the higher is this number, the closer is the overall ZTT to the regular cell one, since the effects of end-cells are less important. Cavity 1 and 2 would need a specific RF design with an RF coupler between the two to reduce the RF losses, as in many IH cavities worldwide. The RF design did not reach this level of detail, and this topic is left open to further studies.

The beam dynamics study of the IH cavities were driven by the main goal of reaching a full beam transmission, together with a minimized emittance growth. The design was also influenced by the 10 MeV/u change from a 750 MHz linac to a 3 GHz one, as for the TULIP design. A longitudinally convergent beam is in fact needed at the output of the 750 MHz IH cavities to allow the design of a matching section without adopting buncher cavities.

A fairly low synchronous phase of 8 deg was chosen for the first IH cavity. This helped the longitudinal matching and limited the RF defocusing, allowing an higher degree of freedom in the following cavities settings.

Cavities 2, 3 and 4 have a synchronous phase of 18, 18, and 16 deg respectively. Here the triplet focusing adopted in the TULIP IH cavity was abandoned for an asymmetric focusing. This choice allows to match in a shorter length the transverse phase space to the FODO acceptance of the DTL. As for the TULIP design, the matching section between the IH cavities and the DTL structures is the crucial point of the beam dynamics design. The 16 deg choice for the last cavity is motivated by the fact that the beam is already longitudinally convergent at the exit of the third cavity. A lower synchronous phase, thus a lower RF defocusing, allows a less transversally divergent beam, easing the matching to the FODO lattice of the DTL.

The matching sections are all composed of 3 quadrupoles. As for the TULIP design, a maximum quadrupole gradient of 240 T/m was considered.

The beam envelopes and emittances of this section are summarized in Fig. 4.2. One could notice a bit of asymmetry in the triplet focusing. This was found to help in decreasing the longitudinal space for a triplet focusing to a FODO focusing transition. With respect to the TULIP matching at 10 MeV, the CABOTO case is a bit more difficult, since the 0.5 charge over mass of each nucleon decreases the energy acceptance as shown in Eq. 3.1.

4.1.2 From 10 MeV/u to 100 MeV/u

Like the IH cavity, also the DTL section could not be improved from RF point of view, being already optimized in terms of ZTT. The choice then was to consider a constant number of 8 RF cells per structure, with a 90 deg transverse phase advance, so to have a beam envelope reduction with the particles momentum. For comparison, the choice adopted in the TULIP project, were dimensions are the main issue, was to increase the number of RF cells in the DTL modules at higher energies, so to increase the active to total length ratio, and so to reduce the overall dimensions. In TULIP the number of cells per DTL tank varied from 5, at 10 MeV/u, to 7 at 70 MeV/u (see Table 3.2). As discussed with Eq. 2.17, the lower q/m permits to have longer structures at 10 MeV/u in CABOTO.

The resulting beam envelope, simulated with the code discussed in Appendix A.1, is decreasing (Fig. 4.3). This tapered bore aperture has been applied to the RF design, though applying a constant conservative coefficient throughout the linac. A gain of approximately 12% in ZTT, with respect to the constant 2.5mm design used in TULIP, has been reached (Fig. 2.25).

The gain in ZTT is considerable. However, it acts on a linac section that accounts for approximately 15% of the total peak power of the project, as shown in Table 4.5. The full benefits of the bore aperture reduction will be evident in the following CCL section, from 100 to 430 MeV/u.

For this section, a constant synchronous phase of 18 deg was chosen. The linac is composed of 50 accelerating structures, hereafter grouped in 5 modules in Table 4.3.

In order to obtain a 90 deg phase advance in this section, the quadrupole strength is higher

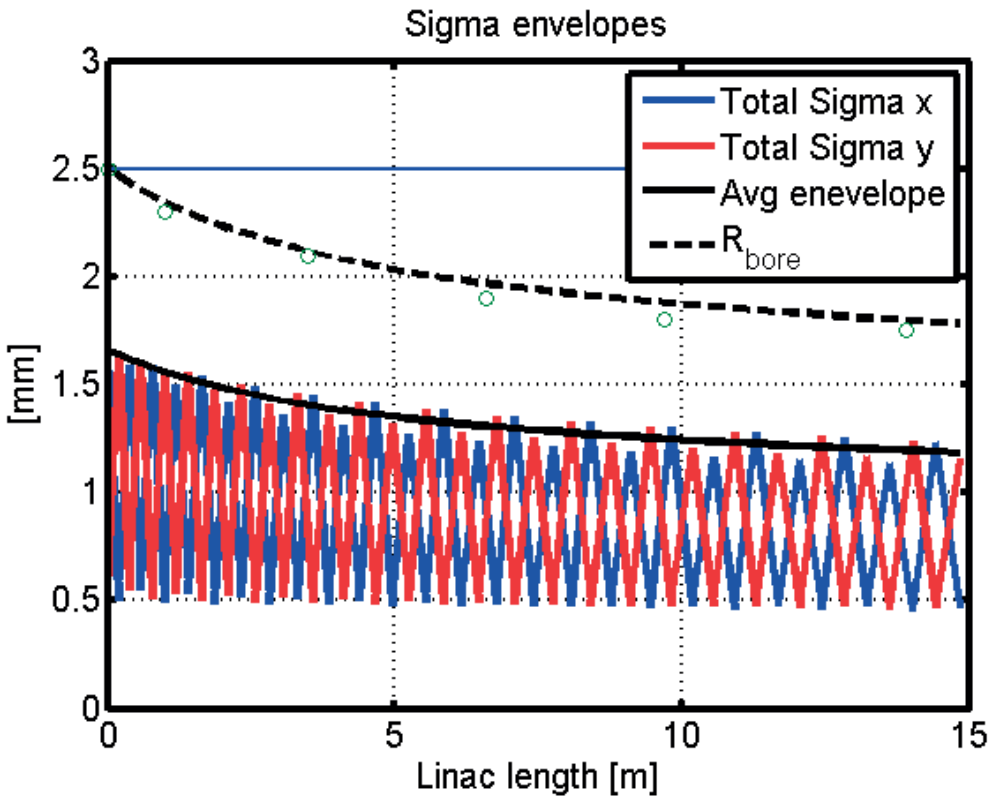

Figure 4.3 – Preliminary beam tracking in the 10-100 MeV/u section of CABOTO performed with the code presented in Section A.1.

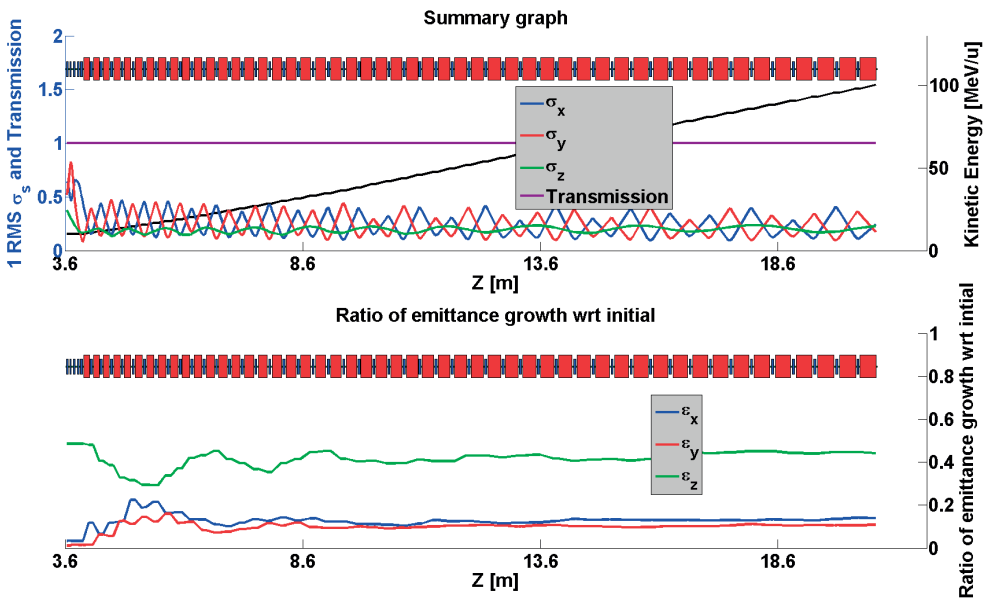

Figure 4.4 – Beam 1 σ RMS envelope through the CABOTO DTL from 10 to 100 MeV/u (top) and ratio of emittance growth with respect to initial (bottom).

Table 4.3 – CABOTO DTL main parameters.

Module	Output energy [MeV]	Act. length [m]	Act./Tot. length	Avg. act. gradient [MeV]	Peak power [MW]	Avg. ZTT [MΩ/m]
1	20.0	1.39	0.60	15.2	3.1	102
2	34.7	1.88	0.66	16.4	4.1	125
3	53.7	2.37	0.72	16.9	5.1	132
4	76.1	2.83	0.73	16.6	6.3	124
5	100.3	3.25	0.75	15.7	7.7	104

than in the TULIP project given the 0.5 q/m ratio. To be consistent with the pole tip field limits of TULIP (1 T), all the quadrupoles from this section onwards had to be enlarged, from 3mm to 4.5mm. This change increased the filamentation problem highlighted in Section 2.3.2.

A quite substantial beating occurs along the linac, which is due to the asymmetries introduced by the IH focusing and short matching section, that did not manage to fully match the beam. This could be solved by a longer transverse matching section, that would in return required one or more buncher cavities. The goal of full transmission of particles and controlled emittance growth is however reached. The beam envelopes and emittances of this section are summarized in Fig. 4.4.

4.1.3 From 100 MeV/u to 430 MeV/u

The CCL section consists of 64 cavities, all of which are composed of 12 RF cells. It was not possible to adopt an higher number of cells with the 100% transmission goal. Interestingly, a constant 12 RF cells design is also proposed for the TULIP HG section. There the accelerating gradient is higher, but at the same time, the FODO momentum acceptance is lower.

In this section, it has been chosen to consider a constant gradient throughout the linac. This has the advantage of fully exploiting the field limitations, and so to have the most compact size for the given design. However, given the ZTT behaviour as a function of the cavities geometric β and the different length of the cavities, it results also in a variable power consumption in each tank. One could either size the power sources for the highest peak power cavity, and reduce the output power in the other sections. Or it could adopt RF power sources with variable output power. Lastly, one could change the design, adopting a constant power consumption per cavity, and so a lower gradient in the cavities with the lowest $ZTT \cdot L$ product. Thus eventually a longer linac.

In this latter case, it has been computed a linac with total length of 31.4 m and peak power consumption of 177 MW. In the case of a constant gradient, a total length of 29.5 m and a peak power consumption of 189 MW. The design here proposed is this second option, thus a a 6 % shorter linac with a 6 % higher power consumption. The solution of increasing the number of cell can not be pursued due to the beam dynamics limitations discussed above. Once a final decision will be taken on the RF power sources to use, and a precise estimation

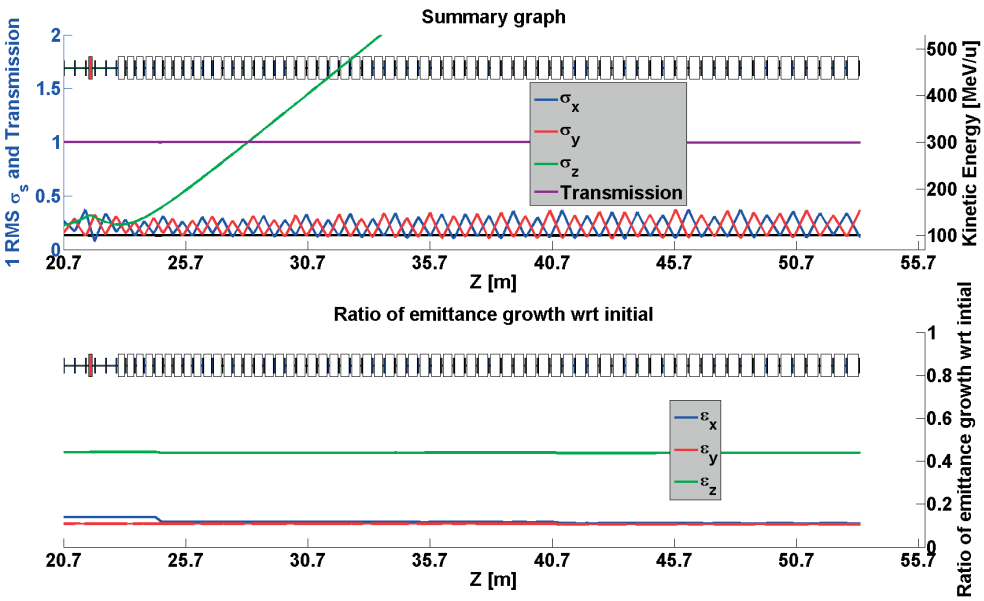

Figure 4.5 – Beam 1 σ RMS envelope through the CABOTO CCL with no acceleration after 100 MeV/u (top) and ratio of emittance growth with respect to initial (bottom).

of the power losses in the RF connections between klystrons and accelerating structures, it will be possible to further refine the design. At the present stage, it has been considered two group the 64 cavities into 32 modules of two cavities each. The peak power consumption of the modules range from 5.2 MW to 6.5 MW.

The synchronous phase is constant and equal to 15 deg. The emittances and beam envelopes are shown in Fig. 4.5 and 4.6 for the two extreme cases of no acceleration and full acceleration, respectively.

The main parameters of this linac section are summarized in Table 4.4.

A buncher cavity was placed in the matching section between the DTL and the CCL linacs. As for TULIP, this does not represent a final solution, but it was necessary to control the beam that otherwise would have been to large to fit into the longitudinal acceptance of the CCL cavities. A 2.2 m long matching section was designed, composed of 6 PMQ including the final DTL and the initial CCL ones. This could well represent a reasonable final solution in terms of overall length, even though the presence of a dipole would call for dispersion suppressors, and so a re-design of the proposed layout.

4.2 Quadrupole misalignments

The quadrupole misalignment study for CABOTO followed the methodology discussed in Section 3.3. The obvious difference with respect to TULIP lies in the linacs length and number

Table 4.4 – CABOTO CCL main parameters.

Cavity	Output energy [MeV]	Act. length [m]	Avg. act. gradient [MeV]	Peak power [MW]	Avg. ZTT [MΩ/m]
1	107.9	0.524	30.3	5.2	93
2	115.8	0.539	30.3	5.2	95
3	123.9	0.555	30.2	5.3	96
4	132.2	0.571	30.0	5.3	98
5	140.7	0.586	30.3	5.3	99
6	149.4	0.601	30.0	5.4	101
7	158.4	0.615	30.1	5.5	102
8	167.5	0.629	30.2	5.6	103
9	176.9	0.643	30.2	5.6	104
10	186.4	0.656	30.1	5.6	105
11	196.1	0.670	30.0	5.7	106
12	205.9	0.682	29.9	5.7	107
13	215.9	0.694	29.8	5.8	107
14	226.0	0.706	29.8	5.8	108
15	236.3	0.718	29.8	5.9	109
16	246.8	0.729	29.8	6.0	109
17	257.5	0.740	29.8	6.0	110
18	268.3	0.751	29.8	6.0	110
19	279.2	0.760	29.7	6.1	111
20	290.2	0.771	29.7	6.1	111
21	301.3	0.781	29.6	6.1	111
22	312.6	0.790	29.5	6.1	112
23	323.9	0.799	29.4	6.2	112
24	335.3	0.808	29.4	6.2	112
25	346.9	0.817	29.4	6.3	112
26	358.7	0.826	29.4	6.4	112
27	370.5	0.834	29.4	6.4	113
28	382.4	0.842	29.4	6.4	113
29	394.5	0.850	29.4	6.5	113
30	406.6	0.857	29.3	6.5	113
31	418.8	0.864	29.2	6.5	113
32	431.0	0.872	29.1	6.5	113

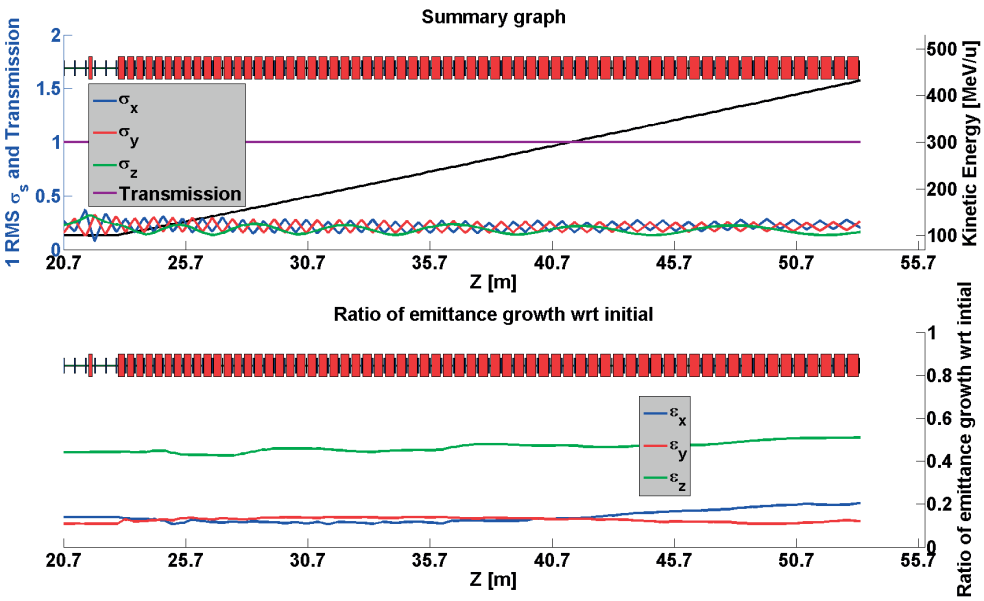

Figure 4.6 – Beam 1 σ RMS envelope through the CABOTO CCL with full acceleration up to 430 MeV/u (top) and ratio of emittance growth with respect to initial (bottom).

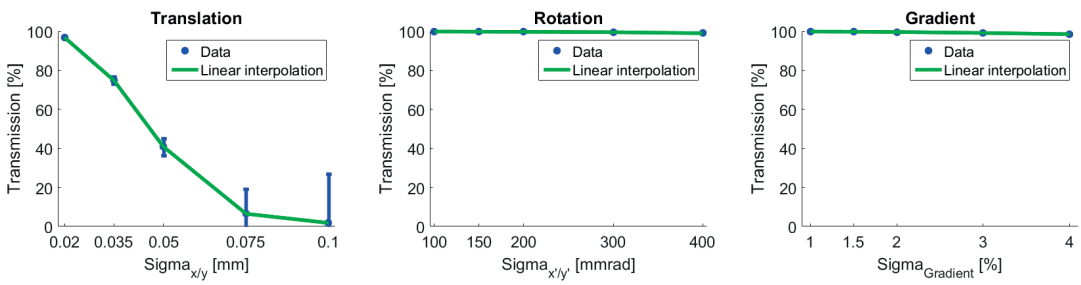

Figure 4.7 – Transverse and rotational quadrupole misalignment study for the IH section of CABOTO. Gradient tolerances to the right.

of quadrupoles. For comparison, the proposed TULIP design has 55 quadrupoles, while the CABOTO one has 136 quadrupoles. The misaligned quadrupoles are 17 for the IH section, 56 for the DTL section, and 81 for the CCL section. The results are presented in Fig. 4.7 4.8 4.9 for the three linac sections, respectively.

As in TULIP, the most sensitive section is the DTL one (Fig. 4.8), though this time also the IH and the CCL sections have tight tolerances. With 95% total transmission as a threshold, and under the assumption of a Gaussian distribution of the quadrupole misalignments, one would need a transverse misalignment smaller than 0.02 mm for both the IH, the DTL and the CCL quadrupoles.

Previously discussed in Section 4.1.2, CABOTO features a tapered bore radius from 2.5mm to 2mm in the DTL linac, and a 2mm bore radius in the CCL section. This is different with

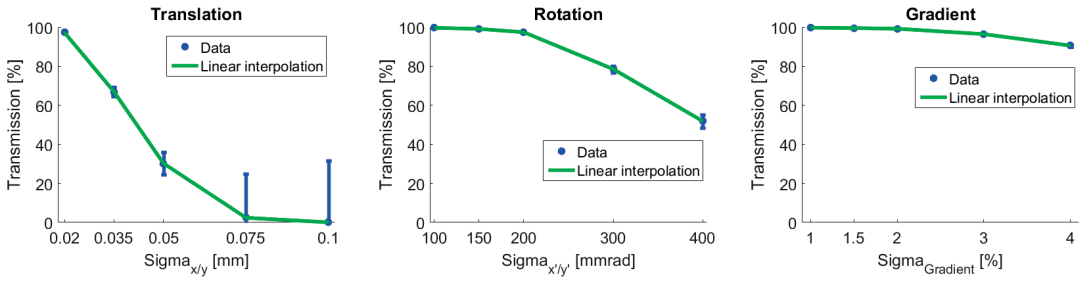

Figure 4.8 – Transverse and rotational quadrupole misalignment study for the DTL section of CABOTO. Gradient tolerances to the right.

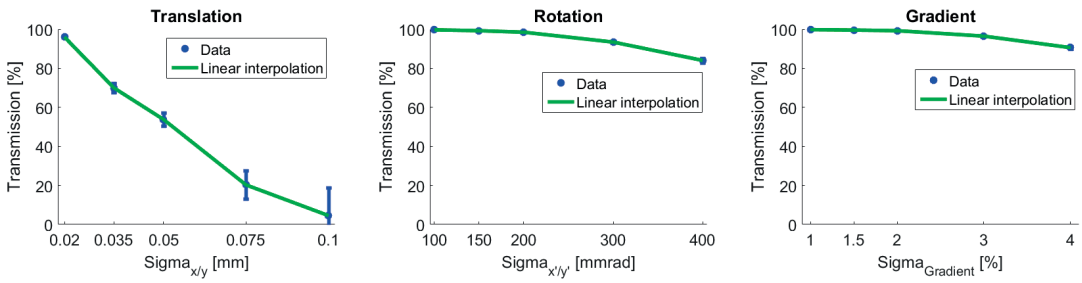

Figure 4.9 – Transverse and rotational quadrupole misalignment study for the CCL section of CABOTO, when all the accelerating cavities are at the nominal voltage. Gradient tolerances to the right.

respect to TULIP, where a constant bore radius was considered, and it is justified by the longer footprint at disposal for the facility, and by the need to maximize the ZTT. However, as just shown, CABOTO has even stricter quadrupole tolerances that TULIP, and this represents a cost, if not a technological issue. Further to what presented, the CCL section of CABOTO was then studied considering a 2.5mm bore radius for the accelerating structures. This choice would relax the quadrupole tolerances, at the price of a lower ZTT of about 14% (see Table 2.11). However, this larger bore aperture would allow to relax the misalignment quadrupole tolerances, of approximately a factor 0.5, from 0.02 mm to 0.03 mm. A more detailed study shall start from these initial sensitivity assessments to propose a final design, taking into consideration technological limitations and costs optimization.

4.3 Start-to-end simulation: from 2.5 MeV/u to 430 MeV/u

The first *all-linac* solution of the CABOTO project has been presented.

The beam dynamics linac design features full transmission and minimized emittance growth, and it has been accomplished with full tracking of the particles from the RFQ output till 430 MeV/u, using RF EM field maps for the accelerating structures computed with HFSS. This is unique for such a long linac.

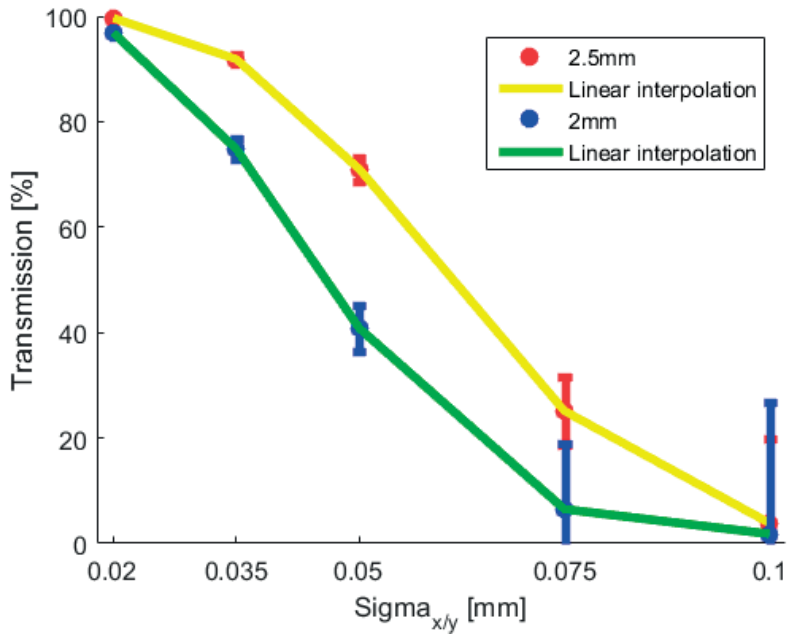

Figure 4.10 – Transverse quadrupole misalignment study for the CCL section of CABOTO for a 2mm and for a 2.5mm bore radius.

Fig. 4.11 shows the main linac design parameters. A graphical way of presenting this data was used, with the aim of having a fast-to-read and complete source of information. It is worth commenting again a few characteristic of the design. The linac is composed by 4 IH cavities, followed by a DTL, a buncher cavity, and the CCL. The accelerating gradient step is clearly observable in Fig. 4.11 top left. A similar way to discuss this difference is by considering Fig. 4.11 bottom left. Here a key characteristic of this design is reported, i.e. the peak power consumption distribution along the linac. The combination of high gradient and lower ZTT, given by the high gradient RF optimization, leads to a major concentration of the peak power installed, approximately 90% of the total, in the CCL section.

The first part of the linac, up to the buncher cavity, was optimized in terms of ZTT. In Fig. 4.11 top right, one can notice the ZTT trend along the structures. In particular, the DTL ZTT optimum saturates well before 70 MeV, due to the RF cells getting too long. As a last piece of information, the RF cell length and diameter is reported in Fig. 4.11 bottom right. This is another way to discuss the ZTT behaviour of the linac. The DTL section, being 2π mode, gets too long towards the end of the linac, and so it looses in ZTT. Interestingly, the resonant frequency of RF cells with the optimum ZTT is obtained mostly by varying the gap, while the cell diameter is approximately constant throughout the linac.

Table 4.5 summarizes this information in a more common numeric form.

As for the TULIP project, the linac dissipated power is reported, rather than the total RF

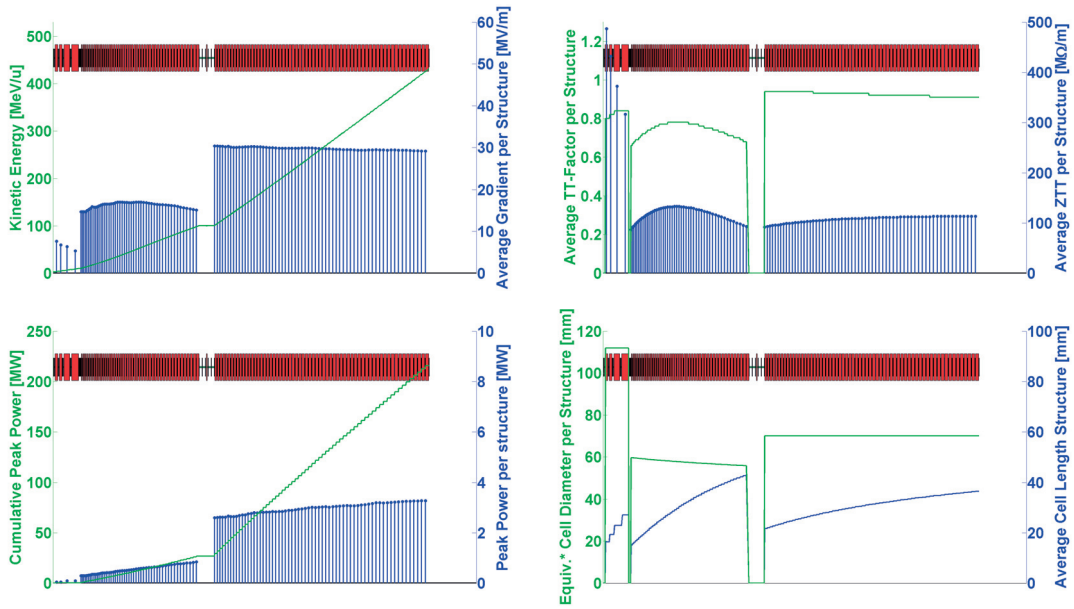

Figure 4.11 – CABOTO *all-linac* main accelerating parameters.

Table 4.5 – CABOTO *all-linac* - A summary.

Linac Section	Operating Freq. [MHz]	Output En. [MeV]	Avg. Grad. [MV/m]	Synch. Phase [deg]	Act. Length [m]	Tot. Cum. Length [m]	Avg.ZTT [MΩ/m]	Peak Power [MW]
RFQ	750	2.5	ND	ND	ND	ND	ND	ND
IH	750	10	6.5	12	2.51	3.6	402	0.257
DTL	2998.5	100	16.2	18	11.7	20.7	117	26.4
BTW-CCL	2998.5	100-430	29.7	15	23.1	53.3	107	189.1

power to be installed. The motivations of this choice are presented in Section 3.4. Assuming a probably conservative 20% losses in the RF network between klystrons and accelerating structures, one should account for approximately 260 MW RF peak power for the CABOTO project.

The beam dynamic design is summarized in Fig. 4.12 for the two extreme cases of no acceleration in the CCL section and full acceleration. Here, a number of facts can be discussed. First of all, one should notice the beating in the beam envelopes, especially after the IH-DTL transition. This part was explained in detail in the previous sections, but as a reminder, the two critical aspects were represented the abrupt change in accelerating gradient, observable by the longitudinal phase advance increase (green curve), and by the change in operating frequency, from 750 MHz to 3 GHz.

Continuing on along the linac, one could notice the difference final beam envelopes, in the two cases of no acceleration in the CCL and full acceleration. As discussed in Section 3.1.3, an optimized line should have the same beam envelopes in this two extreme cases. However, some residual mismatch at the beginning of the line, together with too high transverse phase

advance, penalizes the CCL no acceleration case, and this are the reasons of this difference. Nonetheless, the main goals of the design, i.e. full transmission and emittance growth control in a compact proton linac, have been achieved.

Finally, Fig. 4.13 shows the classic representation of the transverse and longitudinal envelopes mirrored around the centre. The case of no acceleration after 100 MeV/u is easily recognizable by the growth of σ_z - in green colour in the plot - as soon as the particles are not accelerated anymore.

4.4 A He therapy facility based on the CABOTO design

Recent raising interest towards using He [65] for radiotherapy is motivated by the lower final energy with respect to carbon ions, and by the higher RBE of He with respect to protons. Thus a solution in between the two extremes, cheaper than carbon ion therapy but more effective towards radio-resistant tumors than proton therapy. He beams have been proposed for atrial fibrillation since they show a lower later spreading than proton beams, while at the same time avoiding the longitudinal tail of carbon ion beams.

From a technological point of view, a linac solution for a He therapy facility would be still applicable. Here the work done for CABOTO is adapted to provide a first general layout design of a He linac for medical purposes.

The main difference from CABOTO lies in the energy modulation range, that is 100-430 MeV/u for C^{6+} and 70-230 MeV/u for He^{2+} to obtain the same penetration in water equivalent tissues (see Eq. 1.3). Thus, the CABOTO design was adapted, with a DTL section up to 70 MeV/u, and a CCL section covering the 70-230 MeV/u branch. The general layout is summarized in Table 4.6 and the overall linac length is sketched in Fig. 4.14.

For the CCL linac it was chosen to propose again a 30 MV/m average accelerating gradient. This choice, as for CABOTO, fixed the accelerating gradient of the DTL linac, that corresponds then to 15 MV/m, in order to equally divide the total length into two branches to minimize the footprint. The IH cavities layout was not changed. It would be then possible to remain below 120 MW of dissipated peak power. As for TULIP and CABOTO, it has been chosen to present the main linac parameters in the graphic form of Fig. 4.15.

The beam has not been tracked through the linacs, bt it is safe to assume that the same general parameters - synchronous phase, maximum quadrupole strength - still holds for this design.

4.5 Cost estimation of linacs for hadron therapy

The present Section aims at giving an approximate estimation of the cost of a linac for hadron therapy. In Table 4.7, some numbers collected by the author during this thesis are reported. For the klystron-modulators and IOTs, very helpful were a report from ESS [66] and [47].

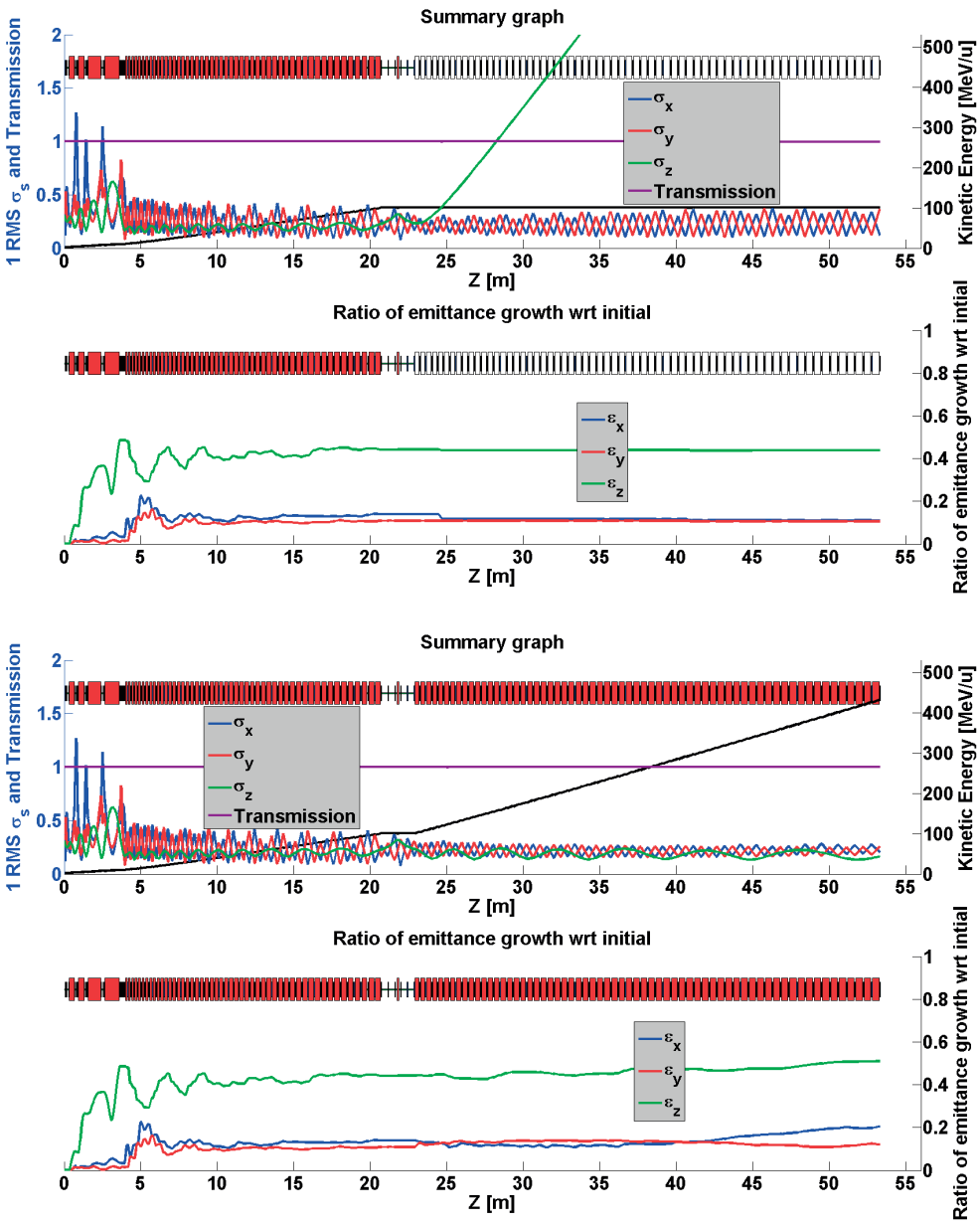

Figure 4.12 – Beam 1 σ RMS envelope through the CABOTO *all-linac* solution and ratio of emittance growth with respect to initial. No acceleration after 100 MeV/u (top) and full acceleration up to 430 MeV/u (bottom).

Table 4.6 – Key parameters of the He linac studied.

Type of structure	Output energy [MeV/u]	Active Length [m]	Peak power [MW]
750 MHz RFQ	2.5	ND	ND
750 MHz IH	10	2.5	0.3
3 GHz DTL	70	7.6	16.6
3 GHz CCL	70-230	11.2	103.1

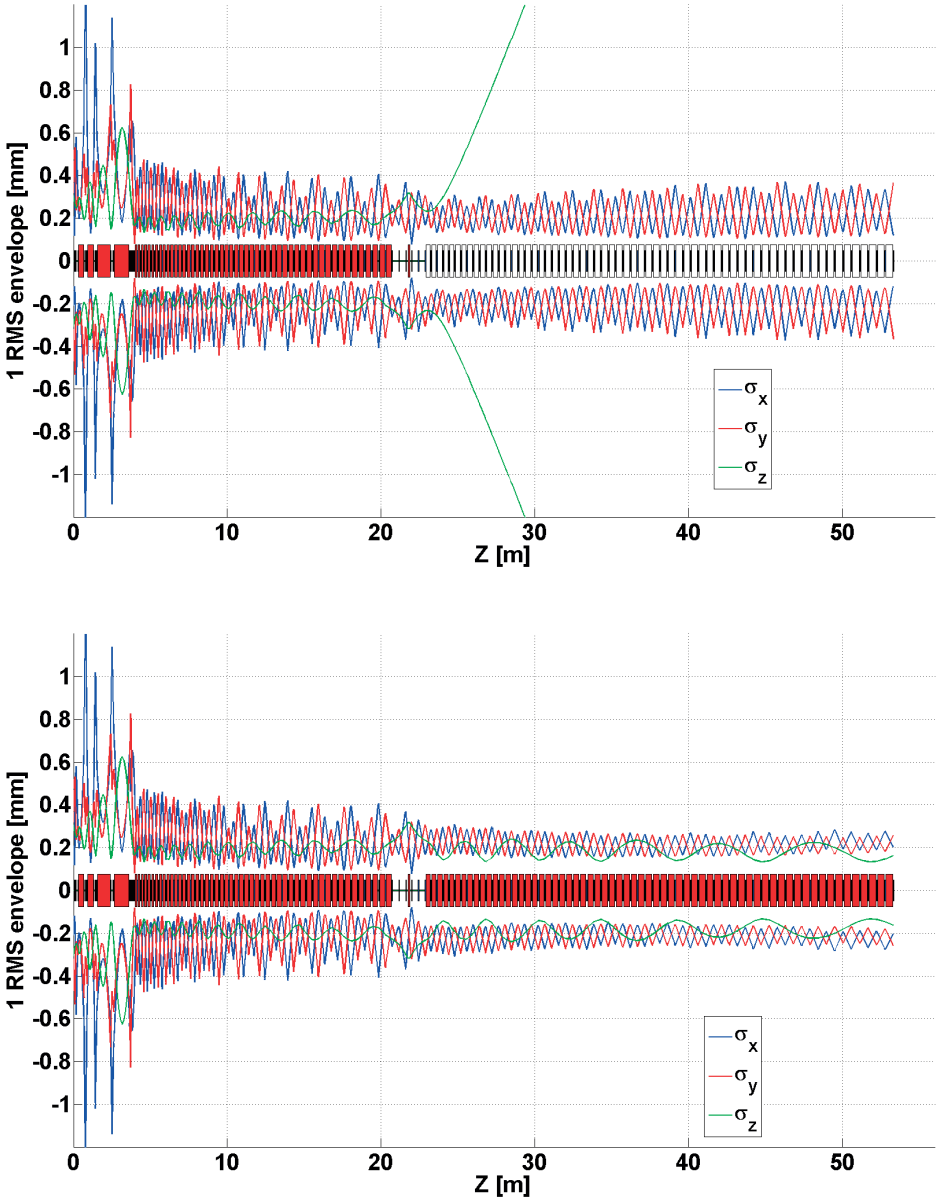

Figure 4.13 – The 100 MeV/u (top) and 430 MeV/u (bottom) beam envelopes along CABOTO *all-linac*. 1 RMS σ_x (red), σ_y (blue) and σ_z (green).

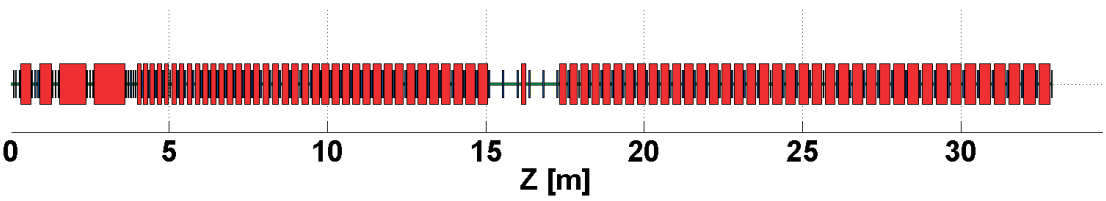

Figure 4.14 – Sketch of the He linac longitudinal dimensions.

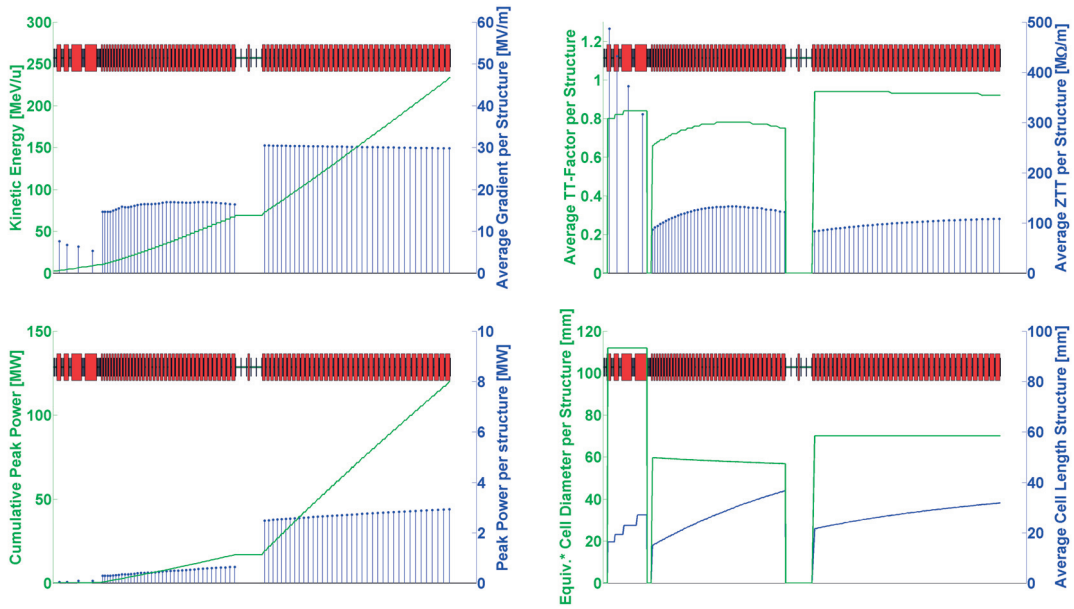

Figure 4.15 – He linac main accelerating parameters.

Table 4.7 – Cost estimation of the major components of a linac for hadron therapy.

Component	Cost
3 GHz Klystron-Modulators	0.05 M€/MW-RF
750 MHz IOTs	1 M€/MW-RF
750 MHz CERN RFQ	1 M€/unit
BTW accelerating structure	0.075 M€/unit

The cost of the CERN proton 750 MHz RFQ was indicated by M. Vretenar at the Linac16 conference and lately confirmed [67] and comprises also subsidiary equipments as vacuum pumps and cooling, and also the IOTs cost. Lastly, the BTW prototype was paid approximately 75 k€, considering material, disks machining, tuning pins, waveguides, flanges, brazing, and baking [68]. These number were considered as the unitary price for the different accelerating structures, clearly simplifying the problem. From one side this is an overestimation, since the production of similar cavities will lower the unitary price. On the other hand, many accelerating structures could be more expensive, being longer or with an higher number of RF cells with respect to the BTW prototype, that is 12 RF cells, 189 mm long. Concerning PMQs, their cost can be estimated in 2 k€ each, for the aperture and strength of interest in the present designs [23]. Thus their contribution on the total price is of the second order. The cost of ion sources, vacuum and cooling system was not addressed.

Table 4.8 is everything but a comprehensive cost analysis of hadron therapy facilities, which was not the goal of this thesis. However, it may help the reader interested in getting a first

[1] total with 20% losses
[2] total with losses

Table 4.8 – Cost estimation of linacs for hadron therapy.

	TULIP		CABOTO		He Linac	
Component	**Quantity**	**Cost**	**Quantity**	**Cost**	**Quantity**	**Cost**
3 GHz RF power[1]	125 MW	6.3 M€	260 MW	13.0 M€	145 MW	7.3 M€
750 MHz RF power[2]	100 (IH only) kW	0.1 M€	300 (IH only) kW	0.3 M€	as for CABOTO	0.3 M€
Linac structures	46	3.5 M€	122	9.2 M€	83	6.2 M€
RFQ	1	1 M€	2 (approx. doubled)	2 M€	as for CABOTO	2 M€
Total		**10.9 M€**		**24.5 M€**		**15.8 M€**

order of magnitude of the costs. Also, it allows to draw some important considerations. First and foremost, as multiple times highlighted throughout the different Chapters, the RF power sources are the most expensive component in this kind of facilities. Their contribution to the overall cost is typically approximately 50 %, but it can gets significantly higher if high gradient designs are chosen, so in the TULIP facility for instance. As a second remark, the total cost of IOTs, though their unitary cost is higher than the 3 GHz klystron-modulators one, does not represent a major contribution overall. One could then decide to privilege the physics arguments, particularly the beam dynamic advantages (see Section 2.3.2), of a 750 MHz IH solution to higher energies than 10 MeV/u. It is in fact here reminded that it was chosen to present a design with a 3 GHz DTL starting at 10 MeV/u, for both TULIP and CABOTO, only as a result of cost considerations.

5 Low and high power measurements of the BTW structure prototype

This Chapter discusses the experimental results of this thesis, which are all related to the high-power test of BTW prototype described in Section 2.4. The Chapter starts with the cavity tuning description, followed by the high gradient test set up and data analysis. Section 5.3 presents the study on dark current capture in accelerating cavities for non ultra relativistic particles.

5.1 RF measurements and tuning of the prototype

Low power RF measurements were performed on the structure prior to bonding, in order to verify that the prototype was within the tuning range. The disks were aligned thanks to a V-shape support whereas azimuthal alignment was performed using the tuning holes as seen in Fig. 5.1. The structure was well within the tuning range, having a total reflection of -23.6 dB (Fig. 5.2 bottom). This value refers to a frequency of 2.9982 GHz to take into consideration the lower temperature in the laboratory with respect to the design temperature.

The stack of disks was joined by diffusion bonding in a partial hydrogen atmosphere following the CLIC baseline fabrication procedure. The fabrication technique was chosen so that the high-gradient test results can be most easily compared to the structures tested in the CLIC high-gradient program. After the structure was assembled by brazing the cooling blocks and vacuum tubes and input waveguides, it was returned to CERN for the final tuning. A summary of the measurements performed on the prototype is shown in Fig. 5.3.

The tuning was performed in a 22 °C temperature control clean room, with the goal of tuning the structure at a operating temperature of 32 °C at 2.9985 GHz under vacuum. Even though the prototype is not supposed to accelerate any particle, the desired phase advance of 150 ± 1.5 degrees was reached. Thus this cavity could accelerate particles with an average input-output β of 0.38.

All 12 cells (10 regular and 2 coupling cells) of the structure were adjusted in frequency by pulling or pushing up to 4 tuning pins in each cell. As discussed in Section 2.4.3, each RF cells

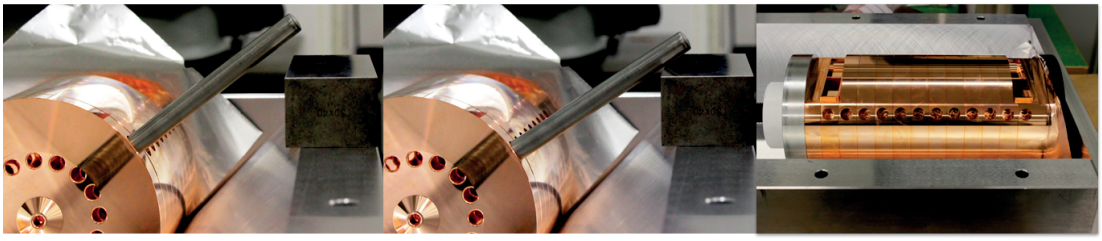

Figure 5.1 – BTW prototype disk alignment procedure (left and middle) and aligned disks without input waveguides (right).

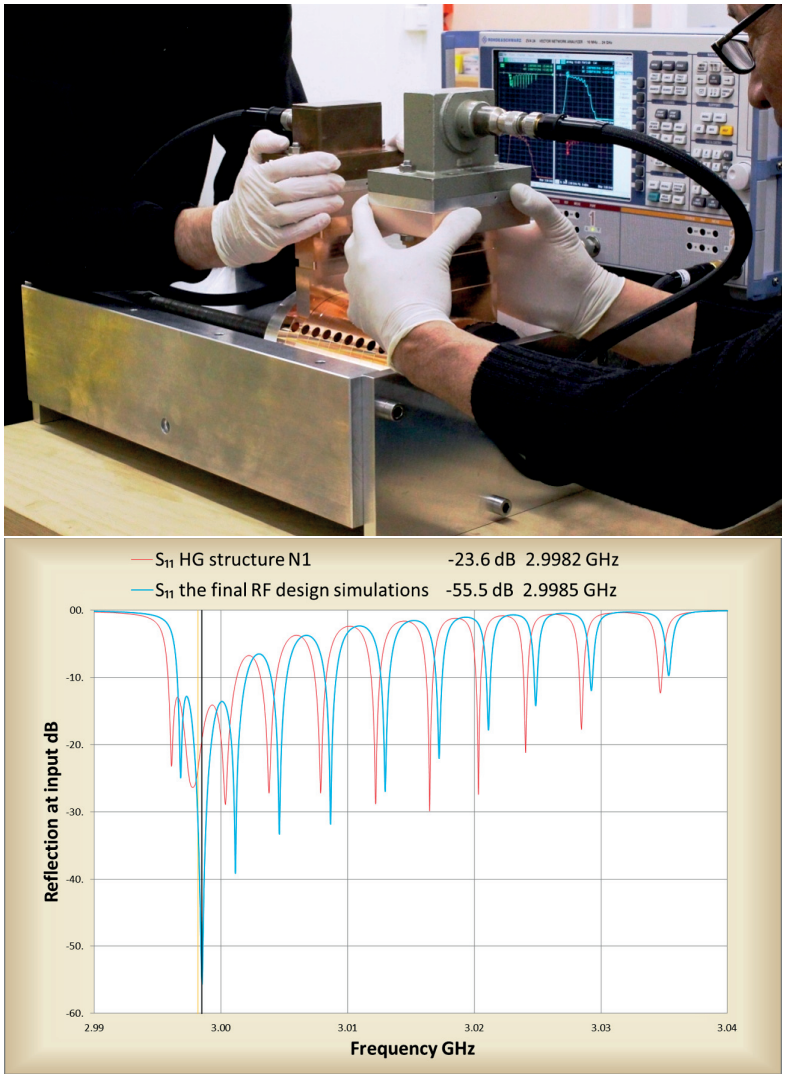

Figure 5.2 – LLRF test (top) and S11 comparison between measured configuration and simulation design results (bottom) [69].

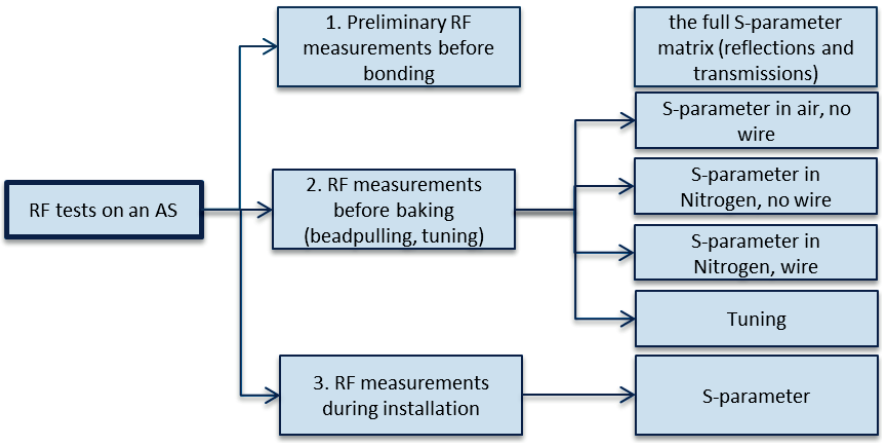

Figure 5.3 – Scheme of the RF tests performed on the accelerating structure (AS).

Table 5.1 – Initial conditions of the two structures prior to tuning.

	Avg. RF phase advance [deg]	**Standard deviation [deg]**	**Total cavity reflection [dB]**
1st structure	-148.7	7.7	-21.2
2nd structure	-149.4	2.8	-23.6

have a tuning range of ± 3 MHz with a 1mm deformation of all the four tuning pins. However, the deformation could be larger, if needed. Eventually, the frequency of the output coupling cell was increased by 2.2 MHz, the frequency of the 10 regular cells was increased between 0.1 and 0.8 MHz (average 0.3 MHz, std 0.2 MHz), while the frequency of the input coupling cell was decreased by 0.6 MHz. Thus, except for the output coupler, the RF tuning and sensitivity analysis was probably too conservative. The whole process lasted a couple of hours.

Fig. 5.4 shows the electric field pattern along the structure, together with the S11 parameters in the complex plane and the RF phase advance per cell before and after tuning. The six arrows configuration of the tuned solution differs from the 12 arrows of Fig. 2.47 because the phase advance difference between cells doubles due to forward and backward path of the signal. So the S11 signals have a doubled phase advance of $5\pi/3$ instead of $5\pi/6$, and thus a 6 arrows symmetry.

5.1.1 Second tuning test

The second BTW prototype was tuned in April 2017. This second structure showed a very good field pattern prior to tuning, and it needed very little effort to be brought to the goal tuned conditions. For comparison, the RF phase advance per cell and the total cavity reflection for the two structures prior to tuning are reported in Table 5.1.

A probable reason of the different initial condition between the two prototype lies in the choice of the brazing material for the tuning pin. For the first cavity, an alloy with a too low melting point was chosen, resulting in many defected pins after the structure bonding. These pins

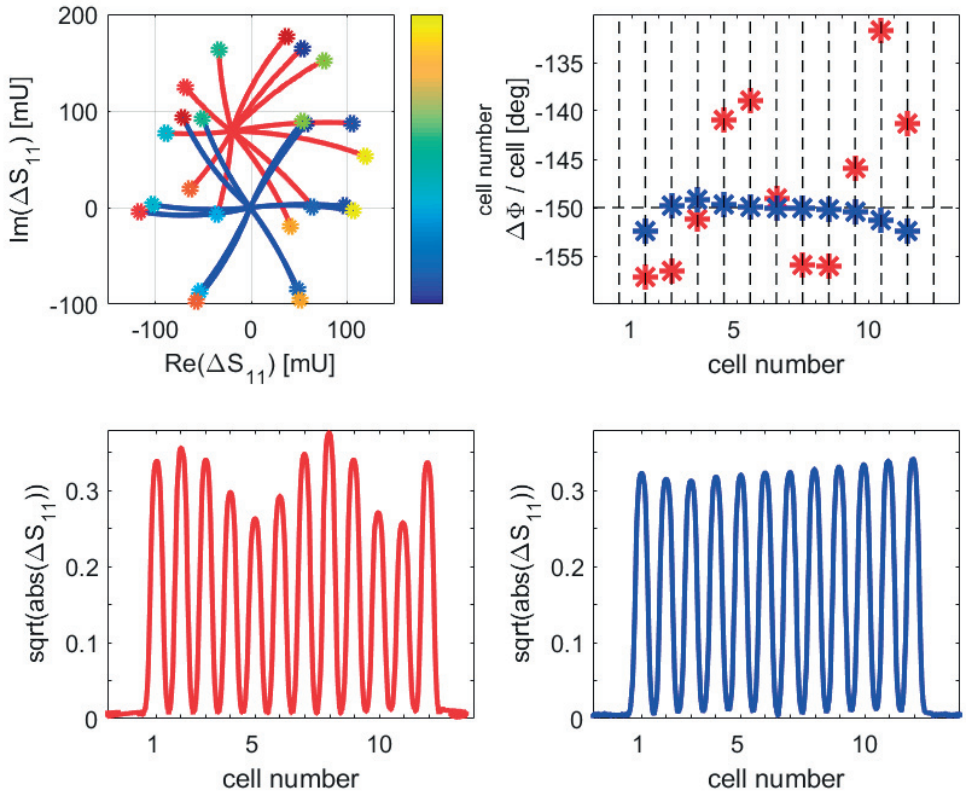

Figure 5.4 – Electric field pattern along the 1st prototype RF cells, before (in red) and after tuning (in blue). Top left: in the complex plane; top right: in phase advance per cell; bottom: in magnitude.

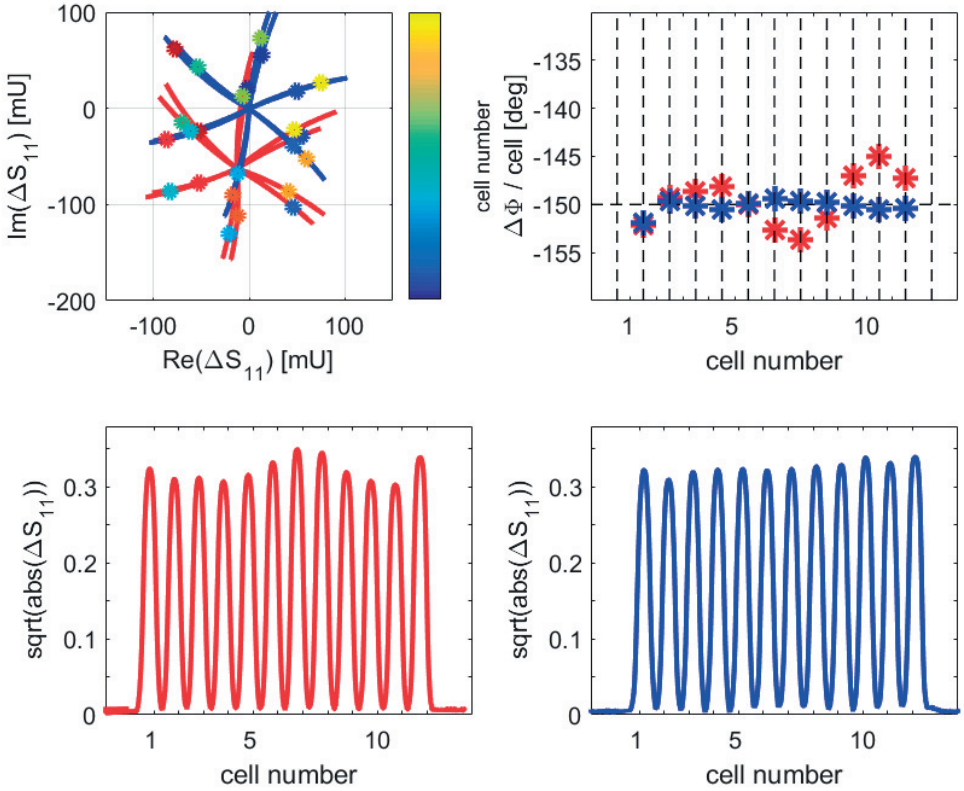

Figure 5.5 – Electric field pattern along the 2nd prototype RF cells, before (in red) and after tuning (in blue). Top left: in the complex plane; top right: in phase advance per cell; bottom: in magnitude.

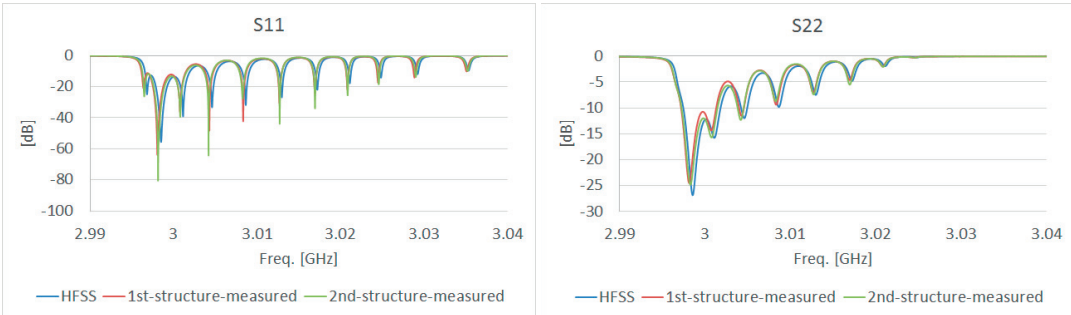

Figure 5.6 – Input (left) and output (right) S-parameters of the two tuned structures, measured at a temperature of 23°C in a dry nitrogen atmosphere, and comparison with the HFSS values simulated in vacuum.

had to be re-brazed to the cavity, and it cannot be excluded that this process slightly modified the outer volume of the RF cells. This issue did not occur on the second prototype, where a ceramic brazing was adopted.

The results of the tuning test are very encouraging. RF designers of future similar structures could either chose to relax the mechanical tolerances, or to tighten them slightly and adopt a tuning-free solution, as in some recent CLIC cavities. A cost-analysis should address this topic in detail, not forgetting that these conclusions refer to a 12 RF cells solution: longer cavity are more demanding also for tuning, and one shall take this into account.

For the two tuned structures, the S11 and S22 parameters are compared with the HFSS simulated values in Fig. 5.6. The small frequency shift that is possible to notice at the resonances is due to the different tuning temperature with respect to the design one.

5.2 High power test

5.2.1 High power test set-up

The high power test started in November 2016. The prototype is installed in the CLIC Test Facility 3 (CTF3). It is connected to a 43 MW klystron via WR284 waveguides. The 3 dB recirculator designed and discussed in Section 2.4.6 was not built, thus the structure is directly connected to the klystron. As a result, approximately 20 MW at the structure input are needed to reach a 50 MV/m accelerating gradient (see Table 2.7). The waveguides are equipped with a circulator to protect the klystron from the reflected power, and from design a maximum power of approximately 35 MW is available in the bunker, so more than what is needed by the cavity to reach the nominal gradient.

The layout of the test set-up is sketched in Fig. 5.7. The structure is connected to an ion pump and to a dedicated chiller unit that can adjust the cooling water temperature. The load is connected to the main CTF3 cooling circuit with water flowing at 32 °C.

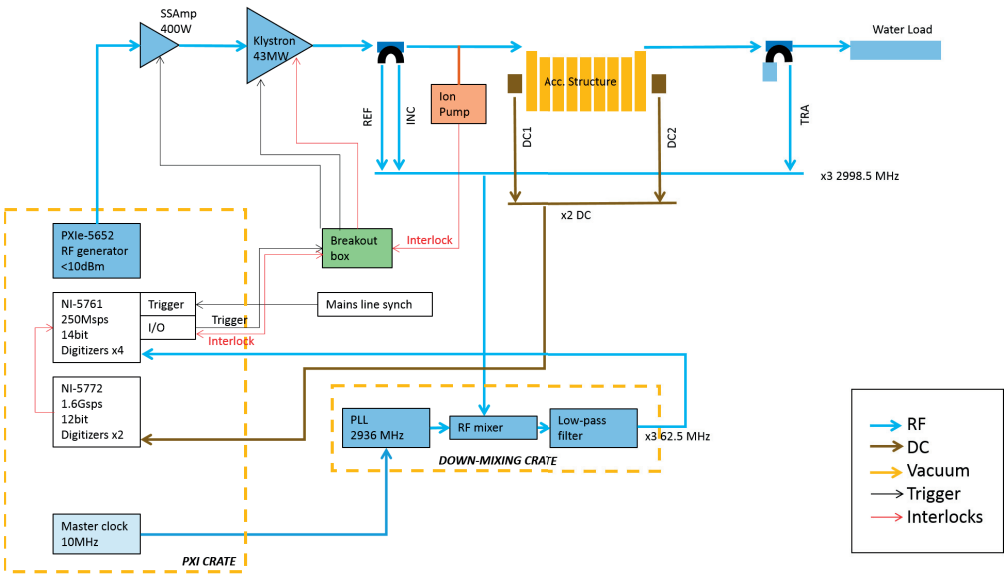

Figure 5.7 – Layout with the main components of the high power test set-up.

The interlock system is composed of four interlocks: two flow-meters on the structure and on the load cooling water, one pressure-meter, and one temperature-meter attached to the load. The bunker and the klystron-modulator are equipped with independent interlocks, which ensure the personal safety (none can enter the bunker while in operation) and the machine safety. In case of any of these interlocks, the system stops the operations.

The acquisition and control system is based on National Instrument electronics, and it is largely a direct adaptation of the Xbox-2 test stand configuration [70]. Two Faraday cups (FC) are attached at both ends of the prototype, for breakdown detection and dark current measurements. The incident and reflected power are measured on the input bidirectional coupler, while the output one measure the transmitted power. Amplitude and phase of these 3 GHz signals are down-mixed to 62.5 MHz and digitize in 250 Msps analog-to-digital converter (ADCs). At the present stage, the data analysis is based on these five signals: 3 RF, incident, reflected and transmitted power, and 2 FC currents.

The control system of the Klystron-modulator unit is composed of two interlocks, two "enablers", and three signals. Some of the signals exiting the PCI eXtensions for Instrumentation (PXI) crate, being 5V, need to be converted to 24V before reaching the Klystron control unit. The cabling set-up is summarized in Fig. 5.8.

The Klystron control unit is equipped with two interlocks, "Authorization RF" and "Modulator Inhibit", that both need to be released in order to authorize the PXI to send RF power. The PXI itself is equipped with two "enablers", "RF ON" and "RF OFF". Lastly, the modulator receives the triggering signals from the PXI.

The RF pulse reaches the 400W Solid State Power Amplifier (SSPA) in a dedicated RF cable. Two

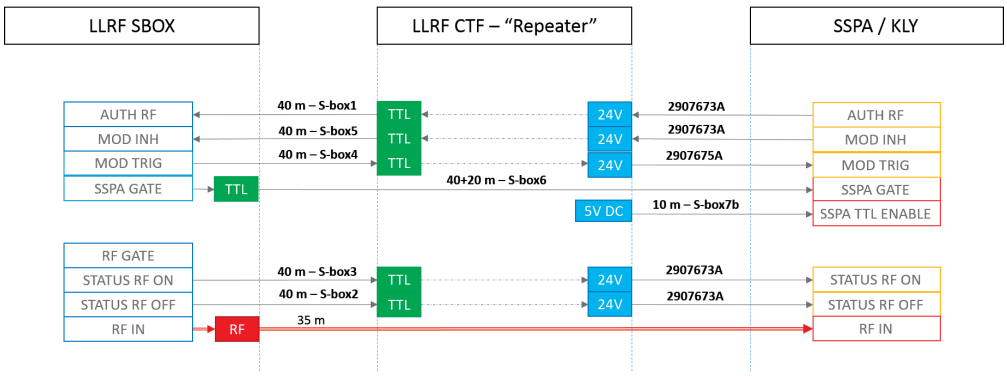

Figure 5.8 – Layout with the cabling of the Klystron-modulator control system.

transistor-transistor logic (TTL) cables are needed for the SSPA, an RF pulse that triggers the device before the real RF signal arrives, and a 5V enabler that maintains the SSPA in operational stage.

The incident, reflected and transmitted power signals have been calibrated. The measured attenuations along the three lines are summarized in Fig. 5.2. The bidirectional couplers, being already installed in the waveguides line, have not been measured during this test. It was assumed that the measurement performed before their installation is reliable [71].

The maximum incident and reflected power during the test will be around 20 MW, that can be more conveniently express in dBm, so the dB power ratio referenced to 1 mW of power:

$$Y[dBm] = 10log_{10}\frac{X[mW]}{1[mW]} \tag{5.1}$$

where X is the power in mW, and Y the correspondent power in dBm. The maximum incident and reflected power will be thus 103 dBm, while the transmitted one will be only one half of it, i.e. 100 dBm. The bidirectional couplers, cables and coaxial couplers attenuations must ensure that an acceptable power reaches the PXI crate, which should not however exceeds a couple of Ws, corresponding to a couple of dBms, in order not to damage the electronic circuits. This is the reason why on all line a -10 dB attenuators were added, and on the power reflected line a further -6 dB was positioned. The -0.2 dB "Additional attenuator" present in the power incident line refers to a high pass filter, which was placed to clean the incident signal from higher harmonics that were disturbing the acquired signal.

The calibration curves have been fitted with a 2nd order polynomial function, with zero intercept (Fig. 5.9), and the obtained values have been used in the Labview code to relate the mV signals read by the PXI crate into MW RF power.

Table 5.2 – Measured attenuations and maximum power coupled to PXI.

Max input power	103	103	100
Measured attenuations [dB]			
Bidirectional coupler	-61.60	-54.00	-60.02
RF cables	-12.75	-12.45	-12.77
10 dB attenuator	-9.92	-9.98	-10.10
Additional attenuator	-0.20	-6.01	Not present
Total attenuation up to the coaxial coupler	**-84.57**	**-82.48**	**-82.89**
Attenuation through the coaxial coupler	0.00	-0.02	-0.04
Total attenuation up to the power meter	**-84.57**	**-82.50**	**-82.93**
Coaxial coupler attenuation towards the PXI	-19.22	-19.44	-19.10
Max output power coupled to the PXI	**-0.79**	**1.08**	**-1.99**

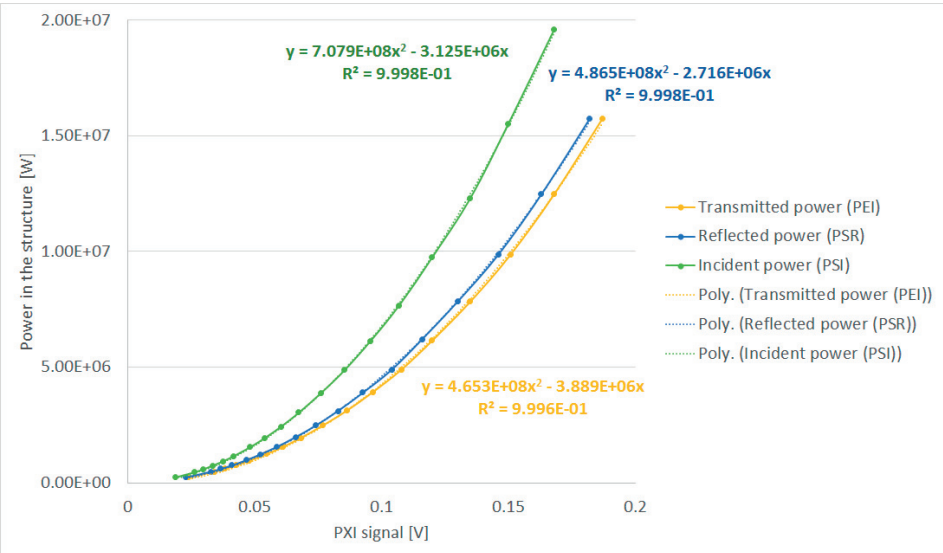

Figure 5.9 – Calibration curves for incident, reflected and transmitted power.

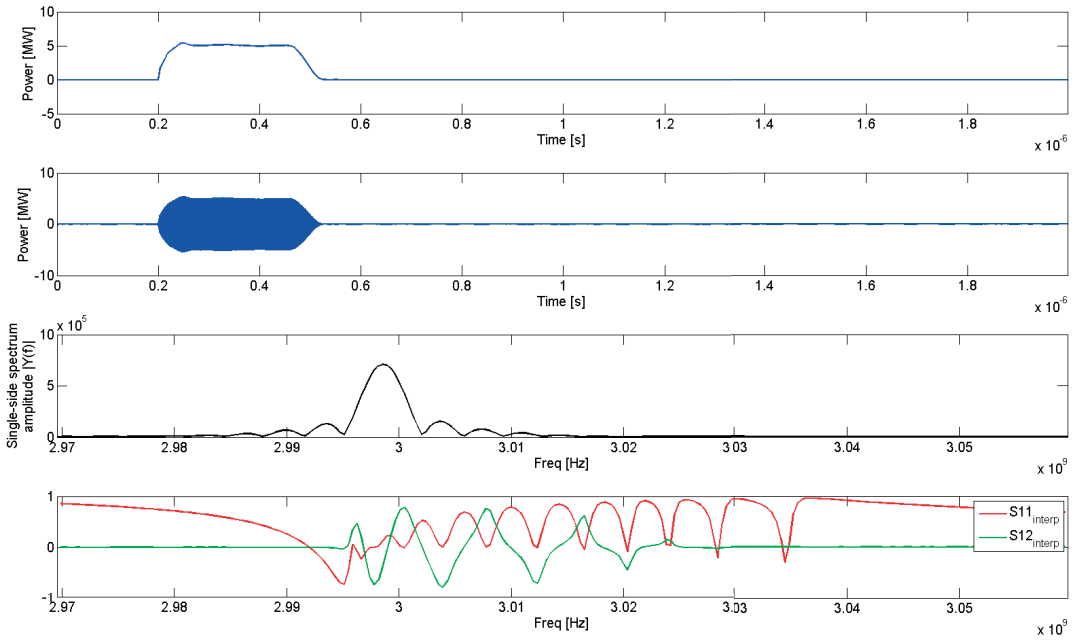

Figure 5.10 – Incident pulse shape in the time domain, corresponding sine waves, FT in the S11 frequency range, measured S11 and S12 of the structure.

5.2.2 First check - The pulse shape

The measured reflected and transmitted pulses can be double checked by multiplying the S11 and S12 parameters to the Fourier Transform (FT) of the incident pulse shape. Goal of this method is to verify that both the acquisition algorithm, and the prototype, are working according to the design.

Any real signal can be represented by a series of sinusoidal wave signals, of different amplitudes, phases and frequencies (Fig. 5.10, first two plots). The Fourier transform of the sinusoidal signal (Fig. 5.10, third plot) can then be multiplied by the S11 and S12 parameters (Fig. 5.10, forth plot), to obtain, in this case, an estimated reflected and transmitted signals respectively. These signals have then to be transformed back to the time domain.

The result of this analysis (Fig. 5.11) is a fairly good agreement between the acquired measured signals and the simulated one. Thus, in first order approximation, both the cavity and the acquisition electronics are working according to the design.

5.2.3 Conditioning phase

The structure started the conditioning process in December 2016. At the moment of writing, the conditioning is continuing. During this phase, a BDR limit of 3e-5 bpp was considered,

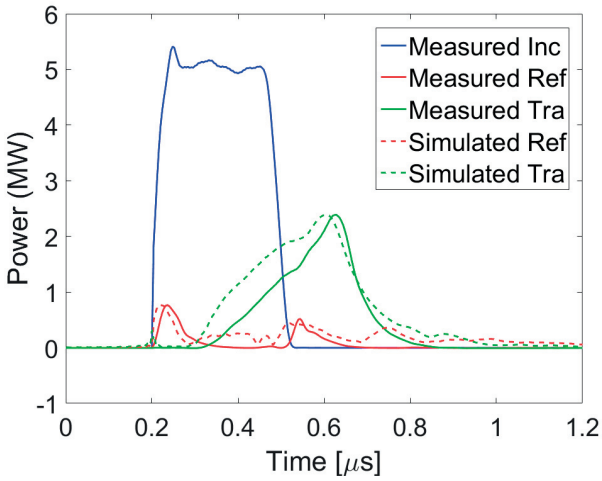

Figure 5.11 – Measured incident, reflected and transmitted pulse in the structure during the conditioning phase, and comparison with the reflected and transmitted signals reconstructed with FT.

which for a cavity 0.2 m long corresponds to 6e-6 bpp/m.

The number of BD allowed during a treatment session is debatable. One could argue that less than 1 BD has to be accepted for a whole treatment composed of many different sessions. On the other hand, since BDs very likely will end-up in a missed spot, one could argue that an higher number of BD can be accepted, provided that the missed spot is corrected in a subsequent treatment. However, if the goal of less than 1 BD is considered, assuming an average treatment [7], one ends up with a BDR limit of 3.4e-6 bpp. On the 4.4 m HG linac (see Section 3) of TULIP, this limit corresponds to 7.7e-7 bpp/m. Thus, for the 0.2 m long prototype under test, a BDR limit of 1.5e-7 bpp when the conditioning will be completed. Nevertheless, it is reminded that the structure has been designed for an higher BDR of 1e-6 bpp/m [7].

There is an increasing evidence that the conditioning of structures is proportional to the number of RF pulses, rather than the number of BDs [72], so an high BDR threshold during the conditioning process is not beneficial, but instead risky for the structure since it could over-damage the cavity walls without improving the high-gradient performances.

For comparison, in the conditioning phase X-box structures presented in [72] cumulated around 3e8 pulses. Concerning the TERA high gradient test program [38], the S-band single cell cavity collected [30] around 5.5e7 pulses, and the C-band single cell cavity [7] around 5e7 pulses. For this latter case the author claimed that the conditioning was likely incomplete. The current test should verify whether there is a frequency dependence in the conditioning, since the BTW prototype is the first S-Band cavity tested at this level of gradient.

The conditioning status of the structure is shown in Fig. 5.12. After a first run at 350 ns RF pulse length, during which the cavity reached the target accelerating gradient of 50 MV/m, at

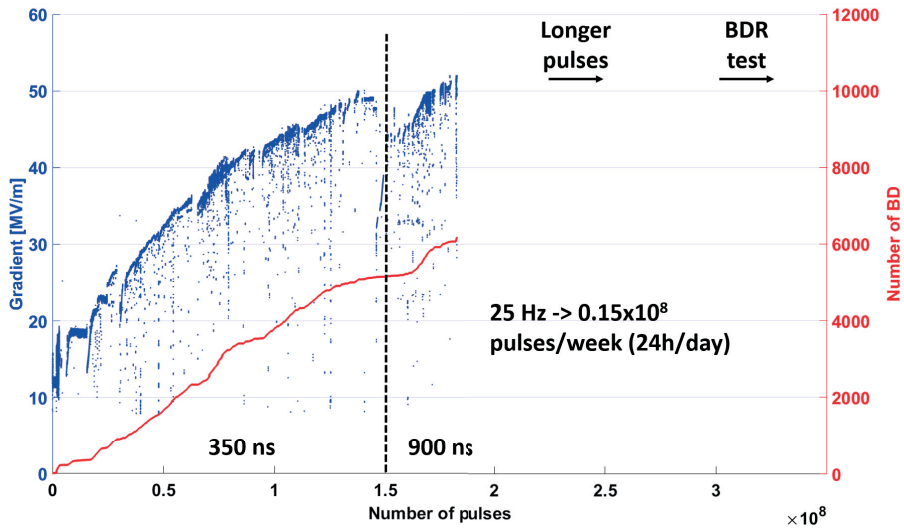

Figure 5.12 – Accelerating gradient and cumulative number of BDs in the structure as a function of the number of RF pulses. Blue dots falling below the main envelope are due to power ramping after a BD event.

the beginning of April 2017 the RF pulse length was increased to 900 ns, with a few days of conditioning at 600 ns prior to that. This longer pulse length, which ensures a flat-top profile of the transmitted power in the cavity, is being tested at higher accelerating gradients than 50 MV/m. At the moment of writing, the cavity reached approximately 52 MV/m, and it is still ramping. The conditioning process is not yet finished at the moment of writing.

So far, the BTW prototype showed a conditioning speed slightly lower than the one showed by CLIC and KEK cavities, though consistent with those values (Fig. 5.13). In fact, those cavities have a design RF pulse length of 250 ns, and they ended the first conditioning run with a 50 ns pulse length in around 1e8 number of pulses. The BTW prototype finished the first conditioning stage with a 350 ns pulse length at approximately 1.3e8 pulses. However, the design pulse length for this cavity is 2.5 μs, thus a factor 7 difference, instead of the factor 5 of CLIC cavities, that, in conclusion, started their conditioning at a more challenging pulse length.

The vacuum pressure in the cavity showed a decrease in time, from approximately 2e-8 at the beginning of the test to approximately 4e-9 in April 2017. While the cavity was baked,the power load was not, and this is the main reason of this trend.

5.2.4 BD identification

A BD manifests with a modification of the reflected and transmitted signals with respect to a nominal pulse. At the same time, one can observe deviations in the FC signals. As discussed in detail in the next Section, the BTW prototype peculiar RF design reflects into a variable RF

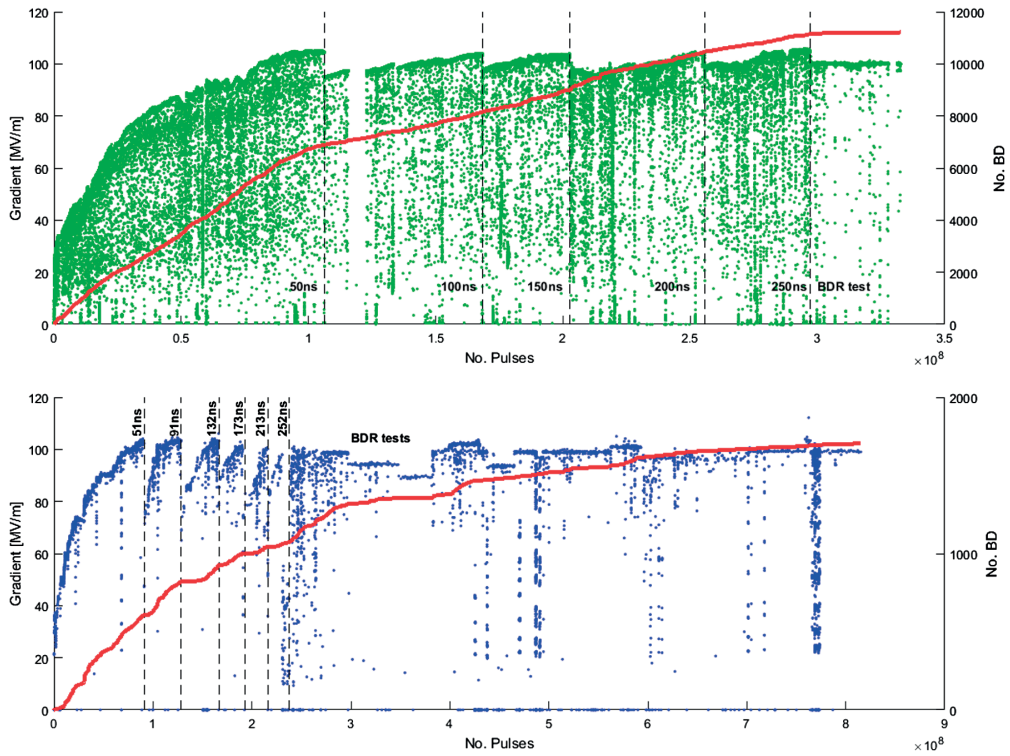

Figure 5.13 – Summary of CERN TD26CC and KEK TD24R05#4 high gradient tests [72].

signals behaviour as a function of the BD location in the cavity. Instead, the BDs are always easily detected by FCs, and in the experiment so far all the events have been recorded in this way.

To convince the reader, three cases of the 350 ns RF pulse length run are presented hereafter. First, an example of nominal RF and FC signals is shown in Fig. 5.14. The upstream FC, i.e. the FC positioned at the RF input coupler side, records a larger signals thanks to the dark current preferred capture direction, which is discussed in Section 5.3. At the same time, one can notice the triangular shape of the transmitted signal. With an approximately 200 ns filling time, the 350 ns RF pulse length used in the first stage of the conditioning does not allow to reach a stable flat-top.

As a second example, a BD event is shown in Fig. 5.15. One can notice that both the RF and the FC signals show a significant deviation with respect to a normal pulse shape. The reflected signal during the BD matches, in amplitude, the incident signal, while the transmitted one drops. This is a classic behaviour during a BD. However, for many events recorded during the BTW prototype test, the RF signals do not show such a clear trend (Fig. 5.16). In this last example, the BD is occurring towards the end of the RF pulse. While it is clearly noticeable from the FC signals, it is hardly to do so by observing the RF signals.

One could argue that the RF response of the cavity is driven by the localization of the BD along

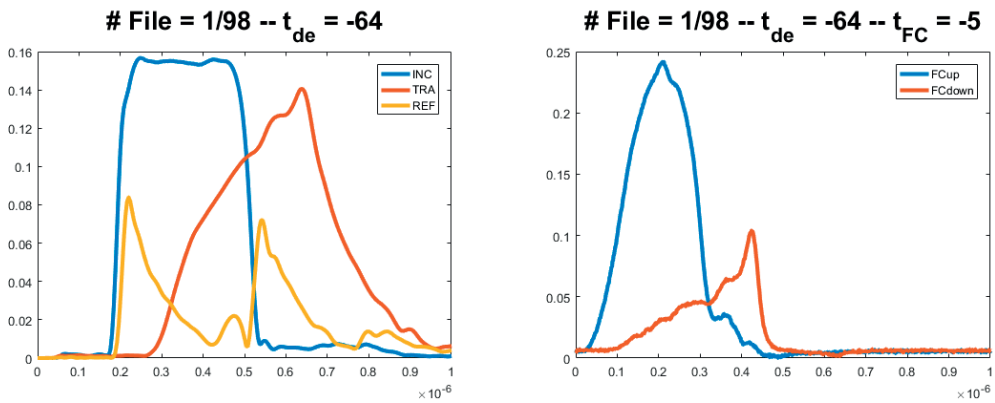

Figure 5.14 – Nominal incident (INC) reflected (REF) and transmitted (TRA) RF signals (left) and upstream FC and downstream FC signals (right).

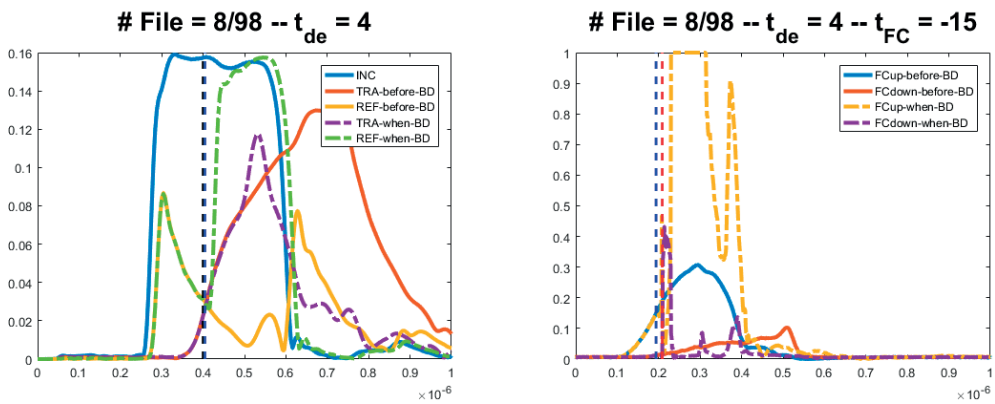

Figure 5.15 – BD incident (INC) reflected (REF) and transmitted (TRA) RF signals (left) and upstream FC and downstream FC signals (right), with comparison with a nominal pulse before the BD event, for a RF pulse length of 350 ns. In this case study, the RF signals show a clear deviation from nominal ones during the BD.

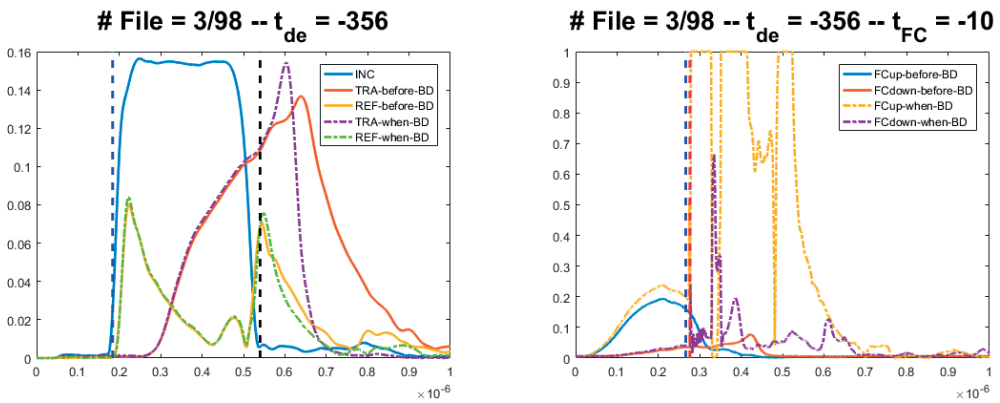

Figure 5.16 – BD incident (INC) reflected (REF) and transmitted (TRA) RF signals (left) and upstream FC and downstream FC signals (right), with comparison with a nominal pulse before the BD event, for a RF pulse length of 350 ns. In this case study, the RF reflected signal does not show a clear deviation from nominal one during the BD.

the RF pulse. In particular, to early BDs correspond large reflected signals, and vice-versa for late BDs. This is surely a major factor, but a preliminary analysis of BDs during the 900 ns RF pulse length conditioning phase revealed that the phenomenon can not be explained purely in this way. In Fig. 5.17, a clear BD is presented, where the reflected signal matches the incident one. In this case, the BD is occurring at the end of the RF pulse, and approximately in the middle of the cavity (see Section 5.2.4). Fig. 5.18 shows instead the example of a BD where the reflected signal is approximately one half of the incident one. This case has been chosen because the BD localization in time is very close to the previous case. This time however, the there is a 3 dB ratio between the reflected and the incident signal.

In the next Section, an attempt to characterize these observations will be presented, together with a discussion on the longitudinal positioning of BD across the cavity with the so-called edge method.

BD positioning in the structure

HFSS has been used with the goal of simulating BD in different regions of the structure. Since the Sc field has a maximum on the noses and on the coupling holes, those parts of the cavity were considered. The BD have been simulated by obstructing a certain volume of the geometry, either a coupling holes, or the gap region. The results are hereafter presented and discussed.

The dispersion curves for the input and output cells of the BTW prototype are shown in Figure 5.19, together with the dispersion curves in case one coupling hole of the RF cell is obstructed. One can notice that in both curves, for the simulated BD case the operating frequency is outside the passband. So, from theory, there should be total reflection in case of a BD obstructing completely a coupling hole, independently on its location along the structure. However, as shown in Fig. 5.21, this is not entirely the case on a whole structure (see Fig. 5.20).

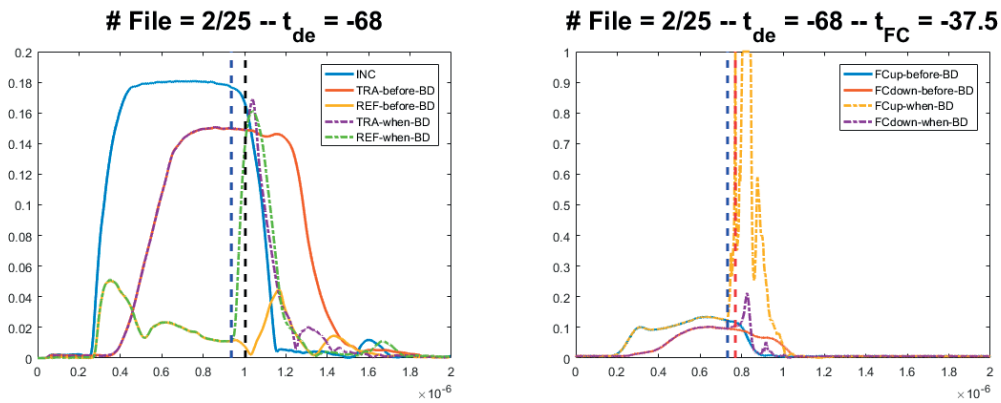

Figure 5.17 – BD incident (INC) reflected (REF) and transmitted (TRA) RF signals (left) and upstream FC and downstream FC signals (right), with comparison with a nominal pulse before the BD event, for a RF pulse length of 900 ns. In this case study, the RF signals show a clear deviation from nominal ones during the BD.

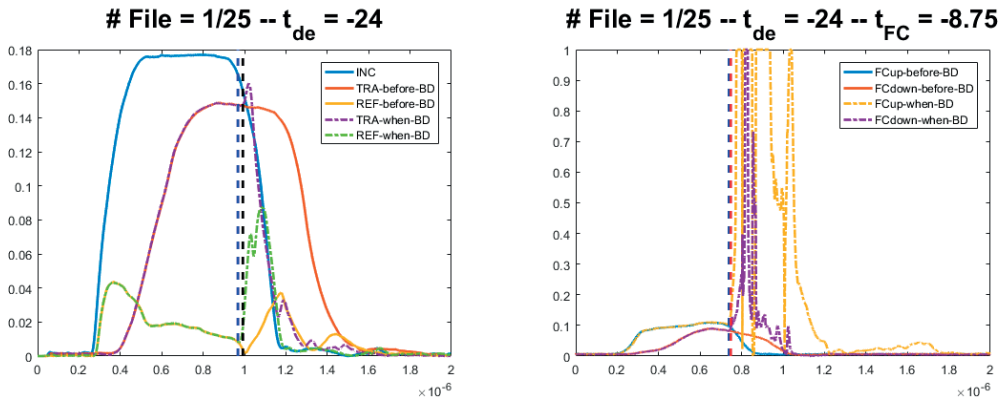

Figure 5.18 – BD incident (INC) reflected (REF) and transmitted (TRA) RF signals (left) and upstream FC and downstream FC signals (right), with comparison with a nominal pulse before the BD event, for a RF pulse length of 900 ns. In this case study, the BD REF signal has a lover magnitude with respect to the previous case.

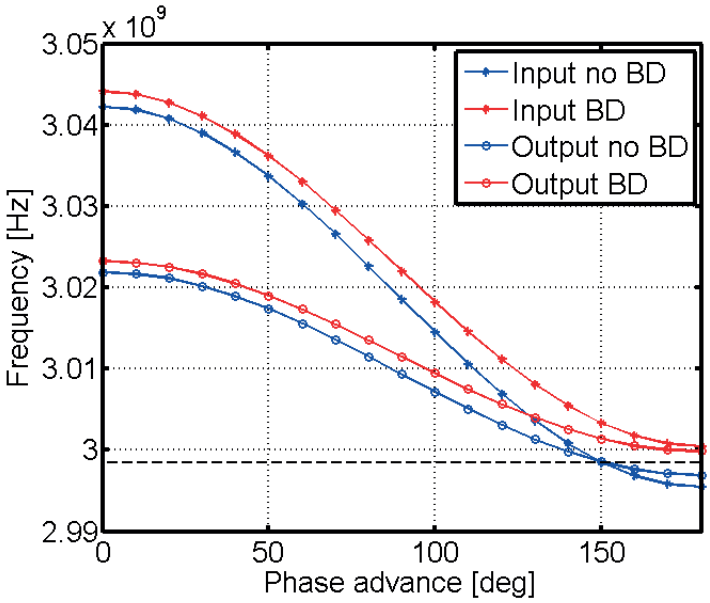

Figure 5.19 – Comparison between input and output cell dispersion curves. Reference case and BD simulation by obstructing one RF cell coupling hole.

Nevertheless, on the single RF cell, the effect is slightly worst for the input cell case, that has the larger group velocity and bandwidth. So one should expect a larger reflection if the BD occurs in a coupling hole at the input rather than towards the structure output. This difference is however not observable when simulating the whole cavity geometry, as hereafter discussed.

HFSS simulations performed on the cavity 3D geometry (Fig. 5.20) highlighted the reflection difference between BD simulated on the noses and on the coupling holes, as shown in Fig. 5.21. In particular, the S11 is much higher when the BD happens on a RF gap, rather than on a coupling holes. A second remark concerns the reflection as a function of the BD position across the cavity: the closer is the BD to the output, the lower is the reflection. There is a pretty linear behaviour of the reflection as a function of the BD position across the regular cells

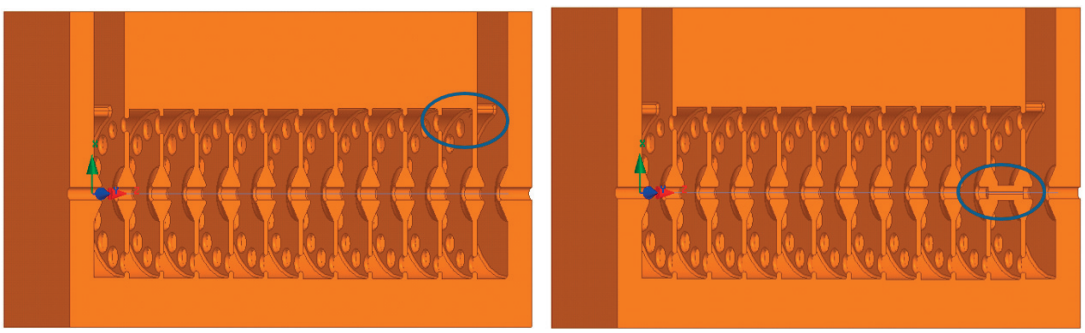

Figure 5.20 – Sketch of the BTW prototype simulated with HFSS. Example of BD simulation in the top hole of the 11th iris (left) and in the 11th cell nose region (right).

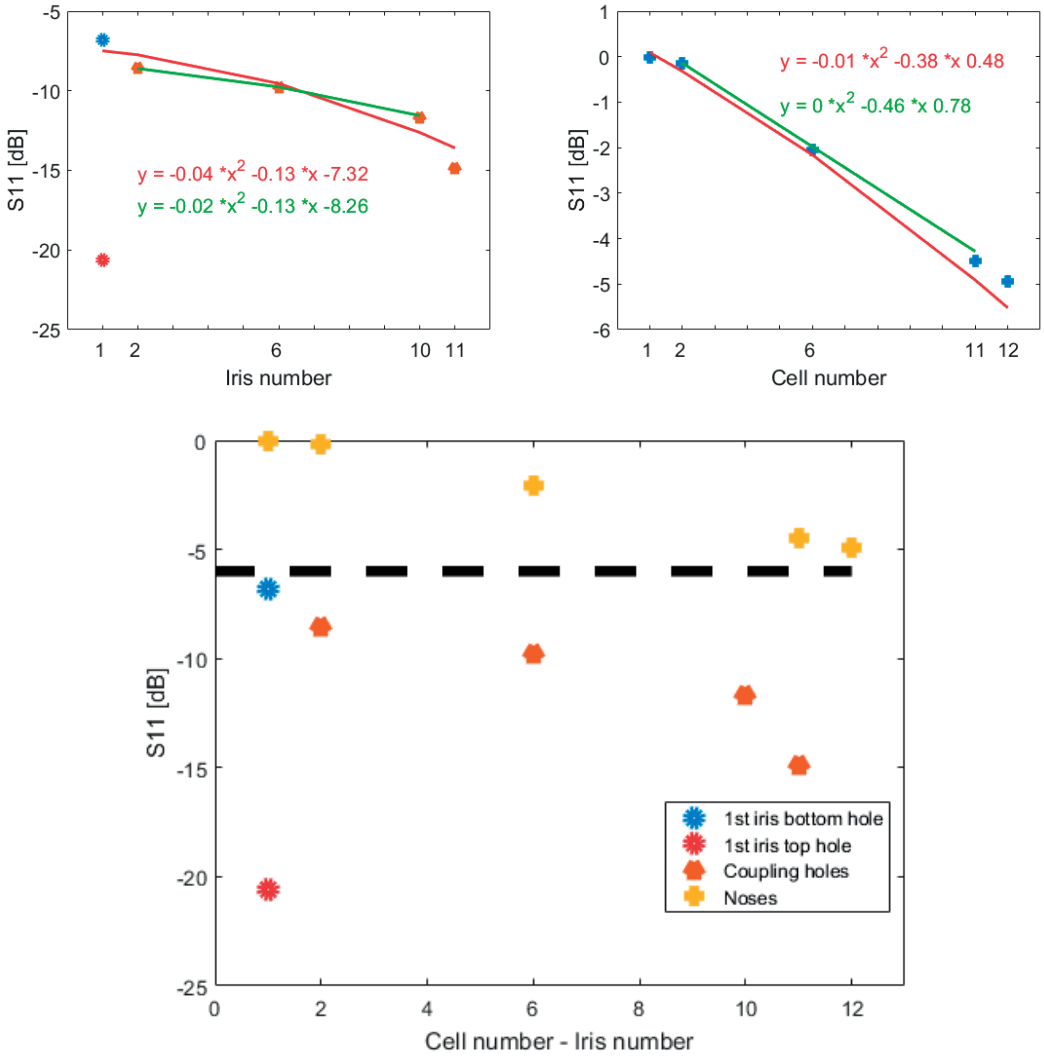

Figure 5.21 – Simulated total structure reflection as a function of the BD positioning along the structure: on the coupling holes (top left), on the noses (top right) and summary (bottom).

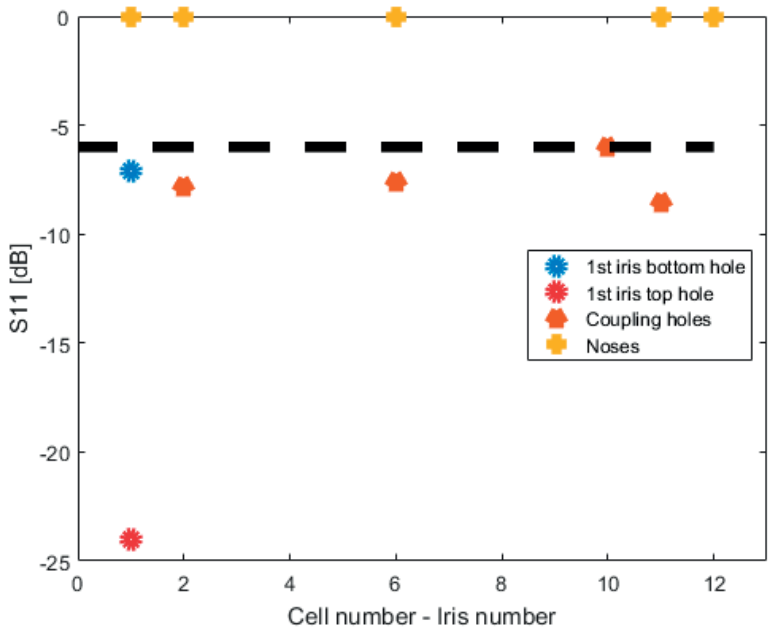

Figure 5.22 – Simulated total structure reflection as a function of the BD positioning along the structure in case of lossless cavity walls.

(green curves in Fig. 5.21 top). This linear trend is entirely due to the power attenuation, while the different group velocity across the RF cells is too low to influence in this regard. In fact, if the BDs in the cavity are simulated considering lossless RF surfaces, the reflection results are the same regardless the longitudinal positioning across the cavity, as shown in Fig. 5.22.

End-cells deserve a dedicated discussion. Since they represent a deviation from a regular tapered cavity, also a BD occurring there shows non-linear behaviours (red curves in Fig. 5.21 top). Quite peculiar is the response of the input cell: it shows a quite low reflection if the BD occurs on the coupling hole close to the waveguide slot, which has the smallest radius (see Section 2.4.4), while having a greater than linear response in case the BD occurs on the bottom coupling hole.

The simulation results presented in Fig. 5.21 would allow to differentiate between BD happening on the noses and on the coupling holes along the structure, simply by observing the S11 parameter. However, measured results do not show such a well defined distinction, so the longitudinal positioning is not achievable with this method.

One could think of differentiating the BD occurring on the cavity noses from those occurring on the coupling holes. There is in fact, from Fig. 5.21 bottom, a quite defined difference in terms of total reflection. The observation of the reflected signal as a function of the number of RF pulses would hint that this is the case (Fig. 5.23 left). While the general trend is upward because of the ramp of the incident power, it is possible to notice a clustering of reflected

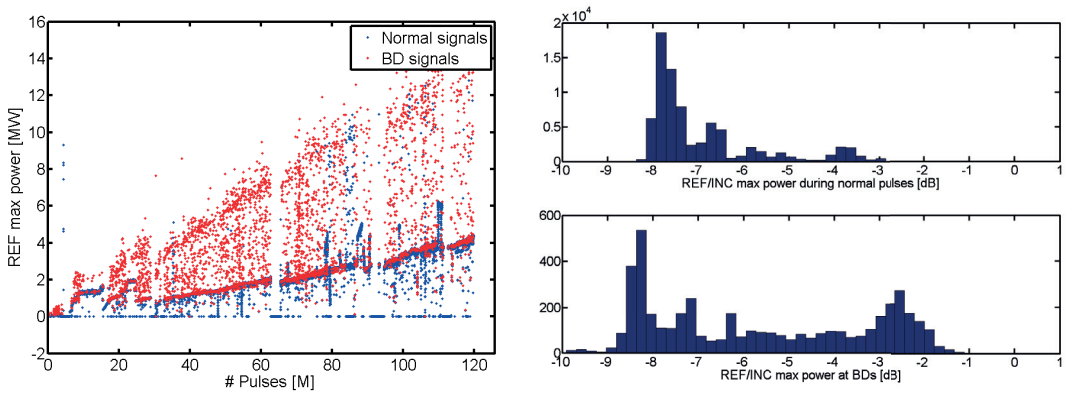

Figure 5.23 – Reflected signal during normal pulses (blue) and BD events (red) to the left, and S11 histogram on the right.

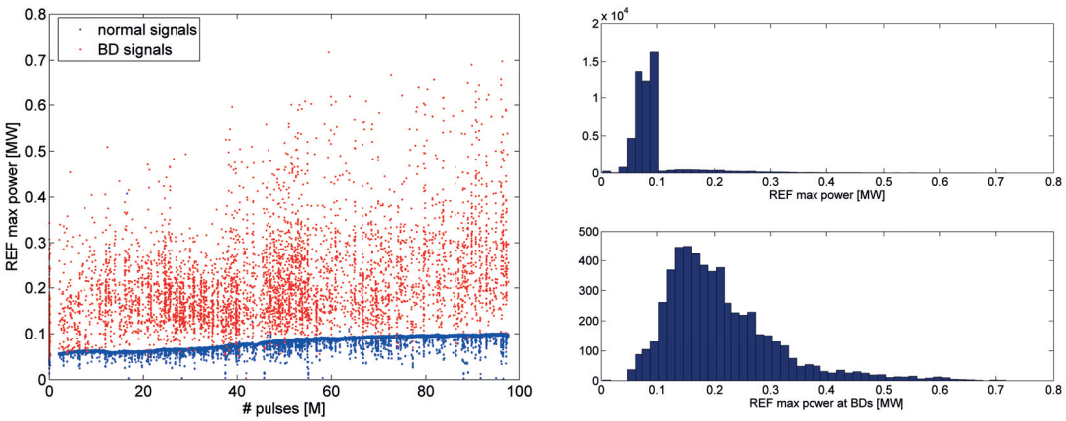

Figure 5.24 – CLIC TD26CC structure reflected signal during normal pulses (blue) and BD events (red) to the left, and reflected power histogram on the right. Data are not scaled. Courtesy of Theodoros Argyropoulos, CERN.

signals on the bottom part of the range, and on the upper part of it. In particular, for many BDs the reflected signal does not change with respect to the normal pulses. This distribution is more clear in a histogram plot of reflected signal divided by the input one, in dB (Fig. 5.23 right).

For comparison, one could consider the CLIC TD26cc cavity. This is an E-coupled cavity, which presents the maximum of Sc and E-field on the walls close to the beam axis. The reflected distribution in this structure is shown in Fig. 5.24. It is evident a more uniform distribution of the reflected power, that in case of a BD is always higher than during a regular pulse.

One should however bare in mind that the positioning of the BD along the RF pulse length has as well an impact on the reflected signal, as highlighted in the previous Section. In particular, all those BDs occurring towards the end of the pulse length will show a maximum peak

reflection as the one of a nominal pulse, because of the initial peak in the reflection pulse shape.

In addition, one could argue whether it is possible to detect BDs occurring on the coupling holes. In fact, it is not straightforward that in those cases the discharged electrons can reach the FCs, considering that they should travel from the coupling holes to the bore region, and eventually out of the cavity.

At the end of the high gradient test, it will thus be very interesting to open the cavity and study the internal surfaces, to clarify whether BDs occurred on the coupling holes, thus confirming the Sc model, and how BDs distributed across the cavity.

Longitudinal positioning

CLIC study developed several methods to longitudinally locate the BDs in their cavities. One of these can be applied to the BTW prototype, though with some cautions. The BTW prototype and the CLIC cavities in fact have some major differences. Firstly and most importantly, CLIC structures are electrically coupled, with the Sc distribution having a maximum near the bore aperture. They also do not present nose cones near the bore aperture, thus there are not major obstacles to electron discharges flowing to the Faraday Cups. In addition, the group velocity is reasonably high, being, on average between input and output cell, approximately 1.2% of the speed of light. The BTW prototype instead is a magnetically coupled cavity with nose cones. The Sc distribution, as discussed in Section 2.4.2, has a maximum on the noses and on the coupling holes. Thus, BD are likely to occur on the noses all along the cavity with equal probability, but also on the coupling holes of the cavity. The probability of a BD occurring on a coupling holes should decrease along the structure, given the decrease of Sc as discussed in 2.4.2. As shown later, the RF response of the cavity is different whether the BD is located on the noses or on the coupling holes. Finally, the group velocity is remarkably lower than the CLIC cavities, with an average between input and output cell of approximately 0.3% of the speed of light.

The longitudinal positioning of BDs along a cavity is achievable with the so-called *edge method* (Fig. 5.25).

When a BD is detected, its reflected and transmitted signals are compared with the those the pulse before the BD. Since a BD manifests with a modification of the reflected and transmitted signals, it is possible to retrieve the times, along the two pulses, at which the BD occurs. Eventually, depending on the time difference between the reflected and the transmitted pulses, one can locate the BD along the z-axis of the cavity. As previously discussed, in the BTW cavity test many BD cases the reflected, as well as the transmitted, power is very little perturbed, thus the exact localization in time of the BD is uncertain (see Fig. 5.16). This problem affects remarkably the longitudinal BD localization during short RF pulse lengths, while already for the 900 ns run the precision increases.

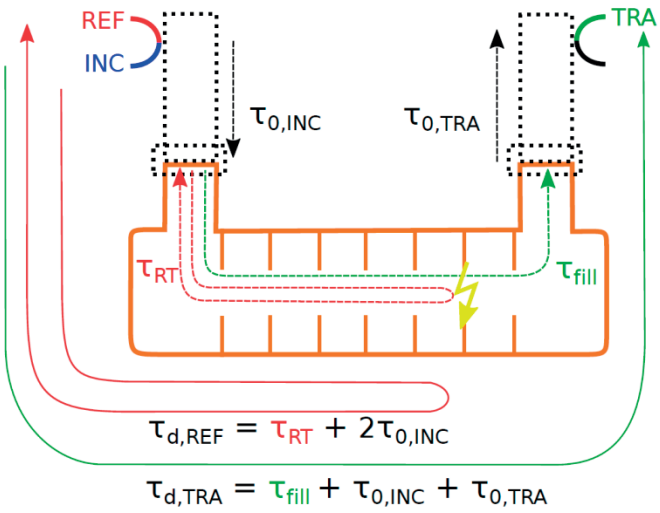

Figure 5.25 – Sketch explaining the edge method [73].

The very same methodology can be applied to the FC signals. A third method investigates the phase of the reflected power. In case of $2\pi/3$ cavities, the phase can only be a multiple of $\pi/3$. However, the $5\pi/6$ RF phase advance of the BTW prototype makes this method difficult to apply (see Fig. 2.47).

5.3 Dark current analysis

At the moment of writing, to the author knowledge the problem of electrons dynamics in a non ultra-relativistic proton accelerator has not been addressed. Here an attempt to characterize the problem is presented.

Theoretically, the problem does not have an analytical solution. Considering simply the Ez component of the EM field, one can find the kinetic energy of the particle by integrating along z the Equation:

$$dW = eE_z(z,t)dz. \tag{5.2}$$

In case of a backward travelling wave, the z component of the electric field can be rewritten as:

$$E_z(z,t) = E \cdot e^{i(-kz-\omega t+\phi)}. \tag{5.3}$$

Since the electron β can vary in the range 0 to 1, the most correct way to integrate Eq. 5.2 is in time rather than in space. Defining βc the velocity of the electron, and remembering that

$k = \omega / v_{ph}$, where v_{ph} is the phase velocity of the wave, one has:

$$E_z(z,t) = E \cdot e^{i\omega t(-\frac{\beta c + v_{ph}}{v_{ph}} + \phi)}. \tag{5.4}$$

One shall not forget that $k = \omega / v_{ph}$ holds only for a single harmonic wave, or in case of an RF cell where the particle velocity change over the gap is negligible. This is clearly not the case.

Anyhow, for a single harmonic wave, the energy gain of an electron in a travelling wave E-field along one direction can be obtained integrating:

$$dW = eE \cdot e^{i\omega t(-\frac{\beta c + v_{ph}}{v_{ph}} + \phi)} \cdot \beta c \cdot dt, \tag{5.5}$$

which is not analytically solvable, given that :

$$\beta = \sqrt{\frac{(1 + \frac{dW}{E_0})^2 - 1}{1 + \frac{dW}{E_0}}}. \tag{5.6}$$

In case of relativistic structures, where the phase velocity v_{ph} matches the speed of light, the problem is simpler, and an analytical solution exists as discussed in [74]. For field-emitted electrons with near zero initial momenta the condition for axial capture and cumulative acceleration is then given simply by [75]:

$$E_c = 1.6/\lambda, \tag{5.7}$$

thus having a theoretical capture gradient for S-band relativistic structures of 16 MV/m, and of 64 MV/m for X-band ones. Eq. 5.7 is very simple because, in $\beta = 1$ accelerators, as soon as the electrons gain enough momentum to move at the speed of light, they then move synchronously with the wave. The dependence with the accelerator frequency is also straightforward, by remembering Eq. 5.2.

Since it was not possible to find an analytical solution of the problem, hereafter is discussed a numerical approach to it.

The motion of a bunch of electrons in a cavity designed for $\beta < 1$ particles was simulated considering three levels of accuracy:

- first a single harmonic $\beta = 0.38$ wave, with 1D motion;
- secondly, the Ez component of the BTW prototype, with 1D motion;

- lastly, RF-Track was deployed, and the real 3D EM field map was adopted, performing a 3D tracking.

In both the three cases, an initial distribution of 12 electrons with zero initial momentum was considered uniformly distributed along the z-axis of the cavity, thus one electron at the middle of each RF gap.

For the first two cases, the algorithm is bases on the integration in time of the particle kinetic energy gain:

$$dW = eE_z(z,t)\beta c \cdot dt. \tag{5.8}$$

An integration step of 0.1 ps was chosen. In such way, a relativistic electron would travel a maximum of 0.3 mm in a time step. Further refinements of the integration step did not change the simulation results.

It is clear that the first two methods cannot have enough details to correctly describe the physics of the phenomenon. In fact, while the electron tracking along the z component can be well simulated, they completely neglect any 3D motion, and so any loss of electrons except for those which exit the longitudinal boundaries. They are thus methods useful only to understand the basic physics.

Hereafter, four cases are discussed. The tracking of electrons and protons in a single harmonic $\beta = 0.38$ 3 GHz travelling wave, and in the z component of the BTW prototype electric field. For comparison, the case of $\beta = 1$ is also presented. This can be obtained by stretching the $\beta = 0.38$ E-fields. The Ez field in the 4 cases is shown in Fig. 5.26.

The motion of a synchronous particle is the same, on average, in the two cases, provided that the average effective accelerating gradient is the same. The motion of a synchronous proton was simulated in Fig. 5.27.

If electrons are tracked, the two field descriptions do not lead anymore to the same results. The $\beta = 0.38$ and the $\beta = 1$ cases are reported in Fig. 5.28 and 5.29, respectively. A simulation time of 1.8 μs was chosen, being this a bit higher than the time needed by the synchronous proton to cross the cavity.

In the simulations of the $\beta = 0.38$ structure, the motion is remarkably more chaotic. In the single harmonic approximation, the electrons get eventually capture by the 0 deg bucket, and move with the phase velocity of the wave, oscillating around the equilibrium, and moving with the same velocity of the synchronous proton (green line in Fig. 5.28 bottom right). In the real Ez field component, the combination of gaps and drift spaces do not allow such capture, resulting into a incoherent motion. In other words, an equilibrium condition does not exist in this case, and this because the electrons have a too high momentum gain to remain trapped

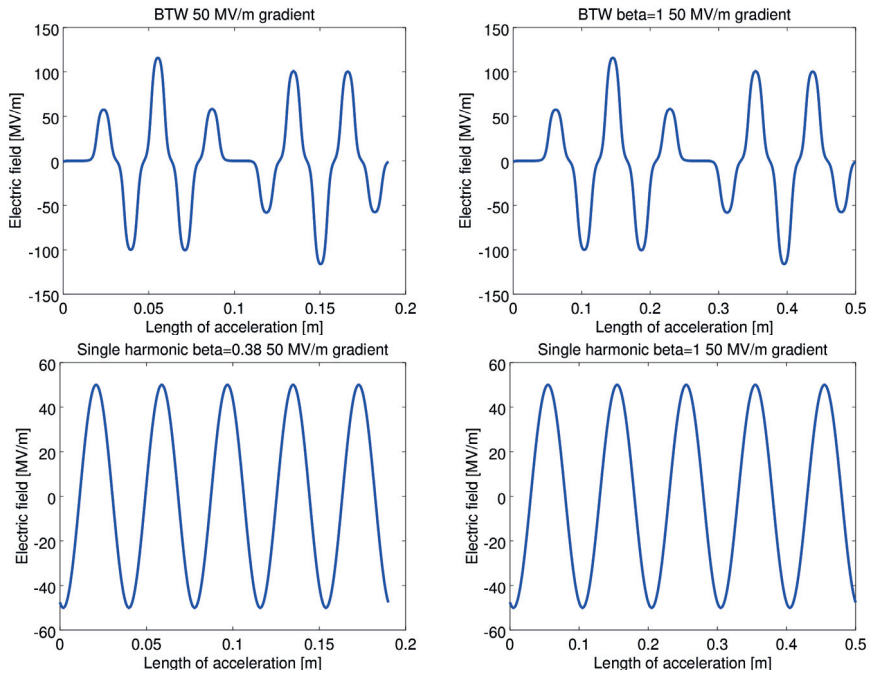

Figure 5.26 – Electric field along z in the BTW structure (top) and first harmonic travelling wave (bottom); for $\beta = 0.38$ (left) and $\beta = 1$ (right).

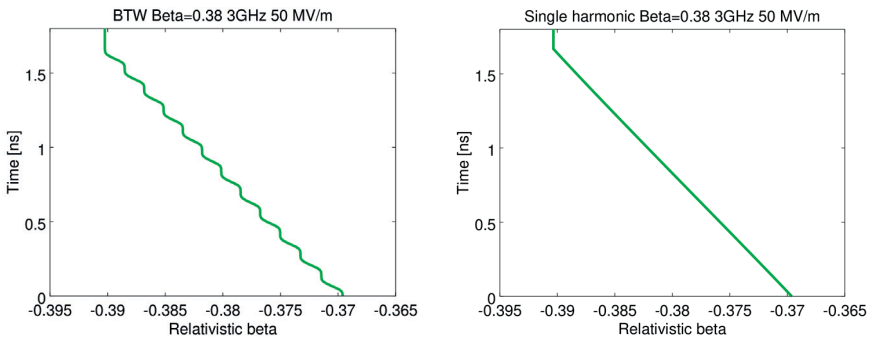

Figure 5.27 – Proton tracking in a 50 MV/m field, BTW structure Ez field (left) and single harmonic TW (right).

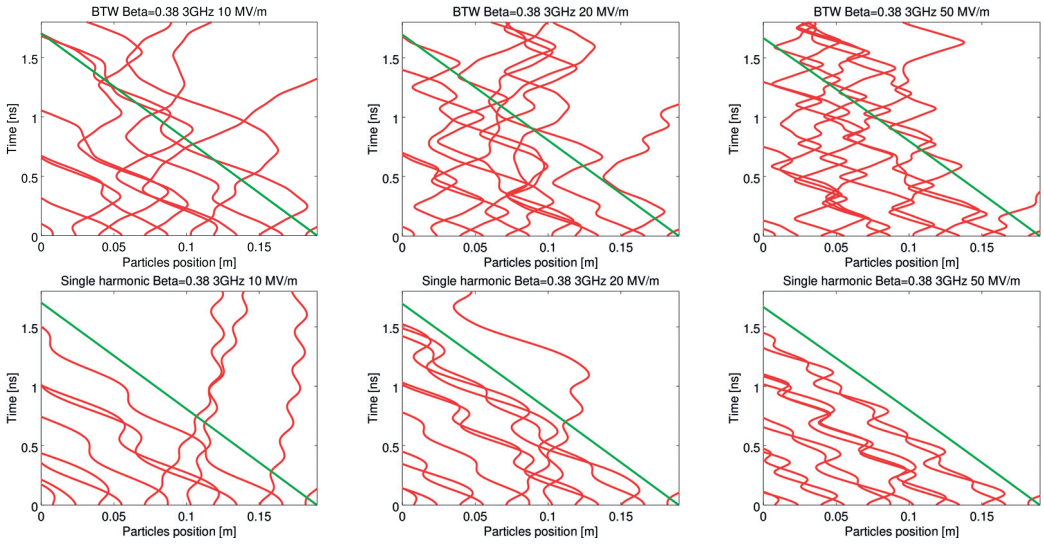

Figure 5.28 – Comparison between a $\beta = 0.38$ electric field for different accelerating gradient. BTW structure Ez field (top, as in Fig. 5.26 top left)) and single harmonic TW (bottom, as in Fig. 5.26 bottom left)). Electrons in red, and $\beta = 0.38$ synchronous proton in green.

into the linac longitudinal bucket.

Instead, if a $\beta = 1$ Ez field is considered, the capture condition manifests in a clearer way (Fig. 5.29), in agreement with Eq. 5.7.

It is possible to simulate the dark current capture at the two Faraday cups by recording the number of electrons crossing the boundaries of the field map. An attempt in this sense is shown in Fig. 5.30. In this case however the electrons cannot be lost on the cavity walls, so eventually they will either exit the boundaries or remain in the field map infinitely. For this reason the graphs in Fig. 5.30 do not show a notable difference in the mean signal. Thus a 3D motion is eventually necessary to attempt to simulate the problem.

RF-Track was used to perform the full 3D simulations of the electron distribution considered so far, thus 12 electrons with zero initial momentum uniformly distributed along the z-axis of the cavity To higher electric fields correspond higher electron losses on the cavity walls, and this result is shown in Fig. 5.31

It is interesting to comment that a zero-momentum electron distribution on the z-axis should not, theoretically, display a 3D motion in a ideal cavity, as on the z-axis of such a cavity only the z component of the electric field is present. However, a field map exported from a electromagnetic code shows some degrees of noise such that on the z-axis transverse components of the electromagnetic fields are present. This, together with the low rest energy of the electrons, explains their 3D motion.

As a second remark, one could notice that the electrons pattern in the 3D case does not entirely correspond to the 1D case, for those electrons not lost on the cavity walls. This respects the

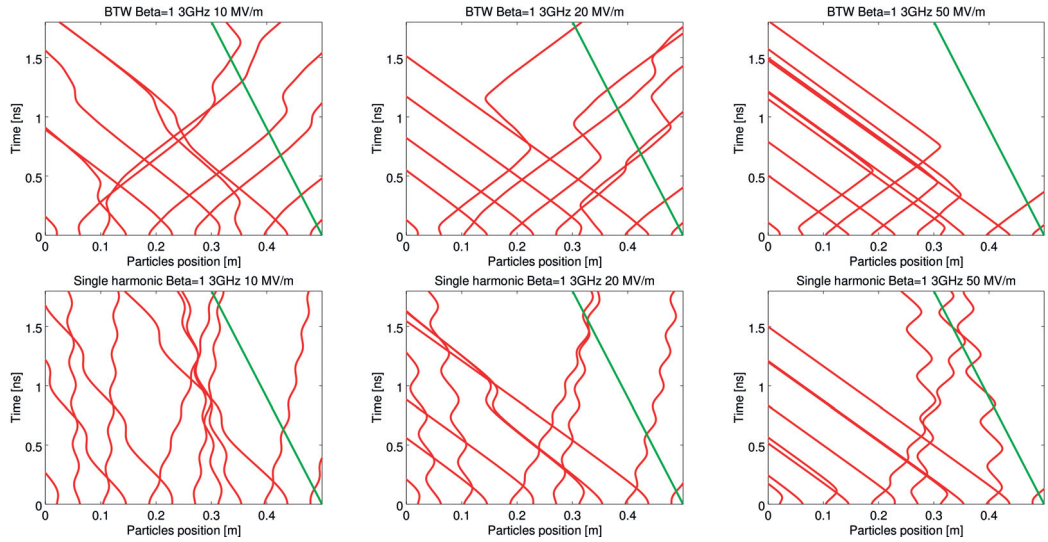

Figure 5.29 – Comparison between a $\beta = 1$ electric field for different accelerating gradient. BTW structure stretched Ez field (top, as in Fig. 5.26 top right)) and single harmonic TW (bottom, as in Fig. 5.26 bottom right)). Electrons in red, and $\beta = 0.38$ proton in green.

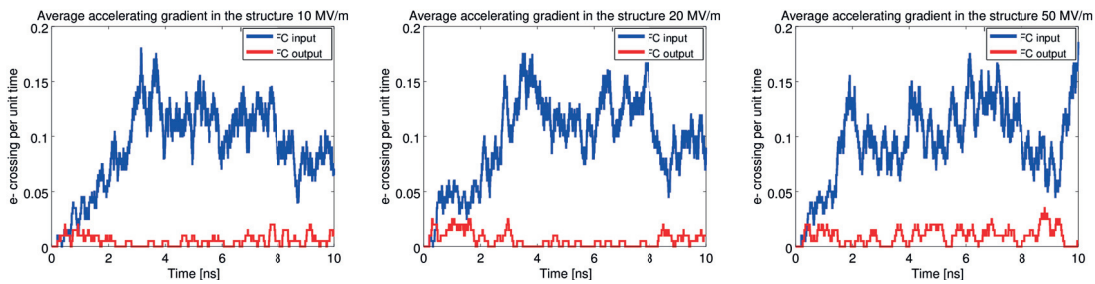

Figure 5.30 – Simulation of dark current at the FCs as a function of the accelerating gradient, considering the BTW structure Ez component. In blue the simulated electrons crossing the left-hand boundary (correspondent to the upstream FC), in red the ones crossing the right-hand boundary (correspondent to the downstream FC).

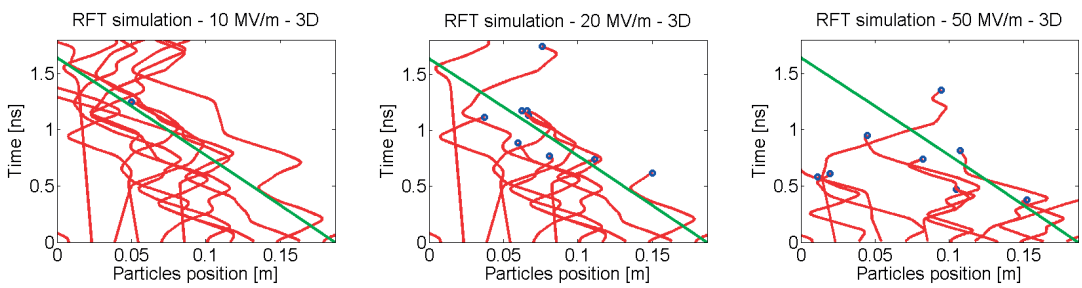

Figure 5.31 – RF-Track 3D tracking of electrons in the BTW cavity. Electrons in red, and synchronous proton in green. Blue circles are lost electrons, i.e. electrons that have hit the cavity walls.

Panofsky-Wenzel theorem [1] since for electrons motion the paraxial assumption does not hold. In conclusions, electron longitudinal motion is affected by their transverse position in the cavity.

There was not time to implement a complete simulation, involving the Fowler-Nordheim [76] dependence of the dark current emission on the surface electric field and on the cavity geometry, considering thus a more realistic initial distribution of the electrons. This activity is left to future works on the subject.

5.4 First results of the high gradient test

At the end of May 2017, the structure accumulated 1.8e8 pulses. As explained in Section 5.2.3, this quantity defines the level of conditioning of a cavity, and for this structure the process is not finished yet. It is thus not possible to present a reliable BDR scaling law at this stage, and future works shall have a final word on the behaviour of this prototype.

However, it is still possible to draw some preliminary conclusions. The BTW prototype has a design maximum surface electric field E_s of 200 MV/m, as the CLIC cavities. In Fig. 5.32 top, this quantity is compared as a function of the number of RF pulses, adopting the scaling law proposed in [72]:

$$\frac{E^{30} \cdot \tau^5}{BDR} = const \tag{5.9}$$

If, instead, a power of 3 is considered for the pulse length, as proposed in [30], one obtains the curves of Fig. 5.32 middle. Finally, one could simply compare E_s without any scaling law, as proposed in Fig. 5.32 bottom. So far, it seems that the best scaling law which describes the conditioning status of X-band and S-band cavities is:

$$\frac{E^{30} \cdot \tau^3}{BDR} = const. \tag{5.10}$$

On the other hand, as highlighted in Section 5.2.3, the number of BD does not seem to define the conditioning level of the cavity. When one compares the surface electric field of CLIC cavities and the S-band prototype, scaled as above, as a function of the cumulative number of BD, the three cavities show different behaviours (Fig. 5.33).

The three cavities can also be compared in terms of a scaled modified Poynting vector Sc. This

[1] The Panofsky-Wenzel theorem states that, in a cavity, to a transverse variation of the longitudinal kick must correspond a transverse deflection kick. This is valid only under the assumption of 1D motion along the cavity.

has been done considering the law proposed in [30] [7]:

$$\frac{Sc^8 \cdot \tau^3}{BDR} = const, \tag{5.11}$$

which has been used in the RF design of the cavity, and a more classic scaling law with power 15 for Sc and 5 for τ. These results are presented in Fig. 5.34, top and bottom respectively. One could conclude that the maximum surface electric field is the field quantity that better describes the high gradient limits of the three cavities. However, it has to be reminded that E_s is similar, while Sc is different for the three accelerating structures. Thus only when the BTW prototype will be fully conditioned it will be possible to study in detail the scaling law that relates the BD limits of normal conducting X-band and S-band cavities.

As a final remark, the structure was designed considering as limiting quantities the maximum surface electric field, 200 MV/m, and the maximum modified Poynting vector Sc. This last quantity was rescaled from CLIC data according to the law proposed in [30] [7], though also a more classic scaling law with power 15 for Sc and 5 for τ was considered, giving similar results. CLIC data were rescaled considering a Sc of 4 MW/mm^2, with a pulse length τ of 200 ns, corresponding to an estimated BDR of 10^{-6}. The pulse length considered for the BTW prototype was 2500 ns. Thus an Sc limit of 1.55 MW/mm^2 for the BTW prototype. However, later on in the design stage a maximum value of 0.75 MW/mm^2 was reached on the noses and coupling holes of the cavity, as a result of the optimization process and of the 200 MV/m surface electric field limit.

If then Eq. 5.11 is applied to the current 350 ns run, considering a nominal Sc of 0.75 MW/mm^2, one would obtain, for a fully conditioned cavity, a BDR of $8.3 \cdot 10^{-12}$ bpp/m. This seems, at the present stage, a challenging goal, since the BDR should decrease of approximately 6 order of magnitude from the present values.

So far the cavity did not developed any major hot spot. Assuming that the edge method (Section 5.2.4) provides a first order longitudinal localization of the BD in the structure, the number of BD as a function of their position and their time is reported in Fig. 5.35.

5.4.1 Remarks on frequency dependence and the Kilpatrick criterion

It is interesting to go back to the Kilpatrick criterion [77], and to draw some considerations on the BD frequency dependence. Though developed in an era before clean vacuum system were common, this law is still widely considered. In the Boyd formulation [78], it can be expressed as:

$$f[MHz] = 1.64 \cdot E_K^2 e^{-8.5/E_K}, \tag{5.12}$$

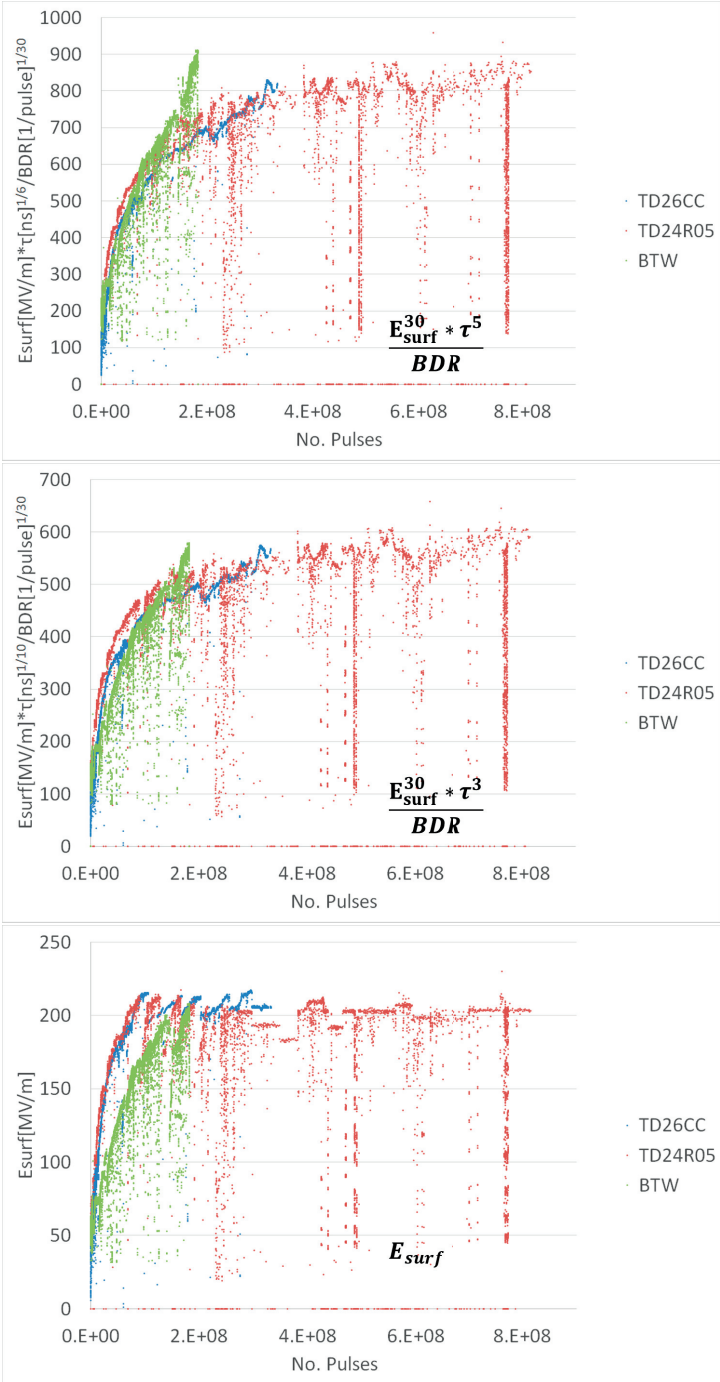

Figure 5.32 – Comparison between scaled maximum surface E-field of reference CLIC cavities and the BTW prototype. Reference power of 5 for the pulse length (top) and proposed in [30] and [7] power of 3 (middle). Non-scaled maximum surface electric field on the bottom.

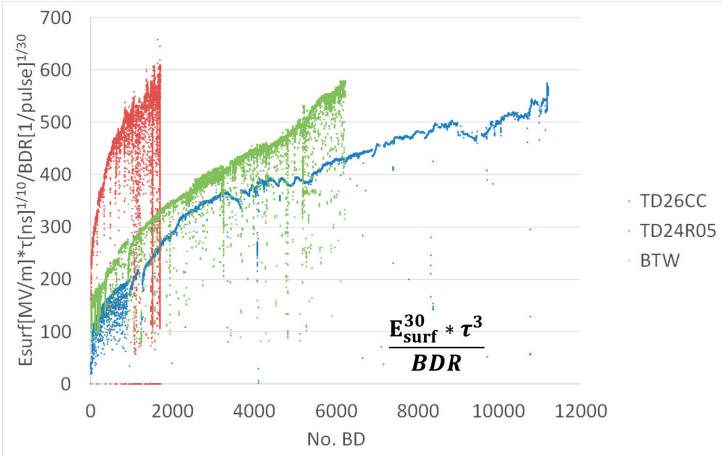

Figure 5.33 – Comparison between scaled maximum surface E-field of reference CLIC cavities and the BTW prototype as a function of the number of BD.

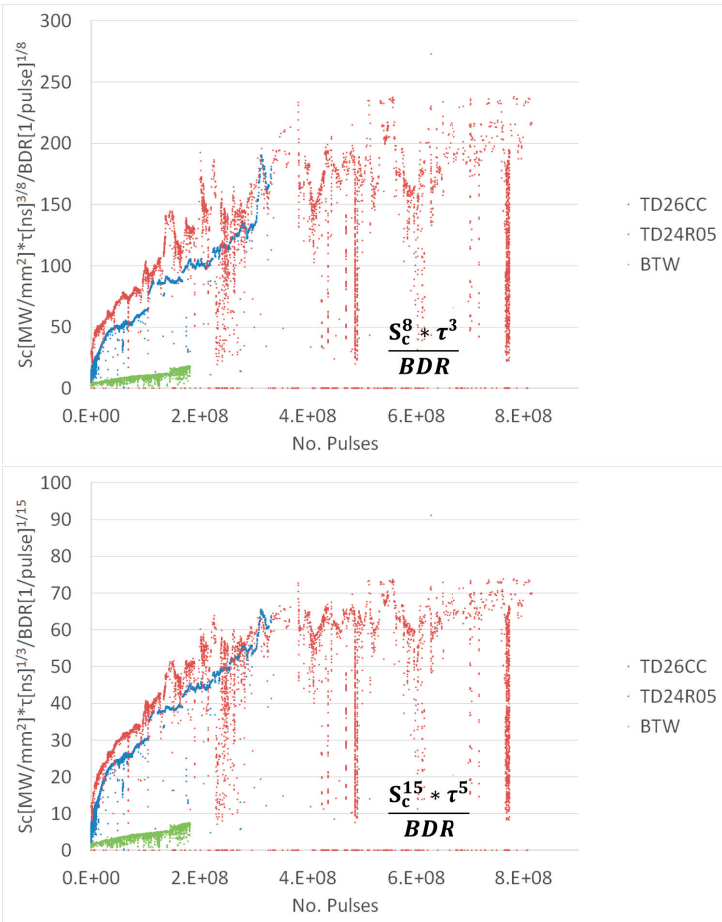

Figure 5.34 – Comparison between scaled modified Poynting vector Sc of reference CLIC cavities and the BTW prototype. Power of 3 for the pulse length (top), as proposed in [30] and [7], and reference power of 5 (bottom).

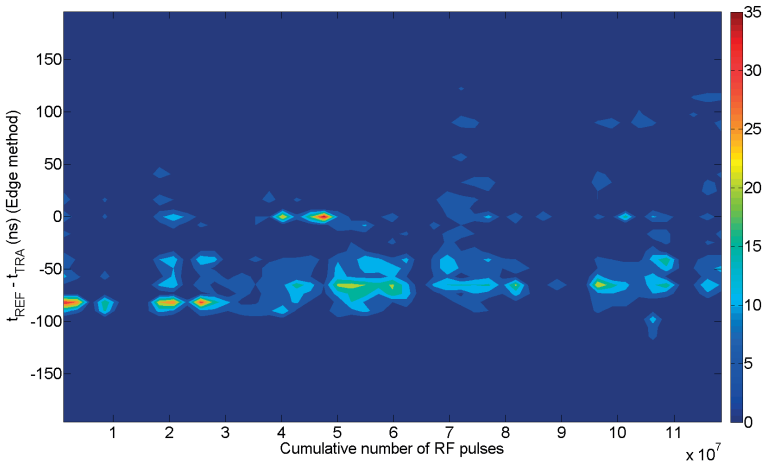

Figure 5.35 – BD density function as a function of the cumulative number of RF pulses and of the longitudinal position in the cavity.

where f is the cavity frequency, and E_K is the peak surface E-field limit for BD-free operation, expressed in MV/m. Thus, according to the Kilpatrick criterion, the cavity frequency defines the maximum gradient achievable. The pulse length is somehow considered with the *bravery factor b*. This is often introduced, considering as peak surface E-field the quantity $E_s = bE_K$. The bravery factor b is higher in case of low RF pulse length, and typically a value of 2 is chosen in case of pulse length lower than 1 ms. Interestingly, with a *bravery factor* of 2, a 12 GHz cavity has a Kilpatrick limit of 200 MV/m. However, a 3 GHz cavity would then have a limit of approximately 100 MV/m, which has been shown not to be the case. For those bounded to the Kilpatrick criterion, the BTW prototype has a *bravery factor* of 4. In conclusion, so far this experiment is confirming that, in the 3 to 12 GHz range, the BDR does not depend on the operating frequency. The main outcome of this experiment will be to define which is the defining BDR field quantity at 3 GHz, whether the maximum surface electric field, or rather the modified poynting vector Sc.

6 Conclusions

The goal of this thesis has been the design of two hadron therapy facilities based on linear accelerators.

The first project, called TULIP, explores the compactness limits of proton therapy linacs. The physical advantage of proton therapy over radiotherapy, discussed in the introductory Chapter, would lead towards the replacement of X-ray therapy machines by proton therapy ones. However, radiotherapy linacs are simpler, smaller and cheaper to build and operate. Ultimately, this economical advantage makes a large scale swap between the two technologies unrealistic at the present time.

TULIP is the attempt to design a proton therapy linac as compact as possible, and so as close as possible to a radiotherapy linac, in order to fit into already existing hospital buildings, and thus save on infrastructural costs. This idea has been widely appreciated by the market, as compact cyclotron-based proton therapy single-room facilities are now booming. For the first time, the TULIP design presented in this thesis permits to understand advantages and technical challenges of a compact linear accelerator solution for proton therapy.

Similar from a technical point of view, but fundamentally different in the main design guidelines, the second design studied in this thesis is a carbon ion therapy linac, called CABOTO. The use of carbon ion in radiotherapy oncology is motivated by their higher radio-biological effectiveness - RBE - in treating radio-resistant tumours. The downside is that they possess an higher mass per unit charge than protons, so carbon ion linacs are bigger, and more expensive. Specifically, carbon ions require twice as much momentum than protons to travel the same distance through matter, and twice as much accelerating voltage, in the most favourable case of fully stripped ions. Thus, a factor four lies between the overall voltage gain per nucleon of a carbon ion therapy linac over a proton one. Compactness is not anymore a wise option, since it would rocket the installation and power consumption costs. The CABOTO design explores thus a compromise between longer linacs and lower accelerating gradients.

As for TULIP, this is the first time that a linear accelerator solution is studied for carbon ion

therapy. Due to their higher costs and complexity, carbon ion therapy facilities are mostly public research centres. Few companies provide the accelerator technology, that so far is based only on synchrotron machines. The CABOTO linear accelerator proposed in this thesis has a number of advantages over them, particularly a lower power consumption, an higher output beam current and a quicker treatment time.

TULIP, discussed in Chapter three, can be summarized by a low gradient linac section, composed by a 750 MHz RFQ followed by an IH cavity operating at the same frequency. From 10 MeV up to 70 MeV, a 3 GHz DTL is considered. These three linacs are approximately 10 m long, and placed on the ground. The high gradient linac, the most characteristic part of the project, is foreseen to be mounted on a mechanical structure rotating around the patient, called gantry. The proposed TULIP design has a footprint of approximately 200 m^2, with an RF peak power installed of 125 MW and an estimated cost of 10.9 M€ for the accelerator part.

CABOTO, presented in Chapter four, is characterized by two linac sections of equal length, joined by a 180 deg bend beam line. The first section is composed, as in TULIP, by an RFQ followed by an IH cavity and by a DTL linac. The final energy of this section is 100 MeV/u. The second section is formed by an RF efficiency optimized CCL cavity, with a smaller bore radius with respect to TULIP. This, amongst others, permitted to decrease the power needs of the linac, which has been discussed being a key issue in a carbon ion linac. The proposed CABOTO design has a footprint of approximately 600 m^2, with an RF peak power installed of 260 MW and an estimated cost of 24.5 M€ for the accelerator part.

For both projects, new accelerating cavities have been designed, as discussed in Chapter two. Notably, two cavities captured most of the efforts, and were studied in greater detail. A 750 MHz IH cavity covering the 5 to 10 MeV range in TULIP, and 2.5 MeV/u to 10 MeV/u in CABOTO. This solution represents an ideal continuation, both from RF and beam dynamics point of view, to the CERN 750 MHz RFQ recently built and tested. It has been demonstrated that previously considered 3 GHz DTL solutions have a lower RF efficiency and beam acceptance, and an higher emittance growth. The 750 MHz IH solution was studied in detail from RF point of view, but it lacks a final mechanical design. A second cavity was instead built and tested: an high gradient 3 GHz backward travelling wave structure. The main goal of this prototype is to explore the BD limits of S-Band cavities, and it represents the completion of long-lasting collaboration between TERA Foundation and CLIC, aimed at redefining the maximum accelerating gradient reachable in medical linacs. The cavity is in fact being tested at a gradient more than twice what has been reached in previously tested cavities at the same frequency. Described in the same Chapter are a 3 GHz DTL solution, already built by colleagues in Frascati, Italy, and a high efficiency CCL operating at 3 GHz, for the CABOTO project. The number of RF cavities considered, operating at different frequencies, accelerating gradients, EM modes and bore apertures, permitted to end the Chapter with some, hopefully interesting, sensitivity considerations of RF normal conducting cavities design parameters.

The 3 GHz backward travelling wave cavity testing, presented in Chapter five, is ongoing. At

the time of writing, May 2017, the cavity is still in the conditioning phase. The structure is behaving quite closely to X-band CLIC and KEK high gradient cavities in terms of conditioning speed, and it has reached the target gradient of 50 MV/m, first at an initial pulse length of 350 ns, and more recently at a longer pulse of 900 ns. The cavity took approximately 10 weeks, 24/7, of RF pulsing at 25 Hz to reach for the first time the 50 MV/m at 350 ns.

In the last months of the thesis, some effort has been dedicated to the understanding of dark current capture in accelerator for non-ultra-relativistic particles. While for $\beta = 1$ cavities a very simple relationship defines the relationship between accelerating gradient and dark current capture, this is not the case anymore for cavities where the geometric β is lower than one. It was discussed that an EM field map representation of the accelerating cavity and a particle tracking code are both necessary to numerically solve the problem.

Almost all the beam dynamic simulations of this thesis have been performed using a novel tracking code, called RF-Track. Many peculiarities of the projects considered called for the development of a new tracking tool, as discussed in Appendix A. The start-to-end tracking of the beam through TULIP and CABOTO, considering EM field maps for all the accelerating cavities, is one of the biggest effort of this thesis. Especially for low-β cavities, any EM asymmetry can remarkably impact on the beam dynamics, thus their understanding and correction is of key importance to achieve a continuous beam tracking. In the CABOTO project for instance, the beam was generated at 2.5 MeV/u and it was tracked until 430 MeV/u, through more than 100 accelerating cavities - and relative focusing systems and matching sections - in a 50 m long lattice.

At the end of this thesis, the reader should have gained a deeper understanding of the use of linear accelerators for hadron therapy. Together with the main design parameters, this work presented a cost estimation of a proton and a carbon ion therapy linac, and it can be considered as a first conceptual design report of full linear solutions in hadron therapy.

Future activities in this field should concentrate on the integration of the linacs with other components, as the ion source, the beam diagnostic and dose delivery system. Amongst others, open topics to be further studied are the beam pulse to pulse stability, both in current and in energy, the experimental verification of the active energy variation principle, and the final beam line design with magnets capable of following the beam energy variation at the linacs repetition rate, or close to it.

A Beam dynamics and linac design codes used

A significant amount of time during this thesis was devoted to the development of beam dynamics codes and linac design codes. This choice was driven by the will to get deeper insight the physics of accelerators, and to improve programming skills. However, it is also justified by the thesis project, where linacs are studied:

- with different phase advance: π-mode for IH and CCL, $5/6\pi$-mode for BTW, 2π-mode for DTL;
- with tapered (IH and DTL) or constant (CCL and BTW) cell length per accelerating structure;
- with cylindrical symmetry (CCL and BTW) or with dipole asymmetries (IH and DTL);
- constant gradient (DTL, BTW and CCL) or constant voltage (IH) structures.
- with different q/m ratios: 1 for protons and 0.5 for fully stripped carbon ions and helium ions.

Many codes are already available, but they are often specific, and different ones should have been considered for different parts of the thesis. For beam dynamics studies, in particular, one can distinguish, in order of complexity, between:

- 2D codes, like Linac [79], which assume a cylindrical symmetry of the cavities;
- 3D codes with SW representation of the EM field, like TraceWin [80];
- 3D codes with complex field map representation, as ASTRA [81] and GPT [82].

It has been thus decided to write two codes. A linac design code, that can work with all types of linacs considered in this thesis, regardless their peculiarities, listed above. This code performs

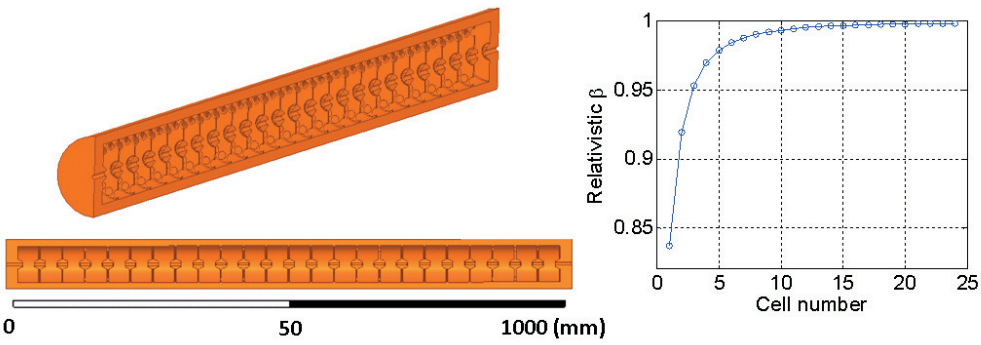

Figure A.1 – 10 MeV electron linac preliminary study performed with the code described in this Section.

also an analytical 2D tracking to get, quickly, a beam dynamics preliminary study and validate the proposed linac layout.

A second code, called RF-Track, was not developed by the author, who participated in the benchmark phase and debugging phase. This latter code perform 3D tracking of particles through complex field maps, and it was used for the start-to-end simulations described in Chapters 3 and 4.

A.1 Linac design code

A linac design code was written by the author. The purpose was to get a deeper insight of the physics, but also to develop a tool capable of being adaptable to the variety of linac structures that have been considered. This code was used for all the linacs presented in this thesis, to define the lattice and get a preliminary estimation of the beam dynamics constraint. At the present stage RF-Track accepts only a field-map representation of accelerating structures. Thus it is more convenient to have a first design based on ZTT and TT profiles together with an analytical tracking, which can then be validated and further optimized with RF-Track

The same tool was used also in quick studies of electron linacs as a side activity [83] (Fig. A.1).

The tool developed has two main subroutines. Subroutines A designs the linac, starting from the interpolated ZTT and TT factor profiles along the structure. Given a certain energy gain goal, one can fix the gradient, or voltage, and have structures length and input power as a dependent parameter, or vice versa.

In case of periodic structures, the code compute the energy gain over one structure to find the average ZTT and TT factor, and then iterates until convergence in β. In case of quasi-periodic structures, this is done cell by cell.

One can also chose to design a constant voltage rather than a constant gradient structure. Ion

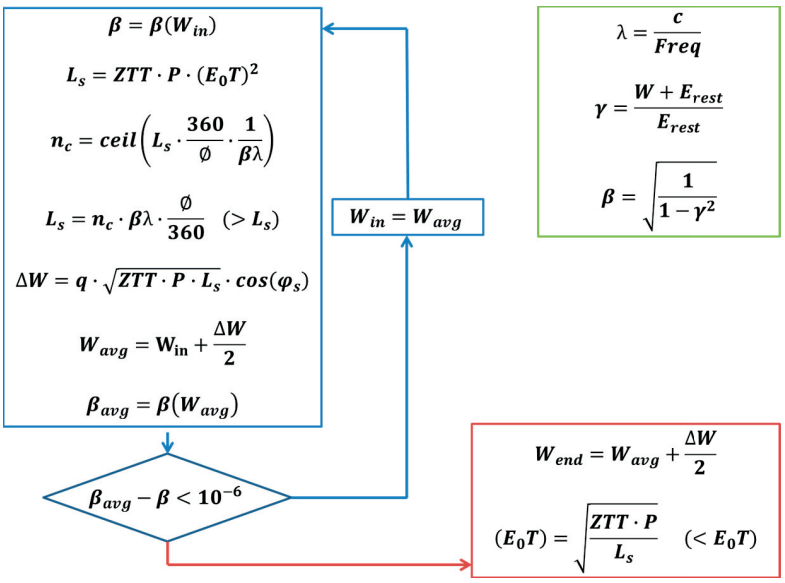

Figure A.2 – Basic block diagram of subroutine A.

species are of course easily changeable.

Phase slippage algorithm was not implemented for periodic structures. However, relatively short structures composed the linacs under consideration, thus making a phase slippage routine not necessary. It is worth point out that from the design obtained by this code, EM field maps are generated, and particles are tracked through them with RF-Track. If the results, as the energy gain per structure, correspond between the two codes, this represents the confirmation of a correct design. This was the case for all the linacs studied in the present thesis.

The main algorithm of subroutine A is summarized in Fig. A.2

Subroutines B performs an analytical tracking with transfer matrices, and it serves as a basis to judge whether the linac layout has a sufficient acceptance with respect to the beam emittance. Drifts, quadrupoles and accelerating structures can be simulated. The first two elements are straightforward, and reported in every basic accelerator book. For accelerating structures, the formulation proposed in [84] is used:

$$M_{acc} = \begin{pmatrix} 1 & 0 \\ \frac{k}{\bar{\beta}\gamma} & 1 \end{pmatrix} \tag{A.1}$$

All the physics is concentrated in the divergence element M_{21}, and k is given by:

$$k = -\pi \frac{qE_aLtan(\phi_s)}{m_0c^2(\bar{\beta}\gamma)^2\lambda}, \tag{A.2}$$

where Ea is the accelerating gradient, L the structure length, ϕ_s the synchronous phase, m_0c^2 the rest energy, $\bar{\beta}\gamma$ the average particle momentum through the cavity, and λ the wavelength.

The subroutines computes the gradients of a FODO cell composed of the elements of the linac. For instance, the first quadrupole, drift and accelerating structures are replicated to form a FODO cell. This is then done for the second quadrupole, drift and accelerating structure, and so on and so forth.

If accelerating gradients and lengths are the same throughout the linac, a constant phase advance corresponds to constant Twiss β_s, independently on the elements considered. In this case, every element is matched to its neighbours, and one can perform an analytical tracking using the calculated quadrupole strength obtaining a smooth envelope.

However, if either the accelerating gradients, or the structure and drift tube lengths change, each FODO has a different Twiss β_s in case of a constant betatron phase advance. This happens also if the RF phase advance changes across the linac. In these cases, each cell is mismatched with the previous and the next one, and it is necessary to average between neighbours FODO cells.

Subroutines B could be improved in case of high gradient and stepwise change in FODO cell length (for instance, an abrupt change in the number of RF cells between one accelerating structure and the next one). Reference codes, such as [79] and [80] have a better mismatch correction algorithm in this sense. However, it was deliberately decided to spend a limited amount of time on this code, since its scope was just to have a preliminary tracking, prior to the final, and reference one, with RF-Track.

A.2 RF-Track: a minimalistic multipurpose tracking code

RF-Track code development started in the framework of the TULIP project [85]. The rationales of this choice lies in the peculiarities of the project, mainly:

- TW accelerating structures were considered, and the goal of start-to-end simulations called for a code capable of dealing with such EM field distribution and evolution in time;
- as discussed in Section 3.1.3, the project rest on the shoulders of a main assumption: to vary the final beam energy by changing the RF EM field in the accelerating structures. This requires, at a simulation level, a significant code flexibility, so it was thought that a in-house code could better adapt to the needs of the project, and to add new features as necessary.

It is worth commenting that RF-Track went much further than its original goals, and it has been so far used to study anti-matter, electron sources, electron gun [86], and dark current

capture (see Section 5.3).

A.2.1 Code description

A TW cavity complicates the particle tracking. In both TW and SW cavities the EM field oscillates according to:

$$A(x,t) = A(x) \cdot e^{-i\omega t}, \tag{A.3}$$

where ω is the angular RF frequency, and $A(x)$ is the complex number spatial distribution of either the electric or the magnetic field. Electric and magnetic field are 90 deg out of phase with respect to each other.

SW cavities are somehow simpler from a beam tracking point of view, since the spatial distribution $A(x)$ is in this case the complex magnitude of the field. In TW cavities instead, the electromagnetic field has a translational component $\pm kx$, with k wave number, and the $\pm$ sign depends whether the wave propagates forward or backward. Thus a complex representation of the EM field is needed.

Very few codes are capable of dealing with TW structures, and to the author knowledge, the most frequently-used ones are ASTRA [81] and GPT [82]. The tracking can also be accomplished with SW codes by superimposing two SW patterns of different frequency [87]. Nevertheless, the need to work with TW field maps and to perform matchings and transmission optimizations, dynamically varying the RF input power as well as the lattice optics (see Section 3.1.3), called for development of a new tracking code: RF-Track.

After the benchmark phase [86] [85], RF-Track has been used to track particles start-to-end, i.e. the beam distribution has not been regenerated, from the RFQ output up to the final energies of TULIP and CABOTO.

This approach, based on accelerating structures EM field maps, is more time consuming than an analytical tracking. In the latter, the field is generated with cylindrical symmetry from Bessel expansion of the average electric field on z axis and the transit-time factor profile along the linac. However, as discussed in Section 2.2.6 for the IH dipolar components, and in Section 2.3 for the DTL quadrupolar asymmetries, the linacs are not always perfectly symmetric structures. The field map approach allowed to correctly take into consideration these aspects.

RF-Track can input and combine the 3D phasor maps of both electric and magnetic fields, in order to represent an RF field in all its complexity, as 3D solvers such as HFSS [41] generate.

RF-Track performs full 6D transport and maintains the proper time of each particle. This allows computing the correct timing of the RF fields felt by each particle. Thanks to this strategic choice, the code is not bounded by the notion of “bunch” or “reference particle”

Table A.1 – Summary of the RF-Track get phase space function options [91].

%x	horiz. position at S	mm	%X	horiz. position at $t = t_0$	mm
%y	vert. position at S	mm	%Y	vert. position at $t = t_0$	mm
%xp	horiz. angle	mrad	%t	proper time	mm/c
%yp	vert. angle	mrad	%dt	delay $t - t_0$	mm/c
%Vx	velocity	c	%Z	-%dt * %Vz	mm
%Vy	velocity	c	%S	S + %Z	mm
%Vz	velocity	c	%deg@f	deg @ f GHz	deg
%Px	momentum	MeV/c	%d	relative momentum	per mille
%Py	momentum	MeV/c	%pt	(%E-E0)/P0c	per mille
%Pz	momentum	MeV/c	%P	total momentum	MeV/c
%px	%Px/P0	mrad	%E	total energy	MeV
%py	%Py/P0	mrad	%K	kinetic energy	MeV
%pz	%Pz/P0	mrad	%m	rest mass	MeV
%N	Particles	#	%Q	charge	e^+

and can track continuous beams consistently. It implements exact transfer maps for drifts, quadrupoles and sector bends in both the transverse plane and the longitudinal planes, with the exception of the quadrupole longitudinal map, which features a second- order expansion of the path length to take into account the particle's incoming position and angles. The approximated solution of the longitudinal quadrupole map (already better than the standard "drift-like" map adopted by many codes) does not undermine the tracking accuracy, because each element can be integrated in an arbitrary number of steps, recovering accuracy whenever a second order tracking is not sufficient.

The code is written in modern, fast, parallel C++ that exploits multi-core CPUs. Its fast computational core is accessible by the user through a SWIG Octave interface [88] [89], which permits to write complex, yet readable and concise, simulation scripts that can directly benefit from a large number of optimization toolboxes already existing for Octave. An analogous interface toward Python [90] exists, for those who prefer this language to Octave.

The Octave-Phyton user interface represents probably the biggest advantage of RF-Track. The initial and tracked particles phase space can be retrieved with two functions, get phase space (see Table A.1) and get transport table (see Table A.2). The first one permits to extract physics information of each particle in the bunch, while the second function has a pre-set number of options which calculate the average beam properties.

The tracking can be carried out integrating the beam motion in space, or in time. This last option is very convenient and can deal with very low, or even zero, momentum particles. Space charge interactions can also be simulated. The very common assumption of $\vec{B} << \vec{E}$ is not present in RF-Track, which computes the electromagnetic interaction between each pair of particles.

The basic architecture of RF-Track is shown in Fig. A.3.

Table A.2 – Summary of the RF-Track get transport table function options [91].

%sigma x|xp|y|yp|t|P	Std(#)	various
%sigma xxx|yyp|tP	Cov(#,#)	various
%mean x|xp|y|yp|t|P|K|E	Mean(#)	various
%alpha x|y|z	Twiss	1
%beta x|y|z	Twiss	see below
%rmax	envelope	mm
%emitt x|y|z	RMS emittance	see below
%S	position	mm
%N	transmission	percent

$\beta_x[mm/mrad]$	$\epsilon_x = \epsilon_{x,geom}\beta_{rel}\gamma_{rel}[mm.mrad]$	$\epsilon_{x,geom} = \sigma_x\sigma_{x'}$	$\sigma_x = \sqrt{\epsilon_{x,geom}\beta_x}[mm]$
$\beta_y[mm/mrad]$	$\epsilon_y = \epsilon_{y,geom}\beta_{rel}\gamma_{rel}[mm.mrad]$	$\epsilon_{y,geom} = \sigma_y\sigma_{y'}$	$\sigma_y = \sqrt{\epsilon_{y,geom}\beta_y}[mm]$
$\beta_z[mm]$	$\epsilon_z = \epsilon_{z,geom}\beta_{rel}\gamma_{rel}[mm.permil]$	$\epsilon_{z,geom} = \sigma_z\sigma_\theta$	$\sigma_z = \sqrt{\epsilon_{z,geom}\beta_z}[mm]$

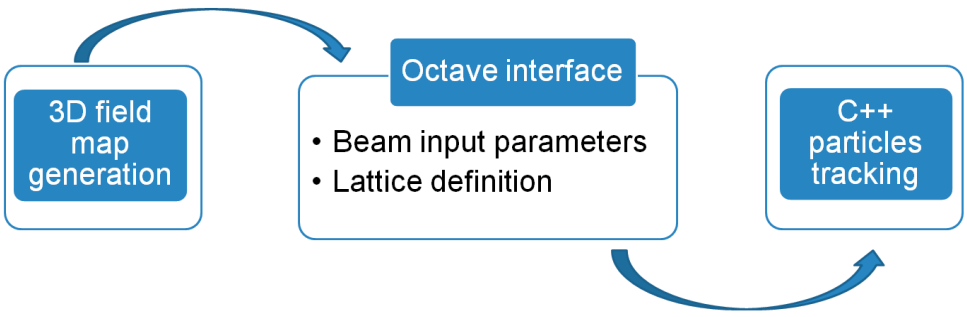

Figure A.3 – Simplified scheme of RF-Track software architecture.

A.2.2 Benchmark of RF-Track with other codes

RF-Track was benchmarked in the following cases [86]:

- ELENA Transfer line, antiprotons simulation with 100 keV kinetic energy, comparison with PTC code;
- 750 MHz CERN RFQ, protons from 40 keV to 5 MeV, comparison with TRAVEL;
- Lead ions source for CERN Linac3;
- CCL cavities in the framework of the TULIP project.

In this Section, one of the first benchmarks performed, on a short SW linac for protons, is presented.

A CCL was considered for the validation study of RF-Track, given the lack of tracking codes capable of accepting travelling wave accelerating structures. Nevertheless, since a standing wave (SW) regime is a particular case of a TW regime, the results are not limited to the first case only. The codes used for the benchmark are Linac [79] and TraceWin [80]. While LINAC demands as an input the shunt impedance (ZTT) and transit-time (TT) factor of the accelerating structures on the z-axis, and then computes the field distribution with a Bessel function expansion, TraceWin, like RF- Track, allows to directly entering a field map distribution computed in 3D. For comparability with RF-track, this last option was used in TraceWin. It must be noticed that TraceWin accepts only maps of real numbers, which can only represent standing wave structures, whereas RF- Track directly accepts maps of complex numbers.

The 2D electromagnetic code Superfish [40] was used to generate the electromagnetic field maps, and a short linac made of three accelerating structures embedded in a FODO lattice was considered in the benchmark. The steps followed in the study are summarized in Fig. A.4.

The three codes agree, both in terms of transmission and phase space distribution of the particles, as reported in Table A.3. The α_x has the biggest deviation, because the beam is at the waist at the end of the simulation. More in general, the codes agree remarkably well in the longitudinal phase space and in the overall transmission. A bit less well in the transverse phase space, especially TraceWin with respect to the other two.

A.2.3 Field map generation and main assumptions

The EM field distribution in a whole accelerating structure can be fully generated with an EM code. However, such solution would raise significantly the computational time.

All the physics is fortunately contain in a single regular RF cell, or in a set of RF cells, that replicate an infinite periodic chain of cells. This under the assumption of a full 3D design

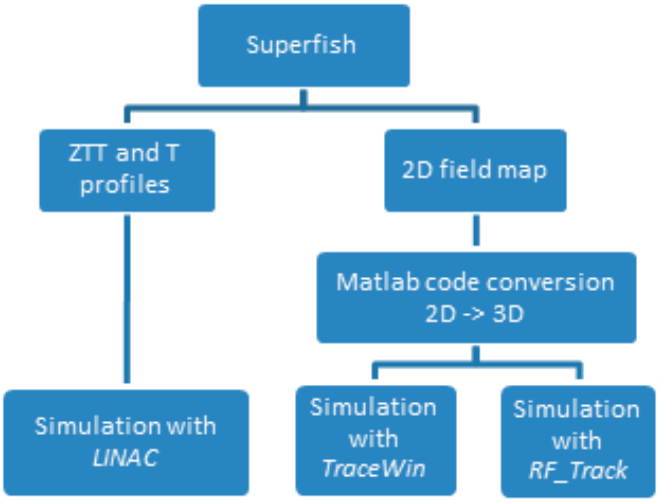

Figure A.4 – Blocks view of the approach adopted for benchmarking the codes.

Table A.3 – Twiss parameters comparison from the benchmark simulation on a three structures linac.

	RF-Track	Linac	TraceWin	Diff. RFT-Linac [%]	Diff. RFT-TraceWin [%]	Diff. Linac-TraceWin [%]
N	2185	2118	2081	-3 %	-5 %	-2 %
α**x**	-0.207	0.124	-0.695	-160 %	236 %	-658 %
β**x[mm/pi/mrad]**	1.669	1.640	1.381	-2 %	-17 %	-16 %
ϵ**x(Norm, RMS)[pi.mm.mrad]**	0.380	0.328	0.488	-14 %	29 %	49 %
α**y**	-0.416	-0.289	-0.484	-31 %	16 %	68 %
β**y[mm/pi/mrad]**	0.275	0.255	0.237	-7 %	-14 %	-7 %
ϵ**y(Norm, RMS)[pi.mm.mrad]**	0.549	0.468	0.577	-15 %	-5 %	23 %
α**z**	2.886	2.773	2.801	-4 %	-3 %	1 %
β**z[deg/pi/MeV]**	274.4	264.4	267.4	-4 %	-3 %	1 %
ϵ**z(Norm, RMS)[pi.deg.MeV]**	3760	3576	3688	-5 %	-2 %	3 %

where the end-cells are properly matched the regular cells, so there are not standing wave patterns trapped in the cavity.

Periodic and quasi-periodic structures require a different approach, and are hereafter discussed separately. Periodic structure refers to cavities where all the RF cells have equal length, while quasi-periodic indicates structures tapered in length.

This case is the simplest of the two. Given the RF phase advance per cell ϕ, one can compute the field in the n-th cell by:

$$E_n = E_0 \cdot e^{-in\phi}, \tag{A.4}$$

with n integer number, and so quickly create a n-th cells structure field map. The E-fields and H-fields have then to be normalized, and scaled to the average accelerating gradient computed with the code discussed in Section A.1. The convention adopted with RF-Track is to express the E-field in [V/m] and H-field in [A/m].

The single RF cell can be either simulated with an EM code, or more simply, one can interpolate it from a set of different β cells that cover the different geometric β of the linac. This last approach permits to change reasonably quickly a linac, without running additional EM simulations.

Quasi-periodic structures are a bit more complex, since there the RF cell length is not constant anymore. So the EM field maps have to be stretched following the variable cell length Lc. Since RF-Track, as many tracking codes, accepts only a constant mesh, a second interpolation is needed in this case to produce a ready to use field map.

It is worth commenting that a certain degree of dipolar component can be present in end-cells. The approach above described does not consider them. While one could always simulate a full 3D geometry, and get the field map from there, a quicker solution would be in this case to superimpose the end-cells dipole component of the EM field to the symmetric field map discussed above. How to distinguished a dipolar component in a field map was discussed in Section 2.2.6.

The codes can work with both cartesian and cylindrical coordinates. This latter capability was introduce after realizing that, on a cylindrical bore radius, a cartesian mesh underestimates the real aperture. In fact, if HFSS is enquired about the EM field in a region outside the simulation geometry, it returns a not-a-number (NaN) for that point. So if one selects a cartesian mesh, with edge equal to the radius of the bore aperture, one would get something similar to the graphic example of Fig. A.5, where a five points mesh is shown.

Since at every time step, or space step, RF-Track interpolates the field at the edges of the cube that surrounds the particle position, if one of the edges is a NaN, also the interpolation result is a NaN, and so the particle is recognized as lost. So, depending on the transverse mesh size

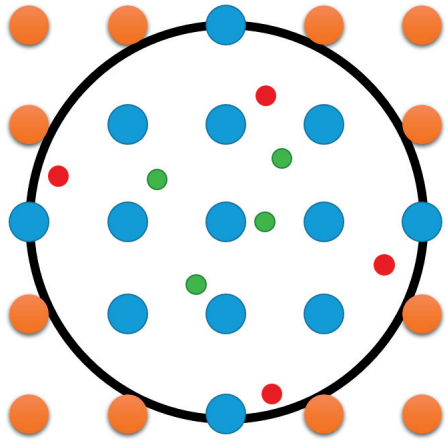

Figure A.5 – Sketch of a cartesian mesh over a cylindrical region. Points with EM field are in blue, NaN in orange. Small green dots are numerical interpolation points, small red dos are interpolation points which are NaN.

adopted, with such solution one could loose a considerable amount of transverse acceptance.

Hereafter this is derived in more detail. The mesh size is assumed isotropic along the two transverse dimensions x and y. The condition to have a not-NaN for the EM field is:

$$\sqrt{(N_x d)^2 + (N_y d)^2} <= R, \tag{A.5}$$

with N_x and N_y integer numbers of grid points along the two dimensions, d grid size, and R bore aperture radius.

The minimum value of the grid size d that permits to have a not-NaN result, except for the (0,0) coordinate, is then:

$$d <= \frac{R}{\sqrt{2}}. \tag{A.6}$$

The biggest square internal to the aperture is instead:

$$N \cdot d <= \frac{R}{\sqrt{2}}. \tag{A.7}$$

However, there could be space for two, or even more, additional squares, provided that Eq. A.5 is respected.

A better way to study the problem is the following. Let's consider the sketch of Fig. A.6 left. To use the most of the space available, a square grid of edge d must be placed as in the image,

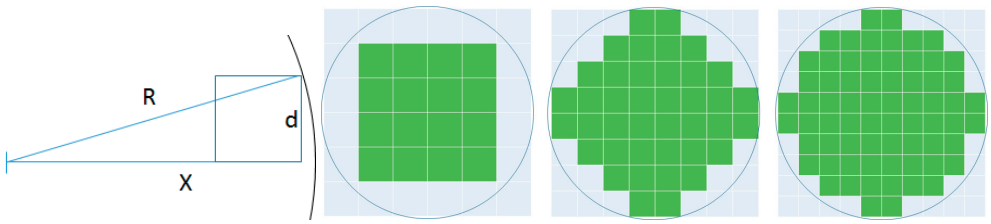

Figure A.6 – Sketch to illustrate the derivation of Eq. A.8 (left) and visual example (right).

and the length X must be such that $X = N_x d$. From basic trigonometric equation, one then find that:

$$N_x = \frac{R}{d} cos\left(\frac{d}{R}\right) \tag{A.8}$$

So the number of points that can be fit in the cylindrical geometry (and so the filling percentage of a square grid in a cylindrical geometry) depends on 1. the cylinder radius and on the inverse of the mesh size, but 2. there is also a fluctuation term given by the $cos\left(\frac{d}{R}\right)$. The first conclusion is intuitive: the smaller the mesh size, the more points will fit into a given geometry. The second conclusion is less straightforward: it come from the fact that the mesh squares have a discrete area, which fits into the available cylindrical one in discrete steps.

The filling percentage of a square grid in a cylindrical geometry was simulated with a code, and is reported in Fig. A.7, which shows the ratio of area cover by the mesh over the total circle area, as a function of mesh size d and radius R. As expected, the fluctuations smooth for higher R/d ratios, since this term becomes predominant in Eq. A.8.

First simulations run during the PhD considered a 0.5mm mesh size over a 2.5mm bore aperture radius. So the first results, later on corrected, were underestimating the transverse acceptance of the linacs of approximately 25%.

A final remark concerns the symmetry condition of each cell. One should pay attention that both the longitudinal EM distribution and the transverse one have the same phase advance. For instance, the symmetry condition in a IH cavity is respected when two RF cells are simulated together. If only one is used in Eq. A.4, the longitudinal EM field distribution is correctly generated, but the dipole kicks point all in the same direction. One shall not try to trick this problem by changing the sign of the transverse electric field components. In this case in fact, while the dipole kicks would be correctly oriented, the RF defocusing would not be (see Section 2.2.6). This was a mistake made by the author at the beginning of the work, and it resulted in wrong results to be corrected. A good lesson, better not to play without a full understanding of the physics behind.

With this Chapter ends the introductory part of this thesis. After the introduction on hadron therapy, Chapter 2 discussed the RF designs carried out in this thesis, while this Chapter

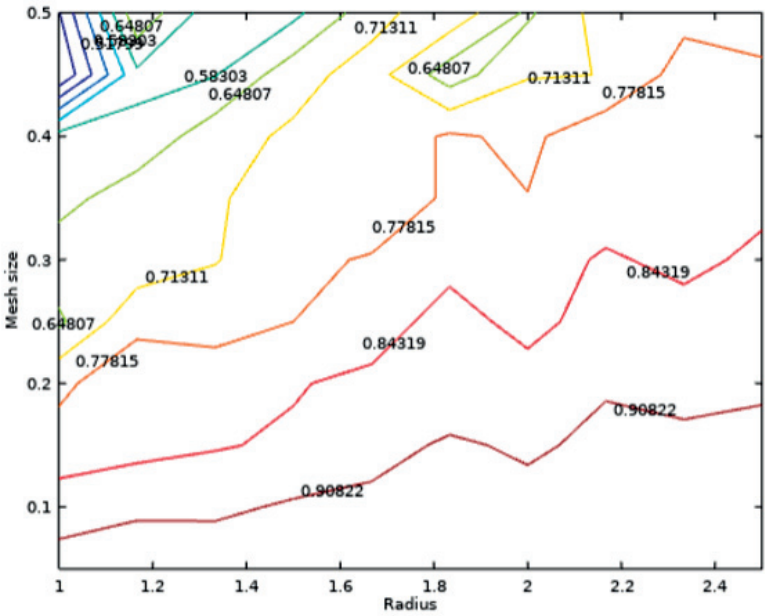

Figure A.7 – Ratio of area cover by a cartesian mesh over a total circle area, as a function of mesh size d and circle radius R

presented the beam dynamic codes that were developed and used. Hereafter, these two ingredients are put together to study a high-gradient proton therapy linac - TULIP - and an high efficiency carbon ion therapy linac - CABOTO. Chapter 3 starts with the TULIP project.

B Selected publications

The publications where the author is the correspondent person are reported in this Appendix. These are:

- S. Benedetti, U. Amaldi, A. Degiovanni, A. Grudiev and W. Wuensch, *RF design of a novel S-Band backward travelling wave linac for proton therapy*, In Proc. of LINAC14 Conference, Geneva, Switzerland (2014).
- S. Benedetti, U. Amaldi, A. Grudiev and A. Latina, *Design of a proton travelling wave linac with a novel tracking code*, In Proc. of IPAC15 Conference, Richmond (VA), USA (2015).
- S. Benedetti, T. Argyropoulos, C. Blanc Gutierrez, N. Catalan Lasheras, A. Degiovanni, D. Esperante Pereira, M. Garlasche', J. Giner Navarro, A. Grudiev, G. Mcmonagle, A. Solodko, M. Timmins, R. Wegner and W. Wuensch, *Fabrication and testing of a novel S-Band backward travelling wave accelerating structure for proton therapy linacs*, In Proc. of LINAC16 Conference, East Lansing (MI), USA (2016).
- S. Benedetti, A. Grudiev and A. Latina, *Design of a 750 MHz IH structure for medical applications*, In Proc. of LINAC16 Conference, East Lansing (MI), USA (2016).
- S. Benedetti, A. Grudiev and A. Latina, *High gradient linac for proton therapy*, Physical Review Accelerators and Beams 20, 040101, April 2017.

The last publication, High gradient linac for proton therapy, was highlighted on APS Physics, MedicalPhysicsWeb and Superconductor Week (link not available).

RF DESIGN OF A NOVEL S-BAND BACKWARD TRAVELLING WAVE LINAC FOR PROTON THERAPY

S. Benedetti#, TERA, Novara, Italy and EPFL, Lausanne, Switzerland
A. Degiovanni, A. Grudiev, W. Wuensch, CERN, Geneva, Switzerland
U. Amaldi, TERA, Novara, Italy

Abstract

Proton therapy is a rapidly developing technique for tumour treatment, thanks to the physical and dosimetric advantages of charged particles in the dose distribution. Here the RF design of a novel high gradient accelerating structure for proton linacs is presented. The design discussed hereafter represents an unicum thanks to the accelerating mode chosen, a 2.9985 GHz backward travelling wave mode with 5π/6 phase advance, and to the RF design approach. The prototype has been designed to reach an accelerating gradient of 50 MV/m, which is more than twice that obtained before [1]. This would allow a shorter linac potentially reducing cost. The complete 3D RF design of the full structure for beta equal to 0.38 is presented.

INTRODUCTION

A collaboration between the TERA Foundation and CLIC has been established to study a novel linear accelerator for proton therapy. The main goal of the collaboration is to transfer the knowledge acquired by the CLIC group, mostly in terms of RF design, high-gradient limitations and linac optimization, to a medical linac. As a result, a low-β structure with an expected accelerating gradient of 50 MV/m has been designed, double that of the gradient reached in equivalent linacs. This design result (high-power tests have not been made yet) is based on a novel RF design approach, which will be discussed in detail in this paper. The KT – Knowledge Transfer – group of CERN has funded the construction of a first prototype of the structure, which will be produced and tested at high power at the beginning of 2015.

This accelerating structure is part of the TULIP project, a single room facility for proton therapy with the unique feature of having a linac mounted on a rotating gantry [2]. In this perspective, the high gradient structure hereafter presented remarkably improves the compactness and lightness of the rotating mechanism, with benefits in terms of cost and reliability.

REGULAR CELL DESIGN

The electromagnetic coupling between cells has been accomplished magnetically by means of magnetic *coupling holes* at the periphery of the cells. N*ose cones* are added to enhance the electric field near the axis and thus the transit time factor for the low beta structure. The regular cell geometry is shown in Fig. 1.

stefano.benedetti@cern.ch

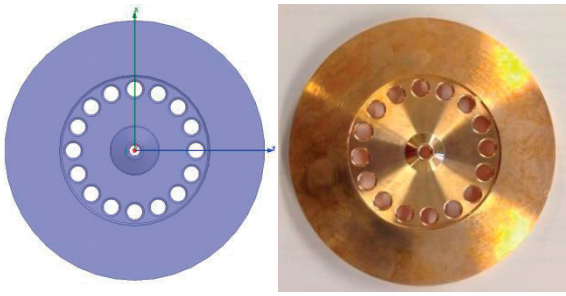

Figure 1: Regular cell design; 3D model (left) and copper piece (right) used in the creep test.

A local field quantity which predicts the high gradient performance of an accelerating structure is the modified Poynting vector S_c, defined in [3]. It has a limiting value of about 4MW/mm^2 at a pulse length of 200 ns and for a breakdown rate (BDR) of 10^{-6} bpp/m (BDs per pulse per meter). This limit is used in the design of the linac (which is approximately 6 m long) in order to have less than one BD per treatment session. By re-scaling these data to the pulse length typical of medical linacs, i.e. 2.5 μs flat-top, a limit quantity of S_c/E_a^2 – where E_a is the average accelerating gradient – lower than $7\cdot10^{-4}$ A/V has been found.

The goal of the regular cell design has been to minimize the value of S_c and at the same time the amount of RF power for a given accelerating field, i.e. the quantity:

$$\mu \equiv \frac{P_w}{E_a^2}\cdot\frac{S_c}{E_a^2} = \frac{v_g}{\omega}\cdot\frac{S_c/E_a^2}{R'/Q}, \qquad (1)$$

where ω is the angular RF frequency, R′ is the effective shunt impedance per unit length and Q is the quality factor of the cell. Eq. (1) equally weights the dissipated power and the modified Poynting vector; thus, minimizing μ one obtains for a given power the highest accelerating gradient with a low BD risk.

The optimum is found when Eq. (1) is minimized simultaneously on the nose, where the electric field is maximum, and on the coupling slot, where the magnetic field is maximum, as shown in Fig. 2.

A parametric study has been performed varying the cell gap, cone angle and phase advance per cell. The thickness of the iris has been carefully studied as well. The thinner the iris, the higher the shunt impedance is, but also the lower the mechanical resistance of the structure and the

Copyright © 2014 CC-BY-3.0 and by the respective authors

possibility of evacuating the heat from the nose to the outer walls of the structure which are water cooled.

Particular effort has been dedicated to the sensitivity analysis and the study of the tuning methodology. The tolerances specified in the mechanical drawings would, from simulations, give no more than ±5 MHz of frequency shift per cell. This possible error will be adjusted by means of 4 dimple tuners. The tuning capability obtained from simulations and mechanical tests on copper cells is higher than 6 MHz per cell, well beyond the tuning needs also in the worst case scenario.

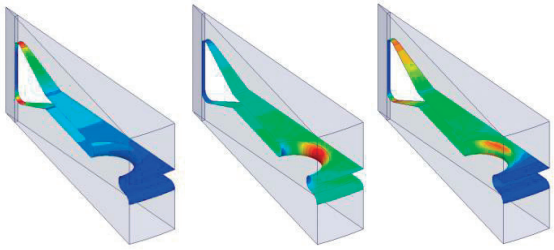

Figure 2: Electric (left), magnetic (centre) and modified Poynting vector (right) field distribution in a regular cell section (1/32 azimuthal symmetry).

TAPERING OF THE STRUCTURE

In a travelling wave linac, the RF power is injected into the structure and propagates along it at the *group velocity* v_g. It is absorbed both by the conductor walls and by the beam, resulting in an attenuation of the field amplitude. At the end of the structure the power is coupled to a load or a re-circulating circuit.

A low group velocity leads to a high accelerating gradient but at the same time to a rapid decay of the power. The group velocity can be adjusted by means of cell-to-cell coupling in the disk-loaded accelerating structure. In particular, the bigger the coupling, the higher the group velocity is. A *constant-gradient* structure has been chosen in the present design with the group velocity ranging between 0.4% and 0.2% of *c* as a compromise between acceptable filling time and efficient acceleration of the beam (Fig. 3).

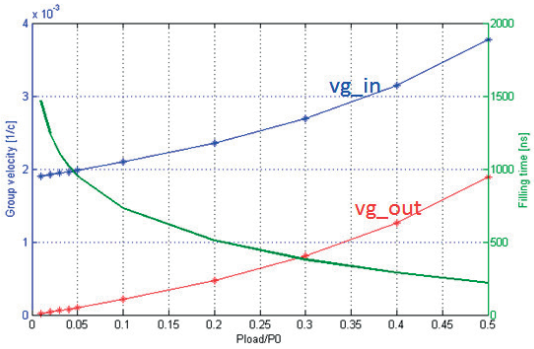

Figure 3: Input and output cells group velocity and filling time of the structure as a function of the ratio between output and input powers.

The tapering has been accomplished by varying linearly the coupling holes radii; the cell diameter and the radial distance of the coupling holes have been varied to adjust the resonant frequency. All the other geometrical parameters have been kept constant throughout the structure.

COUPLERS DESIGN

The input and output power couplers (or end-cells) represent a very delicate part of the design process. The presence of a slot to allow the RF power to penetrate into the structure enhances the electromagnetic field distribution and modifies the accelerating parameters of the coupling cell. The goal of the couplers design is to minimize the power reflections while perturbing as little as possible the field distribution and the accelerating performance of the end-cells.

The power coupling is made magnetically via a single slot, the area of which together with the coupling cell diameter is chosen for matching. The coupling holes radius in the input cell has been reduced in the coupling holes closer to the coupling slot, to compensate for the enhancement of the S_c due to the local increase of the power flow. The remaining coupling holes have been resized to maintain the design group velocity in the cells (Fig. 4 left), and as a result the end-cells provide the same acceleration as the regular cells (Fig. 4 right).

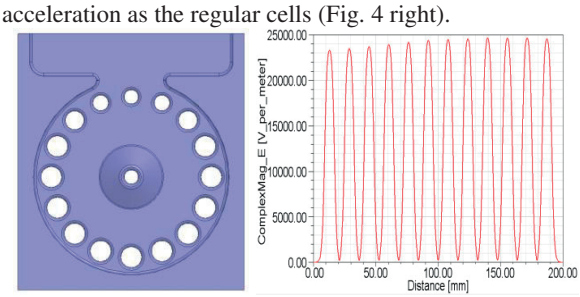

Figure 4: Input coupling cell (left) and electric field profile in the structure (right) for 1 W input power. It can be noticed the asymmetry in the coupling holes radii.

Eventually, an even distribution of the modified Poynting vector on all the accelerating structure noses and coupling holes has been reached, as shown in Fig. 5, and the limit of S_c/E_a^2 lower than $7\cdot10^{-4}$ A/V has been widely respected.

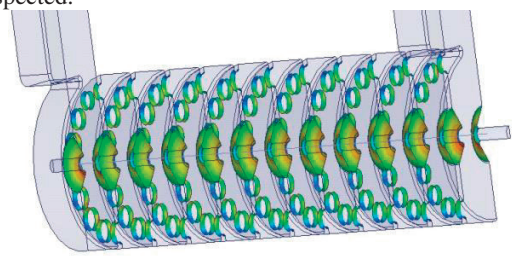

Figure 5: Modified Poynting vector normalized to the average accelerating gradient squared distribution on the structure noses and coupling holes. Red colour corresponds to $3\cdot10^{-4}$ A/V.

ISBN 978-3-95450-142-7

Copyright © 2014 CC-BY-3.0 and by the respective authors

Figure 6 shows (top) the frequency distribution of the resonating peak and (bottom) the phase advance per cell, which is equal to 150° at the chosen operating frequency. A reflection lower than 50 dB was reached at the resonant frequency of 2.9985 GHz.

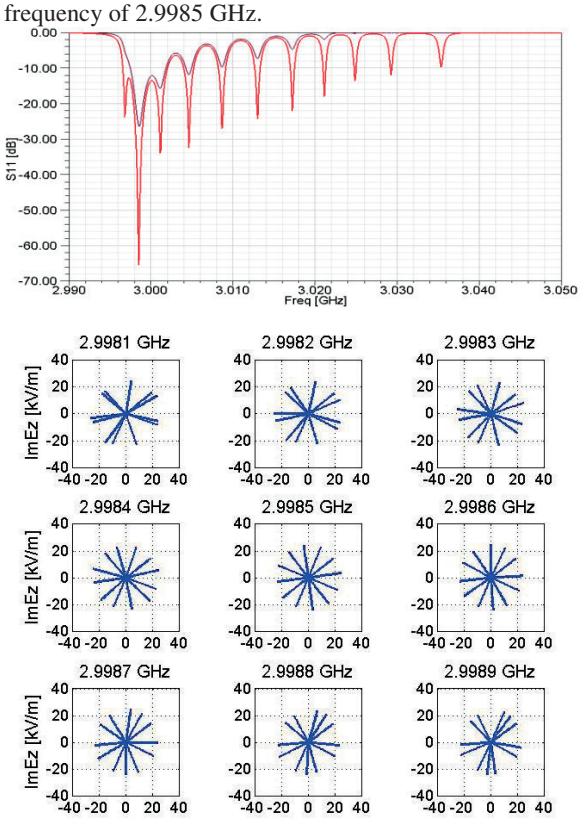

Figure 6: Input (red) and output (brown) couplers matching (top) and phase advance per cell (bottom) versus frequency.

ACCELERATING STRUCTURE PARAMETERS

The most important parameters of the backward TW accelerating structure (bwTW) are summarized in the first column of Table 1. The second column refers to a SW CCL (Coupled Cavity Linac) structure which has been previously designed for the TULIP project [4]. That structure has been optimized to maximize the shunt impedance, which is larger also thanks to the greater phase advance, but cannot withstand the same maximum gradients of the bwTW structure.

Table 1: Main parameters of the accelerating structures

Parameter	bwTW	CCL
RF phase advance per accelerating cell [rad]	5π/6	π
Wall thickness [mm]	2	3
Gap [mm]	7	5.1
Nose cone angle [deg]	65	25
Number of cells	12	10
Structure length including end-cells [mm]	189.9 (active)	189.9 (active)
Average accelerating gradient [MV/m]	50	31
Q factor (first/last cell)	6997/7463	8290
R'/Q (first/last cell)	7425/7369	8410
Normalized shunt impedance (first/last cell) [MΩ/m]	52.0/ 55.0	69.7
Filling time (w/o re-circulator) [ns]	900 (224)	1050
Peak input power (w/o re-circulator) [MW]	9.3 (20.6)	2.6
Max S_c/E_a^2 [A/V]	3.1e-4	7.8e-4
Max E_a (for BDR of 10^{-6} bpp/m) [MV/m]	74.9	47.1
Maximum surface electric field [MV/m]	219	159

SUMMARY AND FUTURE STEPS

A novel high gradient S-band accelerating structure for a proton therapy linac has been designed in collaboration between TERA and CLIC. The unique feature of such design is the capability of reaching an accelerating gradient never reached so far in equivalent structures.

In June 2014 the tender for the mechanical pieces has been launched. The final assembly of the prototype will start in autumn 2014, with the final goal of testing the structure at high power in 2015.

ACKNOWLEDGMENT

The authors are very grateful to the CERN KT group for having funded the accelerating structure prototype construction and test.

REFERENCES

[1] U. Amaldi et al, "LIBO – a linac-booster for protontherapy: construction and tests of a prototype", NIMA 521 (2004) 512.

[2] A. Degiovanni et al, "Design of a Fast-Cycling High-Gradient Rotating Linac for Protontherapy", in Proceeding of IPAC (2013).

[3] A. Grudiev, S. Calatroni and W. Wuensch, "New Local Field Quantity Describing the High Gradient Limit of Accelerating Structures", Phys. Rev. ST Accel. Beams 12 (2009) 102001.

[4] A. Degiovanni, "High Gradient Proton Linacs for Medical Applications", EPFL PhD Thesis (2014).

Copyright © 2014 CC-BY-3.0 and by the respective authors

DESIGN OF A PROTON TRAVELLING WAVE LINAC WITH A NOVEL TRACKING CODE

S. Benedetti#, TERA, Novara, Italy and EPFL, Lausanne, Switzerland
A. Grudiev, A. Latina, CERN, Geneva, Switzerland
U. Amaldi, TERA, Novara, Italy

Abstract

A non-relativistic proton linac based on high gradient backward travelling wave accelerating structures was designed using a novel dedicated 3D particle tracking code. Together with the specific RF design approach adopted, the choice of a 2.9985 GHz backward travelling wave (BTW) structure with 150° RF phase advance per cell was driven by the goal of reaching an accelerating gradient of 50 MV/m, which is more than twice that achieved so far.

This choice dictated the need to develop a new code for tracking charged particles through travelling wave structures which were never used before in proton linacs. Nevertheless, the new code has the capability of tracking particles through any kind of accelerating structure, given its real and imaginary electromagnetic field map. This project opens a completely new field in the design of compact linacs for proton therapy, possibly leading to cost-effective and widespread single room facilities for cancer treatment.

INTRODUCTION

A collaboration between TERA Foundation and CLIC was established to study a novel linear accelerator for proton therapy. The main goal of the collaboration is to transfer the knowledge acquired by the CLIC group, mostly in terms of RF design, high-gradient limitations and linac optimization, to a medical linac.

Funds of the Knowledge Transfer group of CERN permitted the construction of a prototype based on the design discussed in [1]. High power RF test of this accelerating structure is under preparation at the present time, to validate its capability to reach the maximum accelerating gradient of 50 MV/m.

A backward travelling wave linac was never used for accelerating protons. Moreover, a medical linac has a certain number of peculiarities with respect to high energy physics linacs, as for instance the need to vary the kinetic energy of particles over a wide range to reach tumour tissues at different depth into the patient body. So it was decided to develop a completely new tracking code, called *RF-Track*. The main features of such code will be discussed in the present paper, together with the results of the benchmark study and a preliminary BTW linac design.

RF-TRACK

In order to evaluate and maximise the transmission through backward-travelling accelerating structures, a new *ad-hoc* tracking code was developed: *RF-Track*. The decision to develop a new code was motivated by the need to perform accurate tracking of continuous, unbunched, inherently relativistic beams of protons or ions (with beta = ~0.35 for the protons, even less for the ions), through 3D field maps of BTW structures. No code in our knowledge featured the required flexibility and had the capability to handle real and imaginary field maps of travelling-wave RF structures (forward or backward).

RF-Track can input and combine the 3D phasor maps of both electric and magnetic fields, in order to represent an RF field in all its complexity, as 3D solvers such as HFSS [2] generate. This possibility allows the accurate representation of (backward) travelling-wave structures, differently from most of the codes, which can only input static field maps or can only simulate standing wave structures (and require to overlap two standing waves to mimic a travelling wave).

RF-Track performs full 6D transport and maintains the proper time of each particle. This allows computing the correct timing of the RF fields felt by each particle. It must be noticed that, thanks to this strategic choice, the code is not bounded by the notion of "bunch" or "reference particle" and can track continuous beams consistently. It implements exact transfer maps for drifts, quadrupoles and sector bends in both the transverse plane and the longitudinal planes, with the exception of the quadrupole longitudinal map, which features a second-order expansion of the path length to take into account the particle's incoming position and angles. The approximated solution of the longitudinal quadrupole map (already better than the standard "drift-like" map adopted by many codes) doesn't undermine the tracking accuracy, because each element can be integrated in an arbitrary number of steps, recovering accuracy whenever a second-order tracking is not sufficient.

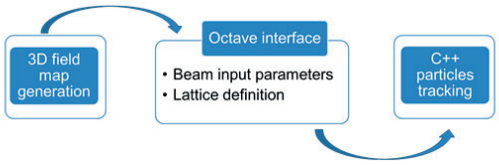

Figure 1: Simplified scheme of *RF-track* software architecture.

The code is written in modern, fast, parallel C++ that exploits multi-core CPUs. Its fast computational core is accessible by the user through a powerful SWIG Octave interface [3,4], which permits to write complex, yet readable and concise, simulation scripts that can directly benefit from a large number of optimization toolboxes

stefano.benedetti@cern.ch

ISBN 978-3-95450-168-7

Copyright © 2015 CC-BY-3.0 and by the respective authors

already existing for Octave. An analogous interface toward Python [5] has also been created, for those who prefer this language to Octave. A simplified scheme of *RF-Track* architecture is shown in Fig. 1.

CODE BENCHMARKING

A Side Coupling Linac (SCL) was considered for the validation study of *RF-Track*, given the lack of tracking codes capable of accepting travelling wave accelerating structures. Nevertheless, since a standing wave (SW) regime is a particular case of a TW regime, the results are not limited to the first case only. The codes used for the benchmark are *LINAC* [6] and *TraceWin* [7]. While *LINAC* demands as an input the shunt impedance (ZTT) and transit-time (TT) factor of the accelerating structures on the z-axis, and then computes the field distribution with a Bessel function expansion, *TraceWin*, like *RF-Track*, allows to directly entering a field map distribution computed in 3D. For coherence with *RF-track*, this last option was used in *TraceWin*. It must be noticed that *TraceWin* accepts only maps of real numbers, which can only represent standing wave structures, whereas RF-Track directly accepts maps of complex numbers.

The 2D electromagnetic code *Superfish* [8] was used to generate the electromagnetic field maps, and a short linac made of three accelerating structures embedded in a FODO lattice was considered in the benchmark. The steps followed in the study are summarized in Fig. 2.

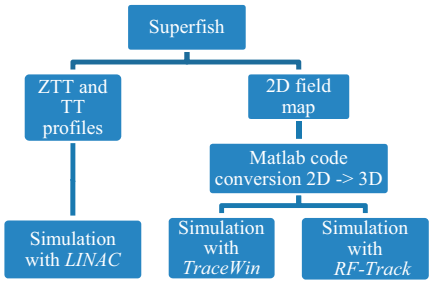

Figure 2: Blocks view of the approach adopted for benchmarking the codes.

The results of the benchmark showed that the three codes agree, both in terms of transmission and phase space distribution of the particles [9].

LINAC DESIGN

The linac design was carried out with two dedicated tools: a Matlab code was developed for setting the accelerating structure lengths, then *RF-Track* was used for optimising the FODO lattice design, maximising the transmission and validating the design.

Accelerating Structures Design

A simplified model was adopted to generate the electromagnetic 3D field maps of the different structures. Regular cells for five different betas of the structure were designed with the 3D electromagnetic code HFSS, in order to compute the shunt impedance and transit-time factor profiles of the linac. This RF design was carried out with the same goals and constraints as the reference 0.38 beta prototype. For this reason the different structures of the linac are equivalent in terms of maximum accelerating gradient and Breakdown (BD) behaviour.

Starting from these data, a Matlab code was written to compute the accelerating structure lengths, the final energy at the end of each structure, and the average beta per structure. Inputs to this program are the initial energy, the minimum final energy of the linac, the RF power per accelerating structure, the synchronous phase, and the average axial electric field. The code was written for a 5pi/6 phase advance linac, but it is fully parameterized and can be easily adapted to other designs.

A compact 18 accelerating structures linac was chosen, with a constant number of 12 cells per structure, and a full recirculation of the power was considered. A synchronous phase of 20 degrees was chosen. The attenuation in the 3dB-hybrid and in the waveguides was taken into account by means of a 10% losses coefficient in the klystrons power. Given the power attenuation in standard S-band waveguides of 0.02 dB/meter, this would lead to the possibility of installing up to 20 m long waveguides. The linac layout is presented in Fig. 3.

3D Field Maps Generation

With the average betas computed, HFSS regular cell design for each of the 18 structures was made. Only one cell per structure was modelled to save computational time. Afterwards, the generated field maps were converted into the whole accelerating structure field maps. This approach cannot take into account the effects introduced by couplers. This aspect will be addressed in the future.

Lattice Design

A round beam has the maximum acceptance with a phase advance of 90° per focusing period. Keeping this as a fixed parameter, the gradient G of the Permanent Magnetic Quadrupoles (PMQ) that will form the FODO-like lattice focusing the beam could be easily computed with the equation:

$$G = \frac{2 \cdot sin(\mu/2) \cdot mc\beta\gamma}{qL_q L}, \qquad (1)$$

where μ is the phase advance per cell, $\beta\gamma$ are the relativistic factors, L_q is the length of the quadrupoles and L is the length between them.

It must be noticed that, in this particular project, Eq. 1 does not apply in a straightforward way, because:

- the linac lattice is not a regular FODO;
- the relativistic β is not constant.

The first bullet comes from the fact that the accelerating structure lengths increase along the linac, following the increase of particles relativistic beta. As a result, so do the distances between quadrupoles. The second bullet comes from the peculiarity of this project, where the kinetic

Copyright © 2015 CC-BY-3.0 and by the respective authors

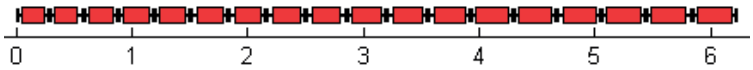

Figure 3: Basic layout of the linac. Transverse and longitudinal dimensions are in scale [m].

energy of the beam has to vary depending of the depth of the tumour tissues to be treated. This is achieved by turning on and off the last active accelerating structures (see Chapter 1 of [10]). In addition, Eq. 1 does not take into consideration the RF defocusing introduced by the accelerating cavities. This contribution is not negligible and has to be counteracted through an increase of the quadrupoles strength with respect to the ideal value of a FODO lattice.

The goal of the FODO optimization is to find the gradient that maximizes the transmission at all the different energies. The simplified approach of Eq. 1 led to a good particles envelope for minimum and maximum energy, while for intermediate energies the FODO could be optimized (Fig. 4). A second method, consisting in zeroing the second derivative of the phase advance for the minimum energy, brought to similar results. The optimum will be reached numerically through an algorithm of *RF-Track* currently under preparation.

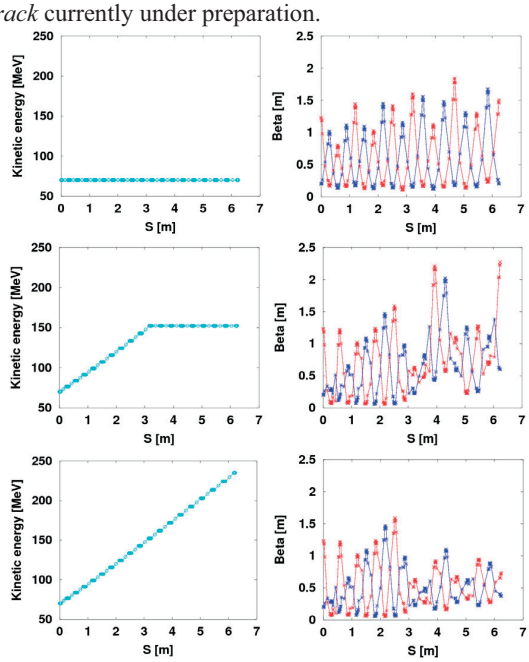

Figure 4: Kinetic energy along the structure S (left) and beta function (right) for 70 MeV (top), 152 MeV (middle) and 236 MeV (bottom) protons.

PRELIMINARY TRACKING RESULTS

Tracking of a bunch of particles was performed with typical input parameters and the results are presented in Fig. 5 for the transverse phase-space and in Fig. 6 for the longitudinal phase-space. In case of *on-crest* acceleration, one can notice the presence of particle *tails*, which are formed by particles outside the longitudinal buckets.

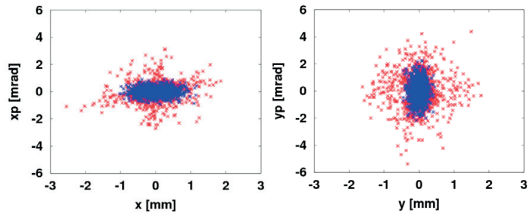

Figure 5: Transverse phase-space representation at the beginning (blue) and at the end (red) of the linac.

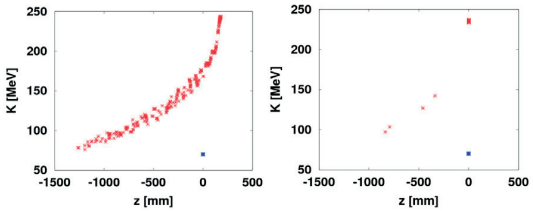

Figure 6: Longitudinal phase-space representation for -20° (left) and 0° (right) input phase. Input (blue) and output (red) particles.

The fraction of transported particles was evaluated using *RF-Track* on the preliminary design here presented.

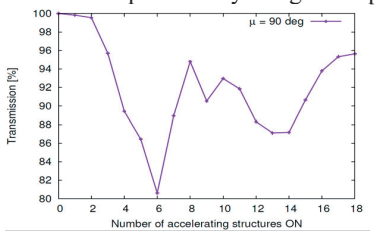

Figure 7: Particles transmission as a function of the final energy of the beam.

Figure 7 clearly shows that the design is not yet optimal, since the transmission varies as a function of the energy. In a medical linac instead, one wants to get a transmission as constant as possible throughout the structure. Such optimization will have to take into consideration the Twiss parameters profile, as well as the emittance growth. Space-charge is not an issue due to the very low currents (below mA peak) needed for tumour treatment.

SUMMARY AND FUTURE STEPS

A new tracking code, called *RF-Track*, was developed to design a novel non-relativistic proton linac based on BTW accelerating structures. The main code characteristics and the successful benchmark were discussed in this paper. The linac accelerating structures were designed and a first lattice was studied and presented. A careful optimisation of the transmission is ongoing.

Copyright © 2015 CC-BY-3.0 and by the respective authors

ISBN 978-3-95450-168-7

REFERENCES

[1] S. Benedetti et al, "RF Design of a Novel S-Band Backward Travelling Wave Linac for Proton Therapy", in Proceeding of LINAC Conference (2014). THPP061.
[2] http://www.ansoft.com/products/hf/hfss/
[3] www.octave.org
[4] www.swig.org
[5] https://www.python.org/
[6] K. Crandall, Documentation for program LINAC
[7] D. Uriot, N. Pichoff, TraceWin Documentation. CEA/SACLAY – DSM/IRFU/SACM, October 2014.
[8] J.H. Billen, L.M: Young, Poisson Superfish, 2006.
[9] A. Latina, S. Benedetti, "*RF-Track* Manual", *in preparation.*
[10] A. Degiovanni, "High Gradient Proton Linacs for Medical Applications", EPFL PhD Thesis (2014).

Copyright © 2015 CC-BY-3.0 and by the respective authors

FABRICATION AND TESTING OF A NOVEL S-BAND BACKWARD TRAVELLING WAVE ACCELERATING STRUCTURE FOR PROTON THERAPY LINACS

S. Benedetti#, T. Argyropoulos, C. Blanc Gutierrez, N. Catalan Lasheras, A. Degiovanni, D. Esperante Pereira, M. Garlasche', J. Giner Navarro, A. Grudiev, G. Mcmonagle, A. Solodko, M. Timmins, R. Wegner, B. Woolley, W. Wuensch, CERN, Geneva, Switzerland

Abstract

Compact and more affordable, facilities for proton therapy are now entering the market of commercial medical accelerators. At CERN, a joint collaboration between CLIC and TERA Foundation led to the design, fabrication and testing of a high gradient accelerating structure prototype, capable of halving the length of state-of-art light ion therapy linacs. This paper focuses on the mechanical design, fabrication and testing of a first prototype. CLIC standardized bead-pull measurement setup was used, leading to a quick and successful tuning of the prototype. The high power tests will soon start in order to prove that the structure can withstand a very high accelerating gradient while suffering no more than 10^{-6} breakdown per pulse per meter (bpp/m), resulting in less than one breakdown per treatment session.

INTRODUCTION

High gradient structures are limited mostly by breakdown (BD) phenomena. CLIC proposed [1] a new method to asses this limit, considering a Modified Poynting Vector (S_c) instead of the maximum Surface Electric Field. This theory was fully verified at high frequency (12 and 30 GHz) by CLIC with many experiments of structures designed for electron linacs. In this structure, the theory is applied to structures designed for particle velocities well below c. TERA Foundation addressed the issue at 3 GHz, hinting that such theory could still be valid at this lower frequency [2].

The test of this prototype, hereafter presented together with the mechanical design and fabrication, is thus of key importance in defining the upper limits in terms of accelerating gradient of S-Band cavities, and in verifying the S_c model in the 3 GHz and the low phase velocity regime.

MECHANICAL DESIGN

The mechanical design had to face a number of challenges, from the required micron-precision tolerances, to the slenderness of the inter-cell wall with respect to the mass of the 'nose'. The latter presents a critical geometrical feature both for machining and for the bonding/brazing steps. Inter-cell wall thickness remarkably affects the accelerating efficiency of a cavity, so it has to be chosen the minimum possible. A series of high-temperature creep tests was thus carried out. More precisely, an experimental campaign was performed to define the minimum septum thickness that can withstand the creep-induced deformation during the hydrogen bonding heat cycle (with a maximum temperature of 1050 °C). A value of 2 mm was eventually chosen for the septum thickness. A machining test was also performed – with a prototype cell being produced in order to validate the following series.

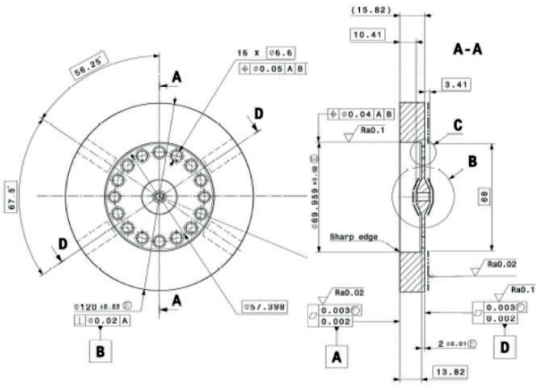

Figure 1: Mechanical drawing of one disk.

Tuning of the structure is made by four dimple tuners per RF cell (Fig.1 left). The number and size of the tuners was determined by an RF sensitivity and tuning analysis. The dimple tuners have a diameter of 10.5 mm, and wall thickness of 1.6 mm. This last parameter has to allow enough deformation of the cavity outer walls to produce a tuning effect, but without rupture. A series of numerical calculations and tests was also carried out on geometries with different diameter/wall thickness ratio, in order to find the best compromise between allowable tuning volume and safety in terms of possible rupture of the copper wall.

A weakly coupled thermo-structural analysis on the full structure was performed by importing the HFSS® electromagnetic field distribution to the thermal and structural packages of ANSYS® (Fig. 2).

The heat dissipation is limited by the peculiar RF design [3], which has 16 coupling holes in each RF cell outer region. As a result, the temperature distribution in the structure is mainly driven by this thermal resistance. Four cooling plates were designed. To prevent plastic deformation, a maximum thermal load of 0.75 kW is allowed, which corresponds to a duty cycle of about 0.075 10^{-3} at a maximum gradient 50 MV/m. Further developments could consider a thicker septum, at the price or reduced rf performance, in case a higher duty cycle is required.

stefano.benedetti@cern.ch, also at EPFL, Lausanne, Switzerland

ISBN 978-3-95450-169-4

Copyright © 2017 CC-BY-3.0 and by the respective authors

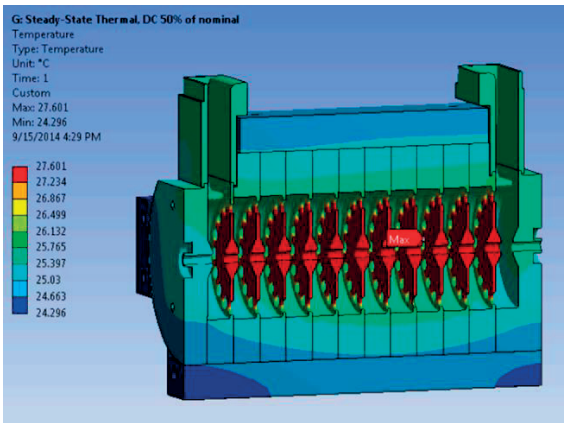

Figure 2: Temperature distribution in the structure in case of a load of 0.75 kW, and cooling water at 22 deg.

The full structure design is presented in Fig. 3. It is possible to notice the details of the cooling plates and pipes, dimple tuners and waveguides transition to standard WR284.

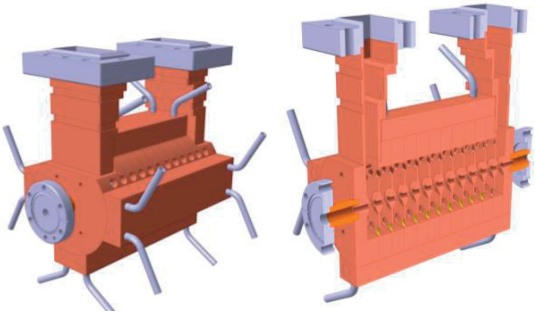

Figure 3: Mechanical design of the prototype.

FABRICATION

Once the ultra-precision machined disks arrived at CERN, they underwent visual and metrological inspection to check the presence of eventual surface defects and compliance with the nominal values indicated in the drawings (Fig. 4).

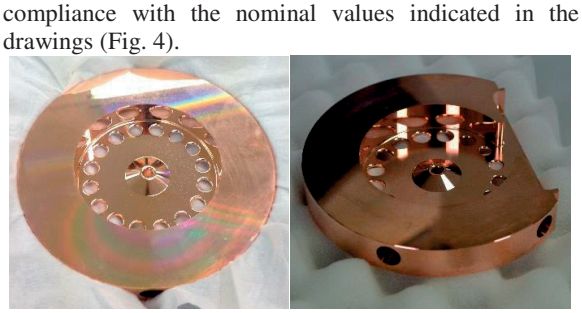

Figure 4: Regular and input cell of the prototype.

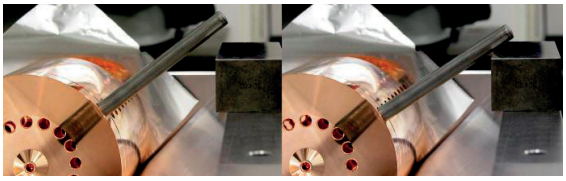

Figure 5: Disks alignment procedure.

A low power RF test was performed on the structure prior to bonding, in order to verify that the prototype was within the tuning range. The stack of disks was joined by diffusion bonding in a partial hydrogen atmosphere following the CLIC baseline fabrication procedure. The fabrication technique was chosen so that the high-gradient test results can be most easily compared to the structures tested in the CLIC high-gradient program. The axial alignment of the disks was ensured thanks to a precise V-shape support whereas azimuthal alignment was performed using the tuning holes as seen in Fig. 5.

After the structure was assembled by brazing the cooling blocks and vacuum tubes and input waveguides, it was returned to CERN for the final tuning. A summary of the tests performed on the prototype is shown in Fig. 6.

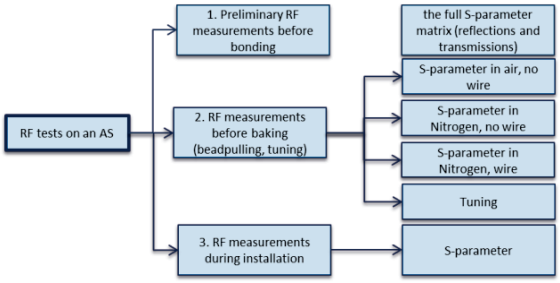

Figure 6: Scheme of the RF tests performed on the accelerating structure.

TUNING

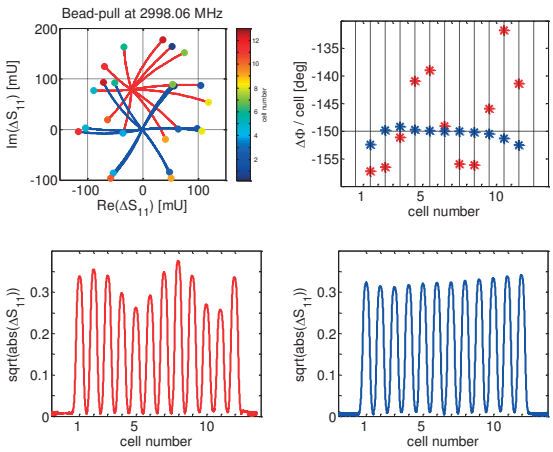

Figure 7: Electric field pattern along the structure for all 12 cells, before (in red) and after tuning (in blue). Top left: in the complex plane; top right: in phase advance per cell; bottom: in magnitude.

Copyright © 2017 CC-BY-3.0 and by the respective authors

All 12 cells (10 regular and 2 coupling cells) of the structure were adjusted in frequency by pulling or pushing up to 4 tuning pins in each cell. The available tuning range per cell is about ±3 MHz. Bead-pull measurements were used to determine the electric field profile along the axis. The standing wave pattern was minimised and the desired phase advance of 150±1.5 ° for regular cells was adjusted for the operating frequency of 2.9985 GHz under vacuum at a temperature of 32 °. The frequency of the output coupling cell was increased by 2.2 MHz, the frequency of the 10 regular cells was increased between 0.1 and 0.8 MHz (average 0.3 MHz, std 0.2 MHz) while the frequency of the input coupling cell was decreased by 0.6 MHz. Fig. 7 shows the electric field pattern along the structure and Fig. 8 the measured S-Parameters after tuning.

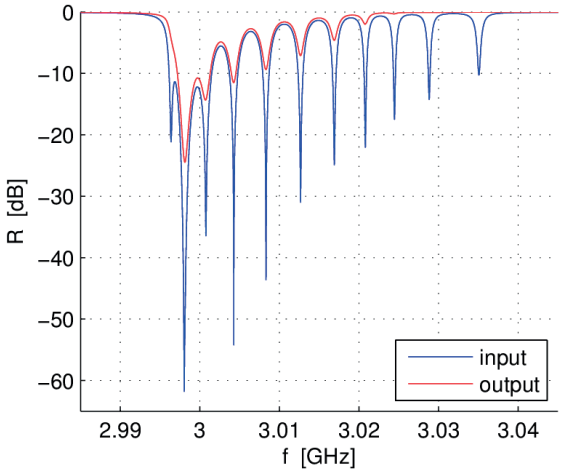

Figure 8: Input and output S-parameters of the tuned structure, measured at a temperature of 23°C in a dry nitrogen atmosphere.

HIGH POWER TEST SET-UP

A high power test of the prototype is under preparation using a bunker and infrastructure of the CLIC Test Facility (CTF3) to evaluate its breakdown performance. An S-band klystron unit is connected to the accelerating structure, located in the CTF2 bunker room, via WR284 waveguides (Fig. 9).

To ensure the ultra-high vacuum in the structure, below 10^{-8} mbar, an ion pump is installed next to the prototype through an RF pumping. In addition, a vacuum leak test of the prototype has been made in situ at the testing place.

The control and acquisition system are based on National Instrument electronics, a largely direct copy of the configuration of the Xbox-2 test stand [4]. The structure is equipped with a complete experimental set-up for breakdown diagnostics. Two Faraday cups are attached to both ends of the prototype for breakdown detection and dark current measurements. Incident, reflected and transmitted RF power is extracted by bi-directional couplers inserted before and after the structure. The amplitude and phase of these 3 GHz signals will be processed by down-mixing to 62.5 MHz and digitizing in 250 Msps ADCs. The analysis of these signals will allow the longitudinal localization of vacuum arcs in the structure [5].

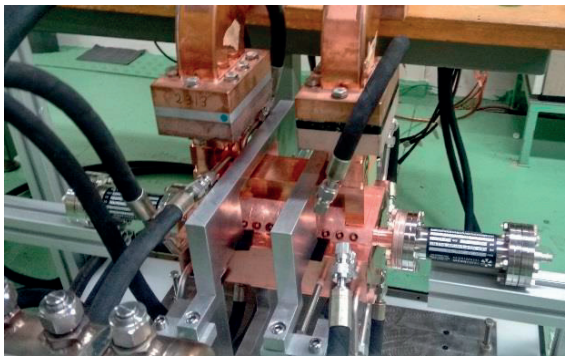

Figure 9: Picture of the prototype under test in CTF2.

SUMMARY AND FUTURE STEPS

A 3 GHz Backward Travelling Wave (BTW) accelerating structure with geometric beta of 0.38 was recently designed and built at CERN. The main goal of the project is to investigate the accelerating gradient limits of the S-band regime. In this paper, the mechanical design, fabrication and tuning of the prototype is discussed, together with the high power test set-up. The prototype is currently installed in CLIC CTF2. The start of high – gradient testing is imminent.

ACKNOWLEDGMENT

The authors are very grateful to the CERN KT group for having funded the accelerating structure prototype construction and supplied important test equipment.

REFERENCES

[1] A. Grudiev, S. Calatroni and W. Wuensch, “New Local Field Quantity Describing the High Gradient Limit of Accelerating Structures”, Phys. Rev. ST Accel. Beams 12 (2009) 102001.

[2] A. Degiovanni, “High Gradient Proton Linacs for Medical Applications”, EPFL PhD Thesis (2014).

[3] S. Benedetti *et al.,* “RF Design of a Novel S-Band Backward Travelling Wave Linac for Proton Therapy”, in Proceeding of LINAC Conference (2014).

[4] B.J. Woolley, “High Power X-band RF Test Stand Development and High Power Testing of the CLIC Crab Cavity”, Lancaster University PhD Thesis (2015).

[5] A. Degiovanni *et al.,* “Diagnostics and analysis techniques for high power X-band accelerating structures”, in Proceeding of LINAC Conference (2014).

Copyright © 2017 CC-BY-3.0 and by the respective authors

ISBN 978-3-95450-169-4

DESIGN OF A 750 MHZ IH STRUCTURE FOR MEDICAL APPLICATIONS

S. Benedetti#, CERN, Geneva and EPFL, Lausanne, Switzerland
A. Grudiev, A. Latina, CERN, Geneva, Switzerland

Abstract

Low velocity particles are critical in every hadron accelerator chain. While RFQs nicely cover the first MeV/u range, providing both acceleration and bunching, energies higher than few MeV/u require different structures, depending on the specific application. In the framework of the TULIP project [1], a 750 MHz IH structure was designed, in order to cover the 5-10 MeV/u range. The relatively high operating frequency and small bore aperture radius led the choice towards TE mode structures over more classic DTLs. Hereafter, the RF regular cell and end cell optimization is presented. An innovative solution to compensate dipole kicks is discussed, together with the beam dynamics and the matching with the 5 MeV 750 MHz CERN RFQ [2]. This structure was specifically designed for medical applications with a duty cycle of about 1 ‰, but can easily adapted to duty cycles up to 5 %, typical of PET isotopes production in hospitals.

INTRODUCTION

R&D developments in low beta linear accelerators sparked in the last two decades. Alvarez drift tube linacs (DTL) are usually the preferred solution after the RFQ for pulsed operation. An alternative to DTLs are H-mode linacs, operating in the TE_{110} mode – inter-digital H (IH), or in TE_{210} mode – cross-bar H (CH), as RFQs. Different hybrid solutions – quasi-Alvarez DTL, H-mode linac with PMQ focusing – were studied [3,4]. Ultimately, the choice of the best accelerating structure depends on the application. Medical linear accelerators are characterized by pulsed, low current beam, and have thus a small aperture radius. In addition, a high accelerating gradient is desirable, in order to reduce the overall length of accelerators that have as a final target medical rooms in hospital. This set of parameters – small aperture and high gradient – is unique amongst low beta accelerators, and thus call for a specific design.

COMPARISON BETWEEN STRUCTURES

The 5 MeV 750 MHz CERN proton RFQ represented the starting point of this study. From preliminary beam dynamics considerations, it was decided to use accelerating structures with 2.5 mm aperture radius. The operating frequencies considered were 750 MHz, as the RFQ, and 3 GHz, as the high-beta accelerating structures already designed [5]. The intermediate harmonics were not considered.

RF regular cells with a simplified geometry were optimized in terms of Shunt Impedance (ZTT), considering both DTL and H-mode cavities at the two different frequencies, when applicable (Fig. 1). The results obtained clearly showed the advantage of IH-mode structures in the 5 to 20 MeV/u range. As we will discuss in the following section, the optimization of IH structures is more complex than the optimization of DTL cavities, for which the gap is the most important parameter. As a result, a detailed cavity optimization remarkably increased the ZTT of the 750 MHz IH solution considered (dark red curve in Fig. 1).

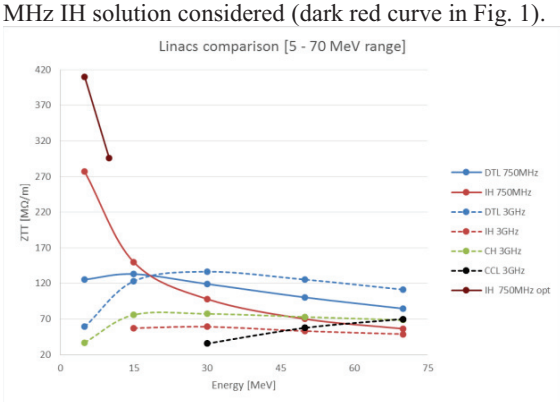

Figure 1: ZTT comparison between different RF cavities.

REGULAR CELL DESIGN

The optimization of TE cavities is more challenging with respect to TM mode ones because of the current flowing in the conductor walls. A DTL RF cell has its ZTT optimum for a given gap, and for stem radius and drift tube thickness the smallest possible. This is not, in absolute terms, the case for IH cavities. For instance, a large stem radius is beneficial because it reduces the Ohmic losses, but it also affects the gap region electric field, thus reducing the ZTT. A careful RF optimization was carried out in order to maximize the ZTT, for a cell length of $\beta\lambda/2$ corresponding to 2.5, 5 and 10 MeV.

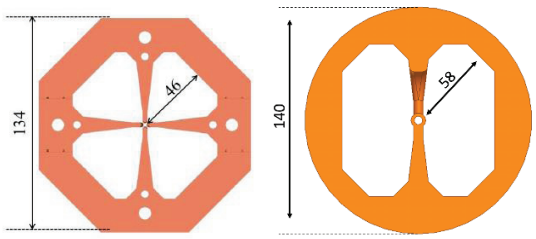

Figure 2: Comparison between the 5 MeV 750 MHz RFQ cell cross section and the IH one.

stefano.benedetti@cern.ch

Copyright © 2017 CC-BY-3.0 and by the respective authors

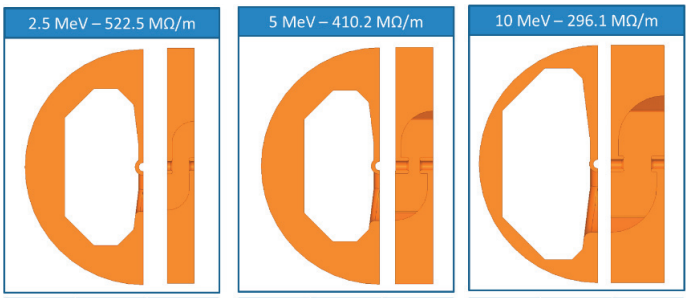

Q	R/Q	T	Q	R/Q	T	Q	R/Q	T
10074	52072	0.780	10732	38224	0.826	11681	25352	0.842
Lcell	Gap	S. Rad	Lcell	Gap	S. Rad	Lcell	Gap	S. Rad
14.561	9	2.5	20.586	11	3	28.949	15	4

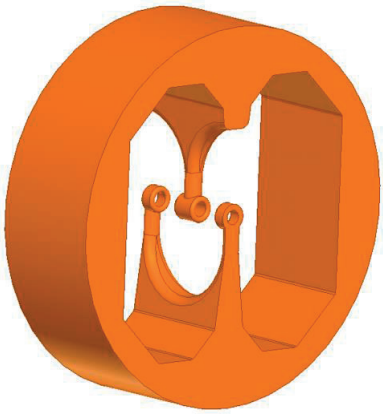

Figure 3: Geometric and main parameters comparison between IH optimized regular cells (left) and structure assembly view (right). Dimensions are in mm, and R upon Q in Ω/m.

The 2.5 MeV regime was investigated in the perspective of further projects with carbon ions. As shown in Fig. 2, the transverse dimension is close to the one of the 750 MHz RFQ. The RF design indeed followed also the goal of having a geometry which is close to the one of the RFQ, in order to maximize the experience gained at CERN in terms of brazing – assembly, and tuning, of structures in these regimes of beta and frequency. The main accelerating and geometric parameters of the optimized cells, together with a view of the structure is reported in Fig. 3.

A thermal and deformation analysis was performed on the optimum geometries found, considering an accelerating gradient of 10 MV/m and a duty cycle typical of medical applications, i.e. 10^{-3} (Fig. 4). It is demonstrated that, at such low DC, cooling of drift tubes is not necessary thanks to the high ZTT. The simulated temperature difference is 1.2 deg, and the maximum temperature induced deformation is 0.5 µm.

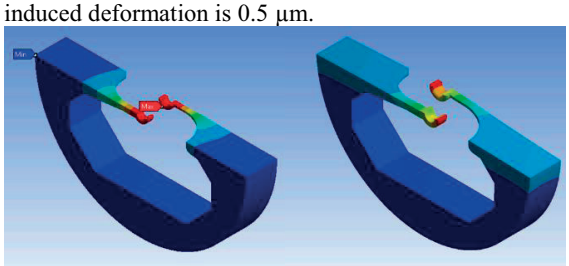

Figure 4: Thermal and deformation analysis for the 5 MeV cell at 10 MV/m accelerating gradient and 10^{-3} duty cycle.

END CELL DESIGN

End-cells are probably the most critical part in the design of an H-mode accelerating structure. The transition from a TE mode to a TM one, due to end-cell walls, forces a strong rupture of the symmetric chain, which can propagates along many regular cells and decrease significantly the overall ZTT. Passing from TE to TM translates into the need of increasing the cavity dimension. The solution adopted is the one presented in [4], though another study proposes a different approach [6]. In this regard, the RF design was completed, but a mechanical study is necessary before validating the proposed solution. The ZTT decrease in the end cells is higher than 50%, thus making this design, as all H-mode cavities, efficient only if the structure is long enough to make the end-cells effect on the overall efficiency negligible.

DIPOLE KICKS

Electrical coupling between drift stems induces a dipole kick component along the stems direction. This effect is a consequence of the small aperture dimension and drift gap, and is not notable in standard low frequency DTLs. While RF defocusing manifests with an imaginary linear component of the transverse voltage over one cell at different transverse axis, dipole kicks are given by the constant real part of the same voltage, as shown in Fig. 5. The slight asymmetry in Fig. 5 comes from higher order terms, sextupoles or octupoles.

Compensation of dipole kicks is usually achieved by modifying the shape of the drift tube, as proposed in [4]. However, authors realized that a simpler solution can be adopted, which is presented in the next section.

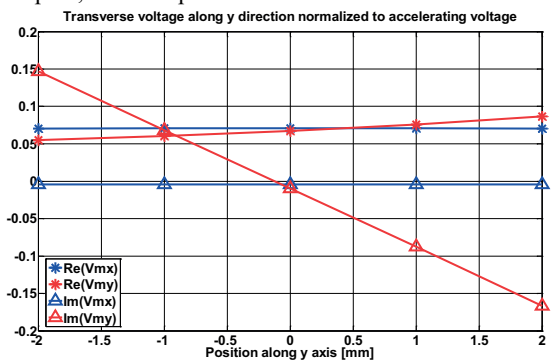

Figure 5: Dipole kicks in a regular cell with drift stems 90 deg rotated.

BEAM DYNAMICS

An accelerating structure approximately 0.9 meter long, length tapered, was designed. The beam dynamics was

Copyright © 2017 CC-BY-3.0 and by the respective authors

ISBN 978-3-95450-169-4

studied considering the structure field map with the code RF-Track [7]. The structure design was driven by the goal of boosting particles from 5 to 10 MeV, assuming as RF power source one 100 kW 750 MHz IOT. For comparison, in the RFQ four 100 kW IOTs are needed. As a result, a 750 MHz RFQ + IH-structure solution would require 500 kW to accelerate protons up to 10 MeV.

Dipole kicks act linearly on particles, thanks to the constant voltage of the IH structures (blue curve in Fig. 6 top). So a compensation as the one proposed in [4] would act as the red or green curve in Fig. 6 top. However, if the kick in the input cell could be reduced, the beam will experience a trajectory similar to the one of a particle in an undulator, because dipole kicks have opposite direction in every gap crossed by the synchronous particle. Quite interestingly, a reduced gap, typical of optimum end-cells design, gives reduced dipole component very close to what is required. In conclusion, the authors have efficiently controlled the beam in simulations simply by a careful design of the end-cells (blue curve in Fig. 6 bottom). The last cell of the structure must also have a reduced dipole component, in order to have zero integrated kick.

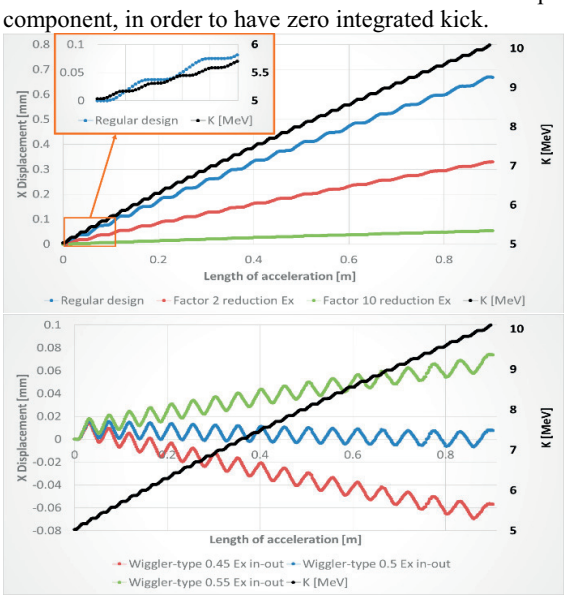

Figure 6: Single particle x-displacement along the IH structure. Transverse component reduced (top) and end-cells compensation (bottom) solutions.

Full beam tracking was then performed, using a triplet focusing between the RFQ output and the IH structure (Fig. 7). The transverse emittance is preserved, while the longitudinal one increases about 50%. It was verified that a modification of the longitudinal phase space at the RFQ output could reduce the longitudinal emittance growth down to 20%.

Though not presented in this paper, it was chosen to accelerate particles from 10 MeV onwards through 3 GHz DTL structures. A relatively high synchronous phase of 20 deg was chosen for the IH structure in order to facilitate the longitudinal matching to the downstream 3 GHz linac acceptance. The transverse matching had to be slightly penalized in order to reach full transmission. However, in the same 5 to 10 MeV energy range, a solution based on 3 GHz DTL, as the one proposed and tested in [8], was studied, and it gives worst performances both in terms of transmission and emittance growth.

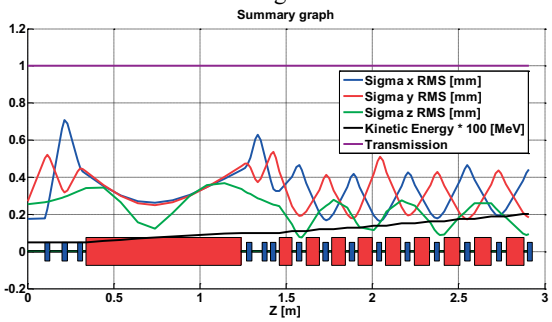

Figure 7: Particles 3D envelopes (1 rms), transmission and kinetic energy from RFQ output to 20 MeV.

SUMMARY

An IH accelerating structure was designed to boost protons from 5 to 10 MeV. This solution represents an ideal continuation of the 750 MHz CERN RFQ to higher beam energies for medical applications, remarkably improving current designs based on high-frequency DTL structures, both from RF and beam dynamics point of view. The longitudinal and transverse matching with a subsequent 3 GHz DTL linac at 10 MeV was studied, and a beam dynamics design from 5 to 20 MeV is presented in this paper.

REFERENCES

[1] A. Degiovanni et al, "Design of a Fast-Cycling High-Gradient Rotating Linac for Protontherapy", in *Proc. IPAC'13*, Shanghai, China, May 2013, paper THPWA008, p. 3642.

[2] M. Vretenar et al, "A compact high-frequency RFQ for medical applications", in *Proc. LINAC14*, Geneva, Switzerland, Aug 31-Sept 5, 2014, paper, THPP040, p. 935.

[3] P. Lapostolle, M. Weiss, "Formulae and procedures usefull for the design of linear accelerators", CERN-PS-2000-001 (DR).

[4] S. Kurennoy et al, "H-mode accelerating structures with PMQ beam focusing", Los Alamos National Laboratory, USA.

[5] S. Benedetti et al, "RF Design of a Novel S-Band Backward Travelling Wave Linac for Proton Therapy", in *Proc. LINAC14*, Geneva, Switzerland, Aug 31-Sept 5, 2014, paper, THPP060, p. 992.

[6] U. Amaldi et al, "CLUSTER: A high-frequency H-mode coupled cavity linac for low and medium energies", NIMA 579 (2007) 924-936.

[7] A. Latina, "RF'Track: Beam Tracking in Field Maps Including Space-Charge Effects. Features and Benchmarks", presented at LINAC16, East Lansing, USA, Sept. 2016, paper MOPRC016, this conference.

Copyright © 2017 CC-BY-3.0 and by the respective authors

[8] C. Ronsivalle et al, "First acceleration of a proton beam in a side coupled drift tube linac", EPL, 111 (2015) 14002.

Copyright © 2017 CC-BY-3.0 and by the respective authors

ISBN 978-3-95450-169-4

High gradient linac for proton therapy

S. Benedetti,* A. Grudiev, and A. Latina
CERN, CH-1211 Geneva-23, Switzerland
(Received 23 January 2017; published 13 April 2017)

Proposed for the first time almost 30 years ago, the research on radio frequency linacs for hadron therapy experienced a sparkling interest in the past decade. The different projects found a common ground on a relatively high rf operating frequency of 3 GHz, taking advantage of the availability of affordable and reliable commercial klystrons at this frequency. This article presents for the first time the design of a proton therapy linac, called TULIP *all-linac*, from the source up to 230 MeV. In the first part, we will review the rationale of linacs for hadron therapy. We then divided this paper in two main sections: first, we will discuss the rf design of the different accelerating structures that compose TULIP; second, we will present the beam dynamics design of the different linac sections.

DOI: 10.1103/PhysRevAccelBeams.20.040101

I. INTRODUCTION

Hadron therapy refers to the treatment of tumors with hadrons. Though different ions, like He, are under study, the two main ones used in daily treatments are carbon ions and protons, with the latter taking the bigger part. At the time of writing, November 2016, 71 facilities are in operation in the world, ten of which can accelerate also carbon ions [1].

Cyclotrons, for protons, and synchrotrons, for carbon ions and protons, are the two accelerator types used in the above-mentioned facilities. Cyclotrons in particular proved to be a very suitable technology for proton therapy facilities, which require beam energies up to 250 MeV, and so do not encounter the ultrarelativistic limitations of cyclotron technology. Moreover, the relatively low beam rigidity permits the use of magnets of reasonable size and power consumption.

In this very competitive and fast growing market, a linac solution could seem unreasonable. Nevertheless, both cyclotrons and synchrotrons present drawbacks that linear accelerators easily overcome. Cyclotrons main drawback is represented by the fixed beam extraction energy. As a result, to target the tumor at different depths into the patient body, movable absorbers are placed in the beam transport line to passively reduce the beam energy. This causes the loss of more than 99% of the beam and the activation of the area. In addition, the beam gets scattered and secondary particles may travel towards the patient. Synchrotrons on the other hand enable the tuning of the extracted beam energy actively. This takes about 1 s, resulting in long treatment time of an average volume tumor, with repercussion on the patient comfort and the number of patients treated per day, so ultimately on the economical sustainability of the facility. So, ultimately, on the economical sustainability of the facility.

The key advantage of linacs lies in the possibility to actively change the output beam energy, as proposed by TERA Foundation and discussed in [2]. This can be accomplished by varying electronically the rf amplitude and phase in the last active accelerating structure at a repetition rate typically of 100 to 200 Hz. These features translate into a quick treatment, with no activation and no scattering of the beam.

Linacs for proton therapy were first proposed in 1991 [3]. This solution was taken up by TERA Foundation, which in 1994–1995 designed in detail a 230 MeV linac for proton therapy [4] and, in collaboration with CERN and INFN, first proved the feasibility of a 3 GHz accelerating structure for protons [5,6]. Since 2001 the activity of TERA Foundation mostly focused on the so-called *cyclinac* concept. In this solution a commercial cyclotron accelerates particles up to tens of MeV, which are then boosted by a linac up to the energies of medical interest, i.e. 70 to 230 MeV in the case of protons.

Following the design of Ref. [4], the ENEA (Italian national agency for new technologies, energy and sustainable economic development) group of Frascati, Italy, worked on an *all-linac* solution, with an rf quadrupole (RFQ) and a drift tube linac (DTL) system covering the particle acceleration up to 40–70 MeV [7], to be followed by the coupled cavity linac (CCL) designed by TERA [5,6]. All these activities have been described in the review paper of Ref. [2].

Arguably, one of the most recent breakthroughs in the field is represented by the 750 MHz CERN RFQ [8]. This solution was specifically designed to inject particles at

*Also at EPFL, Lausanne, Switzerland.
Previous address: TERA Foundation, via Puccini 11, Novara, Italy.
stefano.benedetti@cern.ch

Published by the American Physical Society under the terms of the Creative Commons Attribution 4.0 International license. Further distribution of this work must maintain attribution to the author(s) and the published article's title, journal citation, and DOI.

5 MeV into a 3 GHz DTL structure as the one proposed by ENEA. Based on these developments, A.D.A.M [9], a spin-off company of CERN, is building on CERN premises a commercial *all-linac* machine for proton therapy, based on a RFQ-DTL complex and a CCL solution [5,6].

II. THE TULIP *ALL-LINAC* SOLUTION

All the developments on linacs for proton therapy previously listed are focused on efficient acceleration and control of the beam. In recent years however, the footprint has became increasingly important, since proton therapy facilities have as a final goal the installation in hospital buildings, where dimensions are an issue. As a result, the number of centers with just one treatment room is growing [1].

TERA Foundation first proposed a single-room facility based on a *cyclinac* concept in 2013 [10], called TULIP (*TUrning LInac for Proton therapy*). The idea consists in having a commercial cyclotron on the floor, which injects into a linac mounted on a rotating structure around the patient (Fig. 1).

To make this structure shorter, TERA launched a high gradient research campaign, in collaboration with the CLIC group at CERN, to investigate the high gradient limit of S-Band accelerating structures [11–13]. Based on the results of these tests, a high gradient backward traveling wave accelerating structure for $\beta = 0.38$ was built and is undergoing testing [14,15]. This development allowed one to almost halve the length of the linac that has to be mounted on the rotating structure, saving size, weight and ultimately costs.

In the past two years, the authors started to work on a *all-linac* solution for TULIP, taking advantage of the development of the high frequency CERN RFQ. Hereafter, we will review in detail the first full design of TULIP *all-linac*.

A. Comparison between *cyclinac* and *all-linac* concepts

The *cyclinac* solution strength comes from the idea of accelerating up to tens of MeV protons in a commercial cyclotron. This has a number of advantages over linear accelerators, mainly: (i) lower complexity, being low beta accelerators often the most critical part of the linac chain; (ii) smaller footprint.

However, cyclotrons are not technically suited to inject particles in a linac. The transverse emittance of cyclotron beam is too large to fit into the linacs acceptance, at least the one proposed in [10]. Moreover, and most importantly, the time structure of the beam in the two machines is inherently different.

As far as the transverse emittances are concerned, the available external sources are very intense and a 25–30 MeV commercial proton cyclotron accelerates typically 500 μA so that the output beam can be locally collimated to fit the transverse acceptance of the linac.

The linac longitudinal acceptance poses a more serious problem because a 3 GHz linac with a synchronous phase of -20, a classic value, has a phase acceptance of about 0.06 ns every rf pulse, which has a 0.3 ns period. On this very short time scale, the cyclotron beam is continuous and, as a result, 10% of the beam is accelerated and 90% is outside the longitudinal bucket of the linac.

On a larger time scale, to minimize the losses the beam injected in the cyclotron is made of 5 μs pulses either by chopping the output of the continuous electron cyclotron resonance source or, preferably, by using an intrinsically pulsed electron beam ion source [16]. The injected proton pulse is about 2 times longer than 2.5 μs of the accelerated pulse. As a summary, in the longitudinal phase space, only 5% of the beam is accelerated while 95% is lost.

Another disadvantage of the *cyclinac* solution is that the beam dynamics, being heavily influenced by the longitudinal losses, is unstable and the beam experiences emittance growth. These aspects are discussed in more detail in Sec. V E.

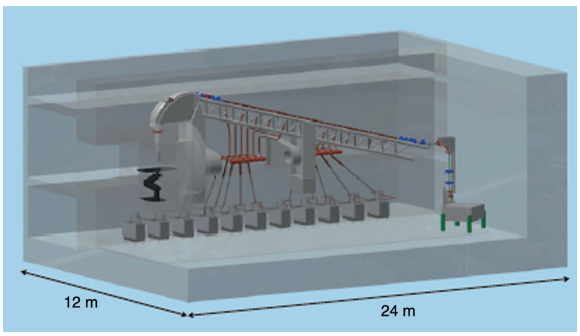

FIG. 1. Sketch of TULIP *cyclinac* solution (courtesy of TERA Foundation).

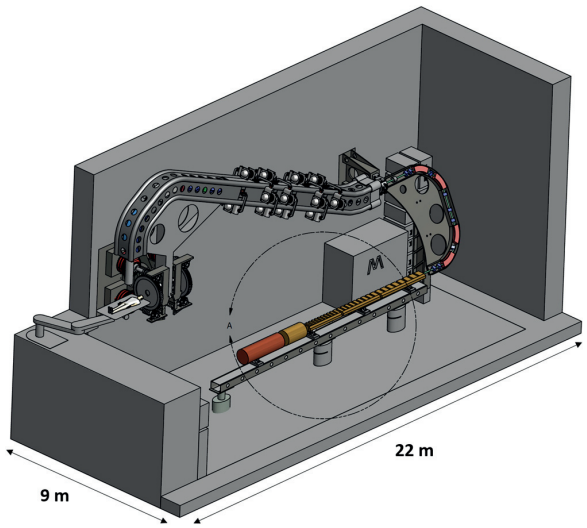

FIG. 2. Sketch of TULIP *all-linac* solution (courtesy of Mohammad Vaziri—TERA Foundation).

An *all-linac* solution instead can reach 100% transmission with a clean beam dynamics, and thus overcome the above-mentioned issues. Linear accelerator chains are used in many laboratories around the world. However, hadron therapy linacs differ from every other application, being characterized by low current and pulsed beam. In addition, the highest possible accelerating gradient is desirable, in order to reduce the overall length of accelerators to be placed in hospital centers. These set of parameters, small aperture radius and high gradient are unique amongst linear accelerators, and thus call for a specific design. A sketch of the TULIP *all-linac* solution studied is presented in Fig. 2.

III. GENERAL LAYOUT

The design is based on a first acceleration up to 10 MeV in 750 MHz structures: the CERN RFQ [8,17] and a newly designed interdigital H mode (IH) cavity. Particles are then injected into a 3 GHz linac chain composed of a DTL, made of many side-coupled modules, up to 70 MeV, and a CCL up to 230 MeV. Table I summarizes the main parameters of the linac design.

The duty factor (DF) of the linac is currently limited by the high gradient section. A typical DF value of 0.05% would be reachable in both the RFQ, the IH and the DTL, but not in the CCL, due to the thin intracell wall thickness chosen to maximize the effective shunt impedance (ZTT). As a result, a final design should decide whether to privilege the acceleration efficiency and the linac compactness, but with a lower DF, or a higher DF but with a lower accelerating gradient or a higher peak power. The design presented hereafter will be limited by the high gradient section to a 0.01% DF, as discussed in Sec. V D 2.

The 750 MHz RFQ was not studied by the authors, and it represents the starting point of the present work. The following three accelerating structures forming TULIP have been studied in detail from both rf and beam dynamics points of view. The high gradient (HG) backward traveling wave (BTW) structure was also built and tested. In the next section we start by presenting the rf design of the cavities.

IV. RF DESIGN

Conceptually, TULIP can be split into a low gradient section, which will be placed on the ground, and a high gradient section that will be mounted on a rotating structure, called gantry. The footprint of the facility is driven by the rotating structure, which has to allocate, together with the high gradient linac, also the high energy beam transfer line (HEBT) and the beam diagnostic. As a result, about ten meters are available on the ground to install the linacs that have to boost the particles up to 70 MeV. This length has been fully exploited, in order to minimize the power consumption for a given energy gain:

$$\Delta W = \sqrt{ZTT \cdot P \cdot L}, \tag{1}$$

where ZTT is the effective shunt impedance of the linac, P is the dissipated peak power and L is the linac active length.

In the following, the different accelerating structures will be revised. Particular attention will be given to the 750 MHz IH and to the 3 GHz HG BTW structures, which were studied by the authors.

TABLE I. Key parameters of the *all-linac* TULIP solution.

Type of structure	Output energy [MeV]	Active length [m]	Peak power [MW]
750 MHz RFQ	5	2	0.4
750 MHz IH	10	0.9	0.1
3 GHz SCDTL	70	4.1	13
3 GHz HG BTW	70–230	4.4	108

A. The low beta section accelerators

With the 750 MHz RFQ as a starting point, the authors investigated the best solution to be placed afterwards, in the 5 to 70 MeV/u range. The rf design of this section was mostly driven by the optimization of the ZTT, together with machinability and thermal constraints. Breakdown (BD) limitations are not an issue here, since as previously discussed the accelerating gradient of this section is relatively low.

Different types of cavities, both TE and TM modes, were considered, at two operating frequencies, 750 MHz and 3 GHz. A simplified geometry was considered, with constant drift tube thickness and stems radius independently on the geometric β. All the structures were studied by optimizing the cell gap at different geometric βs, from 5 to 70 MeV/u. The bore aperture radius chosen was 2.5 mm, from preliminary beam dynamics considerations. The result of this study is shown in Fig. 3. The very high values of

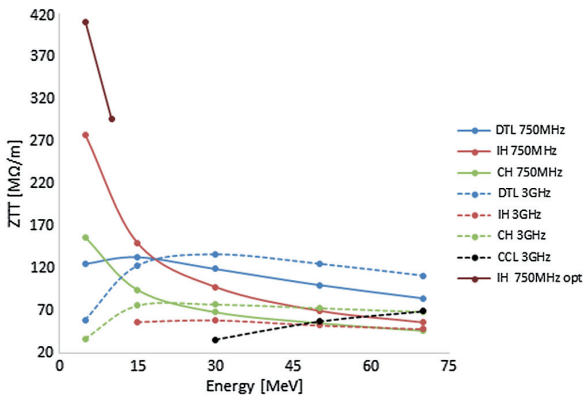

FIG. 3. ZTT as a function of the geometric βs for the cavities considered.

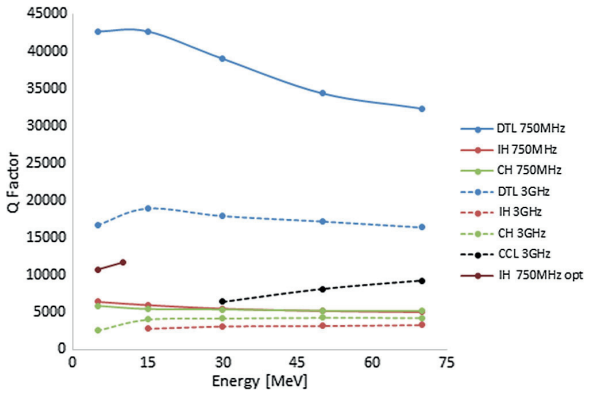

FIG. 4. Q-factor as a function of the geometric βs for the cavities considered.

ZTT found are not common in literature, but should not surprise. Indeed, the very small bore aperture, together with the high operating frequencies, represent a *uniqum* amongst linac designs, and are the reason of these results.

The results of Fig. 3 can be further understood by looking at the quality factor (Q) values, presented in Fig. 4. One can notice that TM mode cavities have a significantly higher Q value. However, they pay a quite high price in terms of concentration of electric field in the nose region and transit-time (TT) factor, being 2π mode cavities. This results in a lower overall efficiency (Fig. 5). This difference gets narrower for higher geometric βs, where the TE cavities lose their advantage.

1. rf optimization of TM and TE mode DTL cavities

In TM mode DTL cavities no current flows through the stems. These have only a structural and heat dissipation purpose. Concerning ZTT, the thinner the drift tube and the drift stems, the higher is this parameter. Indeed, if it were possible to build a structure with drift tubes suspended in the void, this would be beneficial in terms of ZTT. TM mode cavities are constant gradient structures. In the assumption of constant transit time factor, the voltage gain grows with the geometric β of the structures, given the increased cell length. Low β TM mode cavities usually works in 2π mode, and this mode was considered in the present study.

TE mode DTL cavities have, on the other hand, current flowing through the stems. Here the stems and the drift tubes have again a structural and heat dissipation role, but in addition they have to force the electric field to be parallel to the z axis in the bore aperture region. TE mode cavities usually work in either dipole magnetic mode—TE_{110}, being called interdigital H (IH)—or as RFQs in quadrupole magnetic mode—TE_{210}, being called cross-bar H (CH). The current flowing through the stems brings to Ohmic losses that can be minimized increasing the size of drift tubes and stems. However, this reduces the electric field concentration near the z axis. Ultimately, a detailed rf optimization is needed to find the optimum ZTT for a given cell length, taking into consideration machinability and thermal dissipation constraints. A more detailed discussion on the rf optimization of TE cavities can be found in [18]. TE mode cavities work in π mode, so they are shorter than TM mode cavities for the same operating frequency and geometric β.

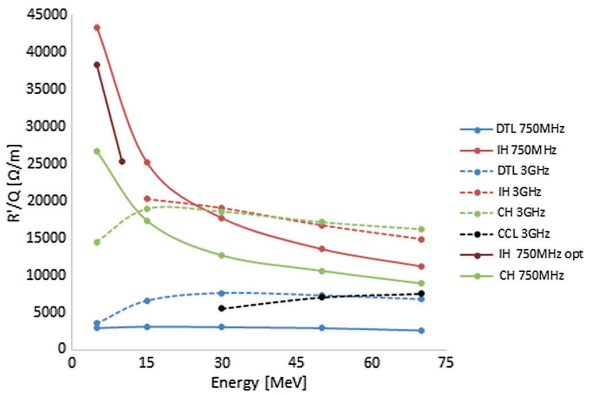

FIG. 5. R'/Q as a function of the geometric βs for the cavities considered.

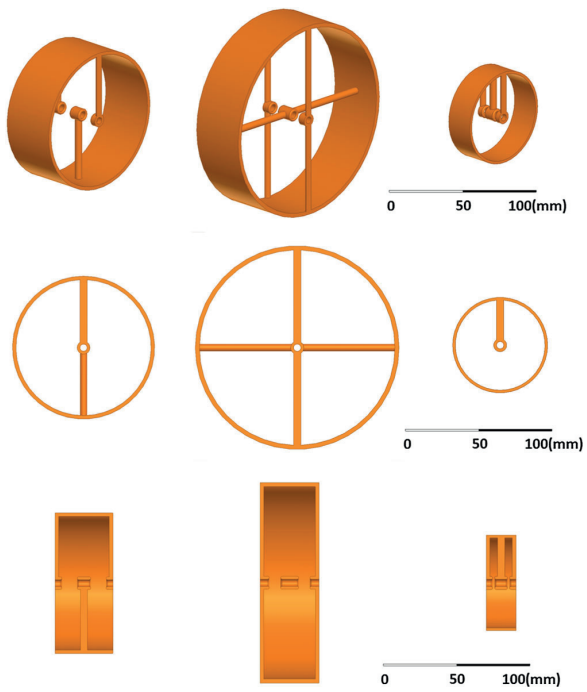

FIG. 6. Comparison between selected 5 MeV/u cells. Asymmetric view (top), transverse (middle) and longitudinal section (bottom). 750 MHz IH (left), 750 MHz CH (middle) and 3 GHz DTL (right).

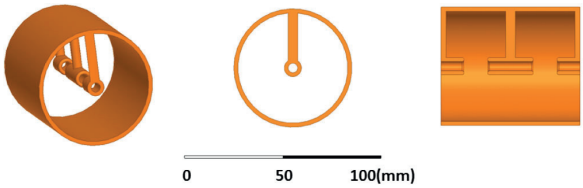

FIG. 7. 3 GHz DTL structure at 70 MeV/u. Asymmetric view (left), transverse (middle) and longitudinal section (right).

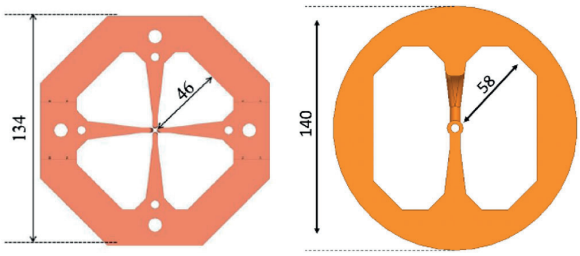

FIG. 8. Transverse section of 5 MeV/u cells. CERN high frequency RFQ (left) and IH (right). Dimensions are in mm.

With respect to the results presented in Fig. 3, the three most promising cavities at 5 MeV/u are the 750 MHz IH, the 750 MHz CH and the 3 GHz DTL, as shown in Fig. 6. One can clearly notice the differences in terms of cell length and diameter of the three solutions.

At 70 MeV/u, the 3 GHz DTL solution reveals to be the better choice. For visual comparison, the cavity dimensions are shown in Fig. 7.

B. 750 MHz IH structure

From the preliminary rf optimization summarized in Fig. 3, it was quite clear that the 750 MHz IH cavity was the best solution in the 5–20 MeV/u regime. The simplified geometry considered in the first comparison was revised [19]. The main goal of the rf design has been to maximize the ZTT, while sticking as much as possible to the cavity geometry considered for the CERN 750 MHz RFQ, to take advantage of the experience gained in the construction of TE cavities at this very high frequency. Indeed both RFQ and H-mode cavities are constant voltage structures, with the only difference that a RFQ is a TE_{210} bunching machine, with vanes, while a H mode cavity is a TE_{110} accelerator, and present drift tubes between cells. This translates in overall comparable dimensions, as shown in Fig. 8.

Three energies were studied in detail: 2.5, 5 and 10 MeV/u. The 2.5 MeV/u regime was studied to verify performances and feasibility of this solution in view of further developments of carbon ion projects, where an RFQ would most likely deliver up to 2.5 MeV/u particles instead of 5 MeV/u. A multidimensional optimization was carried out, considering gap, drift tube thickness, stem radius, and vane distance from z axis. The result of this study is a remarkably improved ZTT over previously found values (see dark red curve in Fig. 3). It is interesting to notice that the improvements do not come from a higher TT factor, since the gap is unchanged, but from an increased Q value (Fig. 4).

This is the first time these values have been obtained in literature. As previously pointed out, this is due to the very small bore aperture considered, which allowed for a previously unreached high rf frequency. As discussed in Sec. V B, such aperture is sufficient to get full transmission of the particles bunched by the RFQ, thanks to the transverse emittances of this machine, and to the absence of space charge.

The main geometrical and accelerating parameters of the cavities studied are shown in Fig. 9, together with a view of two cells joined together.

The thermostructural analysis was performed by importing the HFSS™ electromagnetic field distribution to the thermal and structural packages of ANSYS™. The results showed that this structure, thanks to the high ZTT and low operating gradient, does not need a cooling channel in the case of a DF up to 10^{-3}.

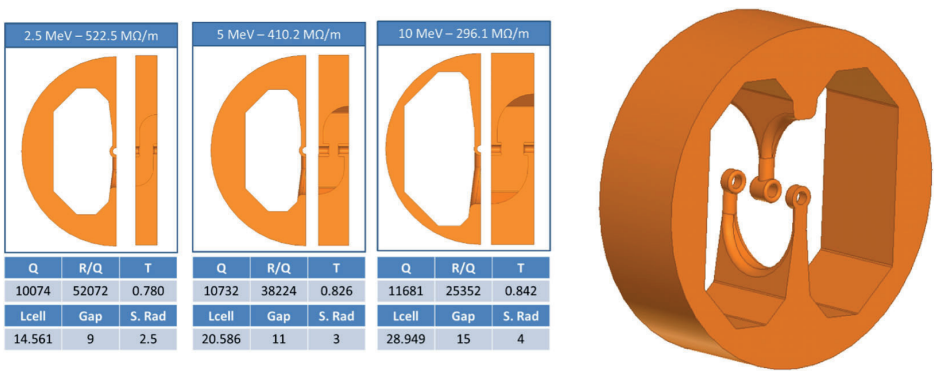

FIG. 9. Regular cell design (left) and assembly view (right) of the IH 750 MHz cavity.

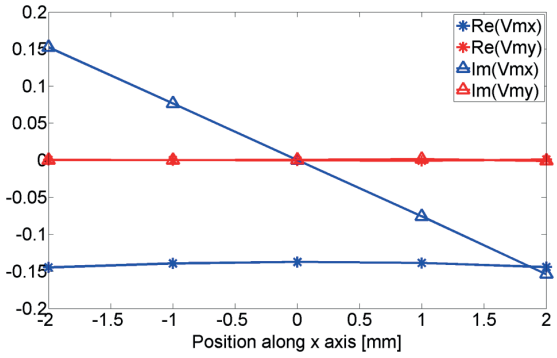

FIG. 10. Transverse voltage along the x axis normalized to the accelerating voltage in the 5 MeV IH cavity.

1. Dipole kicks and transversally focusing IH cavities

The small bore aperture, together with the thin drift tubes and large gaps of the IH cavity result in a non-negligible dipole kick. Analytically, a dipole kick is represented by a real part of transverse voltage:

$$\vec{V}_m = TT \int_0^{L_{\rm cell}} (\vec{E} + \vec{\beta} c \times \vec{B}) dz, \tag{2}$$

which is constant across the bore diameter, as shown in Fig. 10. In Eq. (2) TT is the transit-time factor. A dipole kick is typically negligible in DTL solutions that have thick drift tubes to allocate the permanent magnet quadrupoles (PMQs), and shorter gap to cell length ratios given the 2π mode regime. In contrast, the rf defocusing, which has 90 degree rf phase shift with respect to the dipole kick component, is represented in Fig. 10 as an imaginary part of the voltage which is linear along the x axis, the axis on which the stems are placed.

From the results of Fig. 10 one can notice that the transverse kick is equal to about 15% of the longitudinal kick per cell, for the 5 MeV/u cell. This contribution increases with the cell length. All these effects have been taken into account in the beam dynamics studies (Sec. V B).

C. 3 GHz SCDTL

The regular cell simplified geometry considered in Sec. IV A cannot be adopted as the reference one, due to limitations coming from structural and rf heat power dissipation considerations. A two stems geometry has been eventually considered (Fig. 11), as proposed in [7]. Such modification allows for a sufficient heat dissipation and mechanical stability, but heavily impacts on the ZTT profile presented in Fig. 3. The reduction is around 25%.

This solution raises a slight quadrupolar asymmetry, i.e. the rf defocusing is stronger in the plane of the stems (y-plane in Fig. 12). The difference has been taken into account in the beam dynamics design.

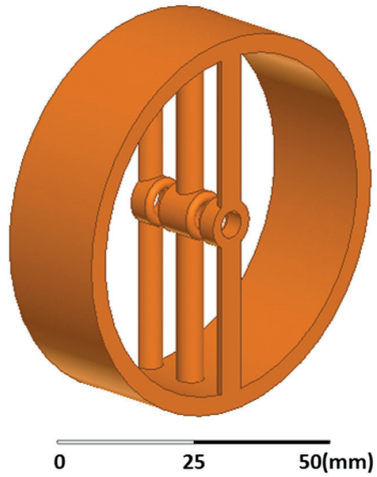

FIG. 11. The 5 MeV reference 3 GHz DTL cavity.

The tuning and field stabilization of a TM mode structure operating in 2π mode at this frequency is without doubt very challenging. This issue has not been addressed yet by the authors. However, Picardi *et al.* presented a working solution in [7].

The advantage of such a solution comes from the possibility of using 3 GHz klystrons, worldwide adopted

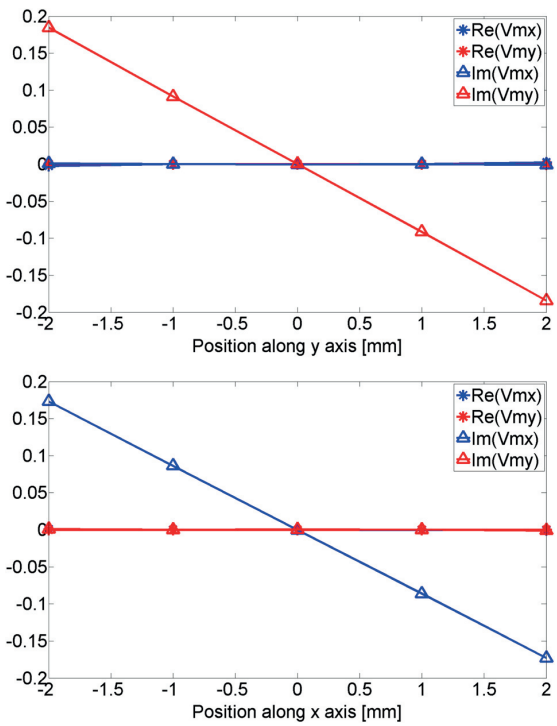

FIG. 12. Transverse voltage along the x and the y axis normalized to the accelerating voltage for the 15 MeV DTL rf cell with symmetric stems.

in more than 1000 electron linacs for radiotherapy, and thus very cheap rf power source.

In the present work, the rf optimization of 3 GHz DTL cavities with the simplified geometry of Fig. 11 was performed, from 5 to 70 MeV.

D. 3 GHz high gradient BTW structure

A high gradient backward traveling wave (BTW) accelerating structure was designed and built at CERN [14,15]. The main goal of the project is to define the high gradient limits of S-band cavities in terms of breakdown rate (BDR). In the design of the prototype a modified Poynting vector (S_c) limit was used [20]. A picture of the prototype, which is 20 cm long and has a geometric β of 0.38, is shown in Fig. 13.

The BTW structure is a constant gradient magnetically coupled traveling wave cavity, with a low group velocity ranging from 0.4% and 0.2% of the speed of light. There are 12 equal length rf cells, ten regular plus two end cells. The phase advance per rf cell is $\frac{5}{6}\pi$. The rf optimization was driven by the minimization of the quantity,

$$\mu \equiv \frac{P_w}{E_a^2} \cdot \frac{S_c}{E_a^2} = \frac{v_g}{\omega} \cdot \frac{S_c/E_a^2}{R'/Q}, \tag{3}$$

where P_w is the power dissipated in one cell, E_a is the accelerating gradient, v_g is the group velocity, ω is the angular rf frequency, R' is the effective shunt impedance per unit length and Q is the quality factor per cell. S_c is a modified Poynting vector that has been used as a new local field to predict the breakdown behavior of the structure.

The minimization of Eq. (3) leads to the maximization of the ZTT for a given limit of $\frac{S_c}{E_a^2}$. The threshold was calculated by rescaling CLIC experimental data (4 MW/mm^2, 200 ns) to pulse lengths typical of medical linacs, i.e. 2.5 μs flattop. CLIC data were rescaled according to Eq. (4):

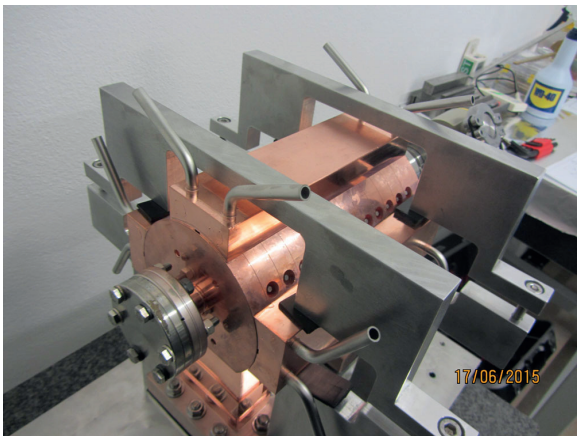

FIG. 13. The 3 GHz BTW prototype.

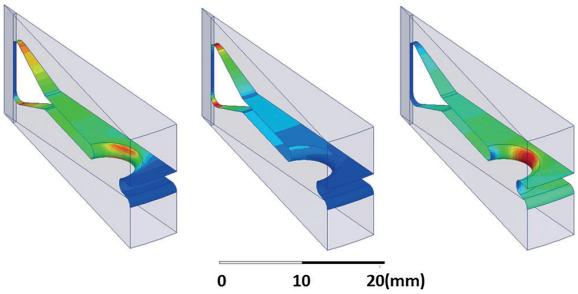

FIG. 14. Electric (left), magnetic (center) and modified Poynting vector (right) field distribution in a regular cell section (1/32 azimuthal symmetry).

$$\frac{S_c^8 \cdot t_{\text{impulse}}^3}{BDR} = \text{const} \tag{4}$$

following a research campaign on S-band and C-band single cavities carried out by TERA Foundation [11,12,21]. An S_c limiting value of 1.55 MW/mm^2 is obtained.

In this particular design, the optimum is found when S_c is minimized simultaneously on the nose, where the electric field is maximum, and on the coupling slot, where the magnetic field is maximum, as shown in Fig. 14.

The structure was mechanically designed at CERN, as well as built, following the CLIC baseline fabrication procedure for high gradient X-band accelerating cavities. The tuning was done at CERN as well. The prototype reached the nominal phase advance between adjacent cells, and total reflection of −60 dB. Currently the prototype is installed in the test area under the high power test.

1. Power recirculation in a TW structure

The BTW structure designed has a power transmission ratio of about 3 dB, i.e. half of the input power is transmitted through the structure and is coupled to either a load or a recirculating circuit. A lower $P_{\text{load}}/P_{\text{in}}$ ratio could have been obtained, but at the price of a longer filling time. To make an efficient use of TW structures, a passive waveguide component, called 3 dB hybrid splitter, has to be used.

A 3 dB hybrid is a four-port passive device. By proper sizing the geometry between the ports, it is possible to equally split the power entering from port 1 towards ports 2 and 3. In this configuration no power goes towards port 4, and there is a 90° phase difference between ports 2 and 3 (Fig. 15).

In the present design, port 1 is connected to the klystron, port 2 to an rf load, ports 3 and 4 to the structure input and output cell, respectively. The power which exits from the structure, entering port 4 and being equally split between ports 2 and 3, makes interference with the power flowing from port 1. If the phase of the rf power entering ports 1 and 4 has 90° phase difference, the interference is constructive

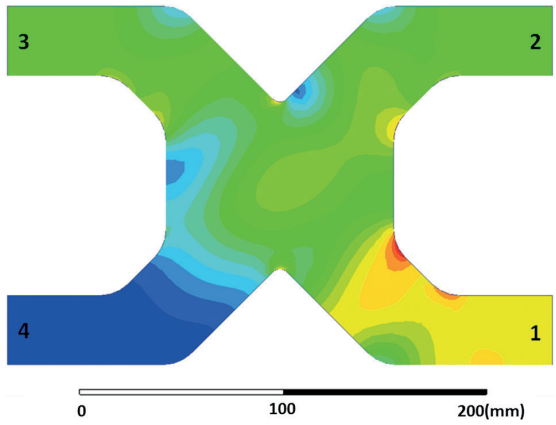

FIG. 15. 3 dB hybrid with power entering from port 1.

towards port 3, namely towards the structure, and destructive towards port 2, the load (Fig. 16).

Taking into consideration the phase difference between the accelerating structure input and output, the length of the transition waveguides which connect the 3 dB hybrid to the accelerating structure can be computed so that there is a 90° phase difference between port 1 and port 4. As a result, this design allows for full power recirculation into a TW accelerating structure.

The power attenuation in S-band (WR-284) waveguides is around 0.02 dB/m. As a result, the power attenuation in the 3 db hybrid is negligible, being lower than 1%. However the drawback of this solution lies in the transverse size of the assembly and in the longer filling time of a factor 4 with respect to the solution without recirculator [22]. A cut transverse view of the structure with the BTW design connected to the hybrid, and with rf power coming from port 1, is shown in Fig. 17.

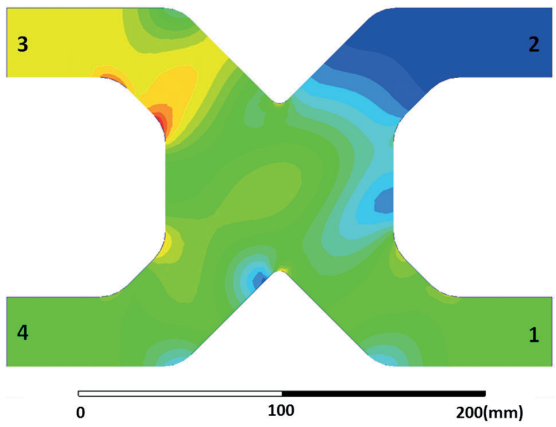

FIG. 16. 3 dB hybrid with power entering from port 1 and port 4 with 90° phase difference.

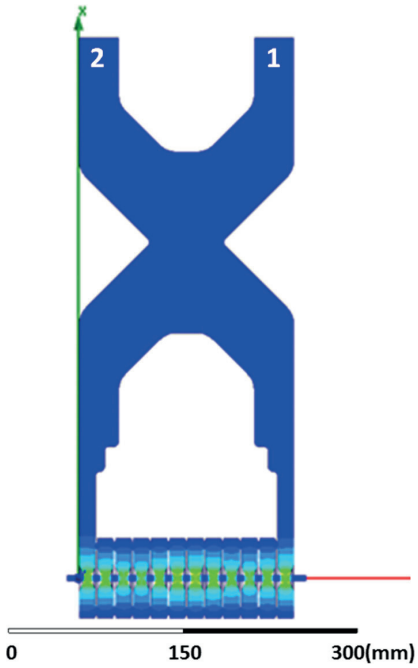

FIG. 17. Complex mag electric field distribution in BTW structure connected to the 3 db hybrid.

E. 3 GHz high gradient CCL and comparison with the high gradient BTW

Historically, CCLs have been a preferred solution for proton acceleration above $\beta = 0.3$ or higher. However, to the authors' knowledge few works addressed the design of 3 GHz CCL above 40 MV/m accelerating gradients: one for $\beta = 0.38$ [11] and a more recent study for $\beta = 0.6$ [23].

The design presented in [12] has been revised, and is here presented, with a few novelties. The very same rf design methodology described in Sec. IV D has been followed, in order to compare the standing wave (SW) solution to the TW one.

The main results are summarized in Table II. The BTW and CCL designs are fully comparable in terms of maximum of the S_c/E_a^2 ratio, but also in terms of key geometrical parameters, like bore aperture and septum thickness. In the CCL case, the limit of S_c/E_a^2 is reached on the nose of the CCL, not on the coupling slot, which is a critical part but not the most critical one in this design.

The mechanical design of the CCL cavities in [5] is based on the production of two half cells that are eventually brazed together. However, a wall thickness of 2 mm, like in the BTW solution, poses a serious challenge to the fabrication and brazing with such a method, because 1 mm walls would be needed. To overcome this issue, a different assembly concept has been proposed [Fig. 18 (middle)].

TABLE II. Main geometric and accelerating parameters of $\beta = 0.38$ cells. HG BTW (left), HG CCL (center), low gradient CCL (right).

Type of structure	BTW150	SCL-HG	SCL-BL
Phase advance per accelerating cell [deg]	150	180	180
Wall thickness septum [mm]	2	2	3
Gap [mm]	7.0	9.0	5.1
Nose con angle [deg]	65	65	25
Number of accelerating cells	12	10	10
Structure active length [mm]	189.9	189.9	189.9
Design accelerating gradient Ea = E0 ∗ TT factor [MV/m]	50	50	26.3
Max ratio surface E-field to accelerating gradient Es/Ea	4	4	6
Max ratio Sc to accelerating gradient square Sc/Ea^2 [A/V]	2.7×10^{-4}	2.7×10^{-4}	7.8×10^{-4}
Quality factor Q (first/last)	6997/7463	9136	8290
R'/Q [Ω/m] (first/last)	7425/7369	6568	8410
ZTT [MΩ/m] (first/last)	52.0/55.0	60.0	69.7

The result of the comparison study is that the ZTT of the CCL solution, even when optimized for high gradients, i.e. 50 MV/m, is higher by about 13% with respect to the BTW solution with full recirculation of the power. For comparison, the last column of the table reports the case of a CCL optimized in terms of ZTT [12]. The maximum gradient here reachable, adopting the S_c model, is 30 MV/m. It is possible to notice, graphically, the difference in the nose shape in Fig. 18. The low gradient case, called base line (BL), has a shorter gap, to maximize the TT factor, and a sharper nose, to concentrate as much as possible the E field near the z axis.

The 3 GHz CCL structure design has a 5% coupling factor, in agreement with a previous designed structure [16], but differs quite substantially in the coupling cell design, pieces manufacturing, and input coupler. The coupling cell design followed the goals of being easy to machine and compact in the transverse dimension.

Another novelty of this design is represented by the single coupler solution adopted. This allows individual power and phase control of each accelerating structure, which as discussed in Sec. V D 1 is a key feature of the TULIP project. A structure made of ten cells, 20 cm long, so exactly identical to the BTW prototype built, was designed and matched to the waveguides. A visual comparison of the solution is shown in Fig. 19.

The two structures were also compared in terms of rf thermal power dissipation. Here the CCL has two advantages: (i) a slightly higher ZTT, which translated into a

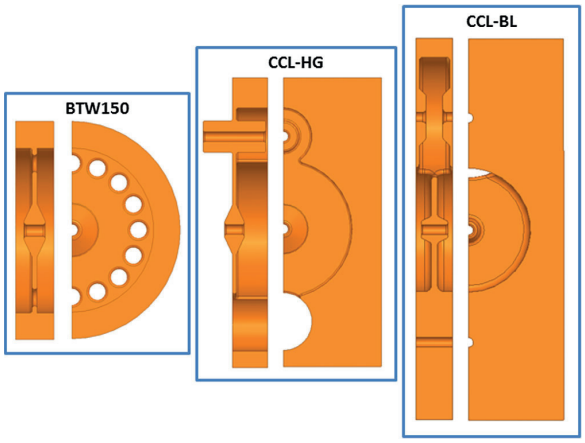

FIG. 18. Mechanical view of the optimized cells.

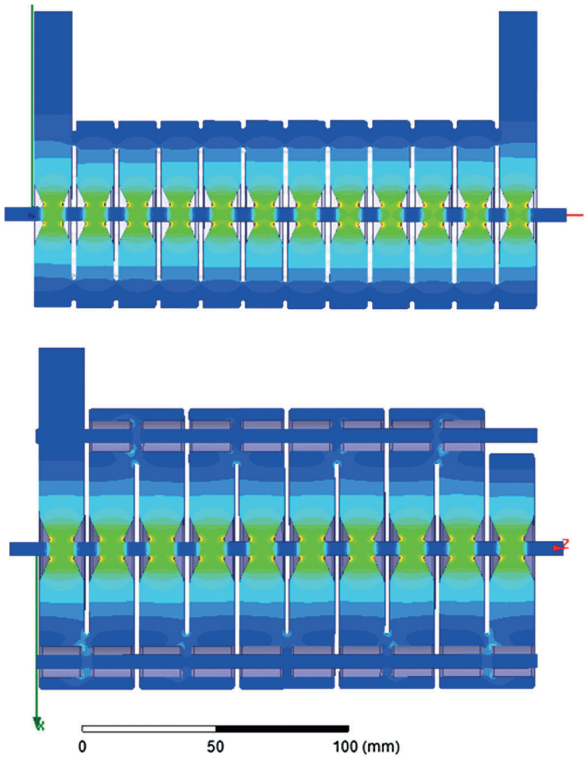

FIG. 19. Cut view with complex mag electric field distribution in the high gradient BTW (top) and CCL (bottom) structures at $\beta = 0.38$.

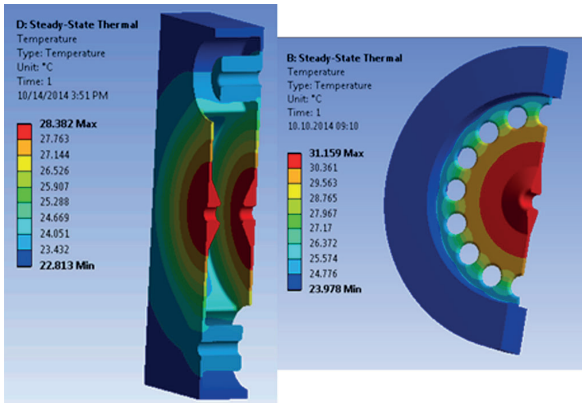

FIG. 20. Temperature distribution in the high gradient BTW (top) and CCL (bottom) structures for a 50 MV/m gradient and 0.0075% DF.

lower rf power dissipated in the copper walls for the same accelerating gradient; (ii) a higher thermal conductivity with respect to the BTW solutions, where the coupling holes are an obstacle to the power dissipation.

The temperature distributions in the two cases are shown in Fig. 20.

1. rf comparison between BTW and CCL structures for a 3 GHz high gradient linac from 70 to 230 MeV/u

The differences between a BTW and a CCL accelerating structure optimized for high gradient operations for a geometric β of 0.38 was discussed in Sec. IV E. The conclusion of this comparison is an advantage of the CCL solution in terms of ZTT, and thermal power dissipation, thus maximum DF achievable. Considering the filling time, the CCL solution takes longer to reach the nominal accelerating gradient with respect to the BTW solution even if a recirculator is installed.

However, if one extends the comparison up to 230 MeV/u, the results change. In particular, a 50 MV/m BTW optimized structure shows about the same ZTT as the CCL solution. The reason for this behavior comes from the difference cell length between the two solutions: the BTW, being shorter, allows for a higher optimization of TT factor (shorter gap) and nose region (sharper nose cone angle) at higher energies. The difference can be observed graphically in Fig. 21.

Three intermediate energies were studied, corresponding to 105, 138 and 181 MeV/u. The TT factor, Q factor and the ZTT along the linac for the two high gradient solutions are shown in Fig. 22. One can notice that the BTW can optimize better the TT factor and the nose region, but shows a lower Q factor with respect to the CCL. This difference

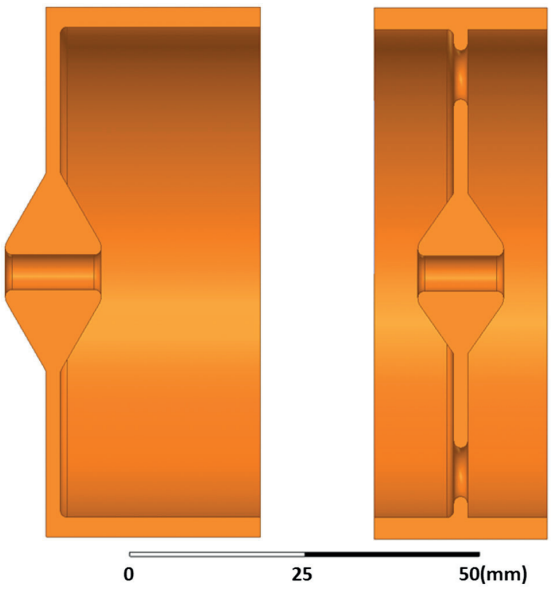

FIG. 21. Uncoupled CCL (left) and BTW (right) cells at 230 MeV/u.

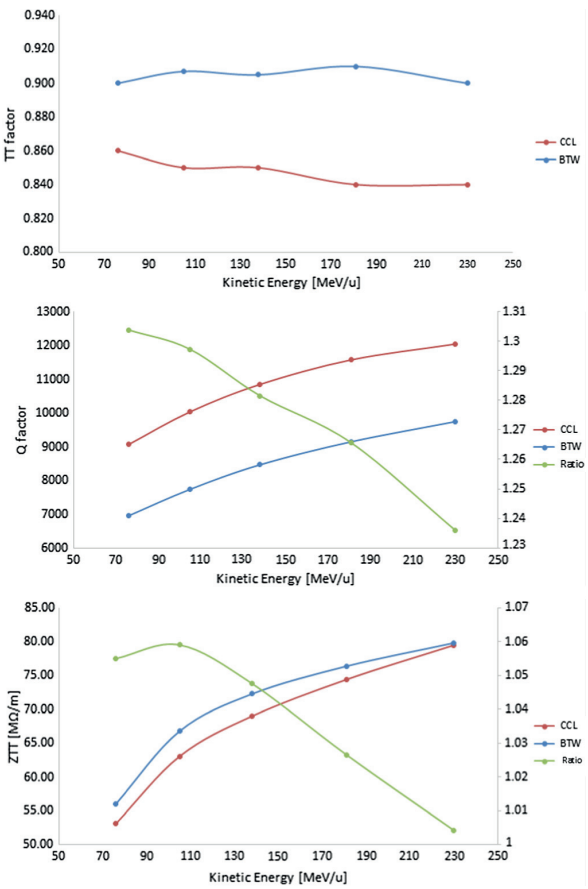

FIG. 22. TT factor (top) and ZTT (bottom) comparison between a CCL and BTW high gradient linacs.

however gets narrower with the increase of the cell lengths, and so does the ZTT.

V. BEAM DYNAMICS STUDY

In this section, we review the beam dynamics design of the different linac sections.

The starting point of the beam dynamics design was the 5 MeV output beam from the CERN 750 MHz RFQ (Fig. 23), here simulated with the code RF-TRACK [24].

The beam emittances are relatively low, with a normalized rms transverse emittance in both planes of 0.027 pi.mm.mrad, and in the longitudinal plane of 0.015 pi.deg.MeV. These values permitted us to consider the very small bore aperture of 2.5 mm used in the IH, DTL and CCL-BTW structures.

The goal of the beam dynamics design was delivering to the high energy beam transfer (HEBT) line beam between 70 and 230 MeV, with full transmission and the lowest possible normalized emittance growth. Both of these goals have been accomplished.

We will start by briefly presenting the tracking code developed for this purpose, RF-TRACK.

A. A new particle tracking code: RF-TRACK

The TULIP *all-linac* project started with the study of the high gradient BTW linac [25]. A TW cavity complicates the particle tracking. In fact, in SW cavities the electromagnetic (EM) field oscillates according to

$$A(x,t) = A(x) \cdot e^{-i\omega t}, \tag{5}$$

where ω is the angular rf frequency, and $A(x)$ is the complex magnitude spatial distribution of either the electric or the magnetic field. The electric and the magnetic field are 90 deg rotated with respect to each other.

In the TW case, a translational component of the field makes it not space independent:

$$A(x,t) = A \cdot e^{i(kx-\omega t)}, \tag{6}$$

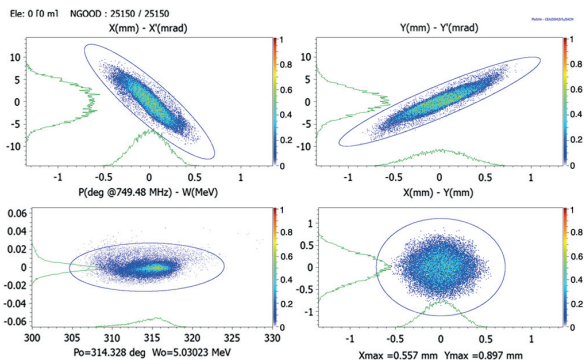

FIG. 23. Phase space of the beam at the RFQ output.

where k is the wave number. A negative kx component characterizes a backward traveling wave.

Very few codes are capable of dealing with TW structures, since in this case both the real and the imaginary components of the field are necessary. To our knowledge, the most frequently used codes are ASTRA [26] and GPT [27]. The tracking can also be accomplished with SW codes by superimposing two SW patterns of different frequency [28]. Nevertheless, the need to work with TW field maps and to perform matchings and transmission optimizations, dynamically varying the rf input power as well as the lattice optics (see Sec. V D 1), called for development of a new tracking code: RF-TRACK. In addition, an in-house developed tool rather than a black-box tool, allowed us to add new features as necessary.

After the benchmark phase [24,25], RF-TRACK has been used to track particles start to end, i.e. the beam distribution has not been regenerated, from the RFQ output up to 230 MeV.

This approach, based on accelerating structure EM field maps, is more time consuming than an analytical tracking. In the latter, the field is generated with cylindrical symmetry from Bessel expansion of the average electric field on the z axis and the transit-time factor profile along the linac. However, as discussed in Sec. IV B 1 for the IH dipolar components, and in Sec. IV C for the side coupled drift tube linac (SCDTL) quadrupolar asymmetries, the linacs are not always perfectly symmetric structures. The field map approach allowed us to correctly take into consideration these aspects.

B. From 5 to 10 MeV

Protons are accelerated by the IH structure described in Sec. IV B from 5 to 10 MeV. The attentive reader may remember from Sec. IV A that the ZTT advantage of IH cavities over the other solutions considered extended well beyond 10 MeV/u. However, at the present stage the cost per unit power of 750 MHz rf sources, currently only inductive output tubes (IOTs), is about 1 order of magnitude higher than the corresponding cost in the case of 3 GHz klystron-modulator based solutions [29]. This difference is largely caused by the high demand of this latter technology working at 3 GHz, caused by the market of x-ray electron linacs. However, even though it is the authors' belief that this price difference will decrease in the future as a consequence of a higher demand of 750 MHz rf power sources, at the present stage the crossing point between a 750 IH solution and a 3 GHz DTL one has been found at 10 MeV/u.

To boost protons from 5 to 10 MeV it has been chosen to use just one 100 kW IOT, resulting in a fairly low gradient of about 5.7 MV/m, and in a 0.9 m long structure. The structure is tapered in length, and composed of 36 drift tubes. The first cell is 20.8 mm long, the last one 28.9 mm long. The average ZTT, taking into consideration the end

cells, is around 350 MΩ/m. The beam from the RFQ was transversally matched with a triplet quadrupole focusing, and then accelerated in the IH structure with a constant synchronous phase of −12 deg. A 16% margin in the IOT nominal power was kept, to take into account waveguide losses, so 84 kW are actually dissipated by the cavity walls.

Given the small bore aperture and thin drift tubes, a not negligible dipole kick component is present, equal to almost 15% of the longitudinal component, as discussed in Sec. IV B 1. Indeed, when the beam was tracked through the structure field map with RF-TRACK, it showed a final displacement of about 0.7 mm out of a 2.5 mm bore aperture. This was clearly not acceptable, and it has been corrected in the following way.

In Fig. 24 (top) one can notice the x displacement of a single particle that enters the field map with no initial displacement and divergence. The particle gets deflected in the first gap, then drifts away in the drift tubes. In the second gap, the dipole kicks have opposite direction but almost equal magnitude. In fact, a IH cavity is a constant voltage structure, so also the transverse voltage is constant. This is true at first order approximation, given that the dipole kick component increases with longer cell lengths. However, so does the beam rigidity. Overall, the particle divergence gets approximately to zero in the second gap of the structure. Then in the third gap it picks again an x divergence, which gets canceled again in the fourth gap. So, traveling through cells, the particle shows a linear displacement with energy, and zero integrated kick. Solutions proposed in previous works [30] were based on the modification of the drift tube shape and relative position with respect to the x axis, to reduce the dipole component. For the IH cavity under study, this presents the disadvantage of reducing the ZTT with respect to the nominal solution. In addition, particles would still experience a linear displacement, simply a smaller one [Fig. 24 (top), red and green curve].

In this work a new solution is proposed. By halving the dipole kicks component in the first accelerating gap, also the divergence picked up by the particles is halved. As a consequence, the second gap, which has a "nominal" dipole kick, oversteers the beam, which has now a negative divergence. This solution is shown graphically in Fig. 24 (bottom), which shows the single particle displacement along the IH structure field map with this solution adopted. The trajectory of the particles recalls the one of an undulator. Eventually, the last gap must also have a half dipole kick component, to zero the integrated kick.

The beam was transversally matched using a triplet focusing [Fig. 25 (bottom)]. A relatively high synchronous phase of −12 deg was chosen only to facilitate the particles injection into the 3 GHz DTL at 10 MeV. Indeed, a much lower synchronous phase (5 to 10 deg) would have been needed to accept and control the particle from the RFQ. The constant synchronous phase solution was adopted rather than the well-known KONUS [31] in view of its higher simplicity and robustness.

Concerning the longitudinal phase space, the Twiss α_z parameter of the RFQ beam was modified from 0 to 0.6 to improve the longitudinal matching. At the present stage, it has been assumed that this will be achievable with a different RFQ design [32]. Alternatively, one should consider to install a buncher cavity between the RFQ and the IH structure.

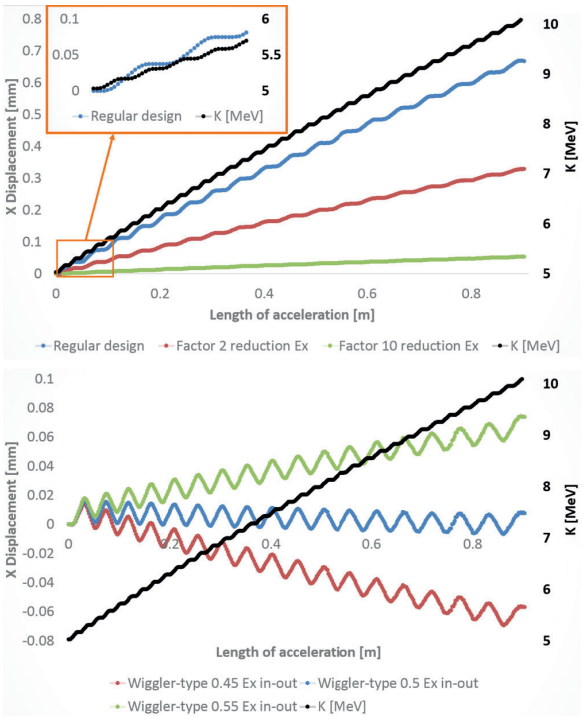

FIG. 24. Single particle tracking through the IH structure. Dipole kicks reduction (top) and undulator solution (bottom).

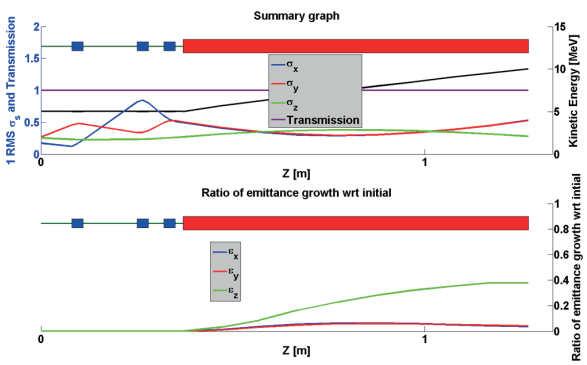

FIG. 25. Beam 1σ rms envelope through the IH structure from 5 to 10 MeV (top) and ratio of emittance growth with respect to initial (bottom).

TABLE III. Beam dynamics comparison between a IH-DTL and a full DTL solution in the 5 to 20 MeV/u range.

Parameter	IH + DTL	DTL
Synchronous phase [deg]	−12 (IH) and −20 (SCDTL)	−30 (5 to 10 MeV) and −25 (10 to 20 MeV)
Transmission	100	99.6
Transverse ϵ growth [%]	7	35
Longitudinal ϵ growth [%]	53	166
Total length [m]	3.01	2.89
Active length [m]	1.68	1.26
Number of accelerating structures	10	19
Number of PMQ	15	20
Peak power consumption [MW]	0.1(750 MHz) + 2.0(3 GHz)	3.7(3 GHz)

1. 750 MHz IH vs 3 GHz DTL beam dynamics comparison

In Sec. IVA it was shown that up to 20 MeV/u, the 750 MHz IH solution is more efficient than a 3 GHz DTL one from an rf efficiency point of view. In this section, the beam dynamics of the two solutions will be discussed. To get a fair comparison, here a IH (5 to 10 MeV) plus DTL (10 to 20 MeV) and full DTL (5 to 20 MeV) solutions will be compared. In such a way, it is possible to compare final beam parameters in similar phase space configurations.

The main aspects that have been compared are (i) particles transmission; (ii) emittance growth; (iii) overall length and space for diagnostic; (iv) number of elements; and (v) power consumption.

The authors decided to prioritize amongst all other parameters the beam transmission.

The SCDTL choice reveals to be particularly challenging in the 5 to 10 MeV range. Together with machinability and tuning considerations, and not forgetting the rf efficiency already mentioned, the beam dynamics also represents an issue. The space between the RFQ and the first SCDTL module is limited by the longitudinal acceptance of the beam. This limits the transverse matching of the beam, with repercussion on the emittance growth. A solution could be the installation of a buncher cavity, which would allow a longer matching section. A second problem arises from the relatively high accelerating gradient. At 5 MeV, the ratio between active and total length is well below 50%, since the rf defocusing has a square dependence with particle momentum [33]:

$$\Delta p_r = -\frac{\pi e E_0 T L r \sin\phi}{c\beta^2\gamma^2\lambda}, \tag{7}$$

and so it is necessary to have short accelerating tanks with PMQs in between. As a result, to accelerate over the same length, the gradient of the full DTL solution must be higher with respect to the IH-DTL solution. This results in a heavily longitudinally mismatched beam. Figure 28 shows the longitudinal phase space evolution of the beam in the first six DTL accelerating structures. As one can notice, the beam fits well in the first structure longitudinal bucket (red contour). However, the combination of high accelerating gradient and long drift sections between the different DTL tanks led to filamentation, eventually resulting in emittance growth and losses.

A higher synchronous phase would not help, since it will increase the rf defocusing. So shorter structures would be needed to transversally control the beam, and the accelerating gradient should be increased to keep the overall length constant. Two solutions could be followed. One could reduce the accelerating gradient to get a smoother acceleration in the first sections, but resulting in a longer linac. Alternatively, it would be possible to match the beam from tank to tank, by designing the DTL such that both the synchronous phase and the gradient adapt to the longitudinal orientation of the beam ellipse. This last proposal would raise significantly the rf design complexity of such linac.

The two designs are summarized in Table III and displayed graphically in Figs. 26 and 27. The overall dimensions are comparable in the two designs. However, the full DTL solution shows losses and a higher emittance growth. In addition, there is not space to allocate beam diagnostic. As a final comment, the full DTL solution requires more PMQs and accelerating structures, so a higher number of brazing and tuning procedures.

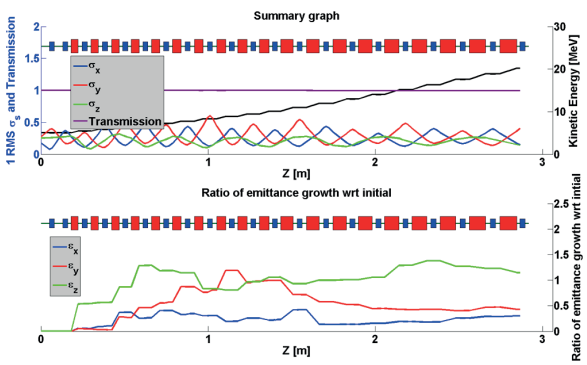

FIG. 26. Beam 1σ rms envelope through a DTL structure from 5 to 20 MeV (top) and ratio of emittance growth with respect to initial (bottom).

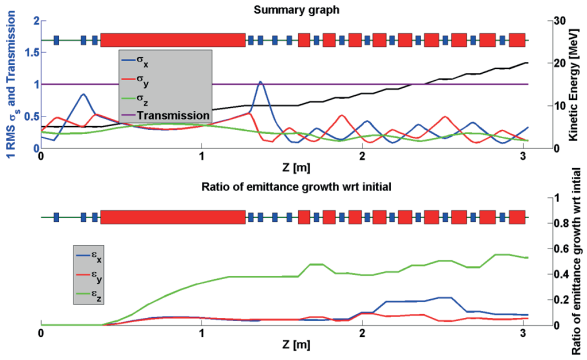

FIG. 27. Beam 1σ rms envelope through the IH + DTL structure from 5 to 20 MeV (top) and ratio of emittance growth with respect to initial (bottom).

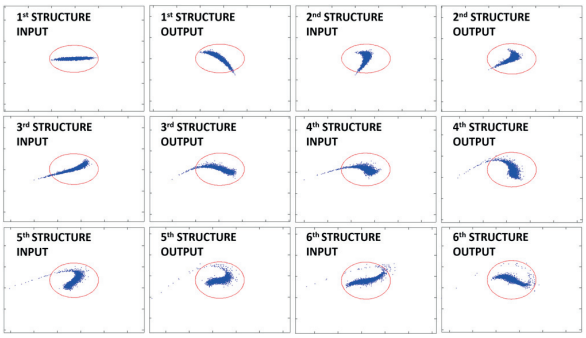

FIG. 28. Longitudinal phase space in and out the first six accelerating tanks of a DTL solution, from 5 to 7.7 MeV, with simplified buckets contour in red. The different pictures are in scale.

C. From 10 to 70 MeV

As it was demonstrated in Secs. IV B and V B 1, a IH-DTL solution is superior over a DTL from both an rf and a beam dynamics point of view. However, cost considerations led towards the decision of accelerating particles from 10 MeV onwards with a 3 GHz DTL linac.

The rf design has been discussed in Sec. IV C. Three modules tapered in length have been designed, each composed of nine accelerating tanks. The number of cells per tank goes from five in the first module, to six and seven in the second and last modules respectively. This in order to increase the ratio of active acceleration length over the total, taking advantage of the lower rf defocusing at higher particle momentum. The synchronous phase is constant and equal to −20 deg in all three modules. A solution with a higher number of cells in the first module was studied, but it was not feasible due to the too strong rf defocusing.

The main parameters of this linac section are summarized in Table IV.

The beam envelopes and emittance growth in this linac section are shown in Fig. 29.

1. Matching between a 750 MHz IH to a 3 GHz DTL

The beam matching between the 750 MHz IH and the 3 GHz DTL is one of the most critical parts of the project. In the longitudinal phase space there is a reduction of a factor 4 in the phase acceptance, given by frequency increase. Concerning the energy acceptance, there is a factor 2 reduction, given by the square root dependence of λ, as shown in Eq. (8):

$$\omega_{\max} = \sqrt{\frac{2qE_0T\beta^3\gamma^3\lambda}{\pi mc^2}(\phi_s\cos\phi_s - \sin\phi_s)}. \qquad (8)$$

However a factor $\sqrt{\beta^3\gamma^3}$ helps in increasing the energy acceptance, which was one of the motivations in delaying the jump at 3 GHz from 5 to 10 MeV/u. In particular, going from 5 to 10 MeV, the acceptance for protons increases by a factor 0.22.

In the transverse phase space, the geometric emittance decreases by a factor $\beta\gamma$, so by about 50% between 5 and 10 MeV. Nevertheless, while the RFQ is a bunching device, and it was specifically developed to inject particles into a 3 GHz structure, the IH is an accelerating structure, so it was not obvious at the beginning to be capable of reaching a good transition and matching at 10 MeV.

A 33 cm long transverse matching section with four PMQs was designed to make the transition from a triplet focusing system, used for the IH structure, to a FODO lattice. The Twiss parameters were matched to have a phase advance of almost 90 deg in the SCDTL structures. A full transmission of the beam is reached, and the transverse emittance growth is well below 5% at the end of the linac (Fig. 29). In the first linac sections there is a local transverse emittance growth up to 20%, due to a residual initial mismatch. This effect cancels out due to the acceleration of the beam.

TABLE IV. SCDTL main parameters.

Module	Output Energy [MeV]	Number of cells	Active length [m]	Ratio Active/Total Length	Average active Gradient [MV/m]	Peak Power [MW]	Average ZTT [MΩ/m]
1	20	5	0.78	0.53	13.6	1.9	75
2	40	6	1.31	0.64	16.2	3.7	94
3	70	7	2.05	0.74	15.6	5.7	88

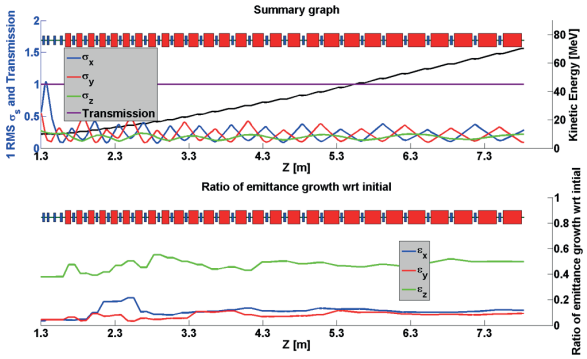

FIG. 29. Beam 1σ rms envelope through the DTL structure from 10 to 70 MeV (top) and ratio of emittance growth with respect to initial (bottom).

D. From 70 to 230 MeV

The protons are eventually accelerated up to 230 MeV in the high gradient linac. Following the considerations of Sec. IV E 1, the authors consider the BTW and the CCL solutions are ultimately even. However, we will review two designs, based on the two technologies, but comparable in length and number of elements. Before presenting the high gradient linac beam dynamics design, in the following section we review the theory of an energy varying beam line.

1. Maximizing the energy acceptance of a beam line

As the other 3 GHZ TERA linacs, the focusing is achieved by PMQs. The energy is varied by adjusting the powers and the phases of the rf pulses produced by the klystrons. In the case of protons, to reach the conventional range of penetration in water equivalent tissues, one needs protons ranging from 70 to 230 MeV.

In the following, we derive the condition to maximize the energy acceptance of a beam line composed of PMQs, for a given lattice geometry. One can start from the basic beam dynamics equations that can be found in the general particle accelerators books [34,35].

The normalized transverse acceptance of a linac is given by

$$A_n = \frac{\beta\gamma}{\beta^+} \cdot {R_{\mathrm{bore}}}^2. \tag{9}$$

For a given bore aperture, the linac transmission can be maximized by minimizing the Twiss betas. Also one can notice that the acceptance increases with the beam energy, because the geometric emittance shrinks. This is valid under the assumption that the normalized emittance remains constant.

It is convenient to express the Twiss beta in terms of phase advance. The FODO theory, even though not entirely correct when describing a linac, works well enough:

$$\beta^{\pm} = 2L\frac{1 \pm \sin(\mu/2)}{\sin(\mu)} \tag{10}$$

where L is the FODO length and μ is the transverse phase advance per cell.

In the case of a magnetic line with PMQs, the transverse phase advance and the Twiss β_s seen by the beam vary with the output energy.

In a round beam, as the RFQ output, we have $\epsilon_x \approx \epsilon_y$, so the geometric dimension of the beam is given by $A = \pi \cdot R^2 = \pi \cdot (\epsilon_x\beta_x + \epsilon_y\beta_y)$. The beam size is minimized in the case of phase advance of 90 deg, as one can verify by plugging Eq. (10) in the above expression, and take the derivative. Having however a varying phase advance as a function of the energy, one needs to find the best compromise that maximizes the acceptance in the range of energy of interest.

The optimum is found when the phase advance is 90 deg at the minimum beam line energy, and then decreases as the beam energy increases. The decrease has to be such that

$$\frac{\beta^+_{E_{\mathrm{min}}}}{\beta^+_{E_{\mathrm{max}}}} = \frac{(\beta\gamma)_{E_{\mathrm{min}}}}{(\beta\gamma)E_{\mathrm{max}}} \tag{11}$$

which simply means that the beam envelope must have the same dimension in the two extreme cases at the end of the line. Since the β^+ and the $\beta\gamma$ curves as a function of the final beam energy have a positive second order derivative, the worst conditions are found at the two extremes.

In conclusion, one shall follow these steps in the lattice design: (i) match transversally the beam for a 90 deg phase advance at the linac minimum energy section, in order to minimize the emittance growth; (ii) maximize the cumulative transmission at the minimum and maximum linac energy; the transmission in all other cases lies in between these two results; (iii) if there are losses, reduce the FODO length, or increase the beam aperture.

2. The high gradient BTW linac

An 18 accelerating structures linac was designed. The target gradient is 40 MV/m, with maximum values of Sc and of the surface electric field equal to 0.48 MW/mm^2 and 160 MV/m, respectively. The linac is approximately 6.2 m long, and accelerates the particles up to 230 MeV. The gradient chosen does not fully exploit the limit at which the structure has been designed (50 MV/m) to maintain a safety margin in terms of BDR. In addition, the compactness goal of the structure was already reached with a 40 MV/m gradient. Finally, this 20% reduction in gradient translates into a 36% reduction in rf thermal load into the structure, allowing a higher DF of 0.01%. The synchronous phase is −15 deg in all the accelerating structures.

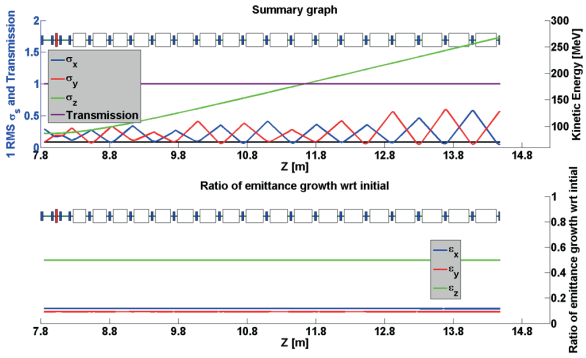

FIG. 30. Beam 1σ rms envelope through the HG BTW linac with no acceleration after 70 MeV (top) and ratio of emittance growth with respect to initial (bottom).

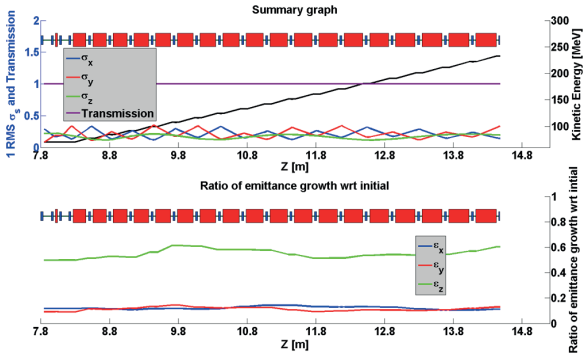

FIG. 31. Beam 1σ rms envelope through the HG BTW linac with full acceleration up to 230 MeV (top) and ratio of emittance growth with respect to initial (bottom).

Varying the phase and amplitude of the rf power in each accelerating structure allows for a smooth variation of the final energy. For this reason, a single coupler solution has been studied (see Sec. IV E).

The emittances and beam envelopes are shown in Figs. 30 and 31 for the two extreme cases of no acceleration and full acceleration, respectively.

The matching section between the SCDTL and the BTW linac is considerably easier than the 10 MeV transition. The solution proposed here comprises four PMQs and a buncher cavity to improve the longitudinal matching. This is just a temporary solution, given that the medium energy beam transfer line (MEBT), as shown in Fig. 2, is much longer and involves also dipoles. This part has not been studied yet since the mechanical design has yet to be finalized.

3. The high gradient CCL linac and comparison with the BTW one

The design presented above reaches full transmission of the particles between 70 and 230 MeV, but is however quite at the limit in terms of maximum Twiss beta. All the BTW accelerating structures are 12 cells long. This means that it is possible to obtain an exactly equivalent CCL design, composed of 18 accelerating structures, ten cells long.

As a result, the different between the two solutions translates in a different peak power consumption, accordingly to ZTT difference reported in Fig. 22. This difference is about 7% at 70 MeV and gets null at 230 MeV.

E. Beam dynamics in a *cyclinac* solution

This article discusses the first design of an *all-linac* solution for the TULIP project. As mentioned, the majority of the studies carried out in the past focused instead on a *cyclinac* solution. Here a detailed beam dynamics study of this concept is presented, in order to point out the major differences.

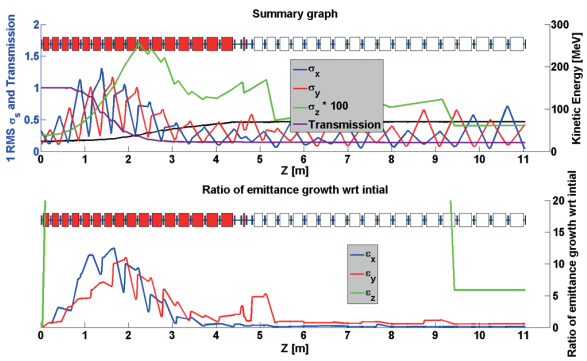

FIG. 32. Beam 1σ rms envelope through a *cyclinac* TULIP solution with no acceleration after 70 MeV (top) and ratio of emittance growth with respect to initial (bottom).

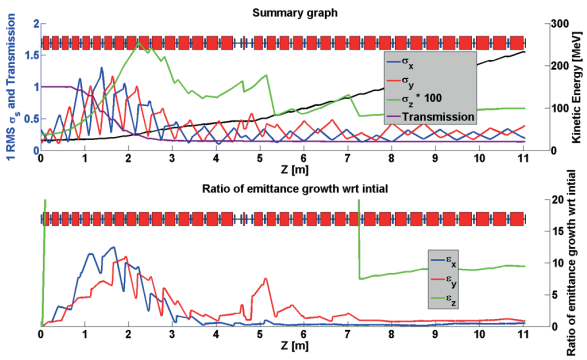

FIG. 33. Beam 1σ rms envelope through a *cyclinac* TULIP solution with full acceleration up to 230 MeV (top) and ratio of emittance growth with respect to initial (bottom).

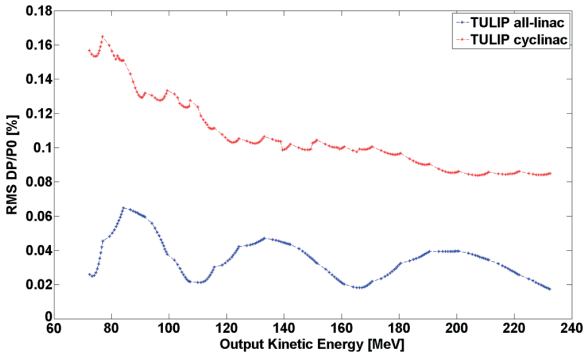

FIG. 34. Beam output energy spread in TULIP *all-linac* and *cyclinac* as a function of the final kinetic energy.

The 11th accelerating structure of the SCDTL linac accepts as input particles at 24 MeV. It has been supposed to replace the previous linac section with a commercial 24 MeV cyclotron. This would result in a bigger transverse emittance, and a continuous beam for the 3 GHz rf frequency, as discussed in Sec. V B 1. The transverse emittance can be collimated, however the beam cannot be chopped at 3 GHz. As a result, the beam will be lost in the linac section, with losses that are proportional to the ratio synchronous phase −360 deg. This situation has been simulated, and the results are presented in Figs. 32 and 33.

The losses are concentrated in the first 3 m of this design, causing activation of the copper structure and surrounding materials. However, here we would like to draw the reader's attention to the emittance growth. While the transverse one is "controlled" by the linac acceptance, so it does not grow uncontrolled, the longitudinal phase space is heavily influenced.

These two aspects reflect into a higher complexity and costs of the beam transport line from the linac output to the patient. The increase in normalized transverse emittance requires bigger magnets aperture, therefore eventually costs. On the other hand, the increased longitudinal emittance results in a more variable energy spread as a function of the beam output energy. This impacts on the design of the magnetic channel, which needs a higher momentum acceptance to control the dispersion.

In Fig. 34 one can notice the difference just explained. The transverse Twiss parameters are instead comparable in magnitude for the two solutions.

VI. SUMMARY

A *all-linac* solution of the TULIP project has been presented. In this paper we first discussed the rf design of the different accelerating structures composing the linac chain. Particular attention has been devoted to two novel accelerating structures studied in detailed by the authors: a 750 MHz IH structure, and a BTW high gradient structure. A 0.38β BTW prototype has been

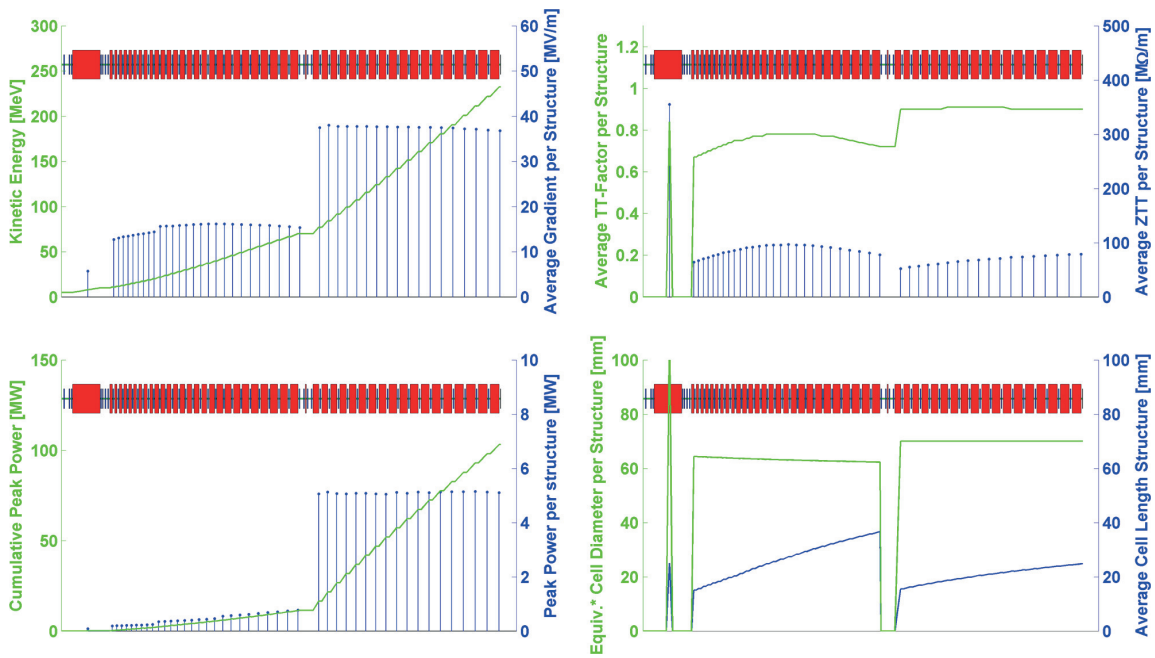

FIG. 35. TULIP *all-linac* main accelerating parameters.

TABLE V. TULIP *all-linac*—A summary.

Linac section	Operating frequency [MHz]	Output energy [MeV]	Average gradient [MV/m]	Synchronous phase [deg]	Active length [m]	Cumulative Length [m]	Average ZTT [MΩ/m]	Peak power [MW]
RFQ	750	5	2.6	15 (final)	2	2	38	0.4
IH	750	10	5.7	12	0.9	3.3	350	0.1
DTL	2998.5	70	15.5	20	4.1	9.8	86	13
BTW-CCL	2998.5	70–230	37.7	15	4.4	17.5	68	108

built and is under test at CERN. The average target accelerating gradient in the structure is 50 MV/m, with a corresponding maximum surface electric field of 200 MV/m, and modified Poynting vector Sc of 0.75 $\mathrm{MW/mm^2}$.

The beam dynamics linac design features full transmission and minimized emittance growth, and it has been accomplished with full tracking of the particles from the RFQ output up to 230 MeV, using rf EM field maps for the accelerating structures computed with HFSS. This is a *uniqum* for such a long linac. The effort is justified by the peculiar cavities considered that, as discussed, show dipolar components, asymmetries and traveling wave regimes that cannot be simulated with standard tracking codes. This is the reason why the novel tracking code RF-TRACK has been developed explicitly for this project.

The TULIP *all-linac* solution with the main design parameters are summarized in Fig. 35 and Table V. Figure 35 top left and bottom left show clearly the division of the two sections of the project: a fairly low gradient and high efficiency section up to 70 MeV, placed on the ground, and a high gradient section that will be mounted on the gantry.

The beam dynamic design is summarized in Figs. 36 and 37 for the two extreme cases of no acceleration and full acceleration.

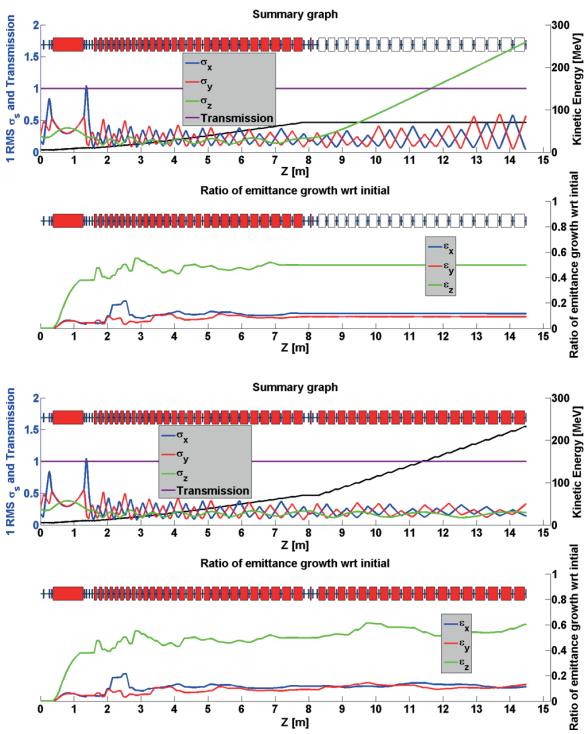

FIG. 36. Beam 1σ rms envelope through the TULIP *all-linac* solution and ratio of emittance growth with respect to initial. No acceleration after 70 MeV (top) and full acceleration up to 230 MeV (bottom).

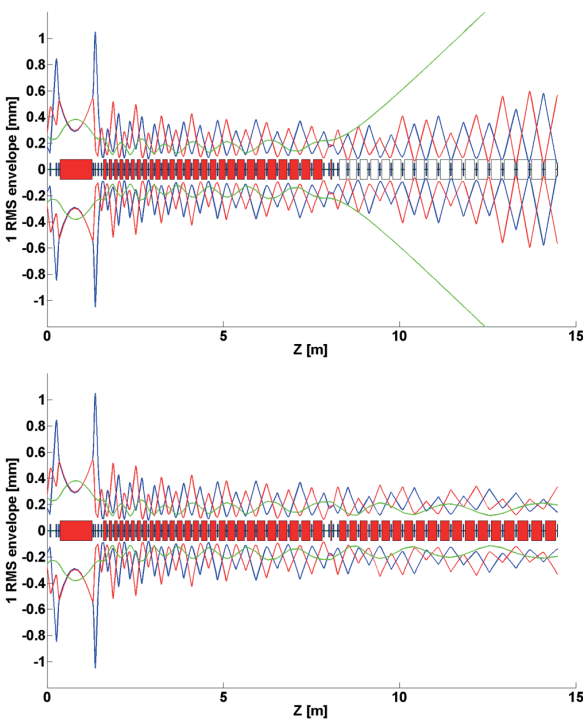

FIG. 37. The 70 MeV (top) and 230 MeV (bottom) beam envelopes along TULIP *all-linac*. 1 rms σ_x (red), σ_y (blue) and σ_z (green).

ACKNOWLEDGMENTS

The authors would like to sincerely thank Professor U. Amaldi for having initiated and supported this study. On different aspects, this work has relied on the fruitful contributions and discussions with many colleagues from TERA Foundation and CERN, in particular A. Degiovanni, M. Vaziri, M. Bucciantonio, I. Syratchev, W. Wuensch, E. Montesinos, A. Lombardi and V. Dimov.

[1] Particle Therapy Cooperative Group (PTCOG) Collaboration, http://www.ptcog.com.

[2] U. Amaldi, S. Braccini, and P. Puggioni, High frequency linacs for hadron therapy, *Reviews of Accelerator Science and Technology (RAST)* (World Scientific, Singapore, 2009), Vol. II, pp. 111–131.

[3] R. W. Hamm, K. R. Crandall, and J. M. Potter, Preliminary design of a dedicated proton therapy linac, in *Proceedings of the 1991 Particle Accelerator Conference, San Francisco, CA, 1991* (IEEE, New York, 1991).

[4] U. Amaldi, M. Grandolfo, and L. Picardi, *The RITA Network and the Design of Compact Proton Accelerators* (INFN, Frascati, 1996), Chap. 9.

[5] U. Amaldi *et al.*, LIBO—A linac booster for proton therapy: Construction and test of a prototype, Nucl. Instrum. Methods Phys. Res., Sect. A **521**, 512 (2004).

[6] C. De Martinis *et al.*, Acceleration tests of a 3 GHz proton linear accelerator (LIBO) for hadron therapy, Nucl. Instrum. Methods Phys. Res., Sect. A **681**, 10 (2012).

[7] C. Roncisvalle, L. Picardi, A. Ampollini, G. Bazzano, F. Marracino, P. Nenzi, C. Snels, V. Surrenti, M. Vadrucci, and F. Ambrosini, First acceleration of a proton beam in a side coupled drift tube linac, Europhys. Lett. **111**, 14002 (2015).

[8] M. Vretenar *et al.*, A compact high-frequency RFQ for medical applications, in *Proceedings of 27th Linear Accelerator Conference, Geneva, Switzerland, 2014* (2014), pp. THPP040https://cds.cern.ch/record/2062619.

[9] http://www.advancedoncotherapy.com/Our-LIGHT-system/Product-overview.

[10] A. Degiovanni *et al.*, Design of a fast-cycling high-gradient rotating linac for proton therapy, in *Proceedings of the 4th International Particle Accelerator Conference, IPAC-2013, Shanghai, China, 2013* (JACoW, Shanghai, China, 2013).

[11] A. Degiovanni *et al.*, High gradient rf test results of S-band and C-band cavities (to be published).

[12] A. Degiovanni, High gradient proton linacs for medical applications, Ph.D. thesis, EPFL, 2014.

[13] A. Degiovanni *et al.*, TERA high gradient test program of rf cavities for medical linear accelerators, Nucl. Instrum. Methods Phys. Res., Sect. A **657**, 55 (2011).

[14] S. Benedetti *et al.*, RF design of a novel S-band backward traveling wave linac for proton therapy, in *Proceedings of 27th Linear Accelerator Conference, Geneva, Switzerland* (2014), pp. THPP061http://cds.cern.ch/record/2062620.

[15] S. Benedetti *et al.*, Fabrication and testing of a novel S-band backward traveling wave accelerating structure for proton therapy linacs, in *Proceedings of the 28th Linear Accelerator Conference - LINAC16, East Lansing, MI, USA, 2016* (2016).

[16] P. Puggioni, Radio frequency design and measurements of a linear hadron accelerator for cancer therapy, M.Sci. thesis, Universita' degli studi Milano Bicocca, 2008.

[17] A. M. Lombardi, V. A. Dimov, M. Garlasche', A. Grudiev, S. Mathot, E. Montesinos, S. Myers, M. Timmins, and M. Vretenar, Beam dynamics in a high frequency RFQ, in *Proceedings of the 6th International Particle Accelerator Conference (IPAC 2015): Richmond, Virginia, USA, 2015* (2015), pp. WEYB2, http://accelconf.web.cern.ch/AccelConf/IPAC2015/papers/weyb2.pdf.

[18] U. Ratzinger, H-type linac structures. CERN Accelerator School: Radio frequency engineering, *Seeheim, Germany, 2000*.

[19] S. Benedetti, A. Grudiev, and A. Latina, Design of a 750 MHz IH structure for medical applications, *LINAC'16, East Lansing, MI, 2016*.

[20] A. Grudiev, S. Calatroni, and W. Wuensch, New local field quantity describing the high gradient limit of accelerating structures, Phys. Rev. ST Accel. Beams **12**, 102001 (2009).

[21] S. Verdu' Andre's, High-gradient accelerating structure studies and their application in hadron therapy, Ph.D. thesis, Universitat de Vale'ncia, 2012.

[22] I. Syratchev (private communication).

[23] S. Pitman, R. Apsimon, and G. Burt, ProBE: Proton boosting extension for imaging and therapy, in *Proceedings of the 28th Linear Accelerator Conference - LINAC16, East Lansing, MI, USA, 2016* (2016).

[24] A. Latina, RF-Track: Beam tracking in field maps including space-charge effects. Features and benchmarks, in *Proceedings of the 28th Linear Accelerator Conference - LINAC16, East Lansing, MI, USA, 2016* (2016).

[25] S. Benedetti *et al.*, Design of a proton traveling wave linac with a novel tracking code, *IPAC'15, Richmond, VA, 2015*.

[26] http://www.desy.de/mpyflo/.

[27] S. B. van der Geer, General particle tracer: A 3D code for accelerator and beam line design, in *Proceedings of the 6th European Particle Accelerator Conference, Stockholm, 1998* (IOP, London, 1998).

[28] E. Jensen, Superfish Exercise. Cern Accelerator School—rf for accelerators, *Ebeltoft, Denmark, 2010* [arXiv:1201.4648].

[29] E. Montesinos (private communication).

[30] S. Kurennoy *et al.*, H-mode accelerating structures with permanent-magnet quadrupole beam focusing, Phys. Rev. ST Accel. Beams **15**, 090101 (2012).

[31] R. Tiede, U. Ratzinger, H. Podlech, C. Zhang, and G. Clemente, KONUS beam dynamics designs using H-mode cavities, Hadron Beam **1**, 2013 (2008).

[32] A. Lombardi and V. Dimov (private communication).

[33] M. Vretenar, Introduction to rf linear accelerators. Cern Accelerator School—General accelerator physics, *Frascati, Italy, 2008*.

[34] H. Wiedemann, *Particle Accelerator Physics* (Springer, New York, 2007).

[35] T. P. Wangler, *RF Linear Accelerators* (Wiley-VCH, New York, 2008).

Bibliography

[1] "Particle Therapy CoOperative Group patients statistics website."

[2] R. R. Wilson, "Radiological use of fast protons," *Radiology*, vol. 47, no. 5, pp. 487–491, 1946.

[3] P. Bryant, L. Weisser, L. Badano, G. Borri, M. Crescenti, P. Holy, S. Reimoser, A. Maier, P. Knaus, M. Pavlovic, *et al.*, "Proton-Ion Medical Machine Study (PIMMS), 2," tech. rep., 2000.

[4] H. Bethe and J. Ashkin, *Experimental Nuclear Physics,*. J. Wiley, New York,, 1953.

[5] M. Durante and H. Paganetti, "Nuclear physics in particle therapy: a review," *Reports on Progress in Physics*, vol. 79, no. 9, p. 096702, 2016.

[6] U. Amaldi, "Notes on medical physics - Trento," 1999.

[7] A. Degiovanni, *High gradient proton linacs for medical applications.* PhD thesis, École Polytechnique Fédérale de Lausanne, 2014.

[8] C. Bert and M. Durante, "Motion in radiotherapy: particle therapy," *Physics in medicine and biology*, vol. 56, no. 16, p. R113, 2011.

[9] M. Bucciantonio, *Development of an advanced Proton Range Radiography system for hadrontherapy.* PhD thesis, University of Bern, 2015.

[10] S. Pitman, R. Apsimon, G. Burt, A. Green, A. Grudiev, H. Owen, A. Solodko, and W. Wuensch, "ProBE: Proton Boosting Extension for Imaging and Therapy," in *28th Linear Accelerator Conf.(LINAC'16), East Lansing, MI, USA, 25-30 September 2016*, pp. 283–286, JACOW, Geneva, Switzerland, 2017.

[11] D. Watts, *Detectors for Quality Assurance in Hadrontherapy.* PhD thesis, Universitat Autonoma de Barcelona, 2013.

[12] J. Gueulette, V. Gregoire, and P. Scalliet, "Radiobiological characterization of clinical proton and carbon-ion beams," in *CERN Accelerator School - CAS*, 2015.

[13] G. Kraft, "Tumor therapy with heavy charged particles," *Progress in Particle and Nuclear Physics*, vol. 45, Supplement 2, pp. S473–S544, 2000.

[14] T. Friedrich, U. Scholz, T. ElsäSser, M. Durante, and M. Scholz, "Systematic analysis of RBE and related quantities using a database of cell survival experiments with ion beam irradiation," *Journal of radiation research*, p. rrs114, 2012.

[15] J. S. Loeffler and M. Durante, "Charged particle therapy—optimization, challenges and future directions," *Nature reviews Clinical oncology*, vol. 10, no. 7, pp. 411–424, 2013.

[16] C. R. Peeler, D. Mirkovic, U. Titt, P. Blanchard, J. R. Gunther, A. Mahajan, R. Mohan, and D. R. Grosshans, "Clinical evidence of variable proton biological effectiveness in pediatric patients treated for ependymoma," *Radiotherapy and Oncology*, vol. 121, no. 3, pp. 395–401, 2016.

[17] C. Baumgarten, "Cyclotrons with fast variable and/or multiple energy extraction," *Physical Review Special Topics-Accelerators and Beams*, vol. 16, no. 10, p. 100101, 2013.

[18] T. Antalya, "Future Trends in Cyclotrons," 2015. CERN Accelerator School: Accelerators for Medical Applications, Vosendorf, Austria.

[19] Y. Jongen, M. Abs, A. Blondin, W. Kleeven, S. Zaremba, D. Vandeplassche, V. Aleksandrov, S. Gursky, G. Karamysheva, N. Y. Kazarinov, *et al.*, "Current status of the IBA C400 cyclotron project for hadron therapy," in *EPAC*, vol. 8, p. 1806, 2008.

[20] J. Flanz, "Future (of) Synchrotrons for Particle Therapy," 2015. CERN Accelerator School: Accelerators for Medical Applications, Vosendorf, Austria.

[21] U. Amaldi, S. Braccini, and P. Puggioni, "High frequency linacs for hadrontherapy," *Reviews of Accelerator Science and Technology*, vol. 02, pp. 111–131, 2009.

[22] R. Mertzig, M. Breitenfeldt, S. Mathot, J. Pitters, A. Shornikov, and F. Wenander, "A high-compression electron gun for C6+ production: concept, simulations and mechanical design," *Nuclear Instruments and Methods in Physics Research Section A: Accelerators, Spectrometers, Detectors and Associated Equipment*, vol. 859, pp. 102 – 111, 2017.

[23] U. Amaldi, "Private communication," 2017.

[24] R.W. Hamm and K.R. Crandall and J.M. Potter, "Preliminary design of a dedicated proton therapy linac," in *Proc. of Particle Accelerator Conference - PAC91*, 1991.

[25] T. Collaboration, *The RITA Network and the design of compact proton accelerators.* Eds INFN Frascati, 1996.

[26] U. Amaldi, P. Berra, K. Crandall, D. Toet, M. Weiss, R. Zennaro, E. Rosso, B. Szeless, M. Vretenar, C. Cicardi, C. De Martinis, D. Giove, D. Davino, M. Masullo, and V. Vaccaro, "LIBO-a linac-booster for protontherapy: construction and test of a prototype," *Nuclear Instruments and Methods A*, vol. 521, pp. 512–529, 2004.

[27] C. De Martinis, D. Giove, U. Amaldi, P. Berra, K. Crandall, M. Mauri, M. Weiss, R. Zennaro, E. Rosso, B. Szeless, M. Vretenar, M. R. Masullo, V. Vaccaro, L. Calabretta, and A. Rovelli, "Acceleration tests of a 3 GHz proton linear accelerator (LIBO) for hadrontherapy," *Nuclear Instruments and Methods A*, vol. 681, pp. 10–15, July 2012.

[28] A. Degiovanni, U. Amaldi, D. Bergesio, C. Cuccagna, A. LoMoro, P. Magagnin, P. Riboni, and V. Rizzoglio, "Design of a fast-cycling high-gradient rotating linac for protontherapy," in *Proc. of International Particle Accelerator Conference - IPAC13*, (Shanghai (China)), pp. 3642–3644, 2013.

[29] A. Garonna, *Cyclotron designs for ion beam therapy with cyclinacs.* PhD thesis, École Polytechnique Fédérale de Lausanne, 2011.

[30] S. Verdú Andrés, *High-gradient accelerating structure studies and their application in hadrontherapy.* PhD thesis, Univeristat de València, 2013.

[31] C. Ronsivalle, L. Picardi, A. Ampollini, G. Bazzano, F. Marracino, P. Nenzi, C. Snels, V. Surrenti, M. Vadrucci, and F. Ambrosini, "First acceleration of a proton beam in a side coupled drift tube linac," *EPL (Europhysics Letters)*, vol. 111, no. 1, p. 14002, 2015.

[32] M. Vretenar, E. Montesinos, M. Timmins, M. Garlaschè, A. Grudiev, A. Dallocchio, S. Mathot, V. Dimov, and A. Lombardi, "A compact high-frequency RFQ for medical applications," in *Proc. of Lineac Accelerator Conference - LINAC14*, 2014.

[33] "http://www.advanceoncotherapy.com/Our-LIGHT-system/Product-overview."

[34] V. G. Vaccaro, M. R. Masullo, C. De Martinis, L. Gini, D. Giove, A. Rainó, V. Variale, L. Calabretta, A. Rovelli, S. Barone, and S. Lanzone, "A side coupled proton linac module 30-35 MeV first acceleration tests," in *Proc. of Linear Accelerator Conference - LINAC10*, (Tsukuba (Japan)), pp. 467–469, 2010.

[35] "https://www.researchitaly.it/en/projects/apulia-infn-itel-technological-transfer-for-the-treatment-of-tumours/."

[36] S. Kutsaev, R. Agustsson, L. Faillace, A. Goel, B. Mustapha, A. Nassiri, P. Ostroumov, A. Plastun, and E. Savin, "High gradient accelerating structures for carbon therapy linac," in *Proc. of Linear Accelerator Conference - LINAC16*, 2016.

[37] A. Fabris, C. Serpico, P. Delgiusto, M. Milloch, and A. Grudiev, "Perspectives of the S-band Linac of Fermi," in *Proc. of Linear Accelerator Conference - LINAC14*, 2014.

[38] A. Degiovanni, U. Amaldi, R. Bonomi, M. Garlasché, A. Garonna, S. Verdú-Andrés, and R. Wegner, "TERA high gradient test program of RF cavities for medical linear accelerators," *Nuclear Instruments and Methods in Physics Research Section A: Accelerators, Spectrometers, Detectors and Associated Equipment*, vol. 657, no. 1, pp. 55–58, 2011.

[39] P. Puggioni, "Radiofrequency design and measurements of a linear hadron accelerator for cancer therapy," Master's thesis, Universitá degli studi Milano Bicocca, 2008.

[40] J. H. Billen and L. M. Young, *Poisson Superfish.* Los Alamos National Laboratory, 2005. LA-UR-96-1834.

[41] "http://www.ansys.com/products/electronics/ansys-hfss."

[42] T. P. Wangler, *Principles of RF linear accelerators.* John Wiley & Sons, 1998.

[43] H. Wiedemann, *Particle accelerator physics.* Springer, 2007.

[44] A. Grudiev, S. Calatroni, and W. Wuensch, "A new local field quantity describing the high gradient limit of accelerating structures," *Phys. Rev. ST Accel. Beams*, vol. 12, 102001, pp. 1–11, 2009.

[45] U. Ratzinger, "H-type linac structures," 2000.

[46] A. Lombardi, E. Montesinos, M. Timmins, M. Garlaschè, A. Grudiev, S. Mathot, V. Dimov, S. Myers, and M. Vretenar, "Beam dynamics in a high frequency RFQ," in *Proc. of International Particle Accelerator Conference - IPAC15*, 2015.

[47] E. Montesinos, "Private communication," 2016.

[48] P. Lapostolle and M. Weiss, "Formulae and procedures useful for the design of linear accelerators," CERN 001, CERN, 2000.

[49] S. Benedetti, A. Grudiev, and A. Latina, "Design of a 750 MHz IH structure for medical applications," in *Proc. of Linear Accelerator Conference - LINAC16*, 2016.

[50] U. Amaldi, A. Citterio, M. Crescenti, A. Giuliacci, C. Tronci, and R. Zennaro, "CLUSTER: A high-frequency H-mode coupled cavity linac for low and medium energies," *Nuclear Instruments and Methods in Physics Research Section A: Accelerators, Spectrometers, Detectors and Associated Equipment*, vol. 579, no. 3, pp. 924–936, 2007.

[51] S. S. Kurennoy, L. J. Rybarcyk, J. F. O'Hara, E. R. Olivas, and T. P. Wangler, "H-mode accelerating structures with permanent-magnet quadrupole beam focusing," *Physical Review Special Topics-Accelerators and Beams*, vol. 15, no. 9, p. 090101, 2012.

[52] N. Alharbi, F. Gerigk, and M. Vretenar, "Field stabilization with post couplers for DTL tank1 of Linac4," No. 012, 2006.

[53] S. Ramberger, "Private communication," 2017.

[54] M. Vretenar, "Introduction to RF Linear Accelerators," 2008. CERN Accelerator School: General Accelerator Physics, Frascati, Italy.

[55] S. Benedetti, U. Amaldi, A. Grudiev, A. Degiovanni, and W. Wuensch, "RF design of a novel S-band backward travelling wave linac for proton therapy," in *Proc. of Linear Accelerator Conference - LINAC14*, 2014.

[56] S. Benedetti, T. Argyropoulos, N. C. Lasheras, A. Degiovanni, M. Garlasché, J. G. Navarro, A. Grudiev, G. Mcmonagle, A. Solodko, R. Wegner, B. Woolley, and W. Wuensch, "Fabrication and testing of a novel S-band backward travelling wave accelerating structure for proton therapy linacs," in *Proc. of Linear Accelerator Conference - LINAC16*, 2016.

[57] A. Lunin, V. Yakovlev, and A. Grudiev, "Analytical solutions for transient and steady state beam loading in arbitrary traveling wave accelerating structures," *Phys. Rev. ST Accel. Beams*, vol. 14, 052001, pp. 1–8, 2011.

[58] I. Syratchev, "Private communication," 2016.

[59] V. Vaccaro, C. De Martinis, D. Giove, M. Masullo, S. Mathot, A. Raino, R. Rush, and V. Variale, "Design, construction and low power RF tests of the first module of the ACLIP linac," pp. 1836–1838, 2008.

[60] R. Tiede, U. Ratzinger, H. Podlech, C. Zhang, and G. Clemente, "KONUS beam dynamics designs using H-mode cavities," *Hadron Beam*, vol. 1, p. 2013, 2008.

[61] A. Lombardi and V. Dimov, "Private communication," 2016.

[62] A. Lombardi, G. Bellodi, M. Eshraqi, F. Gerigk, J. Lallement, S. Lanzone, E. Sargsyan, R. Duperrier, and D. Uriot, "Beam dynamics in Linac4 at CERN," *HB2008 Proceedings, Nashville, USA*, 2008.

[63] R. Augusto, T. Mendonca, F. Wenander, L. Penescu, R. Orecchia, K. Parodi, A. Ferrari, and T. Stora, "New developments of 11C post-accelerated beams for hadron therapy and imaging," *Nuclear Instruments and Methods in Physics Research Section B: Beam Interactions with Materials and Atoms*, vol. 376, pp. 374 – 378, 2016. Proceedings of the {XVIIth} International Conference on Electromagnetic Isotope Separators and Related Topics (EMIS2015), Grand Rapids, MI, U.S.A., 11-15 May 2015.

[64] P. Nadin and A. Garonna, "Private communication," 2016.

[65] U. Amaldi, "Use of linear ion accelerators for the treatment of atrial fibrillation and ion accelerator system there for," 2015. WO Patent App. PCT/IB2014/001,514.

[66] R. Seviour *et al.*, "Comparative Overview of Inductive Output Tubes," *ESS report, June*, 2012.

[67] M. Vretenar, "Private communication," 2017.

[68] A. Solodko and M. Garlasche', "Private communication," 2017.

[69] A. Olyunin and A. Solodko, "Rf measurements of high-gradient accelerating structure 03snv38012-yb01cs (medical n1) before bonding," cern internal report - edms n. 1495290, CERN, 2015.

[70] B. Woolley, *High power X-band RF test stand development and high power testing of the CLIC crab cavity*. PhD thesis, Lancaster University, 2015.

[71] A. Degiovanni and J. Navarro, "Private communication," 2016.

[72] A. Degiovanni, W. Wuensch, and J. Giner Navarro, "Comparison of the conditioning of high gradient accelerating structures," *Phys. Rev. Accel. Beams*, vol. 19, p. 032001, Mar 2016.

[73] R. Rajamaki et al, "Breakdown positioning in clic prototype rf accelerating structures." CLIC Workshop, 2016.

[74] R. Helm and R. Miller, *Particle Dynamics*. North-Holland Publ. Co., 1969.

[75] J. Wang and G. Loew, "Field emission and RF breakdown in high-gradient room-temperature linac structures," PUB 7684, SLAC, 1997.

[76] R. Fowler and L. Nordheim, "Electron emission in intense electric fields," *Proc. R. Soc. Lond. A,*, vol. 119, pp. 173–181, May 1928.

[77] W. Kilpatrick, "Criterion for vacuum sparking designated to include both RF and DC," *The Review of Scientific Instruments*, vol. 28, p. 824, October 1957.

[78] T. Boyd, "Kilpatrick criterion," AT-1 report 28, Los Alamos Group, February 1982.

[79] K. Crandall, *Documentation for program LINAC*. TERA internal note (TERA c/o CERN).

[80] D. Uriot and N. Pichoff, "Tracewin documentation," *CEA internap report CEA/DSM/DAPNIA/SEA/2000/45*, 2011.

[81] "http://www.desy.de/ mpyflo/."

[82] S. Van der Geer, M. De Loos, and D. Bongerd, "General Particle Tracer: A 3D code for accelerator and beam line design," in *Proc. 5th European Particle Accelerator Conf., Stockholm*, 1996.

[83] M. Vretenar, "General design considerations on structures, power sources and accessories," 2016. Workshop on design of a novel Linac for challenging environments - CERN.

[84] K. R. Crandall and D. P. Rusthoi, *Trace 3-D Documentation*, 1997. Third Edition, Los Alamos National Laboratory.

[85] S. Benedetti, U. Amaldi, A. Latina, and A. Grudiev, "Design of a proton travelling wave linac with a novel tracking code," in *Proc. of International Particle Accelerator Conference - IPAC15*, 2015.

[86] A. Latina, "RF-Track: beam trackng in field maps including space-charge effects. Features and benchmarks," in *Proc. of Linear Accelerator Conference - LINAC16*, 2016.

[87] E. Jensen, "Superfish exercise," 2010. CERN Accelerator School: RF for Accelerators, Ebeltoft, Denmark.

[88] "https://www.gnu.org/software/octave/."

[89] "www.swig.org."

[90] "https://www.python.org/."

[91] A. Latina, *RF-Track: a minimalistic multipurpose tracking code featuring space-charge*. CERN HSI Meeting - Feb 12, 2016.

Stefano Benedetti

CERN Meyrin, 6/R-025, L04500
☎ *+41 2276 64218*
✉ *stefano.benedetti@cern.ch*

Education

Mar 2014 – Nov 2017 **Ph.D. in Accelerator Physics**, *École Polytechnique Fédérale de Lausanne (EPFL)*, Switzerland.
Thesis title: "High-gradient and high-efficiency linear accelerators for hadron therapy"
EPFL Advisor: Prof. L. Rivkin
CERN Supervisor: Dr. A. Grudiev

Sep 2009 – Oct 2011 **Master of Science in Nuclear and Energetic Engineering**, *Politecnico di Torino*, Italy.
Thesis title: "Neutronic coupling between the MYRRHA core and the In-Vessel Fuel Storages" - Belgian Nuclear higher Education Network (BNEN) Master Thesis
University Advisor: Prof. S. Dulla
BNEN Supervisors: Prof. P. Baeten and Dr. A. Stankovskiy

Sep 2006 – Dec 2009 **Bachelor of Science in Energetic Engineering**, *Politecnico di Torino*, Italy.
Thesis title: "Confronto fra metodi per il calcolo del fattore di utilizzazione termica di una cella di combustibile nucleare"
University Advisors: Prof. P. Ravetto and Prof. S. Dulla

2001 – 2006 **High School in Science**, *Liceo A. Rosmini*, Rovereto, Italy.

Research Experience

Apr 2017 – Present **Accelerator Physicist - Senior Fellow**, *CERN*, Genève, Switzerland.
Beam dynamics simulations and measurements on CERN Linac 3 and RFQ redesign

Mar 2013 – Mar 2017 **Accelerator Physicist - Ph.D. Student**, *CERN and TERA Foundation*, Genève, Switzerland.
Research activity on linear accelerators for hadron therapy. TERA Foundation group coordinator from October 2013 to Aug 2015. Main fields of work:
- RF design of standing-wave and travelling-wave cavities
- Linear accelerators design
- Particle tracking simulations
- Code developments and data analysis
- Thermal analysis of accelerating cavities

Apr 2011 – Jul 2011 **Intern**, *SCK•CEN Research Centre*, Mol, Belgium.
Internship in the framework of the BNEN, followed as Erasmus student, in the Advanced Nuclear Systems group
- Neutronic, thermal, and safety study of the in-vessel fuel storage of nuclear reactor MYRRHA, by means of Monte Carlo probabilistic code
- Writing of an internal technical report to assess the effect of nuclear fuel rods accidentally dip into fresh water

Professional Experience

Jan 2012 – Mar 2013 **HSE&RAMS Engineer**, *RAMS&E s.r.l.*, Turin, Italy.
Engineering consulting company founded by a professor of the Polytechnic University of Turin. Safety and production efficiency activity in sectors such as energy, oil&gas and transport industries
- Safety Report writing for major industries, eventually with the role of project manager;
- Safety integrity level studies in accordance to IEC61508 and IEC61511, eventually with the role of project manager;
- Gained the role of company expert in the potentially explosives atmospheres area classification.

Publications

Apr 2017 S. Benedetti, A. Grudiev and A. Latina, *High gradient linac for proton therapy.* Physical Review Accelerators and Beams 20, 040101, April 2017

Sep 2016 S. Benedetti, A. Grudiev and A. Latina, *Design of a 750 MHz IH structure for medical applications.* In Proc. of LINAC16 Conference, East Lansing (MI), USA, 2016

Sep 2016 S. Benedetti, T. Argyropoulos, C. Blanc Gutierrez, N. Catalan Lasheras, A. Degiovanni, D. Esperante Pereira, M. Garlasche', J. Giner Navarro, A. Grudiev, G. Mcmonagle, A. Solodko, M. Timmins, R. Wegner and W. Wuensch, *Fabrication and testing of a novel S-Band backward travelling wave accelerating structure for proton therapy linacs.* In Proc. of LINAC16 Conference, East Lansing (MI), USA, 2016

May 2015 S. Benedetti, A. Grudiev, A. Latina, U. Amaldi. *Design of a Proton Travelling Wave Linac with a Novel Tracking Code.* In Proc. of IPAC15 Conference, Richmond (VA), USA, 2015

Jul 2016 A. Degiovanni, S. Benedetti, , M. Garlasche', J. Giner Navarro, P. Magagning, G. Mcmonagle, I. Syratchev and W. Wuensch, *Design and High Power Measurements of a 3 GHz Rotary Joint for Medical Applications.* CLIC Note 1071

May 2015 S. Benedetti, A. Grudiev, A. Latina, U. Amaldi. *Design of a Proton Travelling Wave Linac with a Novel Tracking Code.* In Proc. of IPAC15 Conference, Richmond (VA), USA, 2015

Sep 2014 S. Benedetti, A. Degiovanni, A. Grudiev, W. Wuensch, U. Amaldi. *RF Design of a Novel S-Band Backward Travelling Wave Linac for Proton Therapy.* In Proc. of LINAC14 Conference, Geneva, Switzerland, 2014

Sep 2013 A. Degiovanni, U. Amaldi, S. Benedetti, D. Bergesio, A. Garonna, G. Molinari, E. van Lier, R.L.Watt, D. Brasse,M. Pellicioli,M. Rousseau, J. Schuler, S. Braccini, and E.V. Kirillova. *Emittance Measurements at the Strasbourg TR24 Cyclotron for the Addition of a 65Mev Linac Booster.* In Proc. of CYC13 Conference, Vancouver (BC), Canada, 2013

Oral Presentations

Mar 2017 **Compact proton therapy: TULIP**, *CLIC workshop 2017*, CERN.

Jun 2016 **Updates on TULIP and CABOTO projects**, *Early-career researchers in medical applications @ CERN – Short talks*, CERN.

Jan 2015 **High-gradient medical accelerating structure**, *CLIC workshop 2015*, CERN.

Feb 2014 **RF design of a high-gradient medical linac accelerating structure**, *CLIC workshop 2014*, CERN.

Courses and Trainings

Jun 2016 **Using Mathematica to analyse and model experimental data**, *EPFL EDPY Doctoral Program course*, Lausanne, Switzerland.

May 2015 **Accelerators for Medical Applications**, *CAS 2015*, Wien, Austria.

Jan 2015 **Transverse Beam Dynamics**, *JUAS 2015*, Archamps, France.

Sep 2014 **Introduction to Accelerator Physics**, *CAS 2014*, Prague, Czech Repubblic.

May 2014 **Power Converters**, *CAS 2014*, Baden, Switzerland.

Jan 2014 **ANSYS-HFSS co-simulations**, *CERN Training Centre 2014*, CERN, Switzerland.

Certifications

Mar 2012	**European Master of Science in Nuclear Engineering**, *ENEN Certification for international education in Nuclear Engineering.*
Feb 2012	**Qualified for the Engineering Profession**, *Italian State Exam.*

Computer skills

Accelerator Physics	HFSS, Superfish, RF-Track, TraceWin, Parmteq, Trace3D, Travel
General Physics	Ansys, Simulink
Data analysis	Matlab, Mathematica
OS	Linux, Mac OS, Windows
Documentation tools	LaTex, Mac iWork suite, Microsoft Office suite

Languages

Italian	Native
English	Fluent
French	Fluent
Spanish	Intermediate
German	Basic

Hobbies and Interests

Outdoor	Travelling, rock climbing, mountaineering, ski touring
Indoor	Cooking, reading, financial markets

References

Dr. A. Grudiev	Supervisor Doctoral Thesis, alexej.grudiev@cern.ch, 022 76 72521
Prof. U. Amaldi	Co-supervisor Doctoral Thesis, ugo.amaldi@cern.ch, 022 76 77565
Dr. A. Latina	Co-supervisor Doctoral Thesis, andrea.latina@cern.ch, 022 76 74859